Standard Model and Exotic Physics with Electrons and Muons at DØ

by

Daniel Ofir Whiteson

B.A. (Rice University) 1997

A dissertation submitted in partial satisfaction of the
requirements for the degree of
Doctor of Philosophy

in

Physics

in the

GRADUATE DIVISION
of the
UNIVERSITY OF CALIFORNIA, BERKELEY

Committee in charge:
Professor Mark Strovink, Chair
Professor Robert Jacobsen
Professor Stephen Derenzo

Fall 2003

The dissertation of Daniel Ofir Whiteson is approved:

Chair Date

Date

Date

University of California, Berkeley

Fall 2003

Standard Model and Exotic Physics with Electrons and Muons at DØ

by

Daniel Ofir Whiteson

Abstract

Standard Model and Exotic Physics with Electrons and Muons at DØ

by

Daniel Ofir Whiteson

Doctor of Philosophy in Physics

University of California, Berkeley

Professor Mark Strovink, Chair

The rate of production and kinematic characteristics of collisions which produce both an energetic electron and an energetic muon provide sensitive probes of Standard Model and exotic processes. We present measurements of the top quark pair production cross section,

$$\sigma_{t\bar{t}} = 10.1^{+9.4}_{-6.4}\ (stat)^{+2.3}_{-2.1}\ (syst) \pm 1.0\ (lumi)\ \text{pb},$$

and the W boson pair production cross section,

$$\sigma_{WW} = 18.5^{+13.9}_{-9.9}\ (stat)^{+4.3}_{-4.0}\ (syst) \pm 1.9\ (lumi)\ \text{pb},$$

from collisions of protons and anti-protons at center of mass energies of 1.96 TeV in a sample with total integrated luminosity of 97.7 pb^{-1}.

We set limits on the production cross section of arbitrary new processes which would produce electrons and muons, set limits on the cross section for the production of supersymmetric particles via the processes: $p\overline{p} \rightarrow \chi_1^{\pm}\chi_2^0 \rightarrow l\nu\chi_1^0 ll\chi_1^0$, $p\overline{p} \rightarrow \chi_1^+\chi_1^- \rightarrow l\nu\chi_1^0 l\nu\chi_1^0$, and $p\overline{p} \rightarrow \tilde{t}_1^+\tilde{t}_1^- \rightarrow bb\chi_1^+\chi_1^- \rightarrow bbl\nu\chi_1^0 l\nu\chi_1^0$. Additionally, we place limits on boson and fermion mass scales in theories of minimal supergravity.

Professor Mark Strovink
Dissertation Committee Chair

To my mother, who knew I could; to my father, who showed me how.

Contents

List of Figures **vii**

List of Tables **xviii**

1 Introduction **1**

2 The Theory of Particles and their Interactions **5**
2.1 Particles and Forces 6
2.2 Quantum Field Theory 9
2.3 The Standard Model 11
2.3.1 Quantum Electrodynamics 11
2.3.2 The Weak Interaction 14
2.3.3 Electroweak Unification 15
2.3.4 Spontaneous Symmetry Breaking 17
2.3.5 The Strong Force 18
2.3.6 Calculations 18
2.4 Particle Production in $p\overline{p}$ Collisions 19
2.4.1 Top Quark Pair Production 20
2.4.2 W boson pair production 22
2.5 Extensions to the Standard Model 22
2.5.1 Supersymmetry 23
2.5.2 Other Theories 25

3 Experimental Apparatus **28**
3.1 The Fermilab Accelerator Complex 28
3.2 Interactions of Energetic Particles with Matter 29
3.2.1 Electrons and Photons 30

3.2.2 Muons . . . 31
3.2.3 Hadronic Particles . . . 32
3.2.4 Neutrinos . . . 33
3.3 The DØ Detector . . . 33
3.3.1 Coordinate System . . . 34
3.3.2 Luminosity System . . . 35
3.3.3 Tracking Detectors . . . 36
3.3.4 Calorimeter . . . 39
3.3.5 Muon Spectrometer . . . 40
3.3.6 Trigger System . . . 45

4 Event Trigger **49**
4.1 Level 1 Efficiency . . . 50
4.2 Level 3 Efficiency . . . 53
4.3 Total Efficiency . . . 54

5 Event Reconstruction and Object Identification **59**
5.1 Event Reconstruction . . . 60
5.1.1 Track Reconstruction . . . 60
5.1.2 Vertex Reconstruction . . . 62
5.1.3 Muons . . . 64
5.1.4 Electrons . . . 66
5.1.5 Jets . . . 68
5.1.6 Missing Energy . . . 72
5.2 Reconstruction Efficiency . . . 77
5.2.1 Muon Reconstruction . . . 77
5.2.2 Muon Distance of Closest Approach . . . 80
5.2.3 Muon Track Matching . . . 80
5.2.4 Muon Isolation . . . 82
5.2.5 Muon Resolution . . . 84
5.2.6 Electron Reconstruction . . . 93
5.2.7 Electron Identification . . . 93
5.2.8 Electron Likelihood . . . 94
5.2.9 Electron Energy Resolution . . . 96
5.2.10 Jets . . . 98
5.2.11 Missing Energy . . . 98
5.2.12 Monte Carlo Corrections . . . 101

6 Contributions to the Data Set **108**
6.1 Instrumental Backgrounds . . . 108
6.1.1 Correlations . . . 110
6.1.2 Prescription . . . 112
6.1.3 Complementary Estimation . . . 115
6.1.4 Variation of Likelihood Efficiency . . . 116
6.2 Physics Backgrounds . . . 117
6.2.1 Simulation of Backgrounds . . . 119
6.2.2 Contamination from τ decay . . . 121
6.2.3 Normalization of σ_Z . . . 122

7 Data **129**
7.1 Run Selection and Luminosity . . . 129
7.1.1 Luminosity . . . 130
7.1.2 Calorimeter Quality . . . 130
7.1.3 Muon Quality . . . 132
7.1.4 Track Quality . . . 132
7.1.5 Integrated Luminosity . . . 133
7.2 Event Pre-Selection . . . 133
7.3 The Dataset . . . 134

8 Measurement of Standard Model Processes **138**
8.1 Measurement of $\sigma_{t\bar{t}} \times BR(t\bar{t} \to e\mu bb)$ . . . 139
8.1.1 Production Cross Section . . . 142
8.1.2 Discussion . . . 143
8.2 Measurement of $\sigma_{WW} \times BR(WW \to e\mu)$ . . . 151
8.2.1 Production Cross Section . . . 152
8.2.2 Discussion . . . 154

9 Searches for Exotic Processes **162**
9.1 Supersymmetric Models . . . 162
9.1.1 $p\overline{p} \to \chi_1^{\pm}\chi_2^0 \to l\nu\chi_1^0 ll\chi_1^0$ . . . 163
9.1.2 $p\overline{p} \to \chi_1^+\chi_1^- \to l\nu\chi_1^0 l\nu\chi_1^0$ . . . 164
9.1.3 $p\overline{p} \to \tilde{t}_1^+\tilde{t}_1^- \to bb\chi_1^+\chi_1^- \to bbl\nu\chi_1^0 l\nu\chi_1^0$ . . . 164
9.1.4 Choice of Parameters . . . 165
9.1.5 Efficiencies and Expected Yields . . . 167
9.2 The QUAERO Package . . . 181
9.2.1 Regions of Sensitivity . . . 182
9.2.2 Evaluation of L . . . 183

9.3 Tests of mSUGRA Processes . . . 184
9.3.1 Interpretation of L . . . 184
9.3.2 Test of a Standard Model Process . . . 185
9.3.3 Tests of mSUGRA Models . . . 187
9.3.4 Discussion . . . 210
9.4 Search for Unanticipated Exotic Processes . . . 215
9.4.1 Discussion . . . 219

10 Discussion **227**

Bibliography **229**

A Global Tracking at Level 3 **238**
A.1 Requirements . . . 238
A.2 Algorithm . . . 239
A.2.1 Axial Track Finding . . . 239
A.2.2 Stereo Tracking . . . 242
A.2.3 Regional Tracking and Caching . . . 248
A.2.4 Track Parameter Definitions . . . 249
A.2.5 Algorithmic Parameters . . . 250
A.3 Performance . . . 251
A.3.1 Efficiency for $Z \to e^+e^-$ candidates . . . 251
A.3.2 Efficiency as a function of P_T^{min} . . . 263
A.4 Errors and resolutions . . . 266
A.4.1 Track Parameter Errors . . . 266
A.4.2 Cluster errors . . . 273
A.4.3 DCA resolution . . . 274
A.5 Stereo Tracking . . . 274
A.6 Tests for Online Running . . . 275
A.6.1 Timing . . . 275
A.6.2 Memory Consumption . . . 275
A.6.3 Trigger Simulator Verification . . . 276

B Electron Likelihood **289**
B.1 Electron Reconstruction and Variables . . . 290
B.2 Sources of Background . . . 292
B.3 Likelihood formulation . . . 293
B.4 Performance . . . 294
B.5 Topological Dependence . . . 297

C Muon Isolation Strategies **308**
C.1 Strategies . . . 310
C.1.1 Jets . . . 311
C.1.2 Calorimeter energy, "Halo Energy" . . . 311
C.1.3 Tracks . . . 313
C.1.4 TrackJets . . . 313
C.1.5 Track Halo . . . 314
C.2 Performance . . . 314
C.2.1 Data samples definitions . . . 314
C.2.2 Jet isolation . . . 318
C.2.3 Track isolation . . . 318
C.2.4 Track-Jet isolation . . . 319
C.2.5 Track Halo . . . 320
C.2.6 Halo Isolation . . . 320
C.2.7 Individual isolations . . . 323
C.2.8 Combined Isolations . . . 323
C.3 Discussion . . . 325

D Support Vector Machines **332**
D.1 Support Vector Regression . . . 333
D.1.1 Linear Regression . . . 333
D.1.2 Non-linear regression: kernel functions . . . 336
D.2 Search for the Higgs Boson . . . 337
D.2.1 Kernel Function Widths . . . 341
D.2.2 Training Sample Size . . . 342
D.3 Discussion . . . 343

List of Figures

2.1 Feynman diagram for the leading order interaction between electron and photon fields in Quantum Electrodynamics. 13
2.2 Parton distribution fuctions at varying scales of transverse momentum exchange (Q^2)[8]. 26
2.3 Feynman diagrams which represent leading order top quark pair production processes. 27
2.4 Feynman diagrams which represent leading order W boson pair production processes. 27

3.1 The Fermilab accelerator complex. 30
3.2 Energy loss through ionization of muons in various energy regimes. From [62]. 32
3.3 Side view of the DØ detector. 34
3.4 The DØ central tracking system. 37
3.5 A view of the structure of the silicon microstrip tracker along the beam axis. 38
3.6 A schematic diagram of an individual calorimeter cell. 41
3.7 Cut-away view of the calorimeter, showing the division into electromagnetic and hadronic sections as well as central and forward regions. 42
3.8 A side view of the DØ detector, highlighting the organization of the calorimeter cells into towers of constant pseudo-rapidity. 43
3.9 The DØ muon system. 44
3.10 Drift tubes in the central muon system. An example tube (*below*) and stacking of tubes in the A (*upper left*) and BC (*upper right*) layers. . . . 45
3.11 Arrangement of drift tubes in the forward muon system. 46
3.12 Arrangement of scintillator pixels in the central muon system. 47

4.1 L1 muon efficiencies, relative to offline reconstructed muons, as a function of offline muon P_T (*left*) and η (*right*). 52
4.2 Per-electron efficiency to fire the L1 CEM(1,5) trigger term, relative to offline reconstructed electrons, as a function of corrected offline electron P_T (*left*) and η (*right*). 54
4.3 Per-jet efficiency to fire the L1 CEM(1,5) trigger term, relative to offline reconstructed jets, as a function of offline corrected jet P_T (*left*) and η (*right*). 56
4.4 Top, distribution of P_T for electrons in $t\bar{t} \to e\mu jj$ events. Center, per-event probability to pass L1 EM trigger, when only electrons are allowed to fire the trigger, or when either electrons or jets may fire it. Bottom, total L1 EM efficiency as a function of corrected electron P_T. 57
4.5 Per-electron efficiency to fire the L3 Ele(1,10) trigger term, relative to offline reconstructed electrons, as a function of offline corrected electron P_T (*left*) and η (*right*). The efficiency is roughly independent of η; the low value is due to the domination of this sample by low-P_T electrons. 58

5.1 Details of the primary vertex reconstruction. The number of tracks associated with the vertex (*top*), and the position in z (*bottom*). 63
5.2 Muon distance of closest approach (DCA), (*top*), DCA error (*middle*), and DCA significance, (*bottom*) in $t\bar{t} \to e\mu jj$ events. 74
5.3 Correction to energies of jets in the data , as a function of jet E_T and η, (*left*). Errors in the correction, (*right*). 75
5.4 Correction to energies of jets in simulation , as a function of jet E_T and η, (*left*). Errors in the correction, (*right*). 76
5.5 Di-muon invariant mass of a local, central-matched muon and a central track. Cases where the second track has a reconstructed muon are also shown. 79
5.6 Muon tracking and matching efficiencies as a function of ϕ and η of the muon,in simulated events. 81
5.7 Muon tracking and matching efficiencies as a function of ϕ and η of the muon, in data. 82
5.8 Correction to simulated tracking efficiency, as a function of muon η. . . . 83
5.9 Muon isolation efficiency, as a function of jet multiplicity. 84
5.10 Comparison of the fitted mean of the dimuon invariant mass spectrum in real and simulated data, for varying values of the smearing parameter f. 89
5.11 Comparison of the fitted mean of the dimuon invariant mass spectrum in real and simulated data, for varying values of the smearing parameters f and C. See text for details. 90

5.12 Kolmogorov-Smirnoff statistic between distributions of muon P_T spectrum in simulated and real data, for central and forward muons from $Z \to \mu\mu$ events. . . . 91
5.13 Agreement between simulated and real data in the di-muon invariant mass spectrum (*left*) and muon P_T spectrum (*right*) for central (*top*) and forward (*bottom*) muons. . . . 92
5.14 Comparison of the fitted mean of the dimuon invariant mass spectrum in real and simulated data, for varying values of the smearing parameters f. For central (*left*) and forward (*right*) muons. . . . 102
5.15 Agreement between simulated and real data in the di-electron invariant mass spectrum (*left*) and electron P_T spectrum (*right*) for central electrons. . . . 103
5.16 Variation in jet multiplicity with variations in the jet energy scale. . . . 103
5.17 Transverse momentum of the Z boson, and the unclustered energy in data and simulation . . . 104
5.18 Correlations between the transverse momentum of the Z boson and the unclustered energy, in data (*left*) and in simulation (*right*). . . . 104
5.19 Correlations between the squared transverse momentum and the squared recoil of the Z boson, in data (*left*) and in simulation (*right*). . . . 105
5.20 Variation in the Kolmogorov-Smirnoff statistic comparing distributions of transverse missing energy in data and in simulation. . . . 106
5.21 Agreement of missing transverse energy distributions in observed and simulated $Z \to ee$ events. The distributions are shown in both log (*left*) and linear (*right*) scales. . . . 107

6.1 Preselected events which contain a loose electron, and the subset of those events which contain a tight electron, (*left*). The rate at which loose electrons pass the tight cuts, as a function of the muon halo energy (*right*). Shown for the central calorimeter. . . . 112
6.2 Simulated heavy flavor QCD events which contain a loose electron, and the subset of those events which contain a tight electron, (*left*). The rate at which loose electrons pass the tight cuts, as a function of the muon halo energy (*right*). Shown for the central calorimeter. . . . 113
6.3 Distributions in missing transverse energy and transverse mass of isolated muon events. . . . 115
6.4 Variation in electron misidentification rate and efficiency with varying likelihood thresholds. . . . 117
6.5 Variation in estimated sizes of real and misidentified contributions to $e\mu$ dataset with likelihood threshold. . . . 118

6.6 Distributions in lepton P_T, missing transverse energy and number of jets for the largest Standard Model contributions to $e\mu$. 125
6.7 Distributions of electron and muon transverse energies for simulated $t\bar{t} \to lljj$ events in which the final state contains a direct ($l = e, \mu$) or indirect ($l = \tau \to e, \mu$) electron and muon. 126
6.8 Jet multiplicity in $Z \to \mu\mu$ events (*top*), inclusive percentage of total rate (*middle*) and invariant mass distributions for leading portions (*bottom*). . 127
6.9 Jet multiplicity in ALPGEN simulated $Z \to \mu\mu$ events (*top*), inclusive percentage of total rate (*middle*) and invariant mass distributions for leading portions (*bottom*). 128

7.1 Transverse momentum of electrons and muons, in data and backgrounds. The same distributions are shown in a log scale (*left*) and linear scale (*right*). 135
7.2 Missing transverse energy, calorimetric missing transverse energy and jet multiplicity for data and backgrounds. The same distributions are shown in a log scale (*left*) and linear scale (*right*) 136
7.3 Difference in ϕ between the leptons (*top*), distribution in η of the electrons (*middle*), and η of the muons (*bottom*). 137

8.1 Data and backgrounds during topological selection to enhance $t\bar{t}$ signal. Top, distribution in H_T^e, the sum of jet and electron transverse energies; prior to requirement $H_T^e > 120$ GeV, four candidates remain. Bottom, distribution in jet multiplicity, prior to requirement $N_{jets} \geq 2$; three candidates survive final selection. The same distributions are shown in a log scale (*left*) and linear scale (*right*) 144
8.2 XY view of candidate event. 145
8.3 RZ and lego views of candidate event. 145
8.4 XY view of candidate event. 146
8.5 RZ and lego views of candidate event. 146
8.6 XY view of candidate event. 147
8.7 RZ and lego views of candidate event. 147
8.8 Analysis of the consistency of the lepton momenta and missing transverse energy with the hypothesis of the decay of two W bosons. The object energies are shown to the left for each event. In the space of neutrino transverse energy components, countors of constant W mass are parabolae. If $p_{\nu_e} + p_{\nu_\mu} = \not{E}_T$, then these parabolae should intersect; here are shown the parabolae corresponding to $m_W = 80.4$ GeV. 148

8.9 Summary of measurements of the top quark production cross section at DØ in Run2. 149
8.10 Summary of measurements of the top quark production cross section at CDF and DØ in Run1 and Run2. 150
8.11 Data and backgrounds after requiring no reconstructed jets in order to enhance WW signal. 156
8.12 Distribution in Missing Transverse Energy and distance in ϕ between leptons; physics backgrounds (*top*), expected signal (*middle*), and data (*bottom*). 157
8.13 Optimization of the point of selection for the quantity $\not\!\!E_T \times [\pi - \Delta\phi(e,\mu)]$ by maximizing $\frac{S}{\sqrt{(S+B)}}$. 158
8.14 XY and RZ views of $WW \to e\mu$ candidate event. The electron appears as electromagnetic (*red*) energy in the calorimeter associated with a central track (*black*); jets appear as electromagnetic and hadronic (*blue*) energy; the muon appears as muon chamber hits (*red, orange, green squares*) and a central track (*black*). 159
8.15 Analysis of the consistency of the lepton momenta and missing transverse energy with the hypothesis of the decay of two W bosons. The object energies are shown to the left for each event. In the space of neutrino transverse energy components, countors of constant W mass are parabolae. If $p_{\nu_e} + p_{\nu_\mu} = \not\!\!E_T$, then these parabolae should intersect; here are shown the parabolae corresponding to $m_W = 80.4$ GeV. 160
8.16 Selection of $WW \to ll$ candidates by CDF [72]. 161

9.1 Feynman diagram for the leading contribution to the process $p\overline{p} \to \chi_1^\pm \chi_2^0 \to l\nu\chi_1^0 ll\chi_1^0$. 164
9.2 Electron and muon energies for $\chi_1^\pm \chi_2^0 \to l\nu\chi_1^0 ll\chi_1^0$ production at selected mSUGRA model points. 165
9.3 Next to leading order corrections to production cross sections for $p\overline{p} \to \chi_1^+\chi_2^0$ and $p\overline{p} \to \chi_1^+\chi_1^-$, adapted from [44]. 166
9.4 Feynman diagram for the leading contribution to the process $p\overline{p} \to \chi_1^+\chi_1^- \to l\nu\chi_1^0 l\nu\chi_1^0$. 167
9.5 Electron and muon energies for $\chi_1^+\chi_1^- \to l\nu\chi_1^0 l\nu\chi_1^0$ production at selected mSUGRA model points 168
9.6 Feynman diagram for the leading contribution to the process $p\overline{p} \to \tilde{t}_1^+\tilde{t}_1^- \to bb\chi_1^+\chi_1^- \to bbl\nu\chi_1^0 l\nu\chi_1^0$. 169
9.7 Electron, muon and jet energies for $\tilde{t}_1^+\tilde{t}_1^- \to bl\nu\chi_1^0 bl\nu\chi_1^0$ production atselected mSUGRA model points 170

9.8 Variation in masses of $\chi^0_{1,2}$ with mSUGRA parameter $m_{\frac{1}{2}}$. Various curves demonstrate a scan of m_0 in the region $[75, 250]$ GeV. 171
9.9 Variation in masses of $\chi^{\pm}_{1,2}$ with mSUGRA parameter $m_{\frac{1}{2}}$. Various curves demonstrate a scan of m_0 in the region $[75, 250]$ GeV. 172
9.10 Variation in masses of $\tilde{t}_{1,2}$ with mSUGRA parameter $m_{\frac{1}{2}}$. Various curves demonstrate a scan of m_0 in the region $[75, 250]$ GeV. 173
9.11 Variation in ratios of masses of relevent particles with mSUGRA parameter $m_{\frac{1}{2}}$. Various curves demonstrate a scan of m_0 in the region $[75, 250]$ GeV. 174
9.12 Variation in mass differences of relevent particles with mSUGRA parameter $m_{\frac{1}{2}}$. Various curves demonstrate a scan of m_0 in the region $[75, 250]$ GeV. 175
9.13 Mean electron (*left*) and muon (*center*) and $\chi^{\pm}$ (*right*) transverse momenta with variations in key mSUGRA parameters $m_0 = m_{\frac{1}{2}}$. 180
9.14 Measurement of $Z/\gamma^* \to \tau\tau$ production. The red line indicates the Standard Model value. 194
9.15 Data and expected backgrounds in like-signed $e\mu$ events. 195
9.16 Estimation of contributions to trilepton final state. No events are seen in the data 196
9.17 Test of the hypothesis $H_{\chi^{\pm}_1\chi^0_2}$with $m_0, m_{\frac{1}{2}} = 150$ GeV in the $e^+\mu^+\not{E}_T$ final state. Clockwise from top left: histogrammed events in the selected variable for the Standard Model (*red*) and the new physics hypothesis (*green*); probability densities for each hypothesis; subregions of the variable determined by placing cuts on the discriminant; and binned values of the discriminant for SM and new physics. 197
9.18 Histogram of the discriminant for the Standard Model (*red*) and the new physics $H_{\chi^{\pm}_1\chi^0_2}$with $m_0, m_{\frac{1}{2}} = 150$ GeV (*red*). All contributing final states have been combined. 198
9.19 Tests of the hypothesis $H_{\chi^{\pm}_1\chi^0_2}$with $m_0, m_{\frac{1}{2}} = 150$ GeV, at varying cross-sections, relative to the theoretical prediction. 199
9.20 Missing transverse energy in $e\mu$ events with no jets, for data and backgrounds in both log and linear scales. 200
9.21 Test of the hypothesis $H_{\chi^+_1\chi^-_1}$ with $m_0, m_{\frac{1}{2}} = 150$ GeV in the $e^-\mu^+\not{E}_T$ final state. Clockwise from top left: histogrammed events in the selected variable for the Standard Model (*red*) and the new physics hypothesis (*green*); probability densities for each hypothesis; subregions of the variable determined by placing cuts on the discriminant; and binned values of the discriminant for SM and new physics. 201

9.22 Missing transverse energy in $e\mu$ events with 2 reconstructed jets, for data and backgrounds in both log and linear scales. 202
9.23 Test of the hypothesis $H_{\tilde{t}\tilde{t}}$ with $m_0, m_{\frac{1}{2}} = 150$ GeV in the $e^-\mu^+\not\!\!E_T jj$ final state. Clockwise from top left: histogrammed events in the selected variable for the Standard Model (*red*) and the new physics hypothesis (*green*); probability densities for each hypothesis; subregions of the variable determined by placing cuts on the discriminant; and binned values of the discriminant for SM and new physics. 203
9.24 Limits on $\sigma_{\chi_1^\pm\chi_2^0}$. $m_0 = m_{\frac{1}{2}}$. 204
9.25 Limits on $\sigma_{\chi_1^+\chi_1^-} \times BR(e\mu)$. $m_0 = m_{\frac{1}{2}}$. 205
9.26 Limits on $\sigma_{\tilde{t}_1^+\tilde{t}_1^-} \times BR(e\mu)$. $m_0 = m_{\frac{1}{2}}$. 206
9.27 Limits on mSUGRA with varying parameters $m_0 = m_{\frac{1}{2}}$. 207
9.28 Limits on mSUGRA with $\mu > 0$ in the $m_0, m_{\frac{1}{2}}$ plane. 208
9.29 Limits on mSUGRA with $\mu < 0$ in the $m_0, m_{\frac{1}{2}}$ plane. 209
9.30 Exclusions in the $m_0, m_{\frac{1}{2}}$ using dilepton and electron+jets signatures in Run1, from [75]. 211
9.31 Exclusions in the $m_0, m_{\frac{1}{2}}$ plane using jets and $\not\!\!E_T$ signatures in Run1, from [74]. 212
9.32 Exclusions in the $m_0, m_{\frac{1}{2}}$, based primarily on searches for hZ (*dark blue*), $\chi\chi$ (*green*), and precision electroweak requirements (*light blue*), from [39]. 213
9.33 Limits on the mass of the lightest supersymmetic particle, derived from limits on $m_{\frac{1}{2}}$, from [39]. 214
9.34 Missing transverse energy in $e\mu$ events with no jets, for data and backgrounds in both log and linear scales. 218
9.35 Missing transverse energy in $e\mu$ events with a single jet, for data and backgrounds in both log and linear scales. 221
9.36 Missing transverse energy in $e\mu$ events with two jets, for data and backgrounds in both log and linear scales. 222
9.37 Upper limits on the production cross section of new physics in the $e\mu$ channel, as a function of the cut on missing transverse energy in the event. 223
9.38 Upper limits on the production cross section of new physics in the $e\mu j$ channel, as a function of the lower threshold on missing transverse energy in the event. 224
9.39 Upper limits on the production cross section of new physics in the $e\mu jj$ channel, as a function of the cut on missing transverse energy in the event. 225

9.40 XY and RZ views of the highest $\not\!\!E_T$ $e\mu j$ event. The electron appears as electromagnetic (*red*) energy in the calorimeter associated with a central track (*black*); jets appear as electromagnetic and hadronic (*blue*) energy; the muon appears as muon chamber hits (*red, orange, green squares*) and a central track (*black*). 226

A.1 Distance in ϕ between the outer two axial CFT hits versus inverse P_T for tracks from $Z \to bb$ events. Units of $\Delta\phi$ are radians and of P_T^{-1} are GeV^{-1}.240
A.2 Residuals in ϕ for axial cluster finding. Clockwise from top left: *(1)* shows the difference between the predicted and actual hit positions. *(2)* shows the difference between the predicted hit position and ϕ_{track}, the ϕ position of the MC track helix at this radius. *(3)* shows the difference between the actual hit position and ϕ_{track}. *(4)* shows the χ^2 contribution. For tracks with $P_t \geq 1.0$ GeV and $|DCA| \leq 1.0$ cm in 10 $t\bar{t}$ events with 1.1 minbias . 254
A.3 Effect of rotation of the rectangular histogram. The left image shows an unrotated histogram represented by the solid red box, where lines from clusters (dashed, in green) have similarly large and positive slopes, generating a longer diagonal peak. The rotated histogram is represented by the dotted blue box. As the image on the right demonstrates, this gives a smaller point of intersection and maximizes the angle between the lines from the clusters. 255
A.4 Residuals in z (cm) for stereo cluster finding. Clockwise from top left: *(1)* shows the difference between the predicted and actual hit positions. *(2)* shows the difference between the predicted hit position and z_{track}, the z position of the MC track at this radius. *(3)* shows the difference between the actual hit position and z_{track}. *(4)* shows the χ^2_Z contribution. For tracks with $P_T \geq 1.0$ GeV and $|DCA| \leq 1.0$ cm in 10 $t\bar{t}$ events with 1.1 minbias. 256
A.5 Track parameter illustration [52] 257
A.6 Residuals between EM object and nearest track in $Z \to e^+e^-$ data. Top is $\Delta\phi$; middle is $\Delta\eta$; bottom shows the correlation. 258
A.7 Efficiency for matching electrons to tracks in $Z \to e^+e^-$ data. Top row shows the absolute numbers of EM objects, axial matched EM's and stereo matched EM's as a function of ϕ (left),η (middle) and run number (right). Bottom shows the axial and stereo efficiency. 259
A.8 Ratio of transverse calorimetric energy to transverse track momentum. . 260
A.9 Residual between electron and the nearest CFT cluster at each of eight axial CFT layers. The solid line shows all the clusters, the blue region shows track matched electrons and the red region shows unmatched electrons. . 261

A.10 Left, the number of layers with a CFT cluster within 0.025 radians of the propagated electron position for matched and unmatched electrons. Right, the layers on which clusters were not found. 262
A.11 Track ϕ for varying values of the P_T^{min} threshold. 264
A.12 Track and hit multiplicities for varying values of the P_T^{min} threshold. . . 265
A.13 P_T spectrum for varying values of the P_T^{min} threshold. 266
A.14 Estimated tracking efficiency as a function of track P_T. 267
A.15 Variation of full efficiency threshold with P_T^{min}. 268
A.16 Residual in the track parameter DCA, for reconstructed and simulated tracks in 100 $t\bar{t} \to lljj$ events, for varying number of SMT clusters on the track. 269
A.17 Residual in the track parameter Z_0, for reconstructed and simulated tracks in 100 $t\bar{t} \to lljj$ events, for varying number of SMT clusters on the track. 270
A.18 Residual in the track parameter ϕ_0, for reconstructed and simulated tracks in 100 $t\bar{t} \to lljj$ events, for varying number of SMT clusters on the track. 271
A.19 Residual in the track parameter $\tan\lambda$, for reconstructed and simulated tracks in 100 $t\bar{t} \to lljj$ events, for varying number of SMT clusters on the track. 272
A.20 Residual in the track parameter $\frac{q}{P_T}$, for reconstructed and simulated tracks in 100 $t\bar{t} \to lljj$ events, for varying number of SMT clusters on the track. 277
A.21 Residual, error and pull for each of the five track parameters, for reconstructed tracks in 100 $t\bar{t} \to lljj$ events. 278
A.22 Top shows hit to track residuals; middle shows cluster errors; bottom shows hit to track pulls. Left column shows quantities in $r\phi$; right column shows quantities in z. From single electron Monte Carlo events. 279
A.23 Top shows hit to track residuals; middle shows cluster errors; bottom shows hit to track pulls. Left column shows quantities in $r\phi$; right column shows quantities in z. From run 160588. 280
A.24 Top, χ^2/N_{dof} for tracks from run 160588. Bottom, the chi^2 probability for each track. 281
A.25 Distance of closest approach for tracks reconstructed with a given P_T^{min} . 282
A.26 Variation of fitted DCA width with P_T^{min} 283
A.27 An estimate of the stereo tracking efficiencies by ϕ, as the ratio of stereo to axial tracks from figure A.11. 284
A.28 Distribution of running time on data with varying P_T^{min}. 285
A.29 Variation of timing with P_T^{min}. 286
A.30 Variation of timing with number of reconstructed tracks. 287
A.31 Total memory consumption by event. 288

B.1 Distributions of variables used in the likelihood for central calorimeter signal and backgrounds samples, as defined in the text. Distributions are shown only for EM objects which have a track candidate. 299
B.2 Correlations between selected variables use in the construction of the likelihood, for the central calorimeter signal sample (*left*) and the background sample (*right*). Distributions are shown only for those electrons which have a track candidate. 300
B.3 Correlations between E_T/p_T and electron p_T for the central calorimeter signal sample (*left*) and the background sample (*right*). Distributions are shown only for those electrons which have a track candidate. 301
B.4 Distributions of the discriminant $D(\overline{x})$ for central calorimeter signal and background samples, as defined in the text. From top, we begin with the simplist discriminant and add information by including more variables in the joint probability. 302
B.5 Efficiencies to have a track candidate for calorimeter EM objects in the signal and background samples. 303
B.6 Signal and background efficiencies in the central calorimeter for varying thresholds of the discriminants shown in Figure B.4. Note that the signal and background efficiencies assume a candidate track, the efficiency for which is detailed in Table 1. 304
B.7 Signal and background efficiencies in the central calorimeter for varying thresholds of the discriminants, where information from an individual parameter is removed in order to probe its individual discrimination power.Note that the signal and background efficiencies assume a candidate track, the efficiency for which is detailed in Table 1. 305
B.8 A comparison of the performance of the track matching, the likelihood and a grid-search in the central calorimeter over the six likelihood variables. . 306
B.9 The topological dependence of the signal and background efficiencies in the central calorimeter given a fixed cut on the discriminant. The distributions in the signal and background samples are the two left columns, respectively. The efficiencies are shown in the rightmost column. 307

C.1 Distance in R from the muon to closest jet. 310
C.2 A hollow cone in R, with inner edge R_a and outer edge R_b surrounding the muon. Calorimeter cell i is included in the cone if $R_b > R_i > R_a$. . . 312
C.3 Distribution of the jet to Muon distance in R (a). Efficiency and purity when R thresholds are varied (b). 315
C.4 Efficiency and purity for Track-Muon isolation with different track P_T thresholds. 317

C.5 Efficiency and purity for TrackHalo isolation with different outer cone sizes. . . . 322
C.6 Halo energies for Z and QCD samples (*left*). Efficiency for both samples as a function of the threshold (*right*). . . . 323
C.7 Efficiency versus purity for varying cone sizes for halo isolation. Optimizing the outer cone (a), and the inner cone (b). . . . 326
C.8 QCD efficiency for different inner cone sizes, at given signal (Z) efficiencies. . . . 327
C.9 Signal and background efficiency for variations on the simple cone summation. . . . 328
C.10 Signal and background efficiency for isolation strategies for central muons ($|\eta| < 1.0$, *left*) and forward muons ($|\eta| > 1.0$, *right*). . . . 329
C.11 Efficiency and purity curves for signal and background samples for track halo cuts, with different calorimeter halo cuts. Each curve begins at the calorimeter halo curve and describes the performance of the combined isolations. . . . 330
C.12 Signal and background efficiency for isolation strategies for central muons ($|\eta| < 1.0$, *left*) and forward muons ($|\eta| > 1.0$, *right*). . . . 331

D.1 Distributions in four parameters for the four processes. Clockwise from top left: reconstructed Higgs mass from two jets, total transverse energy, unbalanced or missing transverse energy and aplanarity. All variables are rescaled to $[-1, 1]$. . . . 344
D.2 Support vector regression (*left*), and artificial neural network (*right*) outputs for signal (Wh) and the three background processes ($Wb\bar{b}$, WZ^0, and $t\bar{t}$). Histograms are normalized to 1. . . . 345
D.3 Left, purity, p and efficiency, ε, as defined in the text, for support vector regression and an artificial neural network algorithm. Right, significance s for both algorithms. See text for detailed discussion. . . . 346
D.4 Variation of support vector regression performance (measured by maximum signficance s, defined in the text), as a function of the width of the Guassian kernel for each physics parameter. . . . 346
D.5 Variation of support vector regression and artificial neural network performance (measured by maximum significance s, defined in the text), as a function of the size of the training sample. . . . 347

List of Tables

2.1 Force carrying bosons. 7
2.2 Particles of the first generation and their interactions 8
2.3 Particle families and their masses in GeV/c^2 9

4.1 Probability to fire the Level 1 muon trigger for various signal processes. . 51
4.2 Probability to fire the Level 1 electron trigger CEM(1,5) for various signal processes, with and without accounting for jets. 53
4.3 Probability to fire the Level 3 electron trigger L3ELE(1,10.0) 55
4.4 Probability to fire the trigger MU_A_EM10. 55

5.1 Derived smearing factors for muon P_T resolution. 87
5.2 Effect of smearing the muon P_T resolution on the efficiency for a threshold of $P_T > 15$ GeV in $t\bar{t} \to e\mu jj$ events. 87
5.3 Summary of muon efficiencies in data and simulation. Only ϵ^{μ} is used in the calculation of κ^{μ}, the ratio of muon reconstruction efficiency in data and simulation. 88
5.4 Efficiency to have an associated track candidate for signal and background samples, in the central and endcap calorimeters. 95
5.5 Sample selection points and their efficiencies 95
5.6 Summary of electron efficiencies in data and simulation and calculation of κ^{e}, the ratio of electron efficiency reconstruction in simulated and real data. In the case of $W\gamma$, the likelihood efficiency $\epsilon^{Likelihood}$ is not included in κ^{e} as the reference sample of electrons is not appropriate; instead the measured efficiency is scaled by κ^{Lhood} measured for WW events. 96
5.7 Derived smearing factors for electron P_T resolution. 97

6.1 Processes which produced events which are misidentified as $e\mu$ events. . . 109

6.2 Calculation of misID background. 114
6.3 Alternative calculation of misID background. 116
6.4 Standard Model contributions to $e\mu$. 119
6.5 Simulation samples. 119
6.6 Efficiencies for dilepton channels to produce final state $e\mu$ events 121

7.1 Requirements for calorimeter data in a run to be marked as GOOD. . . . 131
7.2 Requirements for calorimeter data in a group of luminosity blocks to be marked as GOOD. 132
7.3 Integrated luminosity for the trigger MU_A_EM10. 133
7.4 Data and Standard Model predictions for events in the $e\mu$ final state. . . 134

8.1 Data and backgrounds at each level of selection, with statistical errors. The $Z \to \tau\tau$ contribution is estimated using the ALPGEN simulation, with the exception of the initial selection where the sample has no predictive power and the Pythia simulation is used. 141
8.2 Data and backgrounds for the final selection, with statistical and systematic errors. 141
8.3 Additional sources of systematic errors. 141
8.4 $t\bar{t}$ candidate events. 142
8.5 Efficiencies in simulation for $WW \to e\mu$. 153
8.6 Data and backgrounds at each level of selection, with statistical errors (*superscript*) and systematic errors (*subscript*). 153
8.7 WW candidate events. 154

9.1 For various mSUGRA model points, the number of generated $\chi_1^{\pm}\chi_2^0$ events, N_{gen}, the theoretical cross section including branching ratios to electrons and muon, σ, the efficiency to pass $e\mu$ selection cuts, $\epsilon_{e\mu}$ and the total expected yield in 97.7 pb^-1 of data, including efficiency correction factors. 176
9.2 For various mSUGRA model points, the number of generated $\chi_1^+\chi_-^1$ events, N_{gen}, the theoretical cross section including branching ratios to electrons and muon, σ, the efficiency to pass $e\mu$ selection cuts, $\epsilon_{e\mu}$ and the total expected yield in 97.7 pb^-1 of data, including efficiency correction factors. 177
9.3 For various mSUGRA model points, the number of generated $\tilde{t}_1^+\tilde{t}_1^-$ events, N_{gen}, the theoretical cross section including branching ratios to electrons and muon, σ, the efficiency to pass $e\mu$ selection cuts, $\epsilon_{e\mu}$ and the total expected yield in 97.7 pb^-1 of data, including efficiency correction factors. 178
9.4 For various mSUGRA points and each selected process, the efficiency of the $e\mu$ selection. 179

9.5 Most heavily populated exclusive final state for simulated $p\overline{p} \rightarrow \chi_1^{\pm}\chi_2^0$ ($m_0 = m_{\frac{1}{2}} = 150$ GeV) events. 188
9.6 Contributions to the like-signed $e\mu$ final state. 189
9.7 Contributions to the trilepton final state. 189
9.8 Data and backgrounds at each cut on $\not\!\!E_T$, for events with no reconstructed jets. 191
9.9 Data and backgrounds at each level of selection, with statistical and systematic errors. 192
9.10 Data and backgrounds at each cut on $\not\!\!E_T$, for events with no reconstructed jets. 216
9.11 Data and backgrounds at each level of selection, for events with a single reconstructed jet. 217
9.12 Data and backgrounds at each level of selection, for events with two reconstructed jets. 217

B.1 Efficiency to have an associated track candidate for signal and background samples, in the central and endcap calorimeters. 296
B.2 Sample selection points and their efficiencies 297

C.1 QCD efficiencies at 90% Z efficiency for various P_T thresholds for single track isolation. 319
C.2 QCD efficiency at 90%Z efficiency for various track halo cone sizes. 320
C.3 QCD efficiency at 90%Z efficiency for various halo outer edges. 320
C.4 QCD efficiencies at 90% Z efficiency for various P_T thresholds for various halo inner edges. 321
C.5 QCD efficiencies at 90% Z efficiency for various P_T thresholds variations of the simple halo energy. 322
C.6 QCD efficiencies at 90% Z efficiency for various P_T thresholds for individual isolation strategies. 324
C.7 QCD efficiencies at 90% Z efficiency for various P_T thresholds for combined isolation strategies. 324

Acknowledgments

I must thank all of those who shared with me their fascination with physics. Antonio Redondo seduced me with his early morning enthusiasm for physics; Glen Wurden, Cris Barnes and Fred Wysocki gave me my first science job; Hannu Miettinen and Jorge Lopez introduced me to the experimental and theoretical sides of particle physics.

As a graduate student, I've had the privilege to work with exceptional scientists: Mark Strovink, whose clear vision for the important and unwavering standard of excellence I have tried to internalize; Marumi Kado, who taught me that the surest path to understanding the complex is laid by establishing the basic; Bruce Knuteson, whose irreverent disregard for tradition will probably lead him to revolutionize methods of analysis in particle physics.

Thanks to: Ela Barberis for directness and unwavering support; Cecilia Gerber, for no-nonsense leadership; Terry Wyatt, for always asking the right question; Dan Claes and Amber Boehnlein, for trusting me with L3 tracking; Markus Klute, for contributions to understanding muons and jets; Lukas Phaf, for collaboration on electrons; Andy Haas, for answering questions ranging from CAB scripts to NT printing; Axel Naumann, for collaborating on support vector machines and suffering with me that first biting referee report; Henry Frisch for giving me desk space and bandwidth at Chicago; Bruce Winstein, for letting me taste cosmology. Thanks to Aaron Pierce, Andy Haas (especially), Paul Balm, Chris Hays and Nate Goldschmidt (abstractly) for reading early drafts.

Graduate school has helped me build or cement some good friendships: Nir, whose sense of humor I can't distinguish from my own anymore; Mala, whose unlikely friendship and astute advice has seen me through a decade of personal and academic growth; Florencia, who, ironically, taught me how to talk straight.

It wouldn't have been the same without: Jasper, with his hard crunchy coating and soft candy center; Nick, "100% tenant"; Mikey-Baby, spades partner and valiant vice-boyfriend; Ben, one of Fermi's best-dressed and my favorite prankster; Kirby, my fellow minister of the irreverent, who introduced me to everyone I know at FNAL; Andy, for a great year, a crazy summer, three great Seders and lots of sweet music; Chris and Liz, for trusting me with an amazing responsibility; Jason and Erica, for many great dinners, leftovers and conversations on your back porch; Nate, for "Cowboys vs. Dinosaurs" and letting me pet his cat; Marumi, for lots of laughter and mock outrage; Ela, for delicious brunches and wonderful imported cookies; Olga, for giving me Siyah and making me a cat person again; Paul, for your refreshing straightforwardness; Matt and Shannon, for thrift stores, barbeques and boardgames; Axel, for PiViBe and badminton versus 15 years girls; Brian, I'll never quite be ready for you; Sondra, responsible for my sanity and entertainment that one crazy summer; Giulia, for many windblown lunches; the Scandinavian Languages Department at Berkeley, for introducing me to Katrine.

And to Katrine, in ways that would be diminished by putting them into words.

Chapter 1

Introduction

The dream of scientific exploration is to understand the basic building blocks of our environment and the rules for putting them together. Understanding the nature of the fundamental particles and the forces between them means uncovering the simplest and most powerful secrets of Nature.

Experimental particle physicists have only a few tools to help them reveal the basic particles. We begin by examining the matter in our environment, smashing particles together to reveal their underlying structure. The building blocks used to construct our environment, however, represent a fraction of the available variety. Studying uncommon, exotic particles requires producing them in the laboratory through collisions of common particles.

When energetic particles collide, they annihilate and exist briefly as an inter-

mediate state in which their energy is converted into mass. This state is fundamentally unstable and must quickly revert to a less massive state. Counter-intuitively, the final state of the collision is not required to reproduce the incoming particles nor to be constructed of the same building blocks; due to the quantum randomness of the process, the particles which appear as collision products are randomly selected from a menu of particles which have a combined mass less than the mass of the intermediate state. Hence, collisions of ordinary light particles such as protons or electrons may produce more exotic or massive particles, if the incoming particles have sufficient energy. Thus, particle collisions at the energy frontier are a powerful tool to probe fundamental particles and to understand the physical laws that govern them.

The quantum nature of the collisions and the fantastically short time and distance scales in which they occur make it impossible to observe the collisions directly. Instead, we must deduce the nature of the interactions from observations made of the relatively long-lived decay products of the short-lived exotic particles. For this reason, it is natural to organize the massive quantity of data collected according to the type and multiplicity of the observed particles.

The most basic test of our understanding is made by measuring the rate at which each type of event is observed. The strength of this understanding, and the relevance of a comparison to theoretical predictions, hinges on a detailed understanding of the experimental ability to correctly identify each class of particle. This thesis represents a

detailed study of the experimental capability to identify and reconstruct a particularly sensitive class of events: those containing both an energetic electron (e) and an energetic muon (μ) produced in high energy collisions of protons and anti-protons. This class of events, which I will refer to as $e\mu$, gains its sensitivity from the experimental detector's strong ability to identify charged leptons and the lack of large contributions from common processes of little interest.

It is not surprising, then, that the $e\mu$ channel is rich in both history and potential for discovery. The third charged lepton, the tau (τ) was discovered [1] in 1975 through an analysis of $e\mu$ events. The $e\mu$ channel provided one of the cleanest signatures of the decay of the top quark, discovered at the Tevatron in 1995 [9, 10]. In this small sample, CDF saw a peculiar $e\mu$ event; the lack of plausible explanation from standard theories sparked much theoretical speculation [2]. Many varieties of proposed theories predict the production of $e\mu$ events, giving us the power to probe the viability of these theories.

The $e\mu$ channel allows us to perform a broad range of sensitive tests of the theories of particles and their interactions. Measuring the rate of production of processes which have been previously observed at lower energies provides a measurement of evolution of the interaction strengths. Some of these processes may be weakly tested or of great interest, such as the spectacularly massive and rare top quark. One may also search for evidence of previously unobserved and unexpected particles. Finally, one can

search for evidence of theorized particles, either discovering or excluding their existence. In this thesis, we present the results of each of these tests.

Chapter 2 describes the current state of the physical theories that govern the particles and their interactions. Chapter 3 describes the accelerator complex used to produce the collisions and the detector used to observe them. Chapter 4 describes the event trigger used to capture relevant events. Chapter 5 details our understanding of the experimental capability to identify the products of the collisions. Chapter 6 discusses the expected contributions to $e\mu$ events. Chapter 7 displays the collected data. Chapter 8 presents a measurement of the production of top quark pairs and their decay to an electron and muon as well as a measurement of the production of W boson pairs. Chapter 9 presents the strategy and results of searches for exotic processes which would produce $e\mu$ events. Chapter 10 discusses the results and places them in context of previous work and prospects for future refinements.

Chapter 2

The Theory of Particles and their Interactions

A modern understanding of the nature of particles and their interactions has its roots in the development of quantum mechanics. The realization that the laws which govern the universe are fundamentally probabilistic led naturally to a description of particles as waves of probability density rather than objects with classical trajectories which could be perfectly predicted and observed [3]. The single particle approach, such as the Schrödinger and Dirac [4] wave equations for non-relativistic and relativistic electrons, respectively, were successful in describing the structure of the hydrogen atom, the mysterious internal quantum property of particle *spin*, and the results of early scattering ex-

periments. While successful, this approach became cumbersome and problematic when applied to systems of many particles and required the development of the theoretical structure of Quantum Field Theory [13, 14, 15]. This chapter introduces the experimentally observed particles and the forces between them, and describes the quantum field theory of the Standard Model, the theoretical structure which has been successful in its description and prediction of the particle properties and interactions.

2.1 Particles and Forces

Theoretical efforts seek to categorize the experimentally observed particles and forces in terms of the fewest number of fundamental building blocks and interactions. In the centuries since the birth of scientific investigation, much progress has been made in reducing the multitude of apparent forces and the hundreds of experimentally observed particles to three forces and sixteen particles.

All experimentally observed forces can be described in terms of three forces:

- Gravity, the attractive force between matter and energy which is intimately connected to space-time itself
- Electroweak Force, a unified description of electricity, magnetism and the weak force.
- Strong Nuclear Force, the force which binds quarks and gluons together.

Particle Name	Symbol	Charge	Spin	Mass (GeV/c^2)	Force
Photon	γ	0	1	0	Electromagnetism
Z	Z	0	1	91.2	Weak Force
$W^{\pm}$	$W^{\pm}$	± 1	1	80.4	Weak Force
gluon	g	0	1	0	Strong Force
graviton	G	0	2	unknown	Gravity

Table 2.1: Force carrying bosons.

Patterns emerge among the particles, which help illuminate fundamental structures. Of the hundreds of different particles, all are understood to be composites of a subset of just sixteen [12]. Efforts to reveal an underlying structure to these particles have so far been fruitless. In this accounting, we consider particles and their antiparticles as one, and do not count separately the similar multitude of particles of different colors.

These sixteen particles fall into two broad classes: twelve spin$-\frac{1}{2}$ *fermions* that are the building blocks of matter, and five spin-1 *bosons* which mediate the forces between matter particles. Of the four bosons which mediate forces, the photon, which carries the electromagnetic force, is the most familiar. The massive W and Z bosons mediate the weak interaction and the gluons carry the strong force. A particle which carries the force of gravity has not been observed. Table 2.1 gives the boson properties.

The twelve matter particles show clear patterns; there are three *generations*, each of which contain a set of four particles identical in quantum numbers to their cousins in other families and distinguished primarily through their weak interactions and their

Particle Name	Symbol	Charge	Forces			
			Gravity	Weak	Electromagnetism	Strong
Up quark	u	$+\frac{2}{3}$	×	×	×	×
Down quark	d	$-\frac{1}{3}$	×	×	×	×
Electron	e	-1	×	×	×	
Electron neutrino	ν_e	0	×	×		

Table 2.2: Particles of the first generation and their interactions

mass. These four basic particles can be distinguished by their properties of interaction, see Table 2.2. Each particle interacts gravitationally and via the weak nuclear force; the two which feel the strong nuclear force are known as *quarks*, the other two are *leptons*. The *neutrino*, which has no electromagnetic charge, interacts only via the weakest of forces: gravity and the weak nuclear force.

Though the relationship between the two quarks and leptons in the first generation is not fully understood, there are many parallels which can be drawn between them. It is an unlikely coincidence that the charge of the proton, a combination of two up quarks and a down quark, exactly balances the charge of the electron; this is crucial for the construction of the basic atom and therefore the structure of our macroscopic universe.

Particles in the second and third families are identical in all quantum numbers to those in the first, and are distinguished by their increased mass. Table 2.3 gives the complete list of twelve fermions and their masses.

First Generation		Second Generation		Third Generation	
		Quarks			
up	$m_u \approx 3 \times 10^{-3}$	charm	$m_c \approx 1.2$	top	$m_t = 175$
down	$m_d \approx 7 \times 10^{-3}$	strange	$m_s \approx 20 \times 10^{-3}$	bottom	$m_b = 4$
		Leptons			
electron	$m_e = 5.11 \times 10^{-4}$	muon	$m_\mu = 0.106$	tau	$m_\tau = 1.78$
neutrino	$m_{\nu_e} \approx 10^{-6}$	neutrino	$m_{\nu_\mu} \approx 10^{-6}$	neutrino	$m_{\nu_\tau} \approx 10^{-6}$

Table 2.3: Particle families and their masses in GeV/c^2

2.2 Quantum Field Theory

The creation and destruction of particles plays a crucial role in relativistic processes, and it is natural to describe these systems in terms of a multi-particle process. Quantum Field Theory, in which particles are described as excited modes of a field, handles these situations naturally and cleanly. The modern theory of particles and their interactions is one of quantum fields; the creation or destruction of particles is understood as the excitement or lowering of the field modes; physical symmetries are derived from symmetries in the structures of the fields.

The basic quantity of field theory is the local field $\phi(x)$, from which is constructed the Lagrangian density $\mathcal{L}$:

$$\mathcal{L}(x) = f(\phi, \partial_\mu \phi)$$

The structure of the Lagrangian determines the equations of motion and inter-

actions of the field. The principle of least action requires that the evolution of a physical system from one configuration to another occurs along a path in which the action S

$$S = \int \mathcal{L}(\phi, \partial_\mu \phi) d^4x$$

is at an extremum. Requiring $\delta S = 0$, we can express the generic equations of motion in terms of the Lagrangian,

$$\partial_\mu \left(\frac{\partial \mathcal{L}}{\partial(\partial_\mu \phi)}\right) - \frac{\partial \mathcal{L}}{\partial \phi} = 0.$$

This prescription allows for the construction of an arbitrary Lagrangian; we seek one which yields the equations of motions of physical particles and which successfully describes and predicts the results of experiments. The requirement that the equations of motions obey known conservation laws, such as momentum or charge conservation, dramatically reduces the number of Lagrangians which must be considered.

A continuous symmetry of the Lagrangian which leaves δS unchanged will not affect the equations of motion. It can be shown that any such symmetry corresponds directly to the conservation of a physical quantity by the equations of motion. Thus, we seek a Lagrangian with specific symmetries.

The structure of the Lagrangian predicts the interactions of the particles as well as their equations of motion. An interaction term of the form

$$g\phi^n(\phi^\dagger)^m$$

predicts an interaction of strength g in which the field ϕ is excited n times, creating n particles, and lowered m times, destroying m particles. That the interaction be physical places strict requirements on the forms these terms may take, see Ref. [15] for details.

2.3 The Standard Model

The Standard Model is a quantum field theory which describes the equations of motion of the fermions and bosons and their interactions.

2.3.1 Quantum Electrodynamics

The first application of quantum field theory to fundamental particles was the attempt to describe the motion and interaction of charged particles in electromagnetic fields [11]. A Lagrangian for quantum electrodynamics must successfully reproduce the experimentally verified equations of motion. The validity of the field theory approach can be probed in the detailed predictions made by such a Lagrangian,

$$\mathcal{L}_{QED} = \overline{\psi}(i\partial_\mu\gamma^\mu - m)\psi - \frac{1}{4}F_{\mu\nu}F^{\mu\nu}$$

where the first portion represents the free electron field ψ and the second the electromagnetic vector potential A_μ in the vacuum ($F_{\mu\nu} = \partial_\mu A_\nu - \partial_\nu A_\mu$). Deriving from this the equations of motion for each field, we recover the expected description of the electron in the form of the Dirac equation,

$$(i\partial_\mu \gamma^\mu - m)\psi = 0$$

and the familiar homogeneous Maxwell equation for the electromagnetic fields,

$$\partial_\mu F^{\mu\nu} = 0$$

This Lagrangian describes the free motion of the electron and photon, but does not address their interaction. In addition, it is not invariant under a local gauge transformation which is required by Maxwell's equations. This transformation rotates the phase of ψ and the gauge of the vector potential:

$$\psi(x) \rightarrow e^{i\alpha(x)}\psi(x), \quad A_\mu \rightarrow A_\mu - \frac{1}{e}\partial_\mu \alpha(x).$$

The requirement is satisfied by extending $\mathcal{L}_{QED}$ to include a term which couples the electron and electromagnetic fields,

$$\mathcal{L}_{QED} = \overline{\psi}(i\partial_\mu \gamma^\mu - m)\psi - \frac{1}{4}(F_{\mu\nu})^2 - e\overline{\psi}\gamma^\mu \psi A_\mu.$$

Exact calculation of physical quantities in such a theory is not currently possible; however, calculations to arbitrary precision can be carried out through a perturbative expansion in powers of the interaction strength e. Feynman devised a clever pictorial scheme to represent and organize terms of increasing order; the leading order QED diagram, which represents a single interaction vertex, order e^1, is shown in Figure 2.1.

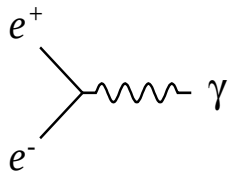

Figure 2.1: Feynman diagram for the leading order interaction between electron and photon fields in Quantum Electrodynamics.

QED accurately predicts the interaction of electrons and electromagnetic fields (photons) to extraordinary precision over a wide range of energies. Note that there is no mass term for the vector boson, which would appear as $m^2 A_\mu A^\mu$; hence the photon is massless. The symmetry of this piece of the Lagrangian is a single real quantity, in the form of a phase rotation in the amount $\alpha(x)$; in group theoretical terms, this is described as a $U(1)$ symmetry. The notation $U(n)$ indicates that the transformation can

be represented by a $n \times n$ unitary matrix.

2.3.2 The Weak Interaction

Experimental patterns of the weak interaction suggest that it respects a symmetry between the particles; symmetries of the Lagrangian may also reflect such internal symmetries. We group particles into doublets

$$\psi = \begin{pmatrix} u \\ d \end{pmatrix}, \begin{pmatrix} e \\ \nu_e \end{pmatrix}, \quad \overline{\psi} = (u\ d), (e\ \nu_e)$$

and form a basic Lagrangian

$$\mathcal{L}_{EW} = \overline{\psi}(i\partial_\mu \gamma^\mu - m)\psi$$

but require that the symmetry reflect an invariance under a local gauge transformation which connects the particles to each other,

$$\psi(x) \rightarrow \psi(x)(1 - \frac{i}{2} g\alpha(x) \cdot \tau)$$

where τ_i are the Pauli spin matrices. The representation of the group element is a two dimensional traceless matrix, or $SU(2)$.

Respecting this symmetry requires the introduction of a triplet of gauge fields W_μ with free propagation and interacting terms in the Lagrangian,

$$\mathcal{L}_{EW} = \overline{\psi}(i\partial_\mu\gamma^\mu - m)\psi - \frac{1}{4}W_\mu W^\mu - \overline{\psi}(\gamma_\mu\frac{g}{2}W^\mu\cdot\tau)\psi$$

The three W_μ fields might be interpreted as the three vector bosons of the weak interaction, though this does not describe the structure of the weak interaction and predicts massless bosons. The weak interaction has been experimentally observed to discriminate between particles of right-handed *helicity*, in which the momentum is in the same direction as the spin, and particles of left-handed helicity, in which the directions are opposite. To build a theory which reflects the true structure of the interactions requires unification of the electromagnetic and weak forces into a single symmetry; accommodation of the massive W and Z bosons requires breaking that symmetry.

2.3.3 Electroweak Unification

We group the fermions into left-handed doublets

$$\psi_L = \begin{pmatrix} u_L \\ \\ d_L \end{pmatrix}, \begin{pmatrix} e_L \\ \\ \nu_{e_L} \end{pmatrix}, \quad \overline{\psi_L} = (u_L\ d_L), (e_L\ \nu_{e_L})$$

and right-handed singlets

$$\psi_R = (u_R), (d_R), (e_R)$$

where we omit the right-handed neutrino with the assumption of zero neutrino mass; recent experiments have revealed conclusive evidence for neutrino mixing, which implies a small but nonzero mass. We require that the Lagrangian be invariant under rotations of left-handed $SU(2)$, and an extension of electromagnetic $U(1)_Q$ to weak hypercharge $Y = 2(Q - T_3)$. For the Lagrangian to respect this $SU(2)_L \times U(1)_Y$ symmetry requires the triplet fields W_μ and a singlet field B_μ and interaction terms of the form,

$$\mathcal{L}_{int} = -\overline{\psi_L}\gamma_\mu(\frac{g}{2}W^\mu \cdot \tau + \frac{g'}{2}B^\mu Y)\psi_L - \overline{\psi_R}\gamma_\mu(\frac{g'}{2}B^\mu Y)\psi_R$$

as well as the standard kinetic energy terms. This Lagrangian predicts four massless bosons $W_{1,2,3}$ and B, linear combinations of which correspond to the four physical bosons, $W^\pm$, Z and γ:

$$W^\pm = \frac{1}{\sqrt{2}}(W_1 \mp W_2)$$

$$Z = -B\sin\theta_W + W_3\cos\theta_W$$

$$\gamma = B\cos\theta_W + W_3\sin\theta_W$$

If the four physical bosons were massless, then there would be no reason to prefer their specific linear combination over any other. However, the symmetry $SU(2)_L \times U(1)_Y$ is broken; three of the physical bosons are massive while one is massless. Hence, it is natural to choose the linear combinations which correspond to specific mass states.

2.3.4 Spontaneous Symmetry Breaking

The non-zero mass of the vector bosons, and the breaking of the symmetry $SU(2)_L \times U(1)_Y$, can be handled naturally and without explicit introduction of mass terms into the Lagrangian [17]. If there exists a complex scalar doublet field ϕ, in general it would require terms of the form

$$\mathcal{L}_\phi = (\partial_\mu \phi)^2 - \mu^2 \phi^2 - \lambda \phi^4.$$

The state with lowest energy, the *vacuum*, occurs at $\phi = \frac{-\mu^2}{2\lambda} = v$, rather than at $\phi = 0$. The energy of the vacuum, $< \phi >= v$, is the *vacuum expectation value*. We can write the ϕ doublet in the unitary gauge in terms of this quantity as

$$\phi = \frac{1}{\sqrt{2}} \begin{pmatrix} 0 \\ \\ v + H \end{pmatrix}.$$

The interaction of the W and B fields with the ϕ fields yields terms of the form

$$(0, v + H)(g\tau \cdot W^\mu + g' B^\mu)^2 \begin{pmatrix} 0 \\ \\ v + H \end{pmatrix}.$$

which represent the interaction of the scalar field with the W and B fields. The physical effect of the non-zero vacuum expectation value is to generate masses of the physical W and Z bosons through terms of the form $\frac{1}{4} g^2 v^2 W^+ W^-$ and $\frac{1}{4 \cos^2 \theta_W} g^2 v^2 Z^2$. The new

field ϕ requires the existence of a new particle, the Higgs boson [18], which is the subject of intense experimental research.

2.3.5 The Strong Force

The strong nuclear force is carried by gluons, which are exchanged between quarks and gluons. The Lagrangian of Quantum Chromodynamics (QCD), which describes this interaction, respects the $SU(3)$ symmetry exactly, and the eight gluons are massless. The Lagrangian contains an interaction term of the form

$$\mathcal{L}_{QCD} = -\frac{1}{4}(F^a_{\mu\nu})^2 - \sum_q \overline{\psi^i_q}\ (\gamma^\mu \frac{g_s}{2} \sum_a \lambda^a_{i,j} G^a_\mu)\ \psi^i_q$$
$$F^a_{\mu\nu} = \partial_\mu G^a_\nu - \partial_\nu G^a_\mu - g_s f_{abc} G^b_\mu G^c_\nu$$

where ψ^i_q is the 4-component spinor of quark q of color i, $G^a(x)$ are the eight gluon fields, f_{abc} are the $SU(3)$ structure constants and λ^a are the 3×3 representations of the $SU(3)$ generators.

2.3.6 Calculations

The cross section for the production of particles via the process $p_A, p_B \rightarrow p1, p2$ may be calculated as

$$\frac{d\sigma}{d\Omega}_{CM} = \frac{|p_1|}{32\pi^2 E_A E_B E_{CM} |v_A - v_B|} |\mathcal{M}(p_A, p_B \rightarrow p_1, p_2)|^2$$

where the matrix element, $\mathcal{M}$, depends on the structure of the interaction and may be assembled with the aid of diagrams such as 2.1, 2.3, 2.4, 9.1, 9.4, and 9.6.

2.4 Particle Production in $p\overline{p}$ Collisions

The formalism of Quantum Field Theory provides a framework for calculating the scattering of fundamental particles. The Tevatron, however, collides protons and antiprotons, each of which is a collection of three fundamental quarks,a sea of virtual quarks that surround them and the gluons which bind them together; these particles are collectively referred to as *partons*. Direct simultaneous calculation of the interaction of all participants in the collision is not feasible with current theoretical tools. Instead, at large energies one can argue that the process is dominated by the interaction of the constituent partons, as the time scale of the hard scattering is shorter than the time scale of the interactions between the partons. To approximate the total cross section then, one must sum over the possible parton interactions, weighing each by its probability

$$\sigma = \sum_{A,B} \int dx_A dx_B F_p(x_A, Q^2) F_{\overline{p}}(x_B, Q^2) \sigma(p_A, p_B \rightarrow p1, p2)$$

where x_A represents the fraction of the (anti)proton's momentum carried by the parton p_A, Q the momentum transfer of the interaction and $F_p(x_A, Q^2)$ the probability to find parton p_A with momentum fraction x_A in the proton.

The function F is the *parton distribution function*(PDF). A derivation of the PDF has yet to be achieved from first principles or perturbative calculations; the shapes must be extracted from data, where deep inelastic scattering experiments and Drell-Yan data [6] have been powerful. The PDFs are fit at specific values of Q^2, and may be evolved to a desired value using the Altarelli-Parisi equations[7].

A fit to all data yields a estimate of these distributions [8]; Figure 2.2 shows PDFs at $Q^2 = 2$ and $Q^2 = 100$ GeV.

2.4.1 Top Quark Pair Production

The top quark is produced in $p\overline{p}$ collisions both singly and in pairs. The larger cross section and more distinct experimental signature make pair production more experimentally feasible. At energies of the Tevatron, the top quark is produced primarily through quark annihilation, although gluon fusion contributes approximately 15%, see Figure 2.3.

The top quark was observed in 1995 by the CDF and DØ collaborations [9, 10] and the cross section of its production at $\sqrt{s} = 1.8$ TeV was measured to be [19, 20]:

$$\sigma_{t\bar{t}} = 7.1 \pm 1.7 \text{ pb} \;\; [m_{top} = 175 \text{ GeV/c}^2] \; (CDF)$$

$$\sigma_{t\bar{t}} = 5.7 \pm 1.6 \text{ pb} \;\; [m_{top} = 172.1 \text{ GeV/c}^2] \; (D\emptyset)$$

in good agreement with theoretical calculations [21]:

$$\sigma_{t\bar{t}}(\sqrt{s} = 1.8 \text{ TeV}) = 5.3 \pm 0.6 \text{ pb} \quad [m_{top} = 172.1 \text{ GeV/c}^2].$$

At the increased energy of $\sqrt{s} = 1.96$ TeV, the theoretical production cross section increases by roughly 20% [22],

$$\sigma_{t\bar{t}}(\sqrt{s} = 1.96 \text{ TeV}) = 6.8 \pm 0.6 \text{ pb}.$$

Top Quark Decay

The top quark decays exclusively to a real W boson and a b quark. Some theories postulate that the top may decay to a charged Higgs boson and a b quark at some small rate; such effects are neglected here. The top quark decays are characterized by the patterns of decay of the two W bosons.

Dilepton: When both Ws decay leptonically, the signature is two energetic leptons, two uncaptured neutrinos which appear as missing transverse energy and two b-quark jets. The dilepton final states account for only 9/81 of the total decay rate.

Lepton+Jets: When one W decays leptonically and the other hadronically, the signature is one energetic lepton, a single neutrino, two light quark jets and two b-quark jets. Each of the three leptonic modes accounts for 12/81 of the decay rate. The largest background is multijet production from QCD and W bosons with four

associated jets.

Hadronic: When both Ws decay hadronically, the signature is four light quark jets and two b-quark jets. Though it enjoys 36/81 of the decay rate, it lacks any energetic leptons and so is a difficult signature to extract from the overwhelming QCD background.

2.4.2 W boson pair production

Pair production of W bosons occurs primarily through interactions represented by diagrams in Figure 2.4. In contrast to top quark pair production, single W production cross section exceeds that of pair production by a factor of ≈ 500. The cross section of production of W pairs is calculated at next to leading order to be [23]

$$\sigma_{WW}(\sqrt{s} = 1.96 \text{ TeV}) = 13.25 \pm 0.25 \text{ pb}$$

The decay of two W bosons is categorized in the same manner as that of top quark pair decay.

2.5 Extensions to the Standard Model

The Standard Model is very successful, correctly predicting a broad range of precision experiments, yet it is unsatisfactory and incomplete. It contains no description

of the force of gravity; it reveals no underlying structure unifying quarks and leptons; it has no explanation for the existence of fermion masses or their peculiar hierarchy; it has more than twenty free parameters for which it has no theoretical prediction; it requires extraordinary fine-tuning of parameters to compensate for a quadratic divergence of the mass of the Higgs boson.

2.5.1 Supersymmetry

Supersymmetric theories postulate that Standard Model particles are half of a larger, symmetric set of particles [24, 25]. Each observed particle would have an as-yet-unobserved super partner, which differs in spin by $\frac{1}{2}$ but is identical in every other respect. The masses of the super partners must be large to be consistent with the lack of experimental evidence, and so the symmetry must be broken. Though these theories introduce roughly 100 new parameters, many parametrizing our ignorance of the mechanism of the symmetry breaking, they promise to solve the fine-tuning problem of the Higgs mass and are central features of many mathematical constructs which have been suggested as foundations for a more fundamental theory.

Supersymmetric models can predict a variety of theoretical structures; the majority of them are constructed in a manner which conserves the quantity $R = (-1)^{3(B-L)+2S}$ [27], which is even for Standard Model particles and odd for their supersymmetric partners. Conservation of *R-parity* is not theoretically required, but failure to conserve it leads

many theories to nonphysical predictions such as proton decay. R-parity conservation implies that supersymmetric particles must be produced in pairs and that the lightest supersymmetric particle (LSP) is stable. The LSP is most likely electrically neutral and colorless, due to cosmological constraints [26].

The mechanism for the breaking of supersymmetry is not well understood theoretically. Most theories suggest that the breaking is due to interactions of particles in a hidden sector, which have no interaction with standard model gauge bosons; the symmetry breaking might then be mediated through gravity [28].

While each particle has a supersymmetric analogue, it is not clear that the direct analogues are mass eigenstates. In general, the electroweak and Higgs partners can mix to form charged and neutral bosons, *charginos* (χ_1^+, χ_2^+) and *neutralinos* ($\chi_1^0, \chi_2^0, \chi_3^0, \chi_4^0$) ordered by mass.

The general supersymmetric theory introduces 105 new parameters [29], primarily due to lack the of prediction for new particle masses, mixing between particles and CP-violating phases in interactions of the new particles. To sharply reduce the number of free parameters and avoid the prediction of experimentally prohibited flavor-changing neutral currents, it is theoretically popular to consider a simplified version, known as mSUGRA and described by five parameters [24],

- m_0, the mass scale of the partners of the quarks and leptons, under the assumption that the mass matrices are flavor-diagonal.

- $m_{1/2}$, the mass scale of the partners of the gauge bosons, under the assumption that the gaugino masses are unified at some large mass scale.

- $\tan\beta = v_u/v_d$, where $v_{u,d}$ describe the coupling of up- and down-like particles to the Higgs bosons through their fractional share of the vacuum expectation value v: $v_u^2 + v_d^d = v^2$.

- A_0, a single parameter to describe the tri-linear coupling between the Higgs and squark pairs or slepton pairs.

- sign(μ), the sign of the electroweak-symmetry breaking parameter μ.

2.5.2 Other Theories

There are many other potential extensions of the Standard Model. Some of current theoretical interest include: theories of extra space-time dimensions [16] which may explain the extraordinary gap in energy scales between electroweak symmetry breaking, 10^2 GeV, and the Planck scale, 10^{19} GeV; leptoquarks, which interact directly with quarks and leptons at a single vertex and violate Standard Model lepton number conservation [30]; models of *technicolor* which posit the existence of a new strong dynamics to explain electroweak symmetry breaking [31].

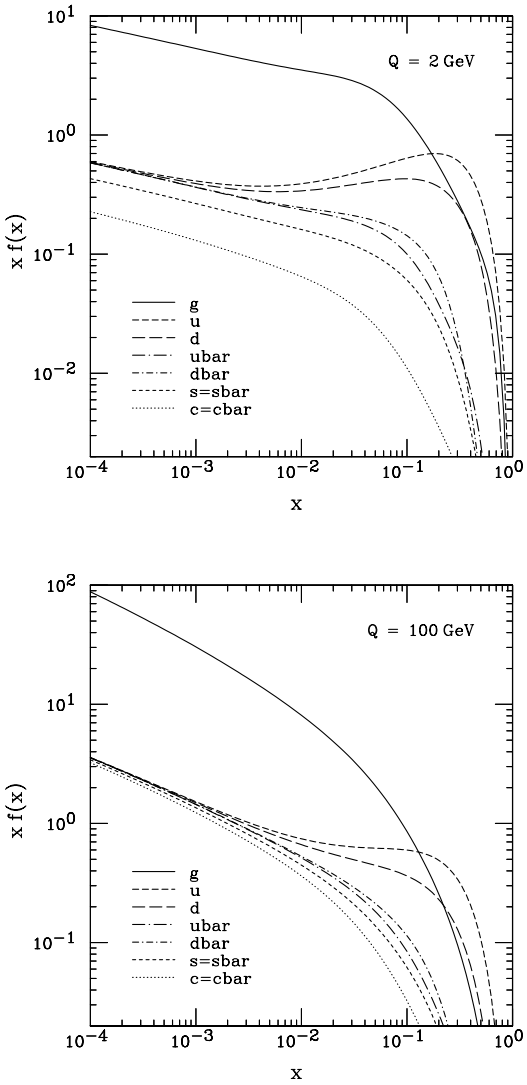

Figure 2.2: Parton distribution fuctions at varying scales of transverse momentum exchange (Q^2)[8].

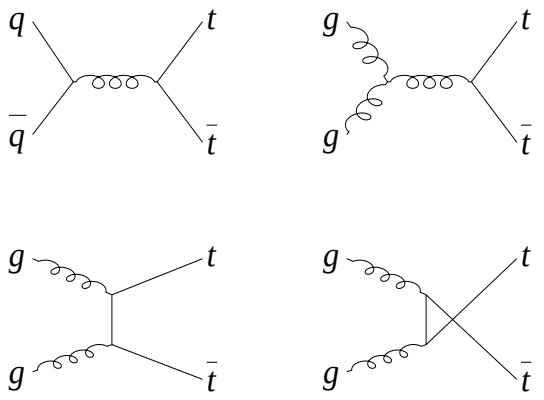

Figure 2.3: Feynman diagrams which represent leading order top quark pair production processes.

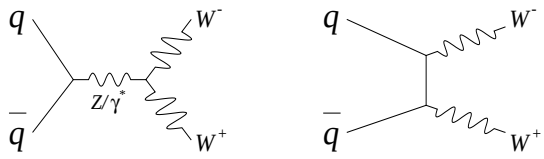

Figure 2.4: Feynman diagrams which represent leading order W boson pair production processes.

Chapter 3

Experimental Apparatus

The data analyzed in this document were collected in 2002 and 2003 from collisions at the Tevatron of protons and anti-protons at a center of mass energy of 1.96 TeV and recorded by the DØ detector. The accelerator and the detector are described in turn.

3.1 The Fermilab Accelerator Complex

Fermilab maintains a series of eight accelerators of increasing energy, culminating in the Tevatron, which collides protons and anti-protons at a center of mass energy of 1.96 TeV, see Figure 3.1.

The protons used in the collisions are extracted from hydrogen ions; the ions

are accelerated to 750 keV by a Cockroft-Walton accelerator and injected into a linear accelerator which boosts their energy to 400 MeV. These ions are stripped of their electrons as they pass through a sheet of graphite and are injected into the Booster, a synchnotron which brings their energy to 8 GeV.

Protons from the Booster are sent to the Main Injector, where they are further accelerated to 150 GeV. Anti-protons used in the collisions are collected from the interaction products of a portion of the 150 GeV proton beam incident on a nickel-copper target. Anti-protons are cooled and debunched in the Debuncher and Accumulator, and accelerated to 150 GeV by the Main Injector.

Protons and anti-protons are injected into the Tevatron, where they are accelerated to their final energy of 980 GeV before colliding at the center of the DØ detector.

Collisions occur in bunches, with 36 bunches each spaced by 396 nanoseconds.

3.2 Interactions of Energetic Particles with Matter

The DØ detector surrounds the collision point and records the kinematics of the collision by examining its long lived products. The most prevalent, and those relevant to this thesis, are electrons, photons, muons, hadronic particles and neutrinos.

The interaction of these particles with detector subsystems results in energy loss which can be detected and measured. Tracking detectors are designed to measure

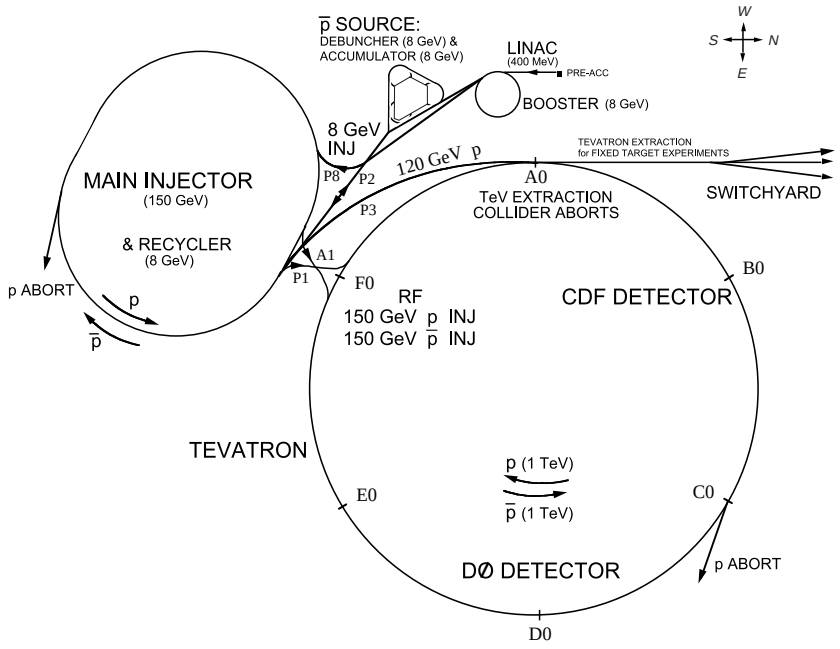

Figure 3.1: The Fermilab accelerator complex.

the particle positions with minimal energy loss. Calorimeters are constructed to fully strip particles of their energy in the process of measurement.

The modes of interactions of the relevant particles with the detector are discussed in turn, followed by a detailed description of each element of the detector.

3.2.1 Electrons and Photons

Electrons passing through matter lose energy primarily through ionization and through *bremsstrahlung*. Above a critical energy [62],

$$E_c = (800MeV)/(Z + 1.2)$$

bremsstrahlung is the dominant process. The emitted photons produce electron-positron pairs, which again produce photons. The resulting shower of electrons and photons grows until the energy of the electrons falls below the critical energy, where they interact primarily through ionization. The mean distance over which an electron loses $1/e$ of its energy is described by X_0, the radiation length [62],

$$X_0 = \frac{716.4 \text{ g cm}^{-2} A}{Z(Z+1)ln(287/\sqrt{(}Z))}$$

Photons interacting with matter will produce electron-positron pairs, and hence an electromagnetic shower.

3.2.2 Muons

Muons with energies typical of the Tevatron interact through *bremsstrahlung* at a much lower rate than electrons due to their larger mass. Their energy loss is primarily through ionization; Figure 3.2 shows the energy loss per unit of material for muons in various energy regimes. Though they ionize the detector elements in their path, they rarely produce electromagnetic showers.

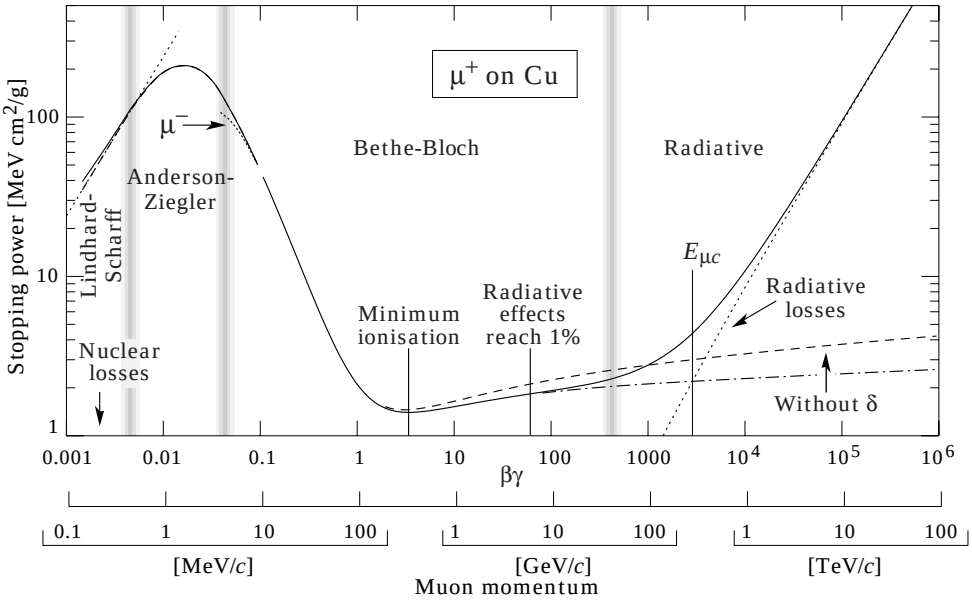

Figure 3.2: Energy loss through ionization of muons in various energy regimes. From [62].

3.2.3 Hadronic Particles

Hadronic particles interact inelastically with the nuclei of the detector element, producing primarily pions and nucleons. At high energies, the resulting particles interact similarly with nearby nuclei, producing a shower of hadronic particles. The characteristic length scale is the nuclear interaction length, which is dependent on the material density and atomic weight, and is roughly independent of energy:

$$\lambda_I = 35 \text{ g cm}^{-2} A^{1/3}$$

A significant fraction of the energy of the initial hadron escapes the hadronic

cascade as neutral pions, which produce a secondary electromagnetic cascade. A smaller fraction results in invisible energy loss through unbinding of nuclei by spallation, non-ionizing collisions and the uncaptured energy of neutrinos.

3.2.4 Neutrinos

As uncharged leptons, neutrinos interact only via W and Z exchange, making their energy loss negligible and their direct detection practically impossible at DØ. Their presence can be inferred, however, from transverse momentum conservation requirements.

3.3 The DØ Detector

The DØ detector consists of three major subsystems. At the core of the detector, a magnetized tracking chamber records precisely the angles of charged particles and measures their transverse momenta. A hermetic, finely grained uranium and liquid-argon calorimeter measures the energy of electromagnetic and hadronic showers, and a muon spectrometer detects and measures the momenta of escaping charged particles. Figure 3.3 gives an overview of the detector.

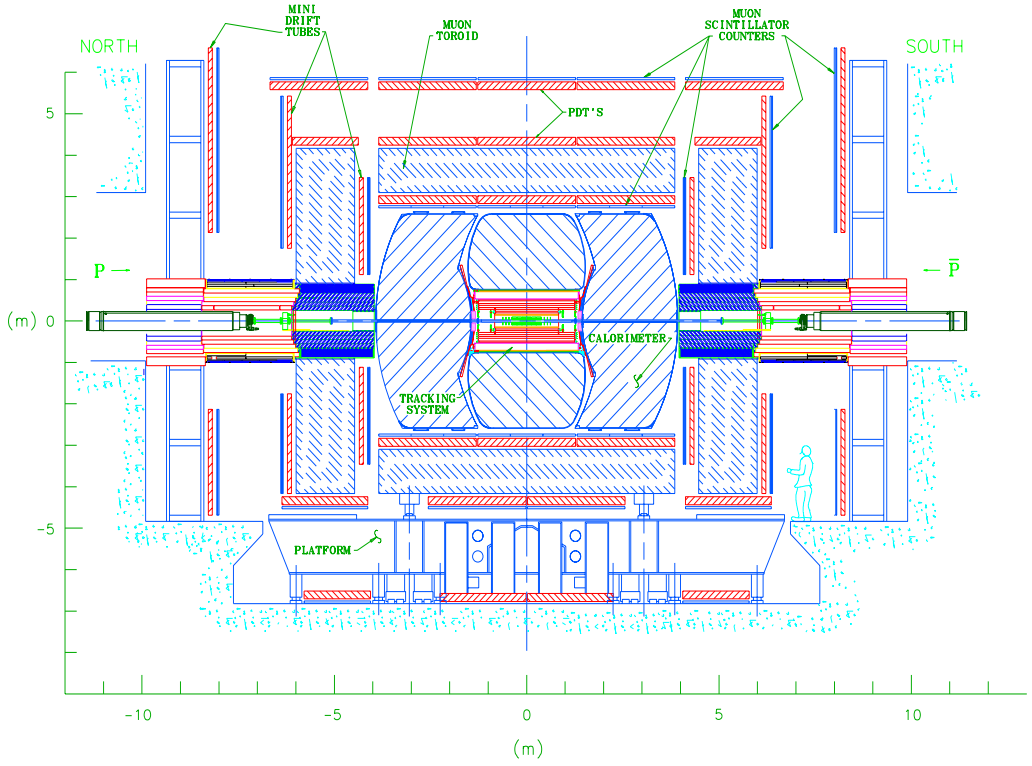

Figure 3.3: Side view of the DØ detector.

3.3.1 Coordinate System

We use a right-handed coordinate system in which the z axis is aligned with the direction of the beam such that the protons flow in the positive z direction. The y axis is then vertical, and the positive x axis points towards the center of the accelerator ring.

A more useful set of coordinates are the standard polar coordinates (r, ϕ)

$$r = \sqrt{x^2 + y^2}$$

$$\phi = \tan \frac{y}{x}$$

in addition to a particular reformulation of the polar angle θ as the *pseudo-rapidity*

$$\eta = -ln(\tan(\frac{\theta}{2})).$$

The pseudo-rapidity is a convenient choice at a hadron collider as the multiplicity of high energy particles is roughly constant in η. Additionally, it is relatively insensitive to boosts along the z axis.

3.3.2 Luminosity System

To detect the presence of a collision and measure the luminosity of the collected data, plastic scintillators are mounted on the inside of the north and south cryostats between $2.7 < |\eta| < 4.4$ Collision products will arrive at each set of scintillators roughly in coincidence, while beam halo products passing through the detector will appear distinctly separated.

3.3.3 Tracking Detectors

The central tracking system is encased in a solenoid which provides a nearly uniform 2T magnetic field parallel to the beam axis. Charged particles produced in the collision are bent around the field lines; this curvature allows for a measurement of transverse momentum.

Closest to the beam pipe itself is the Silicon Microstrip Tracker (SMT), which allows for the precision measurements crucial for accurate measurement of impact parameter and identification of secondary vertices. Surrounding the SMT is the Central Fiber Tracker (CFT), comprised of 16 layers of scintillating fiber. The CFT extends to a radius of 50 cm, giving a lever arm long enough to provide effective transverse momentum resolution. Figure 3.4 shows the geometry of the tracking system.

Silicon Microstrip Detector

Charged particles passing through the 300 μm wafers of n-type silicon which comprise the SMT produce pairs of electrons and holes. The ionized charge is collected by strips of p-type or n^+-type silicon strips, whose minute construction provides for measurement of the position of the ionization with excellent resolution in one dimension. The wafers have p-type strips parallel to the beam axis; many have n^+-type strips on the reverse side, placed at 2° or 90° for measurement in two dimensions.

The wafers are arranged in four barrels of hermetic layers, each comprised of

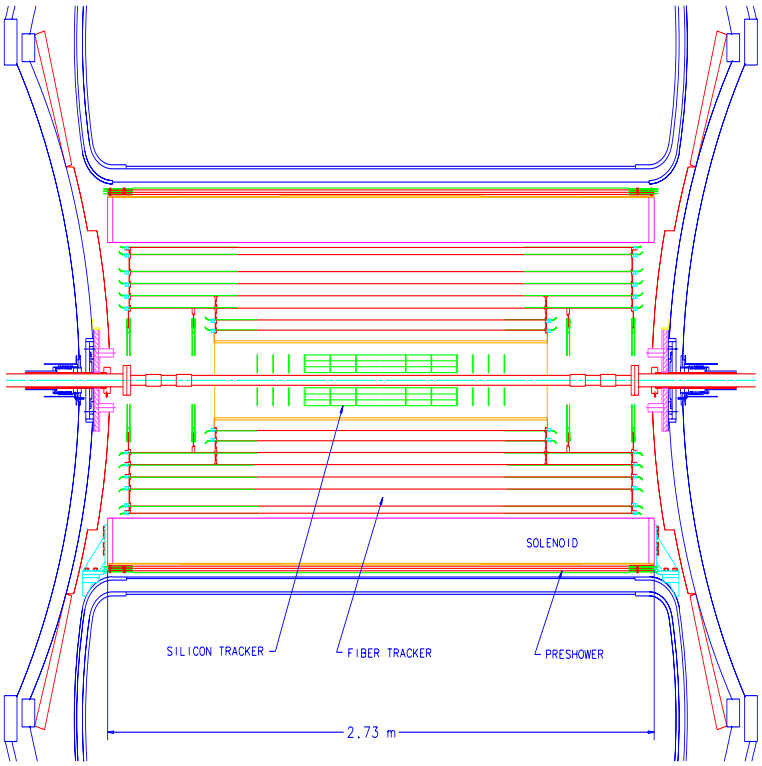

Figure 3.4: The DØ central tracking system.

two overlapping sublayers, see Figure 3.5. In addition, ten discs of wafers are arranged perpendicular to the beam to provide improved position measurement along the z-axis.

The charges accumulated in the silicon strips are collected into a capacitor by the SVXIIe readout chip. For each channel, an array of 32 capacitors allows the chip to hold the information from an event while a trigger decision is made. If the event is triggered, the charges are digitized and sent to the data acquisition system.

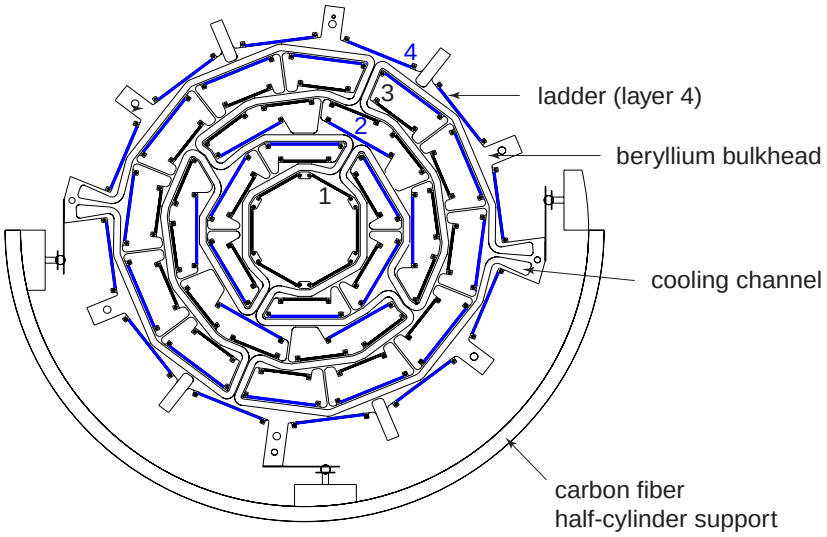

Figure 3.5: A view of the structure of the silicon microstrip tracker along the beam axis.

Central Fiber Tracker

The Central Fiber Tracker [32] features sixteen layers of 835 μm polystyrene wave-length shifting scintillating fibers. The polystyrene is doped with the organic fluorescent dye paraterphenyl which significantly improves the scintillation. Paraterphenyl receives the ionization energy from the polystyrene via a non-radiative dipole-dipole interaction and rapidly fluoresces at $\lambda \approx 340$ nm. In order to increase the mean free path of the light in polystyrene, a wave-shifting dye, 3-hydroxyflavone, is added which features minimal self-absorption. The 3HF absorbs well at $\lambda \approx 340$ and emits at $\lambda \approx 530$ nm, at which wavelength light can be successfully propagated over 4 meters in the fiber.

Each layer consists of a doublet of fibers, with the outer layer offset by a half

a fiber width to provide improved coverage. The fibers are coated on one end with aluminum to reflect the produced light to the collection end, where a wave guide sends the light to the extremely sensitive Visible Light Photon Counters which convert it into an electronic pulse. The readout and digitization is very similar to that of the SMT.

Eight of the sixteen layers are parallel to the beam, providing excellent resolution in ϕ. Eight layers are placed at alternating angles of $\approx \pm 3^\circ$ relative to the beam axis, which provides a measurement of the z position with less precision.

3.3.4 Calorimeter

The function of the calorimeter system is to measure the energy of particles by inducing them to produce electromagnetic and hadronic showers. Inert layers of dense material in which the shower begins are followed by active layers, where the surviving fraction of the shower energy is sampled through ionization.

These elements are combined in the basic unit, a calorimeter cell, depicted in Figure 3.6, which contains absorber plates of depleted uranium (or copper), the active liquid argon and a copper readout pad laminated to G10 and covered in resistive epoxy for collecting the ionization. The surface of the pad is held at high voltage to function as an anode; the ionization of the active material creates an image charge in the readout pad.

The calorimeter system is divided into two sections, see Figure 3.7. The first

is designed to measure precisely energy of electromagnetic particles, and the second to capture hadronic particles. The electromagnetic section contains in total 65.6 mm of uranium, which represents more than 20 radiation lengths ($X_0^{Ur} \approx 3.2$mm) to capture the overwhelming fraction of the electromagnetic energy.

As the nuclear interaction length is much larger than the radiation length, ($\lambda_I^{Ur} \approx 10.5\text{cm} \approx 30X_0$), hadronic particles typically deposit most of their energy in the outer section of the calorimeter, which contains $\approx 6.4\lambda_I$ of uranium and copper.

The calorimeter is composed of three cryostats which maintain the argon's liquid phase. As depicted in Figure 3.8, the central calorimeter extends in pseudorapidity to roughly $|\eta| = 1.1$, and the forward calorimeters extend to $|\eta| = 4.0$.

The calorimeter cells are arranged and sized such that each covers roughly an area of $\eta \times \phi = 0.1 \times 0.1$. The electromagnetic calorimeter is divided into four layers; the third layer is placed where the shower is expected to reach its maximum and the cells measure $\eta \times \phi = 0.05 \times 0.05$ to provide improved spatial resolution. The fine hadronic calorimeter has 3 (4) layers of cells in the central (forward) region; the coarse hadronic calorimeter provides the final stopping power.

3.3.5 Muon Spectrometer

Charged particles which do not cause electromagnetic or hadronic showers are detected by the muon spectrometer, which consists of drift tubes and scintillating pixels

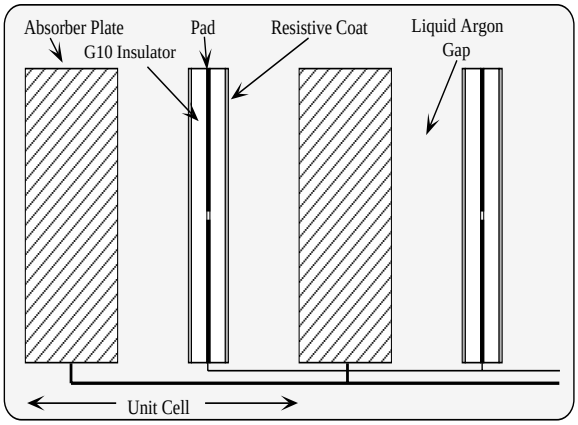

Figure 3.6: A schematic diagram of an individual calorimeter cell.

arranged around a 1.9T toroidal magnet, as seen in Figure 3.9. The 1973 ton magnet provides a magnetic field in perpendicular to the beam axis.

The spectrometer is divided into the central system covering $|\eta| < 1.0$ and the forward system covering $|\eta| > 1.0$ through $|\eta| < 2.0$.

Drift Tubes

The muon system has three layers of drift tubes. The first (A) is positioned closer to the beam than the magnet, and the second two layers (B and C) encase the magnet. The combination allows for a calculation of the particle momentum through measurement of the curvature.

Drift tubes are rectangular gas filled volumes; the ionization created by a pass-

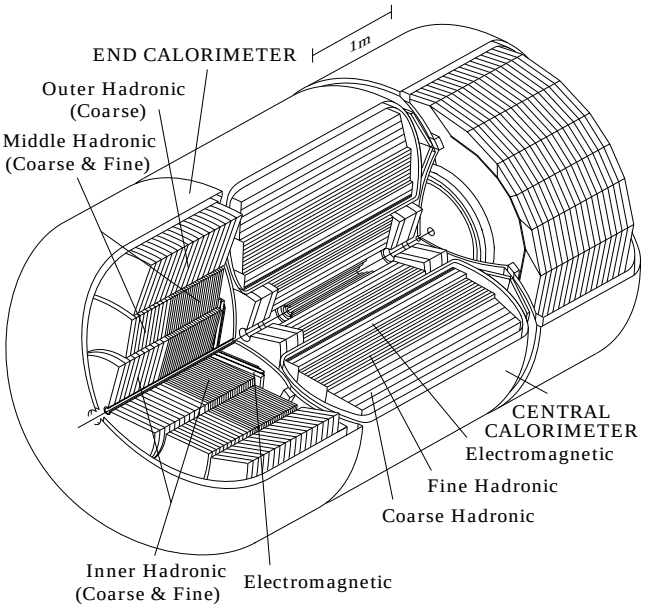

Figure 3.7: Cut-away view of the calorimeter, showing the division into electromagnetic and hadronic sections as well as central and forward regions.

ing charged particle is collected and amplified by a sense wire which runs through the center of the chamber. Figure 3.10 shows the geometry of an example drift tube, and the arrangement of central drift tubes in the A (4 banks) and B and C layers (3 banks). Central drift tubes are constructed of extruded aluminum coated with steel foil and a gold-plated tungsten sense wire and filled with a mixture of 80% argon, 10% CH_4 and 10% CF_4; they are 5.5×10.0 cm in cross section and 240 cm long. Forward drift tubes are significantly narrower, at 1×1cm in cross section and varying lengths, see Figure 3.11.

A measurement of the arrival time of the pulse from the sense wire and a calibration of the drift time of the gas allows for calculation of the radial distance from

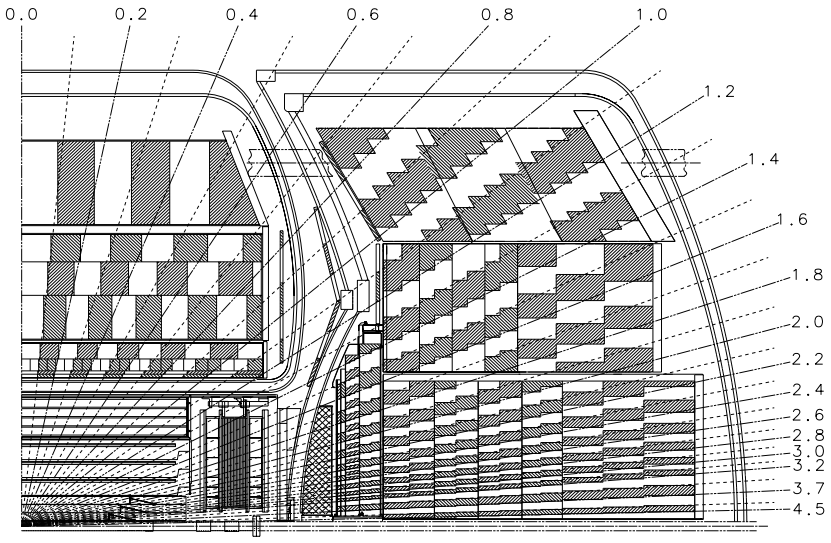

Figure 3.8: A side view of the DØ detector, highlighting the organization of the calorimeter cells into towers of constant pseudo-rapidity.

the sense wire. In order to measure the position of the ionization along the wire in the central region, sense wires for the tubes have been joined at one end; a comparison of arrival times from adjacent wires provides a rough measurement in this dimension.

As their measurement precision is quite asymmetric, drift tubes are arranged so that their sense wires run parallel to the magnetic field and perpendicular to the particle trajectories.

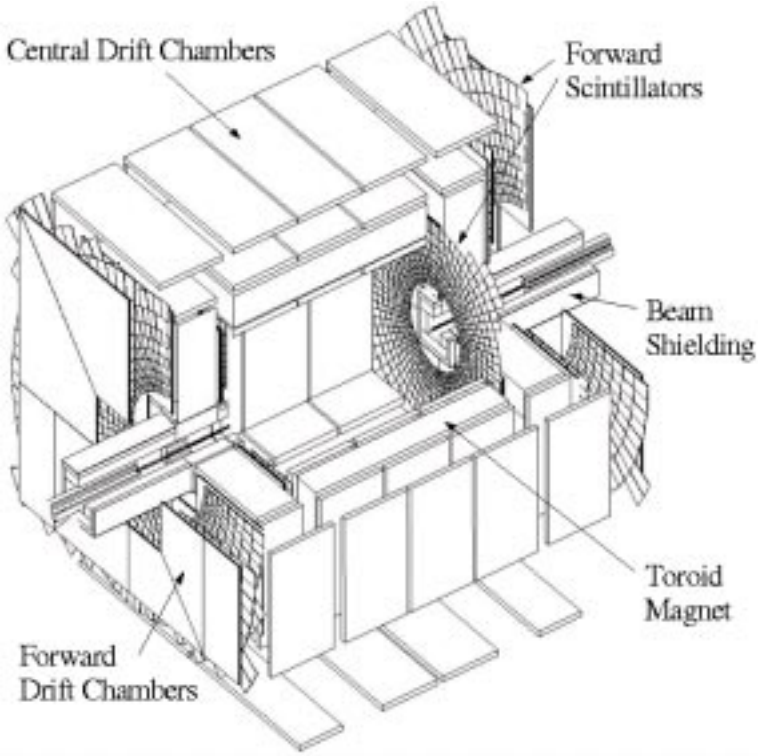

Figure 3.9: The DØ muon system.

Scintillating Pixels

Sheets of scintillating pixels accompany each layer of drift tubes, with the exception of the B layer in the central system. Designed to cover roughly 4.5° in ϕ, they provide additional position measurement along the direction of the drift tube sense wires, and make precise measurement of particle arrival times. Figure 3.12 shows the arrangement of the central scintillators, and Figure 3.9 shows the forward scintillators.

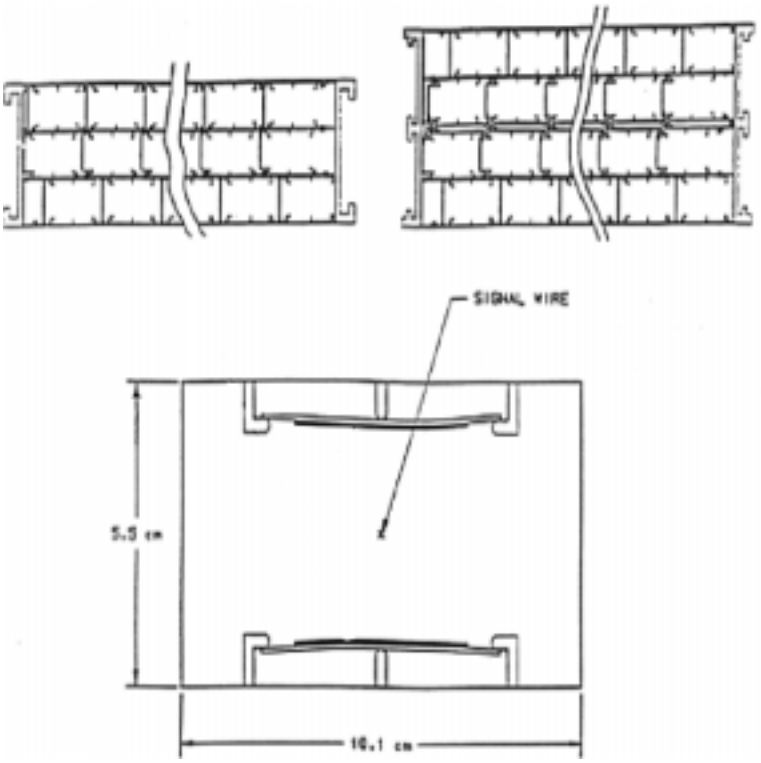

Figure 3.10: Drift tubes in the central muon system. An example tube (*below*) and stacking of tubes in the A (*upper left*) and BC (*upper right*) layers.

The pixels consist of a slab of scintillator in which light-collecting fibers have been set in grooves. A photomultiplier tube collects the light and provides an analog voltage pulse to the digitizing electronics.

3.3.6 Trigger System

The overwhelming majority of proton anti-proton encounters result in collisions of little interest. Collisions which produce massive particles such as W,Z,t and those

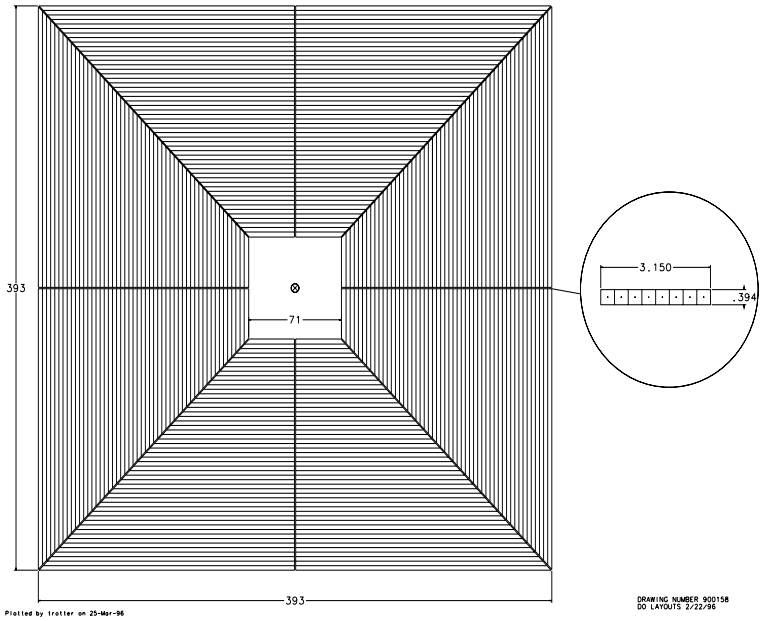

Figure 3.11: Arrangement of drift tubes in the forward muon system.

which might provide evidence of new physics occur extremely rarely. To accumulate a large sample of events of interest without having to store and reconstruct a staggering number of uninteresting collisions, DØ employs an event trigger which decides whether to store an event or to disregard it. The trigger system is a three tiered pipelined system; each tier examines the event in more detail than lower tiers and restricts the rate of events to higher tiers.

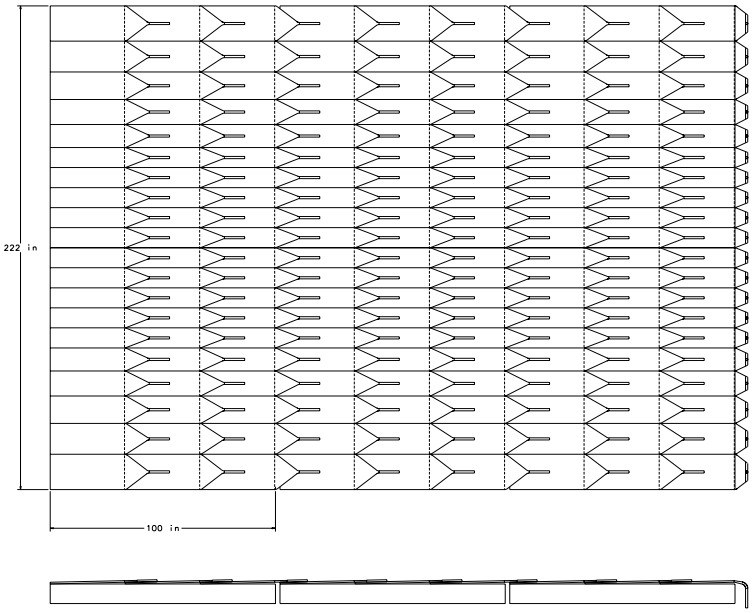

Figure 3.12: Arrangement of scintillator pixels in the central muon system.

Level 1 Trigger

Collisions occur at a rate of 2.5 MHz; the first level trigger has a pipe line, which allows it 4.2μs to make a decision; it must reduce the rate to 10 kHz. The trigger decision is made by a framework built of field programmable gate arrays, which take inputs from the luminosity monitor, the calorimeter and the muon system.

The luminosity system provides an indication that a collision occurred with a position on the z axis which would place it within DØ's volume. The calorimeter employs a special data path which performs a very quick summation of electromagnetic

and hadronic towers at a resolution of $\eta \times \phi = 0.2 \times 0.2$; the trigger requires that the energy in these towers be above a certain threshold. The muon trigger requires a coincidence between the scintillators in the A and (B or C) layers.

Level 2 Trigger

The Level 2 system is comprised of two stages, a preprocessor stage and a global trigger stage. The preprocessors, DEC ALPHA processors running simple C programs, identify objects such as tracks, electrons, jets and muons. The global stage allows the first opportunity to examine the correlation between objects, such as tracks and leptons. The Level 2 trigger has a time budget of 100 μs and must reduce the rate to 1 kHz.

Level 3 Trigger

The Level 3 trigger is implemented entirely in software; it employs a small farm of computers to perform an approximate reconstruction of the event and make a trigger decision using the full event information. Algorithms for electron, muon and jet reconstruction mimic those used in the full reconstruction program described below. See Appendix A for a detailed description of the Level 3 tracking algorithm. The Level 3 trigger has a time budget of 100 ms and must reduce the readout rate to 50 Hz.

Chapter 4

Event Trigger

Collisions at the Tevatron occur at a rate far beyond the capabilities of the data recording or analysis structures. As discussed in Section 3.3.5, a trigger system selects the events of interest.

To ensure that the relevant data are recorded, a trigger to select events with both an electron and a muon was designed by balancing efficiency and simplicity with a need for rejection. The trigger, named MU_A_EM10 in trigger list versions 8.0 through 11.0, has the conditions:

- Level 1
  - L1PTXATXX: Level 1 muon scintillator coincidence, $|\eta| < 2.0$
  - CEM(1,5): At least one tower with at least 5 GeV of EM energy, $|\eta| < 2.4$

- Level 2
  - none
- Level 3
  - L3Ele(1,10.0): One electron above 10 GeV, $|\eta| < 2.4$.

In the case of the muon, the rejection that could be achieved by additional Level 2 or Level 3 terms was marginal and the inefficiencies and complications were substantial. In the case of the electron, the Level 3 term is important in reducing the rate at which heavy flavor events (muon plus jet events) fire the trigger. As the Level 3 reconstruction code is very similar to the offline electron reconstruction code, it provides almost unit efficiency.

4.1 Level 1 Efficiency

The Level 1 muon trigger provides P_T-independent efficiency of

$$\epsilon_\mu = 95.0 \pm 0.5\%,$$

see Figure 4.1. The measurement is made on an unbiased set of data, events which have a reconstructed medium muon [47] and which were triggered by calorimeter-only triggers. The L1 muon term is considered inefficient if the L1 muon trigger did not fire in the

Process	$< N_{muons} >$	$P(\mu^{L1})$
$t\bar{t}$	1.27	$96.5\% \pm 0.5$
WW	1.00	$95.9\% \pm 0.2$
WZ	1.31	$96.7\% \pm 0.2$
$W(\rightarrow \mu\nu)\gamma$	1.00	$95.9\% \pm 0.2$
$Z \rightarrow \tau\tau$	1.02	$95.1\% \pm 0.5$

Table 4.1: Probability to fire the Level 1 muon trigger for various signal processes.

specific octant and region in which the muon was reconstructed offline. This definition of inefficiency avoids biases due to other muons in an event which may independently fire the muon triggers. It provides a measure of the per-muon trigger efficiency. While there is not a strong P_T-dependence, we find a significant dependence on the η of the reconstructed muon, see Figure 4.1.

For processes with exactly, or nearly exactly, one muon, this is equivalent to the per-event efficiency. Top quark decay, however, is often accompanied by a secondary muon from the decay of b hadrons. To measure the per-event efficiency, we account for the distribution in η of muons in each process as well as the number of muons:

$$P(\mu^{L1}|event) = 1 - \prod_{N_\mu} (1 - \epsilon_\mu(\eta))$$

where N_μ is the number of muons in the event and $\epsilon_\mu(\eta)$ describes the efficiency as a function of the muon η. In $t\bar{t} \rightarrow e\mu bb$ events, this provides a modest increase in the trigger efficiency, see Table 4.1.

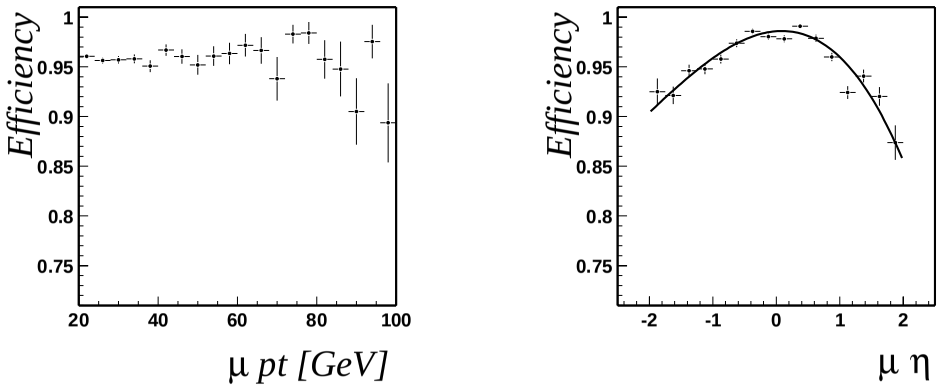

Figure 4.1: L1 muon efficiencies, relative to offline reconstructed muons, as a function of offline muon P_T (*left*) and η (*right*).

The Level 1 electron trigger may be fired by jets in the events as well as electrons. One must, therefore, take into account the specific topology of a process in measuring this efficiency, which requires use of the signal simulation. Unfortunately, the response of the trigger in simulation does not presently model well the performance of the detector. To compensate, we measure the per-electron and per-jet efficiencies $\epsilon_{j,e}(P_T, \eta)$, as functions of P_T and η, and fold them into the signal simulation to measure the probability that an individual event would fire the trigger condition:

$$P(e^{L1}|event) = 1 - \prod_i [1 - \epsilon_{j,e}(P_T^i, \eta^i)].$$

The per-electron efficiencies are measured in events with an offline reconstructed electron

Process	$P(e^{L1}\|e)$	$P(e^{L1}\|e+jets)$
$t\bar{t}$	$98.1\% \pm 0.1$	$99.6\% \pm 0.1$
WW	$97.8\% \pm 0.1$	$97.8\% \pm 0.1$
$W(\rightarrow \mu\nu)\gamma$	$97.8\% \pm 0.1$	$97.8\% \pm 0.1$
WZ	$99.1\% \pm 0.1$	$99.2\% \pm 0.1$
$Z \rightarrow \tau\tau$	$97.8\% \pm 0.1$	$97.8\% \pm 0.1$

Table 4.2: Probability to fire the Level 1 electron trigger CEM(1,5) for various signal processes, with and without accounting for jets.

which are triggered by muon-only triggers. The electrons are required to have a 5 GeV L1 EM tower within $R < 0.5$, where $R = \sqrt{\Delta\phi^2 + \Delta\eta^2}$. The efficiencies are shown in Figure 4.2. The per-jet efficiencies are measured in a similar manner, requiring 5 GeV of EM energy in an L1 tower within $R < 0.5$, see Figure 4.3.

The per-event efficiency is measured by folding the per-electron and per-jet efficiencies together, see Figure 4.4. As the P_T of electrons in top events is much higher than that in the sample on which the efficiencies were measured, the per-event efficiency is generally very high. The probability to fire the Level 1 electron trigger is given in Table 4.2 for relevant physics processes.

4.2 Level 3 Efficiency

The Level 3 electron efficiency is measured in events with an offline reconstructed electron which were triggered by an unbiased muon trigger. In this case, the trigger efficiency is sufficiently high that we need not consider the topology dependence,

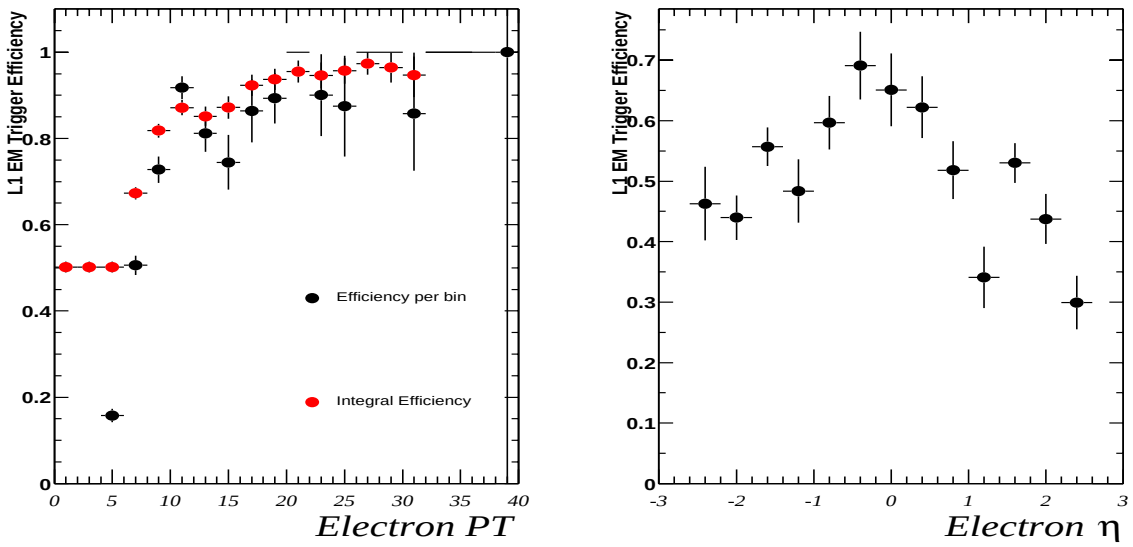

Figure 4.2: Per-electron efficiency to fire the L1 CEM(1,5) trigger term, relative to offline reconstructed electrons, as a function of corrected offline electron P_T (*left*) and η (*right*).

see Figure 4.5. The trigger efficiencies are derived by folding this parametrized efficiency with the momentum spectrum of electrons, see Table 4.3.

4.3 Total Efficiency

The total trigger efficiencies for the physics processes are given in Table 4.4

Process	$P(e^{L3})$
$t\bar{t}$	$99.98\% \pm 0.02$
WW	$99.98\% \pm 0.02$
WZ	$99.99\% \pm 0.02$
$W(\rightarrow \mu\nu)\gamma$	$99.98\% \pm 0.02$
$Z \rightarrow \tau\tau$	$99.90\% \pm 0.02$

Table 4.3: Probability to fire the Level 3 electron trigger L3ELE(1,10.0)

Process	P(MU_A_EM10)
$t\bar{t}$	$96.1\% \pm 0.5$
WW	$93.7\% \pm 0.5$
WZ	$95.9\% \pm 0.5$
$W(\rightarrow \mu\nu)\gamma$	$93.7\% \pm 0.5$
$Z \rightarrow \tau\tau$	$93.0\% \pm 0.5$

Table 4.4: Probability to fire the trigger MU_A_EM10.

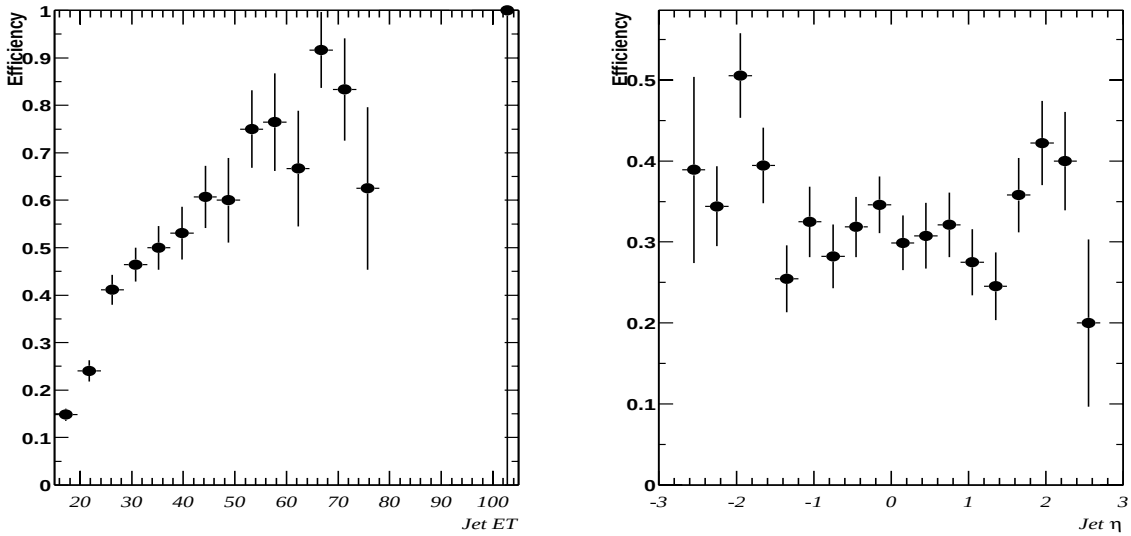

Figure 4.3: Per-jet efficiency to fire the L1 CEM(1,5) trigger term, relative to offline reconstructed jets, as a function of offline corrected jet P_T (*left*) and η (*right*).

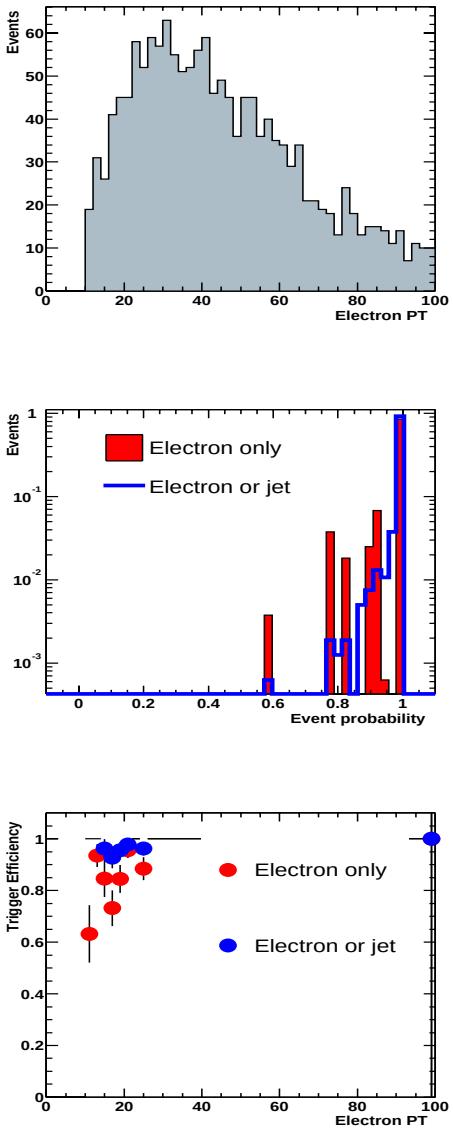

Figure 4.4: Top, distribution of P_T for electrons in $t\bar{t} \to e\mu jj$ events. Center, per-event probability to pass L1 EM trigger, when only electrons are allowed to fire the trigger, or when either electrons or jets may fire it. Bottom, total L1 EM efficiency as a function of corrected electron P_T.

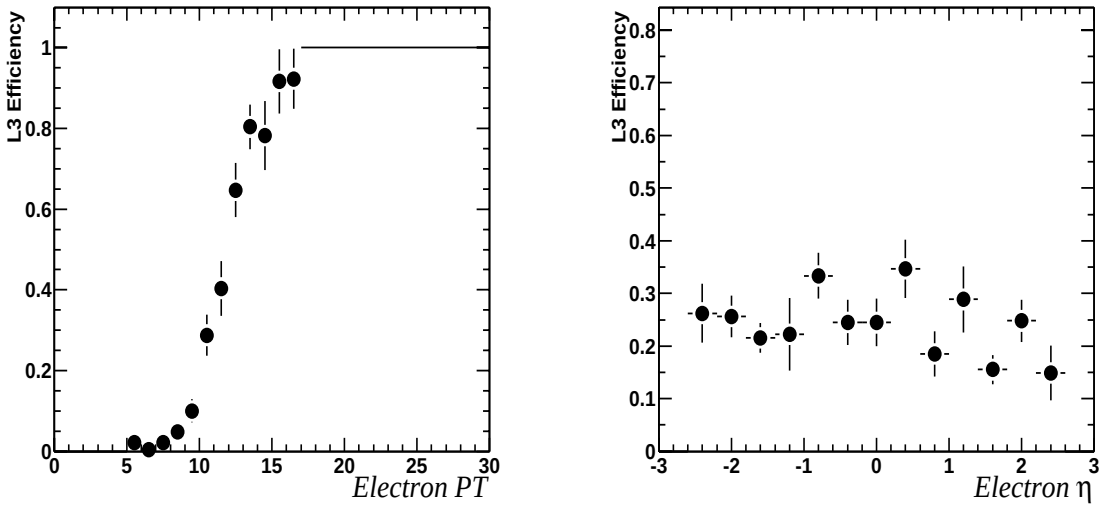

Figure 4.5: Per-electron efficiency to fire the L3 Ele(1,10) trigger term, relative to offline reconstructed electrons, as a function of offline corrected electron P_T (*left*) and η (*right*). The efficiency is roughly independent of η; the low value is due to the domination of this sample by low-P_T electrons.

Chapter 5

Event Reconstruction and Object Identification

The data as collected consist of nearly a million channels of immediate detector response; these channels must be carefully processed for evidence of the products of the collision which provide information as to the kinematics of the interaction.

Especially important to this analysis is the identification of energetic electrons, muons and hadronic jets. Algorithms have been developed to identify the signature of these objects in each detector subsystem, and then optimized to provide the best possible measurement of the magnitude and direction of their momenta. In addition, one must minimize the misidentification of other objects which may mimic these.

High quality reconstruction is vital to disentangle the objects in an event. It is equally important to understand in detail the strengths and weaknesses of these algorithms, as they translate directly into sensitivity or lack of sensitivity for physical measurements.

In this chapter, strategies for reconstructing these objects from the detector responses are described, and studies detailing the efficiency and performance of those algorithms are presented.

5.1 Event Reconstruction

All events in this data sample have been reconstructed with DØReco versions p13.05.00 through p13.06.01. The DØ standard has been followed, and in some cases refined.

5.1.1 Track Reconstruction

The central tracking system is responsible for a large fraction of the individual channels of detector response. Sifting through these channels for the signature of a charged particle curving through the magnetic field is a difficult and time consuming task. It is abstracted into two pieces: hit clustering, which groups individual channels of a specific layer which are likely to represent the passage of an individual particle; and track finding, which finds groups of clusters located along a physical path.

Hit Clustering

A particle passing through a layer of the Central Fiber Tracker will illuminate either one or two fibers. To form clusters out of the individual fibers is simply to group them into pairs of adjacent fibers. If more than two adjacent fibers are illuminated, then every possible pair of fibers are grouped as an independent cluster; the ambiguity is resolved by the tracking algorithm. A detailed description is given in [46].

Particles traversing the Silicon Microstrip Detector may deposit charge in a number of strips, depending on their angles of incidence. Additionally, ionization may leak from one strip to the next. A simple grouping of adjacent strips above a noise threshold provides satisfactory clusters. The position of the cluster is an average of the strip positions, weighted by the deposited charge.

Track Finding

Track finding is further abstracted into two algorithmic pieces: pattern recognition and track fitting. The task of pattern recognition is to search the list of clusters for a set which lie along a physical path; a sophisticated algorithm is required, as examination of every possible combination would take a prohibitive amount of time. Attempting to fit a candidate charged particle track to a physical path allows for the measurement of the consistency of the hits with the path of a particle, via a χ^2 test, and for extraction of physical parameters, such as the particle momentum.

DØ employs two track finding algorithms. One, known as GTR, performs the tasks of pattern recognition and track fitting simultaneously; it begins by forming a large number of candidate tracks in one region of the detector and evaluating the χ^2 of these candidates as it propagates them through the detector searching for additional hits. The other, known as HTF, separates the tasks; it uses a histogramming approach to identify likely candidates before evaluating their quality. The results of the two algorithms are combined to produce a final set of charged particle tracks.

5.1.2 Vertex Reconstruction

The point of collision between the proton and the anti-proton, the vertex, is limited in the transverse plane by the size of the beam spot, which is of the order of tens of microns. Along the beam axis, however, the vertex position varies by tens of centimeters.

As the calorimeter is unable to disentangle transverse and longitudinal momentum, reconstruction of the vertex position is crucial for accurate estimates of the transverse momentum of electrons, jets and for reconstruction of missing transverse energy.

The vertex is reconstructed [36] by clustering tracks which approach each other near the beam axis. A vertex position is reconstructed, and tracks inconsistent with that position are iteratively removed, until a consistent vertex is established.

In order to ensure the quality of the event reconstruction, we impose requirements on the reconstructed primary vertex. We require that it have at least three associated tracks, and that it be within the volume of the silicon detector, $|z_0 < 60.0|$ cm. Figure 5.1 shows the distributions of these values for simulated $t\bar{t} \to e\mu jj$ events.

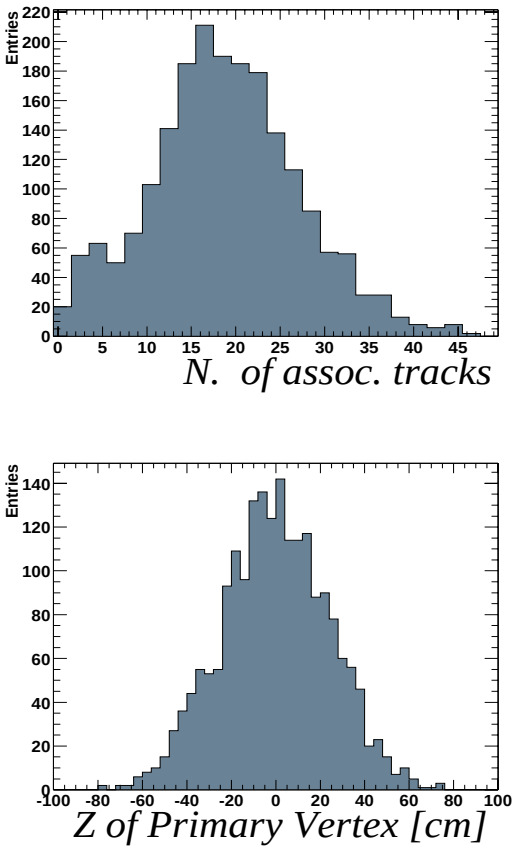

Figure 5.1: Details of the primary vertex reconstruction. The number of tracks associated with the vertex (*top*), and the position in z (*bottom*).

5.1.3 Muons

Muons are reconstructed using information from the muon system and the central tracker. A signature in the calorimeter is used only for measuring identification efficiencies. A veto on cosmic muons is applied by requiring the time difference between scintillator hits in B or C Layer and the A layer to be consistent with a muon coming from the interaction region ($\delta t > -10$ns).

Muon Track Reconstruction

Muons are identified in the outer chamber by matching segments on either side of the toroid. In each region, segments are straight lines fit to groups of nearby drift chamber and pixel hits. Tracks are constructed from segments in the BC region by searching for matching segments in the A layer. If a segment satisfies loose proximity conditions, then a more careful fit is performed to ensure that the track represents a physical path. An estimate of the muon's momentum is performed from the bending angle through the toroid; in the case that a central track is matched to the muon track, this estimate is discarded.

In the muon system, a track must have

- at least 1 wire hit in the A segment
- at least 1 scintillator hit in the A segment

- at least 2 wire hits in the BC segment
- at least 1 scintillator hit in the BC segment

Central Track Finding

The muon tracks are then extended to the point of closest approach (PCA) to the beam and their parameters are compared with those of central tracks at PCA. For all central tracks within 1 radian in azimuthal and polar angle of a muon track at PCA a global fit is performed. Only the best match (smallest χ^2) is kept.

Muon Isolation

We require that the muon appear isolated in the detector; specifically:

- Halo$(0.1, 0.4) < 2.5$ GeV, requiring a small amount of calorimeter energy in a hollow cone surrounding the muon.
- TrackHalo$(0.5) < 2.5$ GeV, requiring a small amount of track energy in a cone surrounding the muon.

See Appendix C for detailed studies and definitions of muon isolation criteria.

Muon Distance of Closest Approach

A high P_T muon from the decay of a W will have a track originating from the primary vertex of the event. To quantify the association of the muon with the primary vertex, we measure its closest approach to the line through the vertex which is parallel to the z axis, called the distance of closest approach (DCA). To remove from consideration muons which do not come from this vertex, we require that the significance of the DCA, defined as the DCA divided by its error, have magnitude smaller than 3.0. Figure 5.2 shows the distribution of DCA, its error and significance in $t\bar{t} \to e\mu jj$ events .

5.1.4 Electrons

At the reconstruction stage, an EM cluster is defined as a set of towers in a cone of radius $\mathcal{R} = \sqrt{\Delta\eta^2 + \Delta\varphi^2} = 0.2$ around an initial tower selected on the basis of its energy content. Among all reconstructed clusters, genuine EM showers are expected to have a large EM fraction $f_{\rm EM} \equiv E_{\rm EM}/E_{\rm tot}$ (where $E_{\rm EM}$ is the cluster energy in the EM section of the calorimeter and $E_{\rm tot}$ is its total energy within the cone), and to have a longitudinal and lateral development compatible with those of an electron. Each cluster is attributed a χ^2 based on the comparison of the values of the energy deposited in each layer of the EM calorimeter and the total energy of the shower with average distributions obtained from simulation.

Electron candidates are selected by requiring that

$$f_{\rm EM} > 0.9 \quad \text{and} \quad \chi^2 < 20(8\ d.o.f.) \quad .$$

We additionally require that the cluster be isolated:

$$f_{\rm iso} = \frac{E_{\rm tot}(\mathcal{R} < 0.4) - E_{\rm EM}(\mathcal{R} < 0.2)}{E_{\rm EM}(\mathcal{R} < 0.2)} < 0.15$$

Electron Likelihood

The electron reconstruction in the calorimeter suppresses a large portion of the QCD background contamination. However, due to the overwhelming nature of this background, further rejection from the central tracking chamber is required. The electron is required to have a track which satisfies an initial selection

$$|\Delta\phi_{EM,Track}| < 0.05, |\Delta\eta_{EM,Track}| < 0.05.$$

For electrons with associated tracks, we require that the electron resembles a canonical sample of electrons by selecting those with a large electron likelihood, [37]. In the central region, we require that the electron likelihood discriminant D be greater than 0.15. These numbers were determined in order to achieve an efficiency of approximately 95%. Details of the efficiencies are given in Section 5.2.8.

5.1.5 Jets

Jets are reconstructed at DØ using the *improved legacy cone* algorithm designed following the recommendation of the Run2 QCD workshop. Seed towers are composed of the sum of all cells not in the coarse hadronic layer which share the same pseudo-rapidity and azimuthal angle. Only towers with positive energy are kept as seeds to the cone algorithm. A cone of $\mathcal{R} = 0.5$ is chosen.

We apply all known corrections to the calorimeter cells, including those which correct for energy sharing and BLS problems. Once jets are clustered, further quality selection cuts are applied to each jets.

- To remove isolated electromagnetic particles a cut on the fraction energy deposited in the electromagnetic section of the calorimeter (EMF) is applied at $0.05 < EMF < 0.95$.

- To remove jets which predominantly deposit their energy in the coarse hadronic section of the calorimeter, a cut on the fraction of the jet energy deposited therein (CHF) is applied at $CHF < 0.4$. This cut is essentially aimed at removing those jets which clustered around noise in the coarse hadronic section in which weights are significantly larger than those of other sections of the calorimeter.

- To remove those jets clustered from hot cells, a cut on the ratio of the highest to the next-to-highest transverse energy cell in the calorimeter ($HotF$) is applied at

$HotF < 10$.

- To remove those jets clustered from a single hot tower, the number of towers containing 90% of the jet energy $n90$ is required to be greater than 1.

- Jets with transverse energy E_T below 15 GeV are not considered.

Despite the numerous quality requirements applied to avoid clustering noise into jets, a large number of such jets survive these requirements. As these jets appear at the reconstruction level but are not seen in the trigger readout, they are most likely due to coherent noise in the precision readout chain which separates from that of the trigger right after the preamplification stage.

These "noise" jets originate from low energy but high occupancy noise in well confined regions of the calorimeter corresponding to specific sets of cells corresponding to a specific set of BLS boards. As the coarse hadronic section has the highest calorimetric weights, most of the energy should appear in that particular section. Noise-jets appear to have numerous seed towers and following the jet clustering scheme these jets are likely to undergo many merges. As these jets have their energy more or less evenly spread throughout all its towers, $n90$ could be used to discriminate them against good jets. However in the case of very wide jets, for example with soft gluon radiation in the final state, which underwent numerous merges, $n90$ could be very large as well and lose its discrimination power. Since noise-jets are also clustered from numerous seed towers,

they are also likely to merge many times. A more suitable discriminating variable would thus be $f90$ which is the ratio of $n90$ to the number of towers.

To remove these noise jets while maintaining efficiency for real jets, we place the following additional cuts. For jets with $P_T > 25$ GeV

- $f90 < 0.8 - 0.5 * CHF$
- or $CHF < 0.05$

and for jets with $P_T < 25$ GeV

- $f90 < 0.7 - 0.5 * CHF$
- or $CHF < 0.025$

Jet Energy Scale

The calorimeter is very effective at absorbing the hadronic energy of the jet. However, there are several mechanisms which cause the energy of the cells clustered into a jet to deviate from the energy of the initial parton. The most important of these are

- Calorimeter Response (R); hadronic showers may lose energy in ways which do not provide visible ionization. The response to electromagnetic and hadronic particles may therefore be imbalanced.

- Energy Offset (O); energy in the clustered cells which is due to noise, the underlying event, multiple interactions, energy pile-up and uranium noise can provide an offset to the energy of the jet.

- Showering Corrections (S); the finite size of the cone used for clustering will certainly exclude a fraction of the jet energy.

To calibrate these effects and provide an energy scale for reconstructed jets, one examines events with an energetic photon which is opposite a jet. The energy of the photon is purely electromagnetic; the EM energy scale may be calibrated independently using $Z \rightarrow ee$ events. The energy of the jet should therefore balance the energy of the photon. The correction may be written as

$$E_{jet}^{corrected} = \frac{E_{jet}^{measured} - O}{R \times S}$$

The correction is derived for both data and simulated jets; Figure 5.3 and Figure 5.4 describe these, respectively.

Jet-Electron separation

Jets which have a very large electromagnetic fraction may be reconstructed as electrons or photons; electrons and photons which overlap with hadronic activity may be reconstructed as jets.

All objects which are reconstructed as electrons or photons are treated with the electromagnetic energy corrections described in Section 5.2.9. Jets which do not overlap with any of the electromagnetic options ($R = \sqrt{\Delta\phi^2 + \Delta\eta^2} > 0.5$) are treated with the jet corrections described above.

5.1.6 Missing Energy

The presence of a neutrino in the final state can be detected only from the imbalance of an event in the transverse plane. It is reconstructed from the vector sum of the transverse energies of all cells with positive transverse energy in all layers of the calorimeter except for those in the coarse hadronic, which are treated separately due to their high level of noise. The only cells of the coarse hadronic calorimeter which are accounted for are those clustered within good jets. The vector opposite to this vector is denoted the missing energy vector and its modulus is the raw missing transverse energy ($\not\!\!E_T{}^{raw}$).

The response of electromagnetic particles such as photons, electrons or π^0's is different from that of hadrons and in particular from that of jets. In events with both electromagnetic objects and jets, this imbalance translates directly into missing transverse energy. As a jet energy scale correction is derived for all good jets, it can also be applied to the missing transverse energy. In order to do so, the absolute JES correction applied to all good jets is subtracted from the $\not\!\!E_T$ vector. The resulting

modulus is denoted the calorimeter missing transverse energy ($\not\!\!E_T{}^{CAL}$).

As a muon is a minimum ionizing particle throughout the entire detector, it will deposit only a small amount of energy in the calorimeter; its presence can thus also fake missing transverse energy in the calorimeter. The momentum of all matched muons present in the event is subtracted from the missing transverse energy vector. We compensate for the the expected energy deposition of the muon in the calorimeter, which is drawn from GEANT lookup tables.

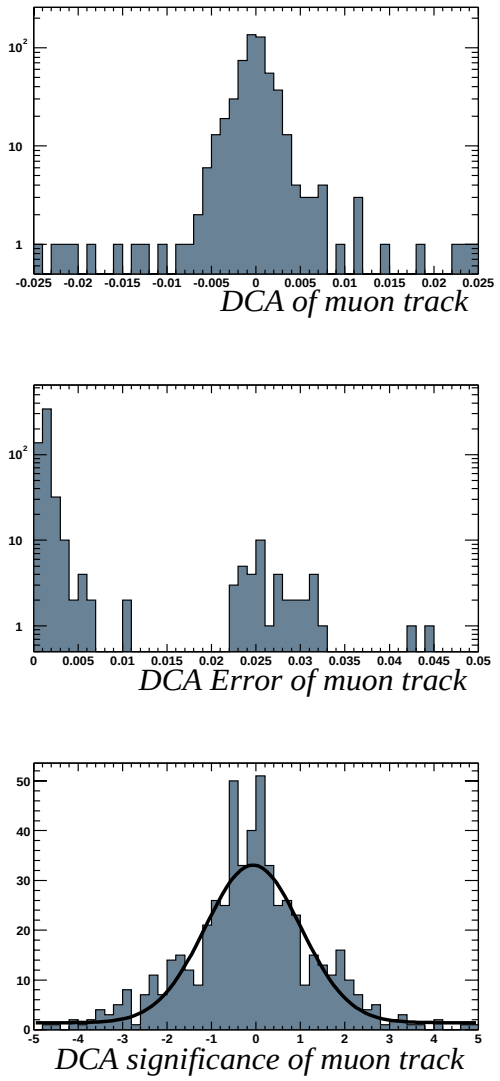

Figure 5.2: Muon distance of closest approach (DCA), (*top*), DCA error (*middle*), and DCA significance, (*bottom*) in $t\bar{t} \to e\mu jj$ events.

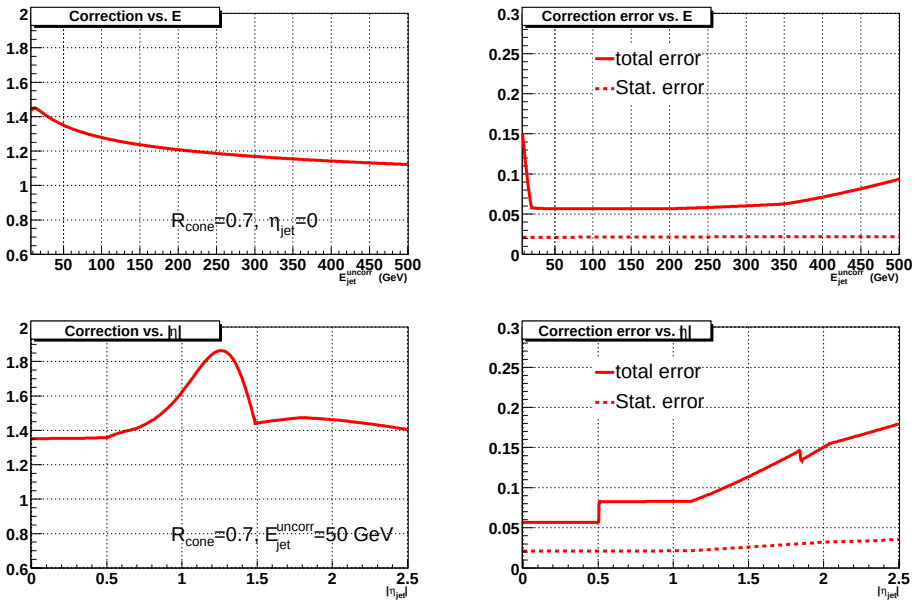

Figure 5.3: Correction to energies of jets in the data , as a function of jet E_T and η, (*left*). Errors in the correction, (*right*).

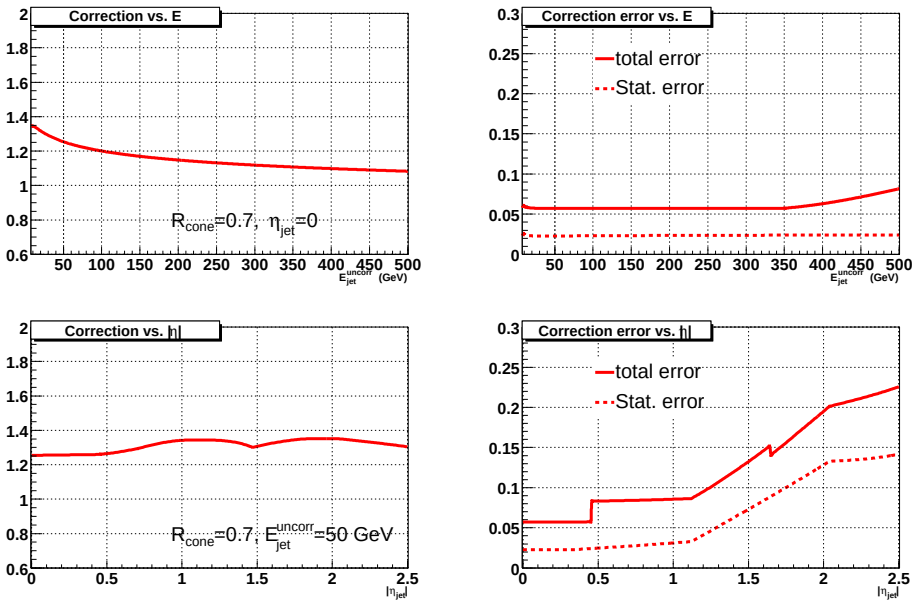

Figure 5.4: Correction to energies of jets in simulation , as a function of jet E_T and η, (*left*). Errors in the correction, (*right*).

5.2 Reconstruction Efficiency

The algorithms described above have been carefully developed; in some cases they have been tuned on simulated data, and in others they have been adjusted to meet challenges in the reconstruction of data events.

To make the measurements outlined in this document, we must rely on simulated data in order to predict the size of the Standard Model contributions to $e\mu$. It is vital, therefore, that the efficiency of reconstruction for simulated events accurately reflects that of collected data. In many cases, the simulation does not describe accurately the physical detector, and performance may differ significantly. Our strategy is to measure the important reconstruction efficiencies both in reference samples in the data and in simulated events. Where the differences are significant, we will correct the simulation to reflect the performance seen in the data.

5.2.1 Muon Reconstruction

The efficiency to reconstruct tracks in the muon system is sensitively dependent on the performance of the muon chambers, as well as the tuning and sophistication of the software. It is likely that this efficiency is significantly different in simulated and real data.

We measure this quantity in simulated $t\bar{t} \to e\mu jj$ events within a very conser-

vative muon acceptance

$$|\eta| < 2.0, \quad !(|\eta| < 1.3, \ (3.9 < \phi < 5.5)).$$

The local muon efficiency in simulation is given in Table 5.3.

To measure this quantity in the data requires a method of muon identification independent of the muon system. As in [38], we identify high P_T muons by looking for $Z \to \mu\mu$ events by identifying two high-P_T tracks, but only requiring one muon to be reconstructed. The second muon is unbiased.

The rate at which these unbiased muons are found in the muon system is a measure of the local muon reconstruction efficiency. Figure 5.5 shows the di-muon invariant mass for all events satisfying the above criteria, as well as those in which the second muon is reconstructed as a medium muon.

The sample with no local muon requirement for the second muon has a much larger background contribution that that with an identified second muon. This demonstrates the impressive purity that the muon system enjoys. Regardless, the background must be subtracted from each sample to obtain a measurement of the Z contribution in each.

We fit the distributions to the function

$$Ae^{-\gamma x} + Be^{(\frac{x-M}{\sigma})^2}$$

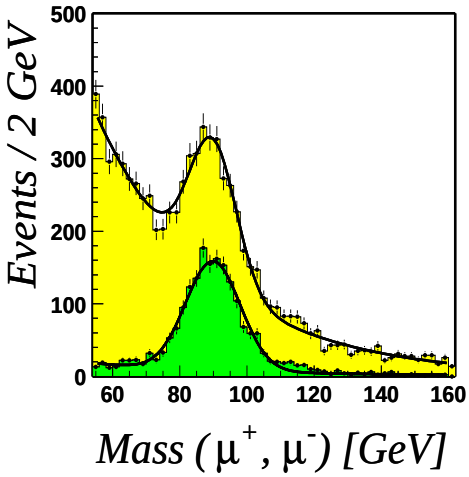

Figure 5.5: Di-muon invariant mass of a local, central-matched muon and a central track. Cases where the second track has a reconstructed muon are also shown.

and in each case obtain the number of Z events as

$$N_Z = N_{\mu\mu}^{76,104} - \int_{76}^{104} Ae^{-\gamma x} dx$$

which allows us to compute the efficiencies. We find

$$\epsilon_{medium}^{\mu} = 86.6 \pm 0.9_{(stat)} \pm 3.7_{(syst)}\%.$$

where the systematic errors are derived from the errors in the fitted background.

5.2.2 Muon Distance of Closest Approach

We measure the rate at which muons satisfy the DCA requirement in simulated events (see Figure 5.2), and in data from $Z \to \mu\mu$ events. Studies [38] have shown good agreement in data and simulation of the efficiency for muons from $Z \to \mu\mu$ to pass this cut.

5.2.3 Muon Track Matching

To measure the rate at which muons are matched to tracks in the central tracker, we study a large sample of di-muon events. We assume that this sample is overwhelmingly dominated by real muons, as punch-through or other mechanisms are negligible at this level of precision. As the background is negligible , we therefore measure the track and matching efficiency simply by measuring the track matching rate.

We ask for an event with two medium isolated muons, each with $\eta < 2.0$. We calculate the per-muon tracking and matching efficiency as functions of ϕ and η of the muons, as shown in Figure 5.6 for simulation and in Figure 5.7 for data.

Figure 5.8 shows the ratio between the two as a function of the muon η.

$$\epsilon_{3D}^{track} = 70.8 \pm 0.1 \pm 1.0\%(Data),\ \epsilon_{3D}^{track} = 90.4 \pm 0.5\%(MC)$$

and

$$\epsilon^{track}_{Axial} = 73.8 \pm 0.1 \pm 1.5\%(Data),\ \epsilon^{track}_{Axial} = 90.4 \pm 0.5\%(MC),$$

where the systematic error on the data is assigned by examining variations over run ranges.

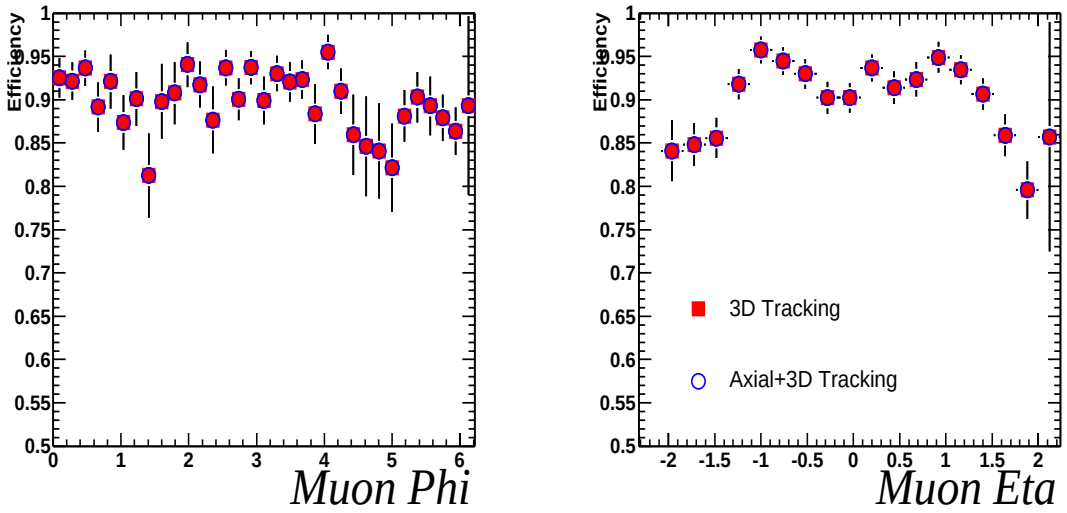

Figure 5.6: Muon tracking and matching efficiencies as a function of ϕ and η of the muon,in simulated events.

In the simulation, the efficiency of the stereo tracking is very high, while the measurement in the data reflects the true performance. This discrepancy cannot be corrected by a simple multiplicative factor; instead, we mimic the inefficiency by applying the correction factor shown in Figure 5.8 to each muon in the simulated data.

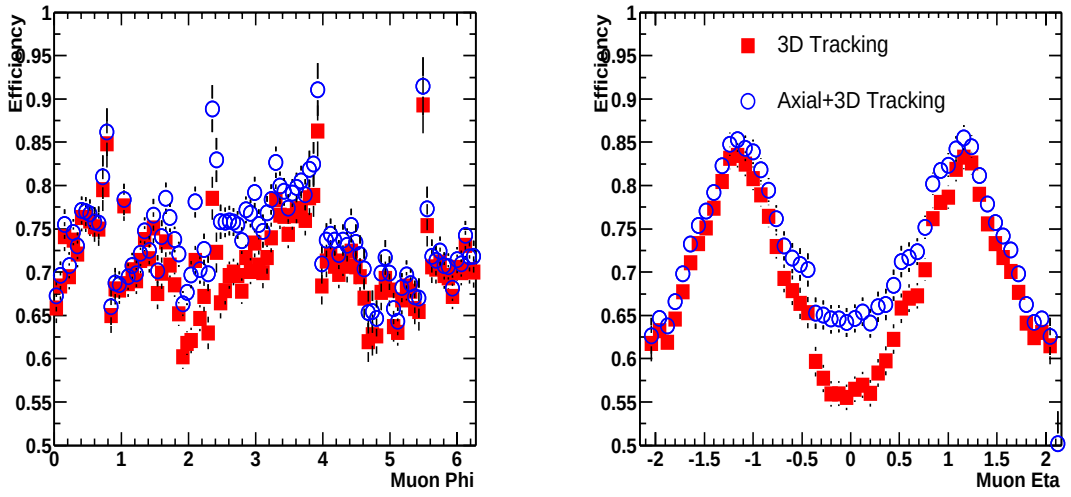

Figure 5.7: Muon tracking and matching efficiencies as a function of ϕ and η of the muon, in data.

5.2.4 Muon Isolation

The muon isolation criterion is inherently topologically dependent. The efficiency has been measured [33] for $Z \to \mu\mu$ events, but this does not accurately reflect the efficiency in events which have distinctly higher jet multiplicities, such as $t\bar{t}$ events. We have measured the isolation efficiency in $Z \to \mu\mu$ events as a function of jet multiplicity both in simulated and in data events. Additionally, we have measured it in $t\bar{t}$ events, see Figure 5.9.

In order to correct the simulation for the performance seen in the data, we compute the isolation efficiency in both the inclusive case, for signals produced without

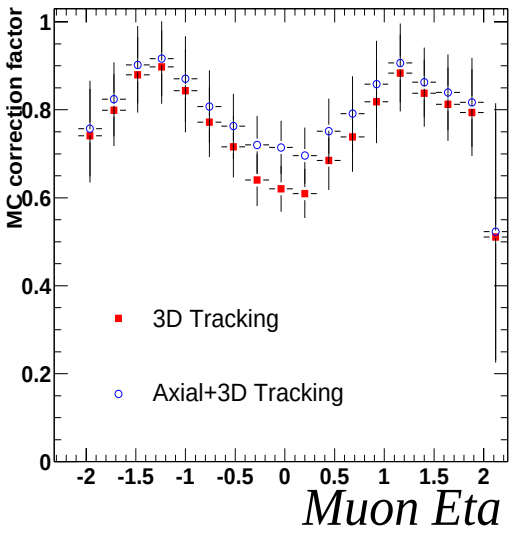

Figure 5.8: Correction to simulated tracking efficiency, as a function of muon η.

jets ($Z \to \tau\tau \to e\mu$ and $WW \to e\mu$) and for those with jets ($t\bar{t}$). Those efficiencies are

$$\epsilon^{Iso}_{Inclusive} = 90.4 \pm 0.5\%(Data), \epsilon^{Iso}_{Inclusive} = 92.7 \pm 0.4\%(Z \to \mu\mu\ MC)$$

$$\epsilon^{Iso}_{jj} = 75.3 \pm 3.2\%(Data), \epsilon^{Iso}_{jj} = 76.1 \pm 1.5\%(Z \to \mu\mu\ MC).$$

The ratio of the efficiency in the data to the efficiency in the simulation will be used to correct the predicted contribution from simulated processes.

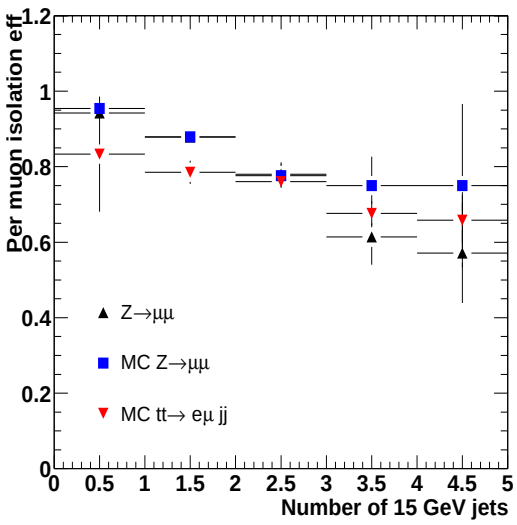

Figure 5.9: Muon isolation efficiency, as a function of jet multiplicity.

5.2.5 Muon Resolution

The transverse momentum of the reconstructed muon is extracted from a global fit of the central track and the local muon track, though it is limited by the resolution of the central tracker.

A substantially different resolution in real and simulated data will bias the efficiency calculation of a transverse momentum threshold. It is therefore important to measure the resolution in real data events and to manipulate the simulated data until it reproduces this performance.

The cleanest sample upon which to perform this study is the sample of $Z \to \mu\mu$ events. To compare the resolution in data and simulation, we examine the shape of the muon P_T spectrum as well as the width of the di-muon invariant mass spectrum. As the resolution of the central tracking system is not anticipated to be constant in η, we separate the sample into central ($|\eta| < 1.0$) and forward ($|\eta| > 1.0$) regions. Note that for the di-muon distributions, *both* muons must be in the central or forward region.

We adjust the measured muon P_T in the simulated data to attempt to reproduce the effects of

- larger cluster position errors
- poor knowledge of the overall scale, due to uncertainty in Bl

by smearing the momentum according to the prescription

$$\frac{1}{P_T} \to \frac{C}{P_T} + fG$$

where C accounts for the calibration of the magnetic field, G is a random variable drawn from a Gaussian distribution of unit width and zero mean, and f is the smearing parameter.

We vary the smearing parameter f, and in each case measure the width of the dimuon invariant mass peak by fitting the distribution to the form:

$$A + Be^{(\frac{x-M}{\sigma})^2}$$

Figure 5.10 shows the variation in the width with f in the simulation, as well as the width measured in the data for both central and forward regions.

The parameter C can be extracted by requiring the simulation to reproduce the mean of the fitted mass spectrum. Figure 5.11 shows the variation in the mean for varying values of f and C.

To confirm these measurements, we compare the shape of the muon P_T spectrum in data and the smeared simulation. For each value of f, we compute the Kolmogorov-Smirnoff statistic; this statistic displays a clear minimum, as shown in Figure 5.12. Unfortunately, these do not agree precisely with the measurement made using the Z mass width, though it provides a rough confirmation.

The mass and transverse momentum spectra for data and smeared simulation are shown in Figure 5.13, and the derived smearing factors are given in Table 5.1. To assess the effect of this smearing on the efficiency of a P_T cut on the muon and to estimate a systematic error due to the resolution, we vary the smearing value by 100%. The efficiencies in Table 5.2 allow us to measure the efficiency of the P_T threshold to be

$$85.1 \pm 1.0_{stat} \pm 0.6_{syst}\%$$

Region	f	C
Forward	0.00300	1.03
Central	0.00275	1.00

Table 5.1: Derived smearing factors for muon P_T resolution.

Smearing	Efficiency
No Smearing	85.4%
Smearing	85.1%
Smearing, $2f$	84.3%
Smearing, $2C$	84.8%
Smearing, $2f, 2C$	84.2%

Table 5.2: Effect of smearing the muon P_T resolution on the efficiency for a threshold of $P_T > 15$ GeV in $t\bar{t} \to e\mu jj$ events.

A summary of the muon efficiencies in data and simulation are given in Table 5.3.

	ϵ^{μ}	ϵ^{track}	ϵ^{Iso}	ϵ^{DCA}	ϵ^{total}	κ^{μ}
$t\bar{t}$	$.810 \pm .003$	$.715 \pm .004$	$.847 \pm .003$	$.918 \pm .003$	$.450 \pm .004$	1.069
WW	$.810 \pm .002$	$.718 \pm .003$	$.913 \pm .002$	$.967 \pm .002$	$.514 \pm .003$	1.069
WZ	$.812 \pm .003$	$.736 \pm .004$	$.917 \pm .003$	$.981 \pm .001$	$.537 \pm .004$	1.067
$W\gamma$	$.813 \pm .003$	$.725 \pm .004$	$.957 \pm .002$	$.971 \pm .002$	$.547 \pm .004$	1.065
$Z \to \tau\tau$	$.817 \pm .002$	$.735 \pm .002$	$.951 \pm .001$	$.887 \pm .002$	$.506 \pm .002$	1.061
$Z \to \mu\mu$	$.821 \pm .003$	$.727 \pm .004$	$.927 \pm .003$	$.980 \pm .002$	$.542 \pm .004$	1.055
Data	$.866^{\pm.009}_{\pm.037}$	$.738^{\pm.002}_{\pm.015}$	$.904 \pm .005$	$.929 \pm .011$		

Table 5.3: Summary of muon efficiencies in data and simulation. Only ϵ^{μ} is used in the calculation of κ^{μ}, the ratio of muon reconstruction efficiency in data and simulation.

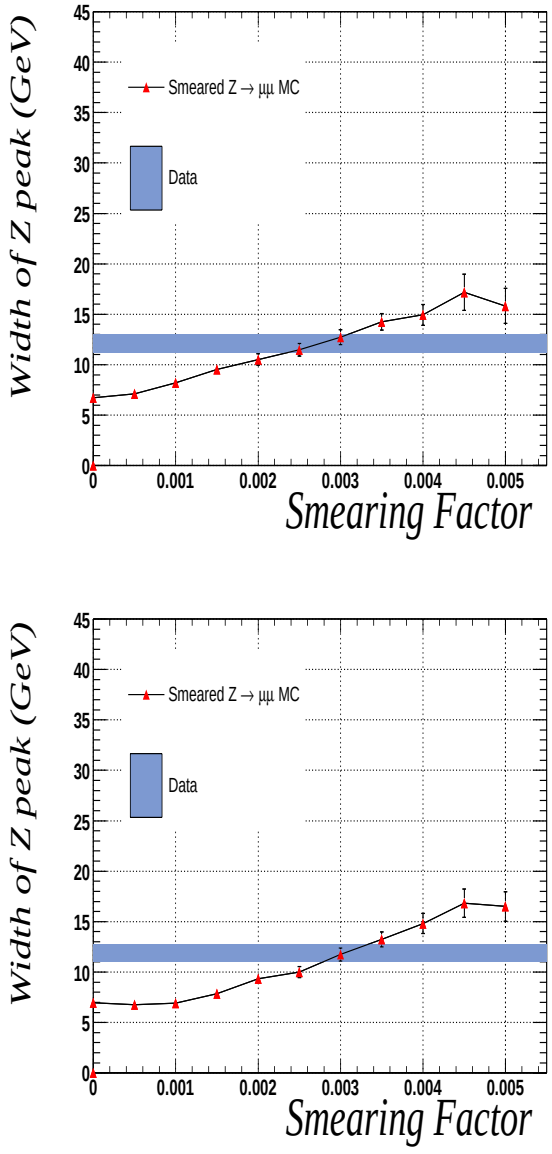

Figure 5.10: Comparison of the fitted mean of the dimuon invariant mass spectrum in real and simulated data, for varying values of the smearing parameter f.

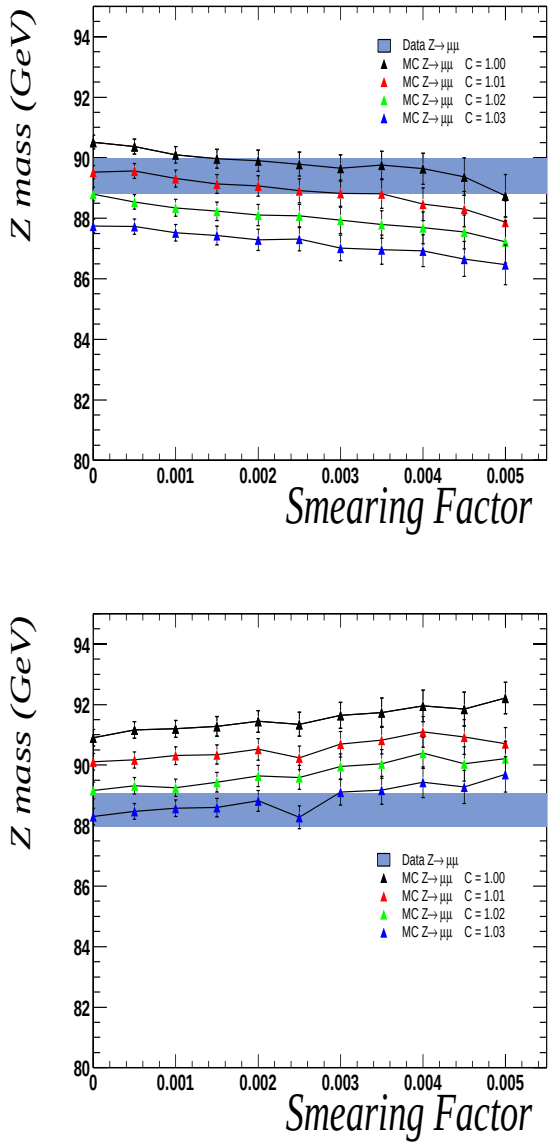

Figure 5.11: Comparison of the fitted mean of the dimuon invariant mass spectrum in real and simulated data, for varying values of the smearing parameters f and C. See text for details.

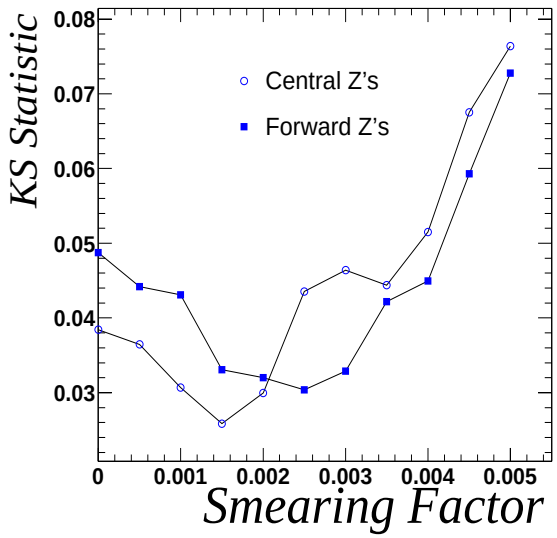

Figure 5.12: Kolmogorov-Smirnoff statistic between distributions of muon P_T spectrum in simulated and real data, for central and forward muons from $Z \to \mu\mu$ events.

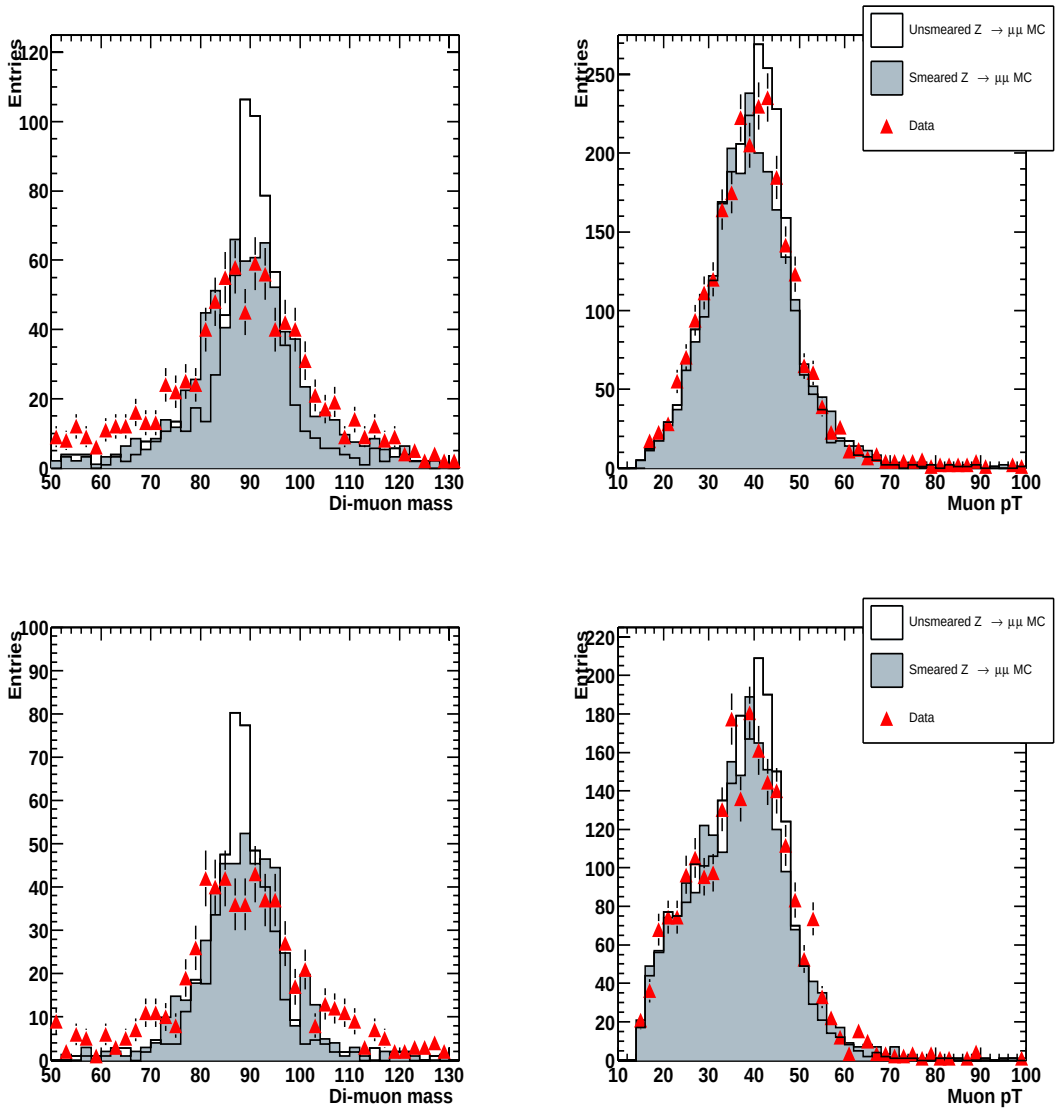

Figure 5.13: Agreement between simulated and real data in the di-muon invariant mass spectrum (*left*) and muon P_T spectrum (*right*) for central (*top*) and forward (*bottom*) muons.

5.2.6 Electron Reconstruction

We measure the electron reconstruction in the simulated data within the acceptance of the central calorimeter,

$$|\eta| < 1.1.$$

Any gaps or cracks in the calorimeter we include in the definition of reconstruction efficiency ϵ^e. This quantity has been measured [48] in data

$$\epsilon^e(Data) = 95.5 \pm 1.0_{(stat)} \pm 2.0_{(syst)}\%.$$

5.2.7 Electron Identification

Reconstructed electrons must satisfy additional cuts to reject QCD contamination; these place requirements on the electron isolation, electromagnetic fraction and χ^2.

The choice of the cut positions and the global efficiency estimation has been performed on an unbiased sample of electrons from Z decays where one electron is used for tagging purposes and the other to evaluate the efficiency. The fraction of electrons satisfying these cuts is

$$\epsilon^{eID}(Data) = 87.7 \pm 0.7_{(stat)} \pm 1.1_{(syst)}\%$$

as measured in [48]

5.2.8 Electron Likelihood

The efficiency for electrons to be confirmed by the electron likelihood is calculated using candidate elelectrons from $Z \to ee$ decays. The efficiency is obtained as the ratio of the number of clusters which are successfully confirmed by the likelihood to the total number of clusters (twice the number of Z events) in the [80, 100] GeV mass range. If Z_0, Z_1 and Z_2 denote the numbers of Z events in which no, one or both clusters are matched to a track, this efficiency reads

$$\varepsilon_{\rm trk} = \frac{Z_1/2 + Z_2}{Z_0 + Z_1 + Z_2}.$$

The efficiency to be associated with an track candidate is summarized in Table 5.4.

Rather than simply requiring the presence of a central track, we require that the electron resembles a canonical sample of electrons by selecting those with a large electron likelihood, [37]. We account for background contamination in the sample by measuring the efficiency in the sidebands, [60-80] and [100-120] GeV and accounting for the discrepancy. The efficiency for electrons to satisfy this criterion is given in Table 5.5;

Sample	Central Cal	Endcap Cal
Signal	$76.5 \pm 0.5\%$	62.8%
Background	$6.0 \pm 0.1\%$	14.7%

Table 5.4: Efficiency to have an associated track candidate for signal and background samples, in the central and endcap calorimeters.

Threshold	Signal Eff.	Background Eff.
Central Calorimeter		
$D > 0.15$	96.8%	50.3%
Endcap Calorimeter		
$D > 0.06$	96.3%	20.0%

Table 5.5: Sample selection points and their efficiencies

the total efficiency, to be associated with a track and to pass the likelihood threshold is

$$e^{eLikelihood}(Data) = 74.0 \pm 0.7 \pm 2.0\%,$$

where the systematic error is calculated by doubling the background estimate. Table 5.6 summarizes the efficiencies of electron reconstruction in data and simulation.

Requiring that the track associated to the electron has a stereo as well as an axial measurement lowers the tracking efficiency further, so that we find:

$$e^{eLikelihood}(Data) = 63.6 \pm 0.7 \pm 2.0\%,$$

	ϵ^e	ϵ^{eID}	$\epsilon^{Likelihood}$	ϵ^{Total}	κ^e
$t\bar{t}$	$.927 \pm .002$	$.934 \pm .002$	$.959 \pm .002$	$.830 \pm .003$	.642
WW	$.956 \pm .001$	$.943 \pm .002$	$.951 \pm .001$	$.858 \pm .002$	.621
WZ	$.959 \pm .002$	$.945 \pm .002$	$.961 \pm .002$	$.871 \pm .003$	.612
$W\gamma$	$.941 \pm .023$	$.948 \pm .023$	$.341 \pm .050$	$.304 \pm .046$	.622
$Z \to \tau\tau$	$.931 \pm .001$	$.937 \pm .001$	$.969 \pm .001$	$.846 \pm .002$	.630
$Z \to ee$	$.963 \pm .003$	$.954 \pm .003$	$.952 \pm .003$	$.875 \pm .005$	.609
Data	$.955 \pm .007 \pm .02$	$.877 \pm .007 \pm .011$	$.636 \pm .007 \pm .020$		

Table 5.6: Summary of electron efficiencies in data and simulation and calculation of κ^e, the ratio of electron efficiency reconstruction in simulated and real data. In the case of $W\gamma$, the likelihood efficiency $\epsilon^{Likelihood}$ is not included in κ^e as the reference sample of electrons is not appropriate; instead the measured efficiency is scaled by κ^{Lhood} measured for WW events.

5.2.9 Electron Energy Resolution

The transverse momentum of the reconstructed electron is a calorimetric quantity; unlike the case for the muon, the central track is used only to help identify the electron, not to measure its energy.

As for the muon, it is crucial to accurately model the electron energy resolution, in order to correctly calculate the efficiency of an energy threshold and to correctly predict the shape of the electron spectrum above the threshold.

In analogy to the measurement of muon energy resolution, we extract the electron resolution from the cleanest sample of electrons available: $Z \to ee$ events. To model the effect of an overall normalization as well as a scale dependence, we search for the combination of smearing parameters f_e and C_e which yield the best agreement between

Region	f_e	C_e
Central	0.05	0.99

Table 5.7: Derived smearing factors for electron P_T resolution.

Z events in data and those smeared by the prescription

$$E_T \rightarrow C_e E_T + f_e(C_e E_T)G$$

where C_e accounts for the calibration of the energy scale, f_e is the smearing parameter and G is a random variable drawn from a Gaussian distribution of unit width and zero mean. Here we construct the prescription such the the resolution smearing is not constant, but rather scaled with E_T.

We vary the smearing parameter f_e and in each case measure the width of the electron invariant mass peak by fitting the function to the form:

$$A + Be^{(\frac{x-M}{\sigma})^2}$$

Figure 5.14 shows the variation in the width with f in the simulation. The parameter C_e can be extracted by requiring the simulation to reproduce the mean of the fitted mass spectrum. Figure 5.14 shows the variation in the mean for varying values of f_e and C_e.

The mass and transverse momentum spectra for data and smeared simulation are shown in Figure 5.15, and the derived smearing factors are given in Table 5.7.

5.2.10 Jets

Jets reconstructed in the calorimeter must be corrected in order to account for mis-measurement due to out-of-cone showering and the hadronic response. The jet energy scale (JES) is derived to make this correction. There is an error associated with this scale, and we must propagate this error as an error on our efficiency to reconstruct jets in the detector. For top event reconstruction, for example, we vary the JES by the quoted error to estimate the error on the efficiency. Varying the scale in the high direction promotes the P_T of all jets, and therefore our efficiency to select them; similarly, lowering the scale reduces our efficiency. Figure 5.16 shows the variation in the number of reconstruction jets in $t\bar{t} \to e\mu jj$ events, after all cuts except the final selection of two 20 GeV jets.

The relative error in the top selection efficiency due to JES uncertainty is

$$\delta\epsilon = {}^{+0.040}_{-0.045}.$$

5.2.11 Missing Energy

The measured transverse missing energy is perhaps the quantity most sensitive to the quality of the reconstruction, as it is impacted directly by the resolutions of each object and the inherent calorimeter noise level.

The missing transverse energy vector is the opposite of the vector sum of all energy measured in the event

$$\not\!\!E_T = -(\sum_{cells} E_T^{Total})$$

this total energy vector can be broken into two classes of measured energy:

$$E_T^{Total} = U + \sum_{objects} E_T$$

where U represents the unclustered energy, that which is not associated with a reconstructed object. The objects have been carefully calibrated to ensure that their resolutions are well modeled. The remaining piece is the unclustered energy, which is largely due to soft recoil R and noise N. If the response to the soft recoil is not correctly modeled, then it may not be accurately measured. We replace R with κR to reflect this possibility and insert a term N to encapsulate the inherent noise of the measurement.

$$U = \kappa R + N$$

The sum of the real energy in the event must be zero

$$\sum_{objects} E_T + R + \nu = 0$$

where ν represents uncaptured energy. In $Z \to ll$ events, there is no significant uncaptured energy, $\nu = 0$. As a result,

$$\sum_{objects} E_T = P_T^Z = -R$$

where we include the P_T of any hard reconstructed jets in P_T^Z, allowing us to write

$$U = -\kappa P_T^Z + N$$

$$U^2 = (\kappa P_T^Z)^2 + N^2 + 2\kappa N \cdot P_T^Z$$

We can measure directly the unclustered energy and P_T^Z; Figures 5.17 and 5.18 show that these distributions agree fairly well in data and in simulation. Direct extraction of the scale factor κ is not possible for an individual event, as it is impossible to disentangle the terms of the unclustered energy. However, as the vector N is uncorrelated to the vector P_T^Z the average over many events will vanish, $\langle N \cdot P_T^Z \rangle = 0$, giving

$$\langle U^2 \rangle = \langle (\kappa P_T^Z)^2 \rangle + \langle N^2 \rangle$$

and allowing for extraction of the mean value of κ. Figure 5.19 show no significant disagreement between data and simulation.

To calibrate the level of the noise, we insert additional noise into the measured missing energy in the simulation, until it agrees with the level seen in data, as measured

by the Kolmogorov-Smirnoff statistics. Figure 5.20 shows the variation in the statistic with the level of injected noise, and Figure 5.21 demonstrates the final agreement.

5.2.12 Monte Carlo Corrections

We correct the simulated data for performance measured in real data by scaling it by a global relative efficiency factor κ. We calculate this factor for each process using values in Tables 5.3 and 5.6.

$$\kappa^{t\bar{t}} = 1.069 \times 0.642 = 0.686$$

$$\kappa^{WW} = 1.069 \times 0.621 = 0.664$$

$$\kappa^{WZ} = 1.067 \times 0.612 = 0.653$$

$$\kappa^{W\gamma} = 1.065 \times 0.622 = 0.662$$

$$\kappa^{Z\to\tau\tau} = 1.061 \times 0.630 = 0.668$$

Simulated data is scaled by the appropriate factors in the sections below.

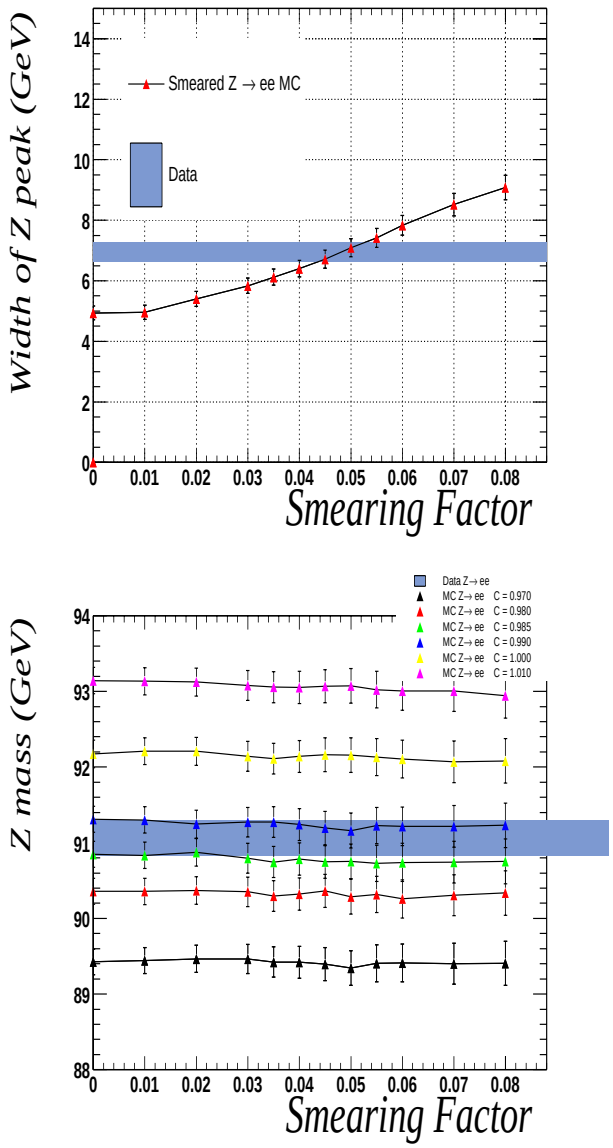

Figure 5.14: Comparison of the fitted mean of the dimuon invariant mass spectrum in real and simulated data, for varying values of the smearing parameters f. For central (*left*) and forward (*right*) muons.

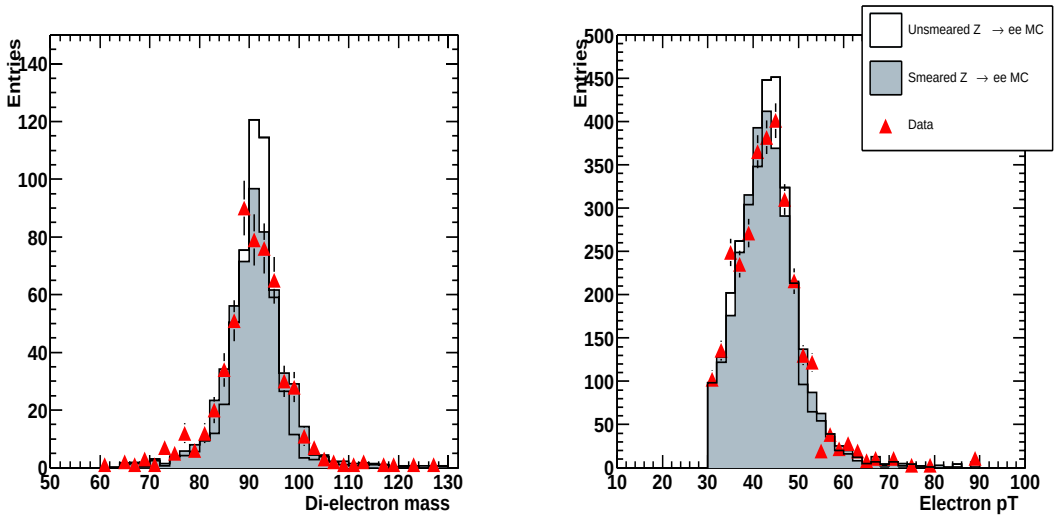

Figure 5.15: Agreement between simulated and real data in the di-electron invariant mass spectrum (*left*) and electron P_T spectrum (*right*) for central electrons.

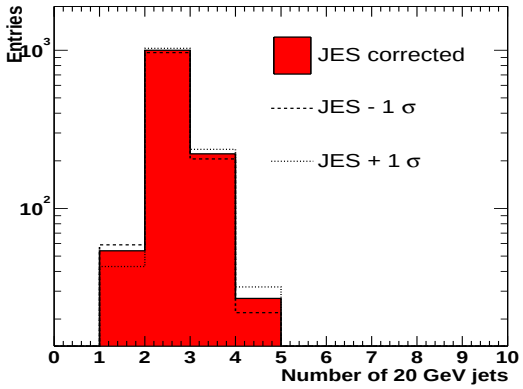

Figure 5.16: Variation in jet multiplicity with variations in the jet energy scale.

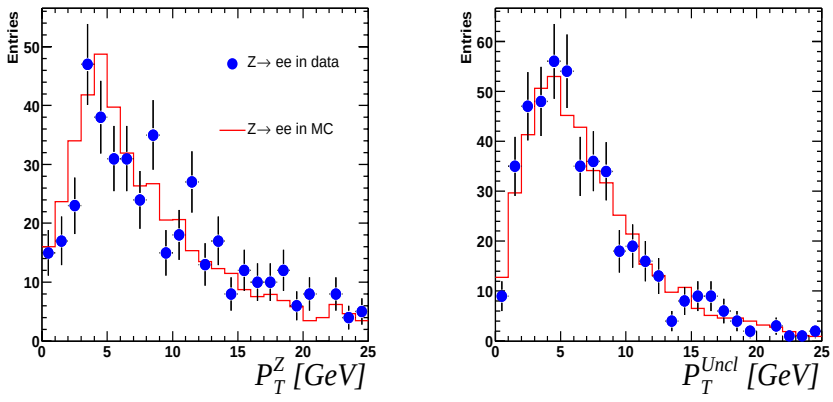

Figure 5.17: Transverse momentum of the Z boson, and the unclustered energy in data and simulation

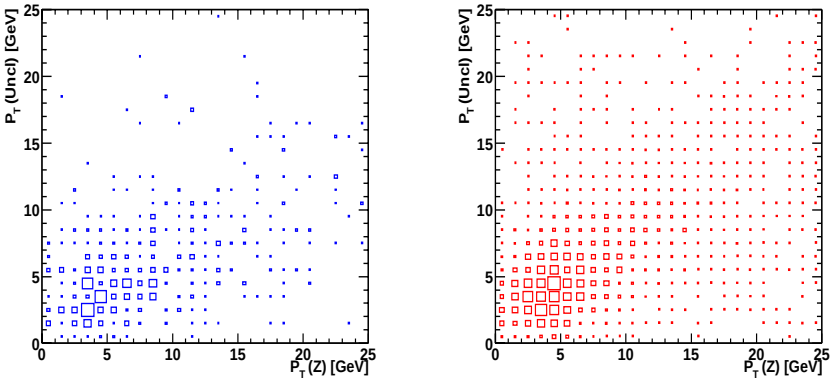

Figure 5.18: Correlations between the transverse momentum of the Z boson and the unclustered energy, in data (*left*) and in simulation (*right*).

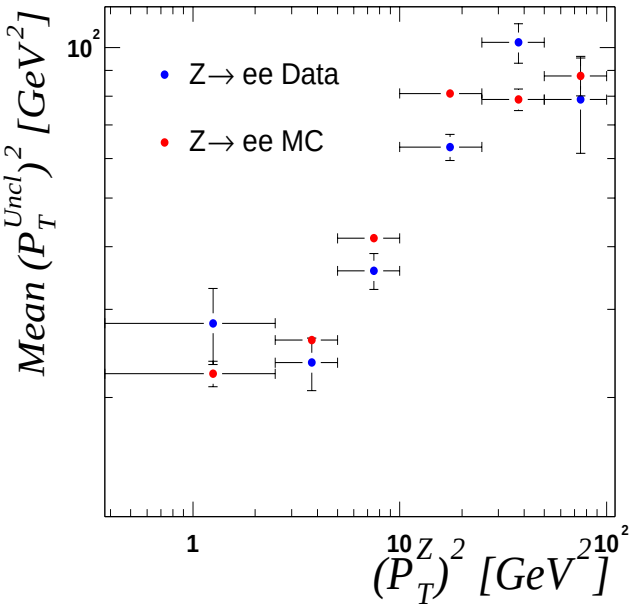

Figure 5.19: Correlations between the squared transverse momentum and the squared recoil of the Z boson, in data (*left*) and in simulation (*right*).

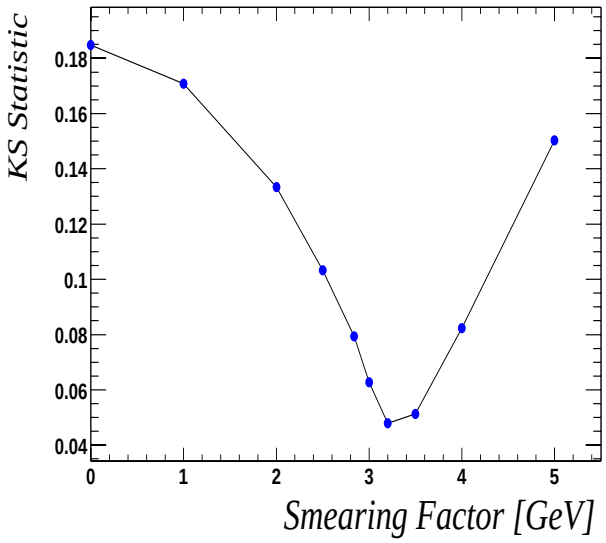

Figure 5.20: Variation in the Kolmogorov-Smirnoff statistic comparing distributions of transverse missing energy in data and in simulation.

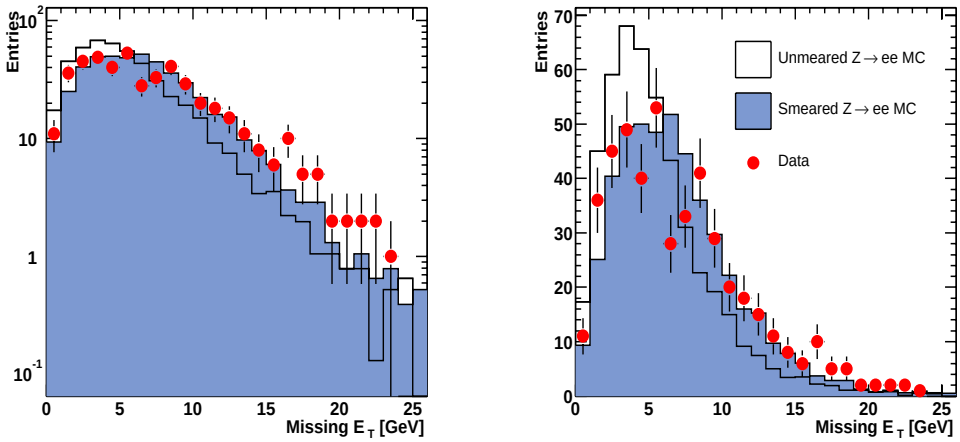

Figure 5.21: Agreement of missing transverse energy distributions in observed and simulated $Z \rightarrow ee$ events. The distributions are shown in both log (*left*) and linear (*right*) scales.

Chapter 6

Contributions to the Data Set

The $e\mu$ final state is especially blessed among the dilepton states in avoiding the direct contribution from Z/γ^* backgrounds which dominate the ee and $\mu\mu$ channels. The background contributions fall into two general categories, instrumental backgrounds arising from mis-identification of objects in the event and physics backgrounds, which contribute real, prompt $e\mu$ events. These are discussed in turn.

6.1 Instrumental Backgrounds

The selected final state topology has two energetic leptons, either of which may be misidentified.

In the case of the muon, the largest source of instrumental background comes

Process	Comments
$q\overline{q}$, $q \to q' + \mu\nu$	Fake isolated muon, jet faking electron
$W(\to \mu\nu) + jet$	Jet faking electron

Table 6.1: Processes which produced events which are misidentified as $e\mu$ events.

not from false muons or jet punch-through, but from muons from heavy flavor production which appear isolated in the detector. Studies [33] have shown that even a thoroughly optimized isolation criterion has a background efficiency of $\mathcal{O}(10^{-1})$ for high P_T muons, allowing a substantial amount of QCD leakage.

The source of electron misidentification is primarily jets, in which a large amount of energy is given to a leading π^0 which produces an electromagnetic shower. The neutral π^0 does not leave an energetic track in the central tracker, so requiring that a track of similar energy be found in the central tracking chamber reduces this background to a manageable, but not negligible level. The processes which produce the mis-identified events are discussed in Table 6.1.

Our strategy is to measure the mis-identification rates, $f_\mu = P(Isolated\ \mu|\mu + q)$ and $f_e = P(e|jet)$ and model the instrumental background to $e\mu$ by scaling the background-producing processes by the appropriate rates. That is

$$N^{misID} = N^{QCD} * f_\mu * f_e + N^{W(\to\mu\nu)+jet} * f_e + ...$$

We note that for the source processes, each jet in the event is equally likely to

produce a mis-identified object. To fold in the multiplicities, we sum over the objects in the events rather than the number of events: $N = \sum N_{jet}$.

The rates f_μ and f_e have meaning only in the context of the precise definitions of the muon isolation and the jet and electron definitions. For clarity, we reiterate them here:

	Loose	Tight
Muon	Local medium track Central-matched	Isolated
Electron	Loose, ID=10 or 11	EMFrac, iso, χ^2 Likelihood confirmed

Given that they are closely tied to the details of the object identification, and are sensitive to detector performance issues, it is highly desirable to measure them directly from the data. While this eliminates many sources of systematic errors due to simulation, it introduces the complication of pollution from the signal and from physics background, which we will have to take care to treat correctly.

6.1.1 Correlations

The fake prescription described above assumes that the misidentification rates f_e and f_μ are uncorrelated and can be factorized. This is straightforward to confirm; we measure the rate f_e as a function of a quantity which discriminates between isolated and non-isolated muons: the energy deposited in the calorimeter in a halo surrounding the muon, a quantity used to select isolated muons. Figure 6.1 shows f_e as a function of

halo energy. In regions which are dominated by QCD, large values of the halo energy, f_e is reasonably flat. In the region of small halo energy, however, the rate at which loose electrons pass the tight cuts is substantially higher.

The substantial increase in f_e for isolated muons indicates that there is a fraction of our sample for which the electron and muon quality are correlated. The portion of the sample with isolated muons, or low halo energy, has a higher fraction of good electrons.

If this enhancement is due entirely to production of real electrons and muons, and the QCD contribution has no correlation in f_e and f_μ, then we can measure f_e in the region where QCD is dominant, and subtract it from the region where our signal exists. In principle, there is no reason why the rate at which electrons and muons are misidentified should be correlated; in fact, a large sample of simulated heavy flavor QCD events demonstrate no significant correlation, see Figure 6.2. A linear fit to f_e as a function of the muon halo yields a slope of $(-0.047 \pm 0.047) \times f_e$, consistent with no correlation. If we were to use this measured slope rather than assuming a slope of zero, it would enlarge our estimate of the background contribution in the signal region by a relative factor of $\frac{0.047}{2}$, which is negligible compared to the error quoted below.

We measure the mis-identification rate f_e in the region of poor muons, those with halo energy larger than 2.5 GeV:

$$f_e^{CC} = 0.49 \pm 0.12\%$$

Our estimate of the background describes those sources which contribute events in which the rate to produce a misidentified electron does not vary with the the muon isolation.

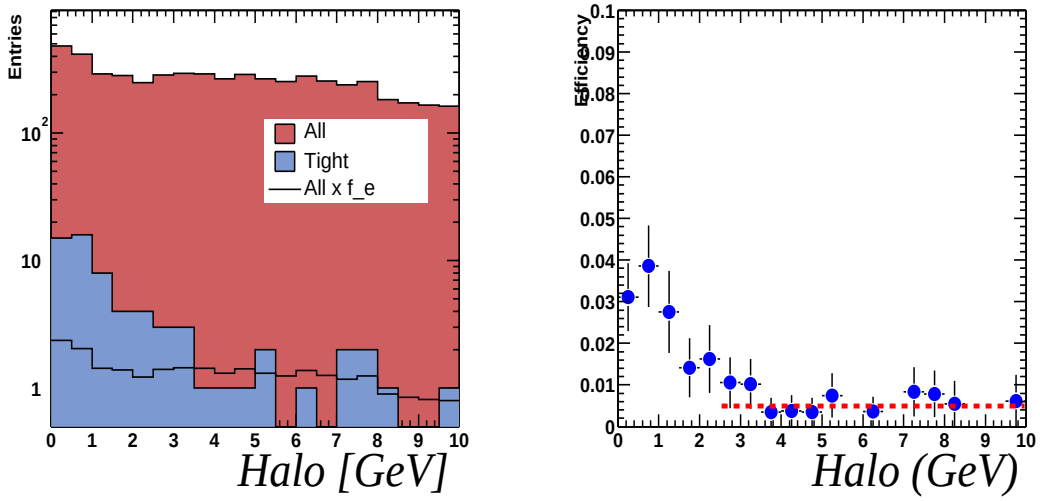

Figure 6.1: Preselected events which contain a loose electron, and the subset of those events which contain a tight electron, (*left*). The rate at which loose electrons pass the tight cuts, as a function of the muon halo energy (*right*). Shown for the central calorimeter.

6.1.2 Prescription

The estimate of the mis-identified background is

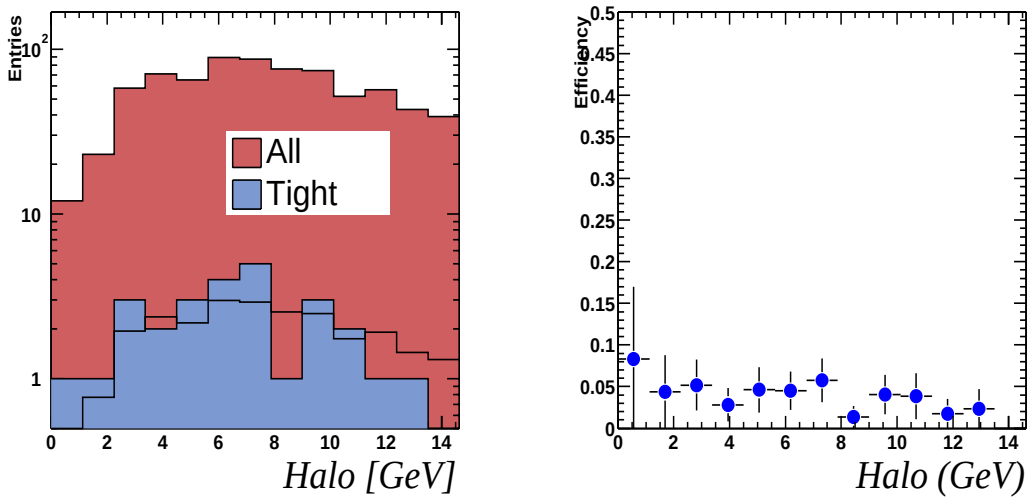

Figure 6.2: Simulated heavy flavor QCD events which contain a loose electron, and the subset of those events which contain a tight electron, (*left*). The rate at which loose electrons pass the tight cuts, as a function of the muon halo energy (*right*). Shown for the central calorimeter.

$$N^{misID} = N^{QCD} * f_{\mu} * f_e + N^{W \to \mu\nu} * f_e$$

We can regroup the terms:

$$N^{misID} = (N^{QCD} * f_{\mu} + N^{W \to \mu\nu}) * f_e$$

Having measured f_e, we need only estimate the term inside the parentheses. We can measure the contribution of this term in the data without needing to estimate each of the individual terms; requiring events in the preselected sample to contain an isolated

Description	Prescription	N_{events}
Isolated muon	$N^{Isolated\ \mu}$	989
Mis-ID	$N^{misID} = N^{Isolated\ \mu} * f_e$	4.85 ± 0.15

Table 6.2: Calculation of misID background.

muon provides this estimate, as the QCD and W processes exist in the correct proportion and are appropriately scaled by this selection. The distributions of the missing energy and the transverse mass of the muon and the presumed neutrino in this sample, see Figure 6.3, are not inconsistent with this hypothesis. Requiring an isolated muon in our preselected sample scales the QCD contribution exactly by the factor f_μ, by definition:

$$N^{Isolated\ \mu} = N^{QCD} * f_\mu + N^{W \to \mu\nu}$$

This leaves us with the simple expression

$$N^{misID} = N^{Isolated\ \mu} * f_e.$$

which gives an estimate of the mis-identified background in the central calorimeter calorimeters of

$$N^{misID} = 4.85 \pm 0.15_{(stat)} \pm 1.02_{(syst)}$$

See Table 6.2 for details. This implies a significant contribution from physics in our selected sample.

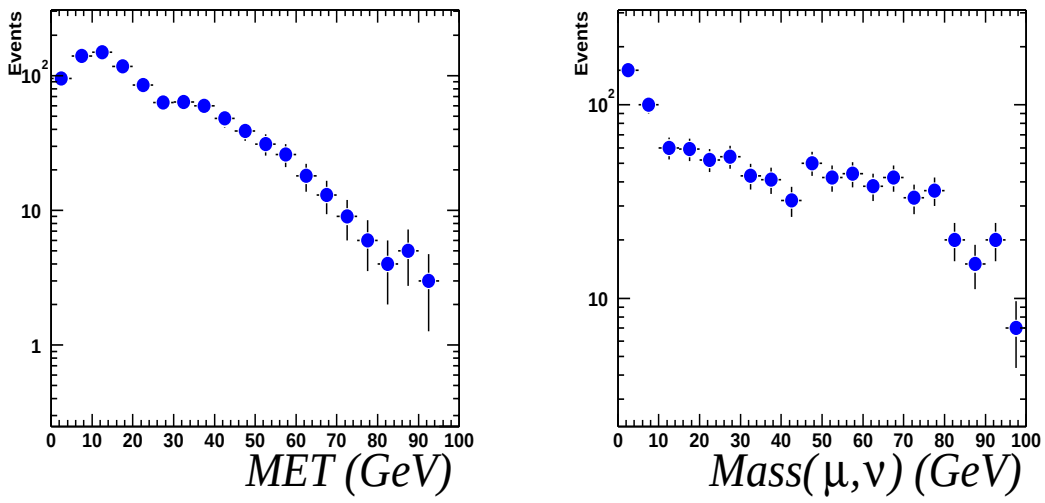

Figure 6.3: Distributions in missing transverse energy and transverse mass of isolated muon events.

6.1.3 Complementary Estimation

We can make an independent measurement of the fake rate to confirm that the sample is not dominated by misidentified events. We estimate the misidentification background in our selected sample by comparing the number of events with like-signed and un-like signed lepton pairs. We argue that in misidentified events, the charges of the leptons will be totally uncorrelated, as the track matched to the electron is purported to be a random fake track. In other words,

$$N^{misID} = 2 * N^{LS}$$

$l^{\pm}$	e^+	e^-
μ^+	1	20
μ^-	23	0

Table 6.3: Alternative calculation of misID background.

Table 6.3 gives the like- and unlike-signed proportion of the selected events. This method gives an estimate of

$$N^{misID} = 2 \pm 2.0$$

in good though imprecise agreement with the previous prescription.

6.1.4 Variation of Likelihood Efficiency

The estimate of the contributions of real and misidentified $e\mu$ events depends on the measurement of the likelihood efficiency and misidentification rate, respectively. To confirm that these measurements are reasonable, we study the behavior of our data sample under variation of the likelihood threshold.

Figure 6.4 shows the variation in misidentification rates, measured as above, for a range of likelihood thresholds. As expected, the rate falls as the threshold is increased; this Figure also shows the correlation between this rate and the efficiency for real electrons to survive the likelihood selection.

Loosening or tightening the threshold would also impact the size of our final

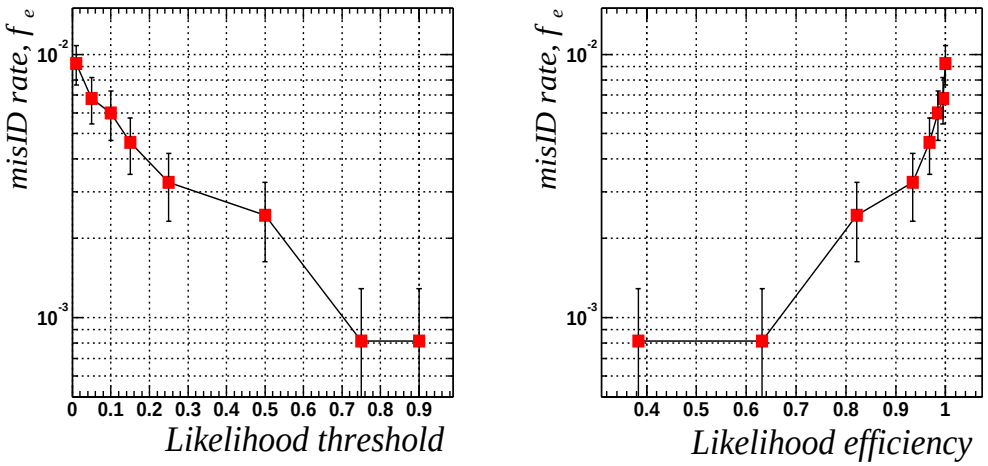

Figure 6.4: Variation in electron misidentification rate and efficiency with varying likelihood thresholds.

data set; the evolution of the real and misidentified contributions to the the data set are shown in Figure 6.5. The samples behave as one would expect; as the threshold is loosened and tightened, the contributions from both constituents grow and shrink. The size of the data set is too small to discern a significant disagreement or trend; note that the points are not independent.

6.2 Physics Backgrounds

The largest Standard Model contributions to the $e\mu$ final state are given in Table 6.4. The contribution from $Z/\gamma^* \rightarrow \tau\overline{\tau}$ has the largest cross section, but it

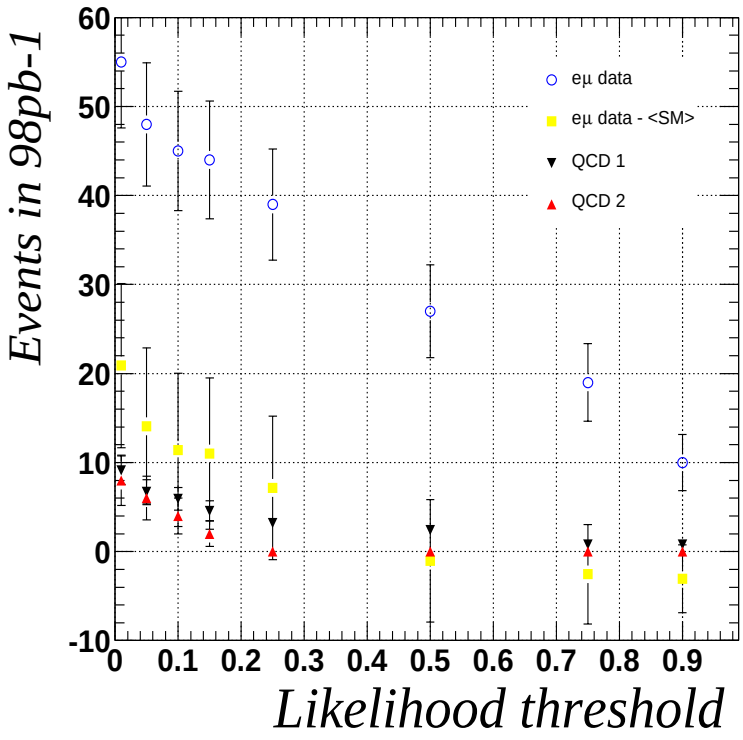

Figure 6.5: Variation in estimated sizes of real and misidentified contributions to $e\mu$ dataset with likelihood threshold.

tends to produce events with softer leptons and little $\not\!\!E_T$, see Figure 6.6. WW and $t\bar{t}$ production are nearly identical in these quantities, but are distinguishable in the number of jets found in the event, as $t\bar{t}$ decays contain two b quarks in addition to the W decay products. WZ is produced more rarely than WW, but its three energetic leptons increase its chances of being reconstructed as an $e\mu$ event. Production of W in association with

Process	$\sigma(pb)$	BR
$Z/\gamma^* \to \tau\tau$	262.0 pb	6.2E-1
WW	13.3 pb	2.5E-2
WZ	2.4 pb	3.6E-3
$W(\to \mu)\gamma$	4.75 pb	1.00
$t\bar{t}$	7.0 pb	2.5E-2

Table 6.4: Standard Model contributions to $e\mu$.

Process	Generator	Kinematic Selections	Sample $\mathcal{L}(pb^{-1})$
$Z/\gamma^* \to \tau\tau$	PYTHIA	$30 < M_{\tau\tau} < 60$ GeV	2486 pb-1
$Z/\gamma^* \to \tau\tau$	PYTHIA	$60 < M_{\tau\tau} < 130$ GeV	21700 pb-1
$Z/\gamma^* \to \tau\tau$	PYTHIA	$130 < M_{\tau\tau} < 200$ GeV	73503 pb-1
$Z/\gamma^* \to \tau\tau jj$	ALPGEN	$30 < M_{\tau\tau} < 60$ GeV	3066 pb-1
$Z/\gamma^* \to \tau\tau jj$	ALPGEN	$60 < M_{\tau\tau} < 130$ GeV	717 pb-1
$Z/\gamma^* \to \tau\tau jj$	ALPGEN	$130 < M_{\tau\tau} < 200$ GeV	66514 pb-1
WW	PYTHIA	–	104500 pb-1
WZ	PYTHIA	–	987200 pb-1
$W\gamma$	PYTHIA	–	14500 pb-1
$t\bar{t}$	PYTHIA	–	46864 pb-1

Table 6.5: Simulation samples.

an energetic photon can mimic $e\mu$ if the photon converts asymmetrically and produces an isolated electron or positron.

6.2.1 Simulation of Backgrounds

These backgrounds were simulated with the PYTHIA [67] and ALPGEN [68] event generators, fragmented with PYTHIA, and processed through the full detector simulation and reconstruction version p14.02.00, using the plate calorimeter geometry.

The integrated luminosity of the samples are listed in Table 6.5.

PYTHIA is a Monte Carlo physics collision simulation program which models the hard-scatter interaction between a proton and anti-proton, the decay of the resulting particles, initial and final state radiation and parton showering of the decay products.

The emission of hard and well separated jets by W and Z bosons represent an important background to the signature of top quark pair decay, which is characterized by the presence of two jets. The model of radiation and parton showering in PYTHIA is not intended to model in detail configurations with more than a single jet. To address this weakness, the ALPGEN package was developed; it calculates the exact matrix element for W/Zjj production. These events are then passed to the PYTHIA code for simulation of the hadronic cascades. Care has been taken to accurately model the $W/Z+N$ jet final states and avoid the dangers of double counting. A detailed discussion is given in Ref. [68].

The predominant physics background is the di-tau decay of the Z; the accuracy of the prediction of Zjj events hinges on the correctness of the model that Pythia uses to simulate the associated production of jets. In order to simulate this in greater detail, and with more significant statistics, we also study a sample of Zjj events produced using ALPGEN to generate the events and Pythia to fragment them. These events are then reconstructed in the same manner as the other events.

ll	BR($t\bar{t} \to ll$)	Kinematic Efficiency	BR($ll \to e\mu$)	$\epsilon^{e\mu}(ll)$
$e\mu$	0.025	0.134	1.000	0.134
$e\tau$	0.025	0.056	0.175	0.010
$\mu\tau$	0.025	0.056	0.175	0.010
$\tau\tau$	0.013	0.022	0.058	0.001

Table 6.6: Efficiencies for dilepton channels to produce final state $e\mu$ events

6.2.2 Contamination from τ decay

Physics processes which produce $e\mu$ directly may also have a secondary contribution from the leptonic decay of taus. The decay of top quark pairs, for example, to $e\tau$, $\mu\tau$ or $\tau\tau$ gives significant contributions to $e\mu$, though reduced due to the softer lepton P_T and the branching ratio of $\tau \to e, \mu$. We measure the acceptance of our top quark selection separately on various flavors of leptonic top decay, see Table 6.6.

Using the efficiencies in Table 6.6, the relative contribution to $e\mu$ from all dilepton channels,

$$\kappa^{\tau}_{ll} = \frac{\sum_{ll} BR(t\bar{t} \to ll) \times \epsilon^{e\mu}(ll)}{BR(t\bar{t} \to e\mu) \times \epsilon^{e\mu}(e\mu)} = 1.153$$

which can be applied to account for the τ contamination in dilepton processes $t\bar{t}$,WW and WZ. The contribution in a single lepton channel is somewhat smaller, and can be written as

$$\kappa_l^\tau = \frac{\epsilon^{e\mu}(e\mu) + BR(l'\tau) \times \epsilon^{e\mu}(l'\tau)}{\epsilon^{e\mu}(e\mu)} = 1.075$$

6.2.3 Normalization of σ_Z

In the case of $Z \to \tau\tau$ events, we normalize the leading order cross section calculated by PYTHIA using a k-factor derived from the data. For the range $30 < M_{\tau\tau} < \infty$ GeV, PYTHIA reports

$$\sigma_{p\overline{p}\to Z} * BR(Z \to \tau\tau) = 177.3\ pb,$$

where the Drell-Yan contribution has been specifically excluded. In [49], DØ reported a measurement

$$\sigma_{p\overline{p}\to Z} * BR(Z \to \mu\mu) = 261.0 \pm 6.76(stat + syst)\ pb,$$

where the measurement has been corrected to account for the Drell-Yan component. From these numbers we derive

$$k = 1.47 \pm 0.04$$

to be applied to the PYTHIA $Z \to \tau\tau$ sample.

The case of specific Zjj generation is slightly more complicated. The ALPGEN

generator uses the exact matrix element for Zjj production, but we must be consistent in our normalization of the inclusive and 2-jet samples. Ideally, we would follow the same prescription as for the inclusive sample, scaling the calculated cross section to match the measured cross section. This is complicated by the non-trivial connection between generated events and those with two reconstructed jets; this connection is very sensitive to the precise jet reconstruction thresholds in P_T and η.

We can remove this complication by requiring the overall rate of 2-jet events to match that seen in the data,

$$\sigma_Z^{data}\epsilon_{jj+}^{data} = k_{jj+} \times \sigma_{Zjj+}^{MC}\epsilon_{jj+}^{MC}$$

where $\sigma_Z^{data}\epsilon_{jj+}^{data}$ is the fraction of the $Z \to \mu\mu$ rate in which two jets are reconstructed, σ_{Zjj+}^{MC} is the cross section for the generated process including all η and P_T thresholds, and ϵ_{jj+}^{MC} is the efficiency for those events to be reconstructed with two jets. The correction factor k_{jj+} can be derived by measuring the rate at which two jets are reconstructed, both for the real Z events and for modeled events.

Figure 6.8 shows the rate of jet production in $Z \to \mu\mu$ events,

$$\epsilon_{jj+}^{data} = 0.0700 \pm 0.0042$$

and Figure 6.9 shows the same results for the Zjj ALPGEN sample

$$\epsilon_{jj+}^{MC} = 0.437 \pm 0.011$$

the ALPGEN sample used to simulate the Zjj background has theoretical cross section in the region $60 < M_{\mu\mu} < 130$ of

$$\sigma_{Zjj+}^{MC} = 26.8\ pb\ (theoretical)$$

which, when normalized to the data as described above, becomes

$$k_{jj+} \times \sigma_{Zjj+}^{MC} = 41.8\ pb\ (data\ normalized).$$

or

$$k_{jj+} = 1.55 \pm 0.05$$

As the ALPGEN calculation is only carried out to leading order, we expect that the normalization to data would be on the same order as for the inclusive sample.

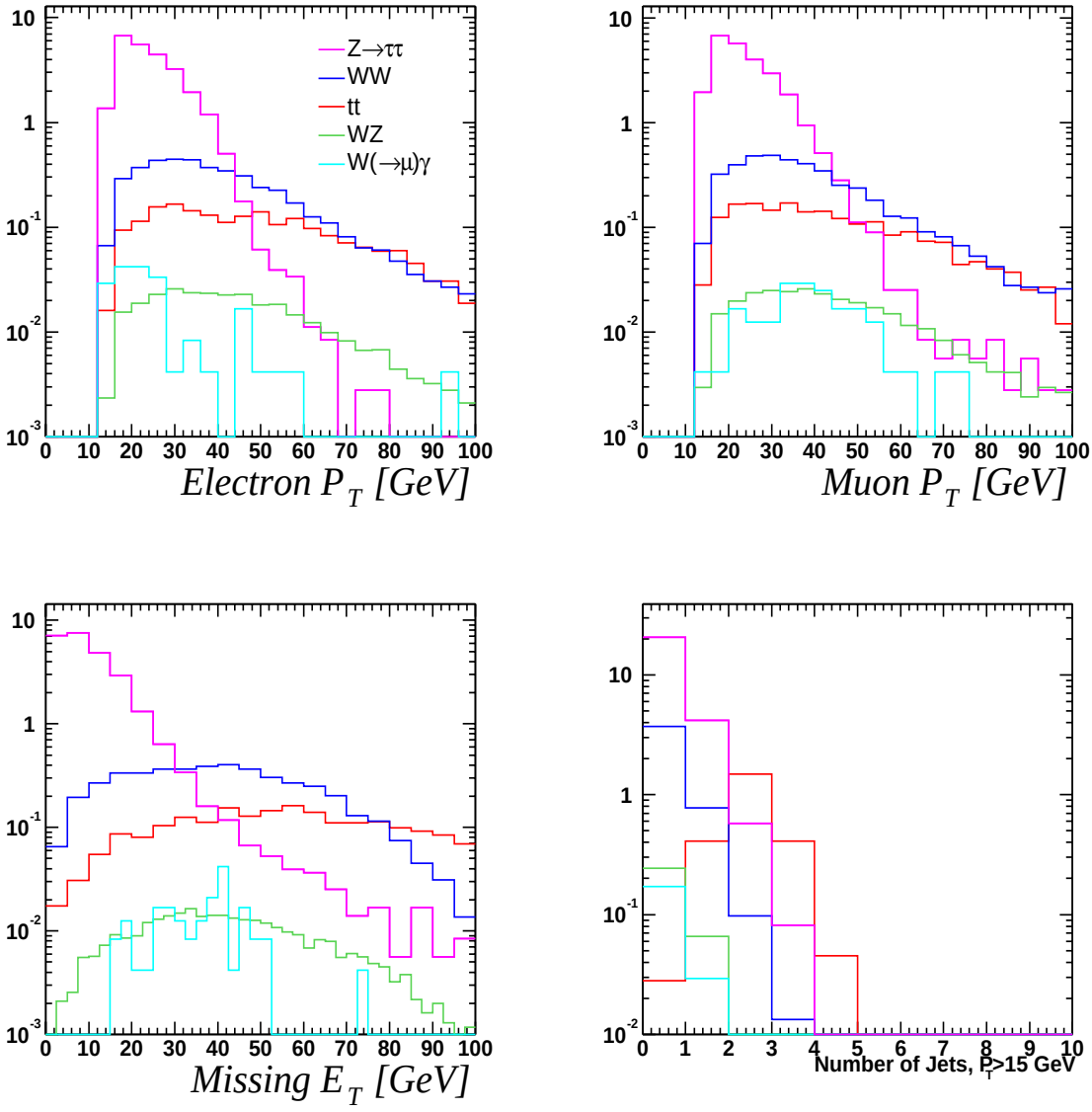

Figure 6.6: Distributions in lepton P_T, missing transverse energy and number of jets for the largest Standard Model contributions to $e\mu$.

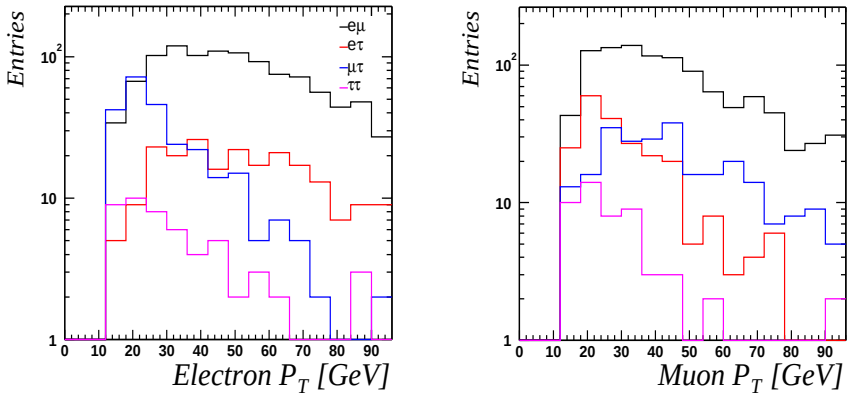

Figure 6.7: Distributions of electron and muon transverse energies for simulated $t\bar{t} \to lljj$ events in which the final state contains a direct ($l = e, \mu$) or indirect ($l = \tau \to e, \mu$) electron and muon.

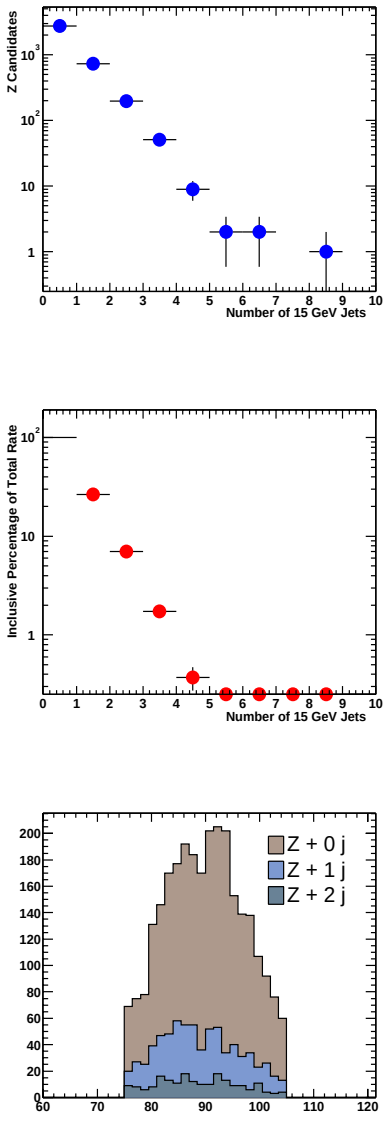

Figure 6.8: Jet multiplicity in $Z \to \mu\mu$ events (*top*), inclusive percentage of total rate (*middle*) and invariant mass distributions for leading portions (*bottom*).

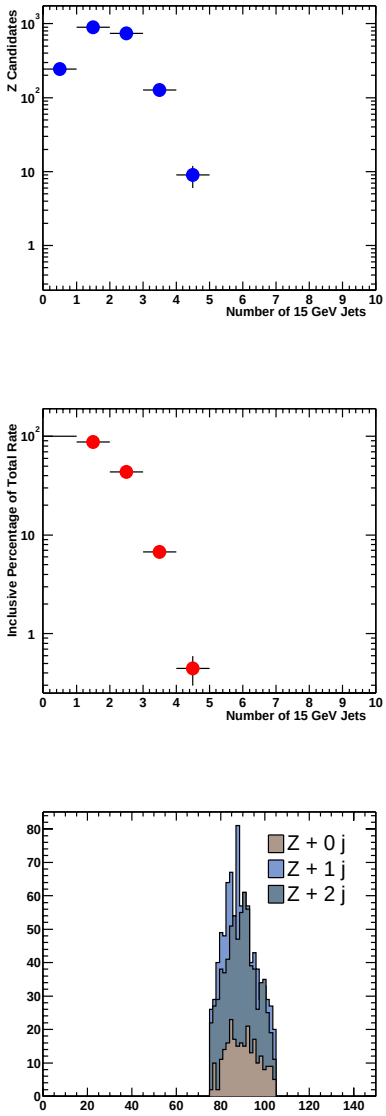

Figure 6.9: Jet multiplicity in ALPGEN simulated $Z \rightarrow \mu\mu$ events (*top*), inclusive percentage of total rate (*middle*) and invariant mass distributions for leading portions (*bottom*).

Chapter 7

Data

Of the data collected by DØ, we make use of the fraction of it for which all detector systems were functioning well such that efficiencies as measured in Chapter 5 may be applied. In this chapter, we discuss the selection of high quality data, the calculation of the integrated luminosity of the sample and discuss the kinematics of the $e\mu$ events observed.

7.1 Run Selection and Luminosity

Events within runs in which the data quality is known to be poor are removed. Specifically, we accept only events within runs in which the quality of the calorimeter data has been marked as good. Additionally, we reject all track and muon runs marked

as bad. The criteria for each selection are detailed below.

7.1.1 Luminosity

The instantaneous luminosity is derived from the rate of coincidence seen in the Luminosity Monitor (LM) compared to the rate expected for a reference process for which the cross section is known. That is, given the event rate dN/dt, the reference cross section σ_{ref}, and the acceptance of the LM ε_{LM}, the luminosity mmay be calculated as:

$$\mathcal{L} = \frac{dN/dt}{\sigma_{ref}\varepsilon_{LM}}.$$

The LM system is well posiitoned to detect collisions resulting in low-angle inelastic $p\overline{p}$ processes, for which the cross section is measured to be 43 mb[34]; though there is some disagreement regarding the most appropriate measurement of σ_{ref}, the error on this value is thought to be less than the 10% error quoted on the luminosity.

The luminosity is summed over each of the potential crossings and grouped into short intervals referred to as luminosity blocks, for which the integrated luminosity is calculated.

7.1.2 Calorimeter Quality

The quantities most sensitive to the quality of all of the data from the calorimeter are the missing and scalar transverse energies. We require that the reconstructed

Quantity	Requirement
$Shift_{xy}$	< 3.5 GeV
RMS_{xy}	< 15 GeV
E_T^{scalar}	> 80 GeV

Table 7.1: Requirements for calorimeter data in a run to be marked as GOOD.

missing energy during a run be centered roughly near zero in both x and y directions, and that it have a reasonable width. These are measured in terms of $Shift_{xy}$

$$Shift_{xy} = \sqrt{< \not\!\!E_T{}^x >^2 + < \not\!\!E_T{}^y >^2},$$

the deviation from zero of the mean values of the x and y components of the missing energy, and

$$RMS_{xy} = \sqrt{RMS(\not\!\!E_T{}^x)^2 + RMS(\not\!\!E_T{}^y)^2},$$

the width of the distributions of the same quantities. The specific requirements are given in Table 7.1.

The conditions which affect the quality of the data may vary on a timescale which is much shorter than the length of an individual run, which may exceed 5 hours. In order to remove portions of good runs which are clearly poisoned by detector performance issues, we scan individual luminosity blocks, which correspond to approximately one minute of running time. Adjacent luminosity blocks are clustered together to form groups

	Quantity	
	$< \not\!\!E_T >$	< 10 GeV
3 GeV $\leq$	$RMS(\not\!\!E_T)$	≤ 12 GeV
-4 GeV $\leq$	$< \not\!\!E_T{}^{x,y} >$	< 4 GeV
4 GeV $\leq$	$RMS(\not\!\!E_T{}^{x,y})$	≥ 12 GeV
65 GeV $<$	E_T^{scalar}	< 100 GeV

Table 7.2: Requirements for calorimeter data in a group of luminosity blocks to be marked as GOOD.

of events with statistics large enough to reliably measure the quality of the data. Blocks which fail the requirements detailed in Table 7.2 are marked as BAD and removed.

7.1.3 Muon Quality

A run is marked BAD if any of the crates were not operating. Each run is then scanned by eye for evidence of poor detector or readout system performance. Details are described in [35].

7.1.4 Track Quality

A run is marked BAD if any of the tracking crates were not operating, or if the performance of the tracker degrades significantly during the run.

Reconstruction	All	Not bad
p13.05.00	36.1 pb^{-1}	23.6 pb^{-1}
p13.06.01	98.3 pb^{-1}	74.0 pb^{-1}
Total	134.4 pb^{-1}	**97.7** pb^{-1}

Table 7.3: Integrated luminosity for the trigger MU_A_EM10.

7.1.5 Integrated Luminosity

The integrated luminosity for the trigger MU_A_EM10 for this run selection is 97.7 pb^{-1}, as detailed in Table 7.3.

7.2 Event Pre-Selection

We define our working dataset to have passed the following pre-selection criteria:

- Trigger MU_A_EM10 fired
- Reconstructed primary vertex, with at least 3 tracks and $|z_0 < 60.0|$ cm
- ≥ 1 loose electron, $P_T > 15$ GeV
- ≥ 1 medium muon, $P_T > 15$ GeV
- $R(e, \mu) > 0.25$

and refer to this as our *preselected sample*, which contains 12,738 events.

Data	All	MisID	$WW, WZ, W\gamma$	$Z \to \tau\overline{\tau}$	$t\bar{t}$
44	$37.86^{\pm 0.35(stat)}_{\pm 2.09(syst)}$	$4.85^{\pm 0.15}_{\pm 1.02}$	$4.58^{\pm 0.10}_{\pm 0.26}$	$26.05^{\pm 0.28}_{\pm 1.79}$	$2.39^{\pm 0.10}_{\pm 0.13}$

Table 7.4: Data and Standard Model predictions for events in the $e\mu$ final state.

7.3 The Dataset

We refine the data sample by imposing the additional cuts:

- ≥ 1 tight electron, passing likelihood cuts, $P_T > 15$ GeV
- ≥ 1 medium muon, isolated, passing DCA cuts, $P_T > 15$ GeV
- $|e_z - \mu_z| < 5.0$ cm, to ensure they are from the same vertex

and refer to this as our *selected sample*, which contains 44 events. Table 7.4 gives the size of the expected Standard Model contributions to this sample. All efficiency corrections have been applied. Figures 7.1- 7.3 show kinematic distributions for the data and expected contributions.

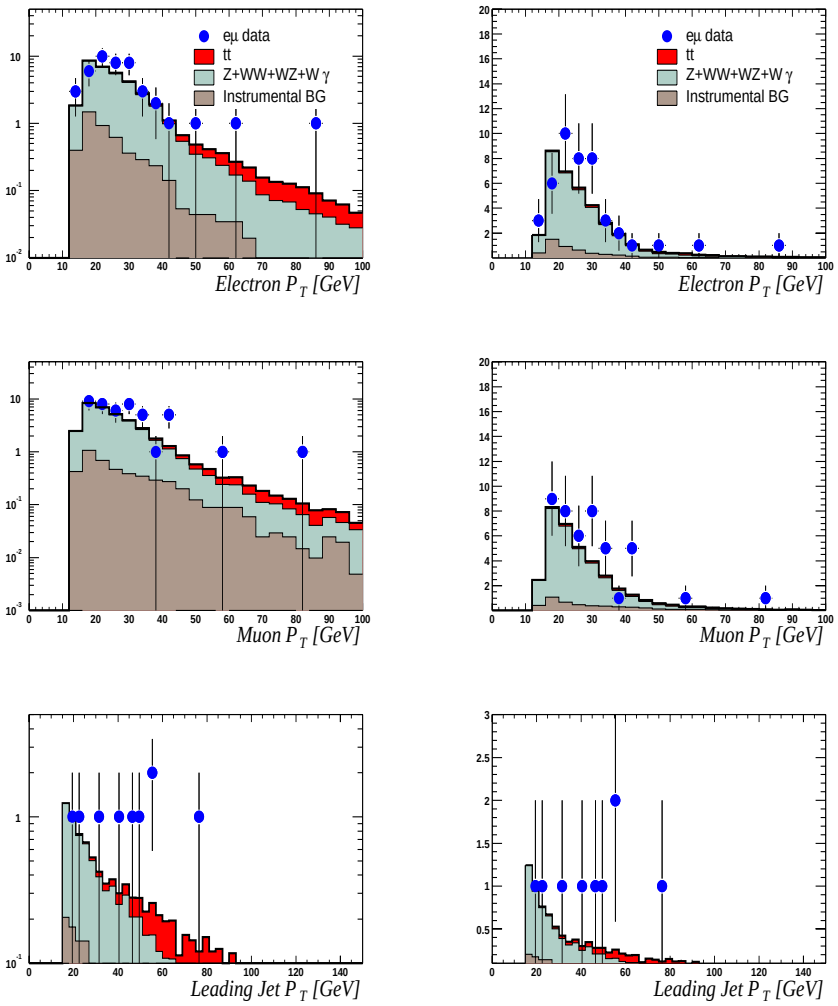

Figure 7.1: Transverse momentum of electrons and muons, in data and backgrounds. The same distributions are shown in a log scale (*left*) and linear scale (*right*).

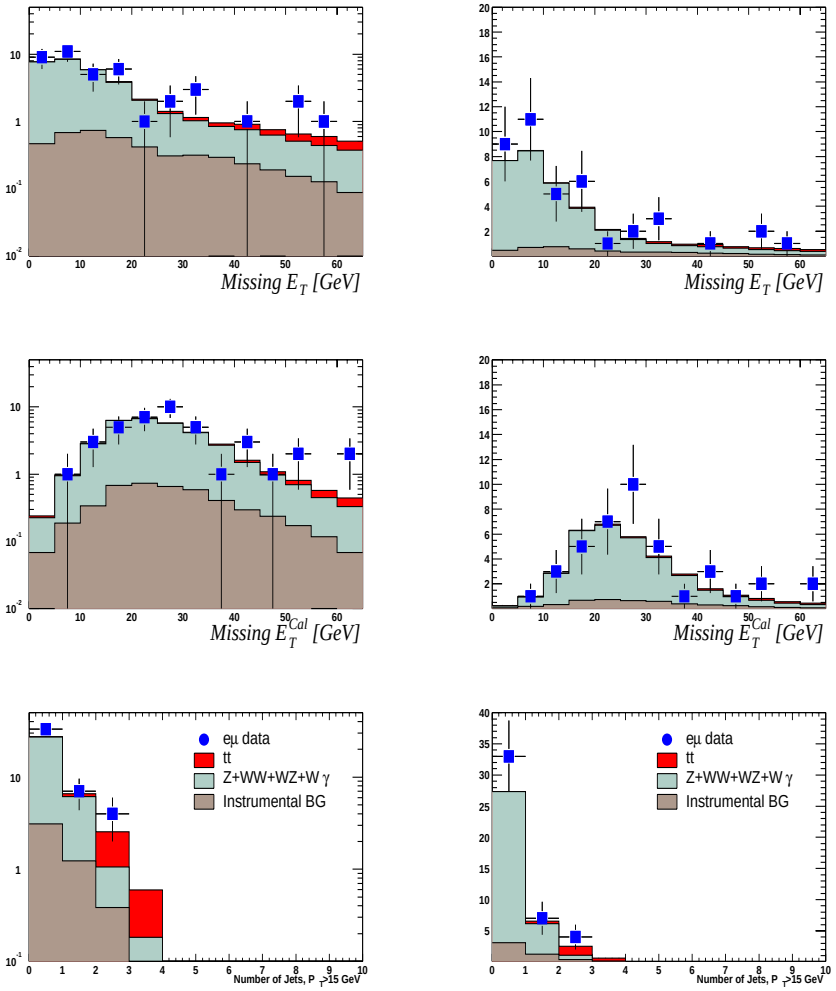

Figure 7.2: Missing transverse energy, calorimetric missing transverse energy and jet multiplicity for data and backgrounds. The same distributions are shown in a log scale (*left*) and linear scale (*right*)

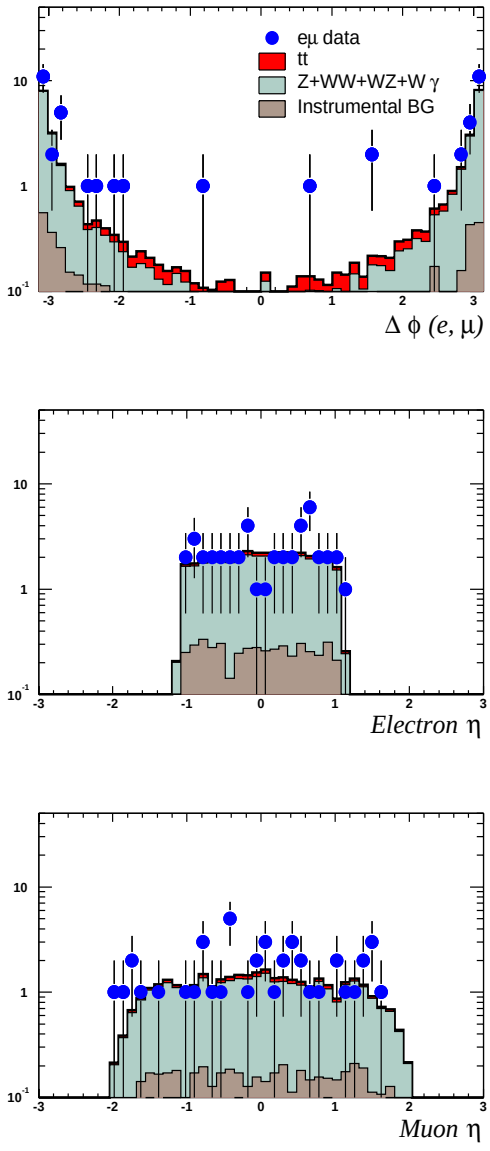

Figure 7.3: Difference in ϕ between the leptons (*top*), distribution in η of the electrons (*middle*), and η of the muons (*bottom*).

Chapter 8

Measurement of Standard Model Processes

In this chapter, we present measurements of the rare processes $p\overline{p} \to t\overline{t}$ and $p\overline{p} \to WW$ through their decay to an electron and muon, which in each case occurs with a branching ratio of 2/81.

Measurement of the production of the top quark tests our understanding of the production mechanism and decay kinematics, which are based on the unproven assumption that the observed top quark is the predicted isospin partner of the bottom quark.

8.1 Measurement of $\sigma_{t\bar{t}} \times BR(t\bar{t} \to e\mu bb)$

The electron-muon final state offers the cleanest opportunity to observe top quark production and decay.

Measuring the rate of production requires identification of a region of kinematic space where the contribution from the top quark is large relative to the expected background levels. In channels involving a single lepton, one must carefully consider taking advantage of the heavy flavor of the associated jets despite the loss in efficiency that comes with requiring an identified b-quark jet. The dilepton channels need not make such a sacrifice; the requirement of two stiff leptons and substantial transverse and missing energy in the event is sufficient to isolate the top quark signal. In this chapter, we present the topological selection of top quark events, estimate the backgrounds to this selection and calculate the visible cross section.

The selected sample contains 44 events, of which a large fraction are due to misidentified events and $Z \to \tau\tau$ production. Figure 7.1 shows the transverse momemtum of the leptons and the leading jet for data and backgrounds. Figure 7.2 shows the missing transverse energy and jet multiplicity. The number of jets in each background process falls rapidly, and requiring two reconstructed jets quickly reduces the background to the order of the top quark signal. To further reduce the Z background, we require significant missing transverse energy; to reduce the W and QCD backgrounds from

electron misidentification, we require significant missing energy in the calorimeter, disregarding the muon momentum. Figure 8.1 shows the expected signal and backgrounds at this point in the selection in terms of a variable which measures the transverse energy present in the event, H_T^e, the sum of jet and electron energies. Requiring $H_T^e > 120$ GeV and a further requirement on the stiffness of the jets produces a sample which is expected to be dominated by top quark production. The number of events after each selection and the contributions from each source are listed in Table 8.1.

In the case of the $Z \to \tau\overline{\tau}$ contribution, the more realistic simulation from ALPGEN can only be used to estimate the expected yield after the selection $N_{jets}^{P_T>15} \geq 2$. Prior to this, the inclusive Z simulated by Pythia is used. The two models do not disagree dramatically with respect to the size of the two-jet portion of Z production, but the models diverge quickly when energetic jets are required, demonstrating that ALPGEN's model provides harder associated jets. To calculate the background to top production, we use the estimate from ALPGEN; its exact leading order calculation is more likely to provide a good estimate of the background in the 2-jet final state. We use the PYTHIA sample to estimate the systematic error due to differences in the models, and take as the error half of the difference in the predictions.

Sizes of the final sample with statistical and systematic errors are given in Table 8.2. Additional systematic errors are given in Table 8.3.

Three events survive the final topological selection, which is consistent with

Cut	Data	All	MisID	$W(W,Z,\gamma)$	$Z \to \tau\overline{\tau}$	$t\bar{t}$
Initial Sel.	44	$37.86^{\pm 0.35(stat)}_{\pm 2.09(syst)}$	$4.85^{\pm 0.15}_{\pm 1.02}$	$4.58^{\pm 0.10}_{\pm 0.26}$	$26.05^{\pm 0.28}_{\pm 1.79}$	$2.39^{\pm 0.10}_{\pm 0.13}$
$N_{jets}^{P_T>15} \geq 2$	4	$3.73^{\pm 0.34(stat)}_{\pm 0.17(syst)}$	$0.49^{\pm 0.10}_{\pm 0.10}$	$0.11^{\pm 0.01}_{\pm 0.01}$	$1.18^{\pm 0.32}_{\pm 0.07}$	$1.95^{\pm 0.08}_{\pm 0.11}$
$\not\!\!E_T > 10$	4	$3.41^{\pm 0.30(stat)}_{\pm 0.15(syst)}$	$0.42^{\pm 0.09}_{\pm 0.09}$	$0.10^{\pm 0.01}_{\pm 0.01}$	$0.98^{\pm 0.29}_{\pm 0.06}$	$1.91^{\pm 0.01}_{\pm 0.11}$
$\not\!\!E_{T\,CAL} > 20$	4	$3.20^{\pm 0.30(stat)}_{\pm 0.13(syst)}$	$0.31^{\pm 0.07}_{\pm 0.07}$	$0.10^{\pm 0.01}_{\pm 0.01}$	$0.98^{\pm 0.29}_{\pm 0.05}$	$1.81^{\pm 0.01}_{\pm 0.10}$
$H_T^e > 120$	3	$2.57^{\pm 0.25(stat)}_{\pm 0.11(syst)}$	$0.15^{\pm 0.03}_{\pm 0.03}$	$0.04^{\pm 0.01}_{\pm 0.01}$	$0.71^{\pm 0.25}_{\pm 0.04}$	$1.67^{\pm 0.01}_{\pm 0.09}$
$N_{jets}^{P_T>15} > 2$	3	$2.28^{\pm 0.25(stat)}_{\pm 0.10(syst)}$	$0.13^{\pm 0.03}_{\pm 0.03}$	$0.02^{\pm 0.01}_{\pm 0.01}$	$0.53^{\pm 0.25}_{\pm 0.03}$	$1.59^{\pm 0.01}_{\pm 0.09}$

Table 8.1: Data and backgrounds at each level of selection, with statistical errors. The $Z \to \tau\tau$ contribution is estimated using the ALPGEN simulation, with the exception of the initial selection where the sample has no predictive power and the Pythia simulation is used.

Sample	Size	Statistical Error	Systematic Error
Data	3	1.73	0.0
misID	0.13	0.03	0.03
$WW + WZ + W\gamma$	0.02	0.001	0.001
$Z \to \tau\tau$	0.53	0.25	0.03
$t\bar{t}$	1.59	0.01	0.09

Table 8.2: Data and backgrounds for the final selection, with statistical and systematic errors.

Source	Size
Jet Energy Scale	4.5%
Jet Energy Resolution	3.4%

Table 8.3: Additional sources of systematic errors.

Run	Event		Electron	Muon	Jet 1	Jet 2	$\not\!\!E_T$
169920	8545882	P_T [GeV]	20.2	60.0	158.1	62.5	101.0
		ϕ	5.23	1.73	4.58	2.39	0.81
		η	1.09	-0.44	-0.33	-0.97	–
177826	15259654	P_T [GeV]	50.3	83.0	166.8	115.2	84.2
		ϕ	2.09	5.59	5.04	2.38	1.65
		η	-1.09	-0.49	-0.10	-0.36	–
174999	40409394	P_T [GeV]	17.2	18.4	56.4	48.9	29.4
		ϕ	5.42	6.06	1.58	3.51	5.60
		η	-0.05	0.18	-0.65	-0.51	–

Table 8.4: $t\bar{t}$ candidate events.

a top quark signal at the level we expected, and less consistent with a background fluctuation. The probability for the background to fluctuate from a mean of $b = 0.60$ events to an observed $N = 3$ is 0.033. Incorporating the uncertainty in the background prediction, and assuming a Gaussian distribution, this probability rises to 0.036.

The three candidate events are shown in Figures 8.2 through 8.7, and their kinematics properties are tabulated in Table 8.4. Their consistency with the decay of two W bosons is analyzed in Figure 8.8.

8.1.1 Production Cross Section

The observed excess over the backgrounds of $N_{bg} = 0.68$ events is

$$N_{sig} = N_{obs} - N_{bg} = 3 - 0.68 = 2.32 \text{ events}$$

The efficiency to trigger, reconstruct and select $t\bar{t} \to e\mu jj$ events is

$$\varepsilon_{t\bar{t}} = Acc_{t\bar{t}} \times \kappa_{Data/MC} \times \varepsilon_{trigger} \times \kappa^{\tau} = 0.134 \times 0.642 \times 0.961 \times 1.15 = 0.095$$

Given a luminosity of 97.7 pb^{-1}, we find

$$\sigma_{t\bar{t}\to e\mu jj} = \frac{N_{sig}}{\mathcal{L} \times \epsilon_{t\bar{t}}} = 0.250 \text{ pb}$$

and assuming that $BR(t\bar{t} \to e\mu jj) = 2/81$, we calculate

$$\sigma_{t\bar{t}} = 10.1^{+9.4}_{-6.4}\ (stat)^{+2.3}_{-2.1}(syst) \text{ pb.}$$

where the statistical errors are driven by the number of observed events, and the systematic error is driven by the error on the measured efficiencies and background estimates.

8.1.2 Discussion

The $e\mu$ channel provided one of DØ's clearest signals of top quark pair production; nonetheless, it is a piece of a larger effort to observe the production and decay in a majority of the available channels. Figure 8.9 shows the measurements made by DØ in each channel [70], and Figure 8.10 shows the Run1 and Run2 measurements for DØ and CDF [71] as well as the theoretical prediction with increasing center of mass energy.

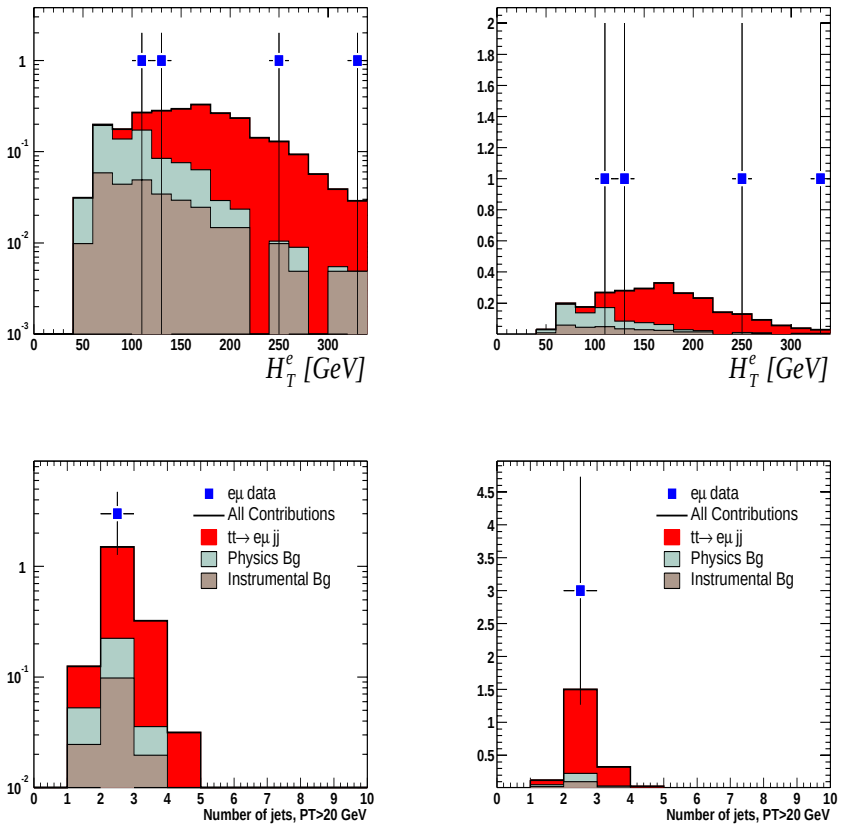

Figure 8.1: Data and backgrounds during topological selection to enhance $t\bar{t}$ signal. Top, distribution in H_T^e, the sum of jet and electron transverse energies; prior to requirement $H_T^e > 120$ GeV, four candidates remain. Bottom, distribution in jet multiplicity, prior to requirement $N_{jets} \geq 2$; three candidates survive final selection. The same distributions are shown in a log scale (*left*) and linear scale (*right*)

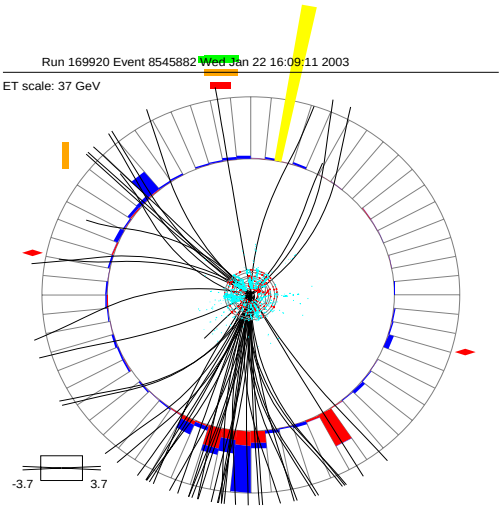

Figure 8.2: XY view of candidate event.

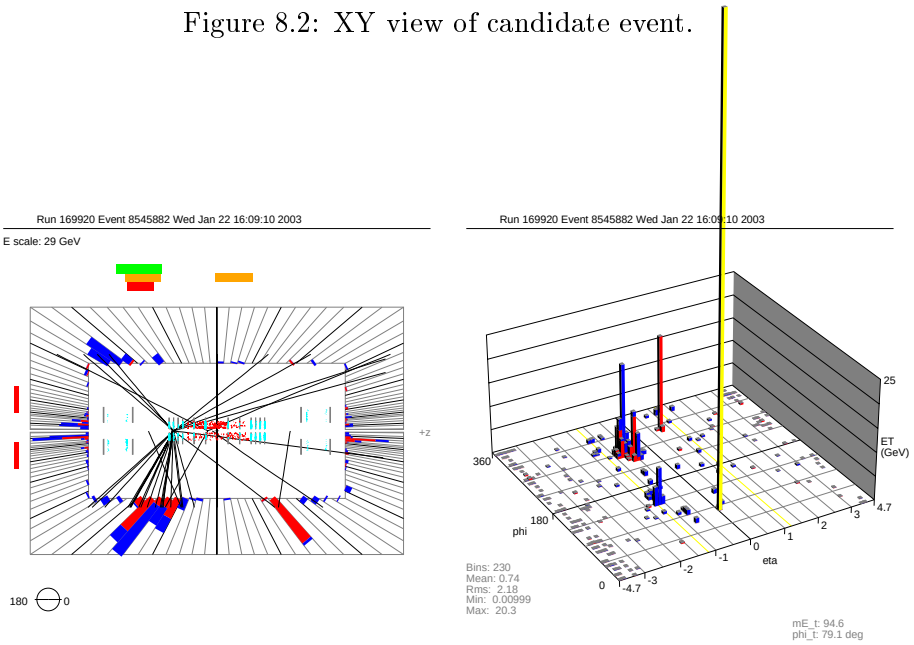

Figure 8.3: RZ and lego views of candidate event.

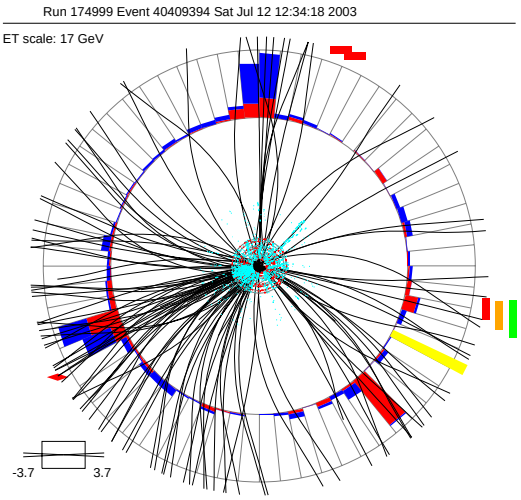

Figure 8.4: XY view of candidate event.

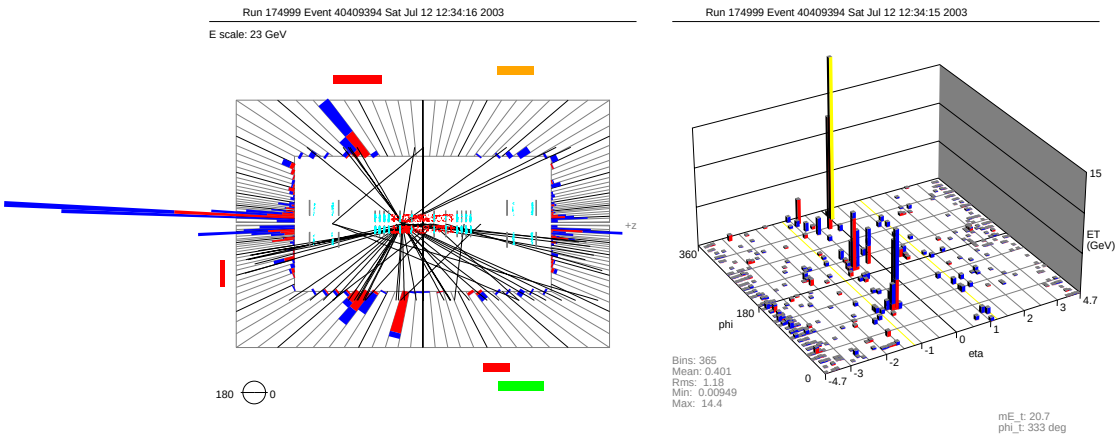

Figure 8.5: RZ and lego views of candidate event.

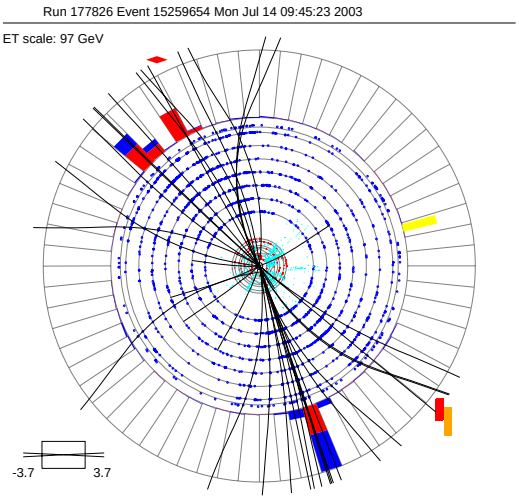

Figure 8.6: XY view of candidate event.

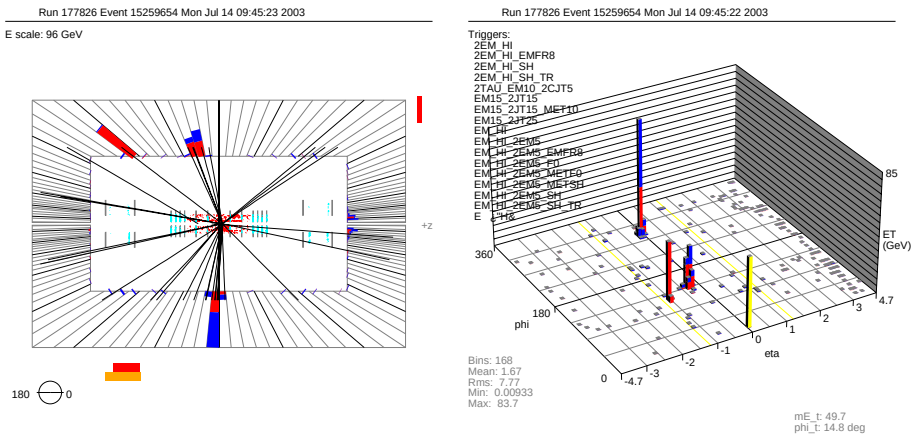

Figure 8.7: RZ and lego views of candidate event.

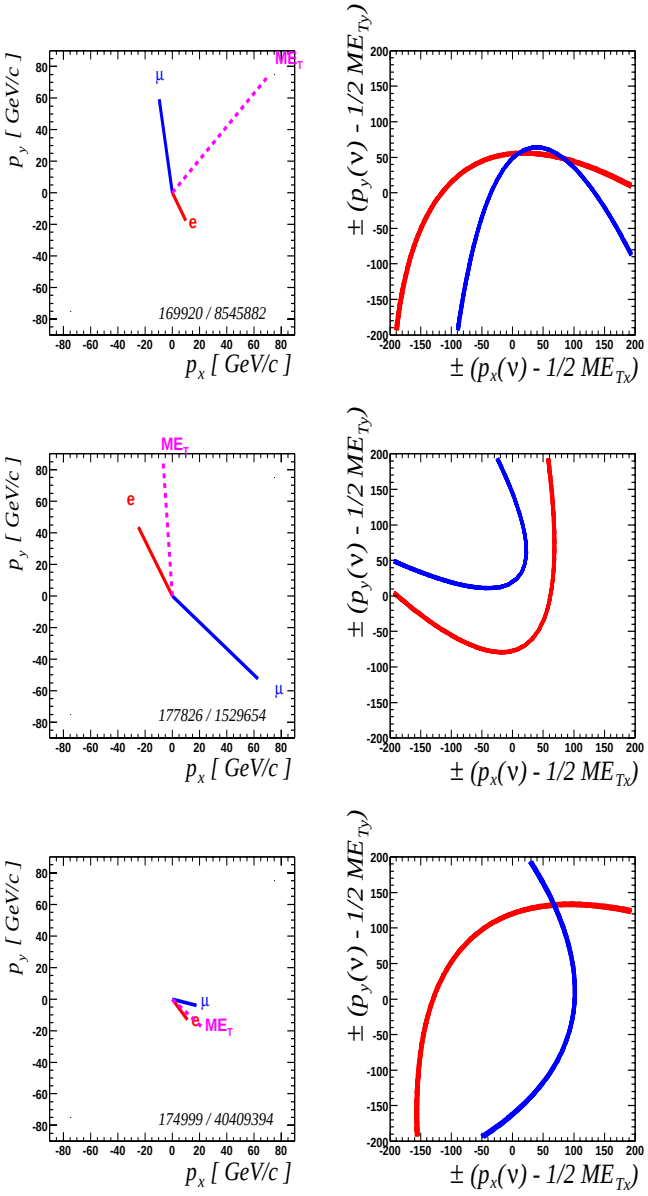

Figure 8.8: Analysis of the consistency of the lepton momenta and missing transverse energy with the hypothesis of the decay of two W bosons. The object energies are shown to the left for each event. In the space of neutrino transverse energy components, countors of constant W mass are parabolae. If $p_{\nu_e} + p_{\nu_\mu} = \not\!\!E_T$, then these parabolae should intersect; here are shown the parabolae corresponding to $m_W = 80.4$ GeV.

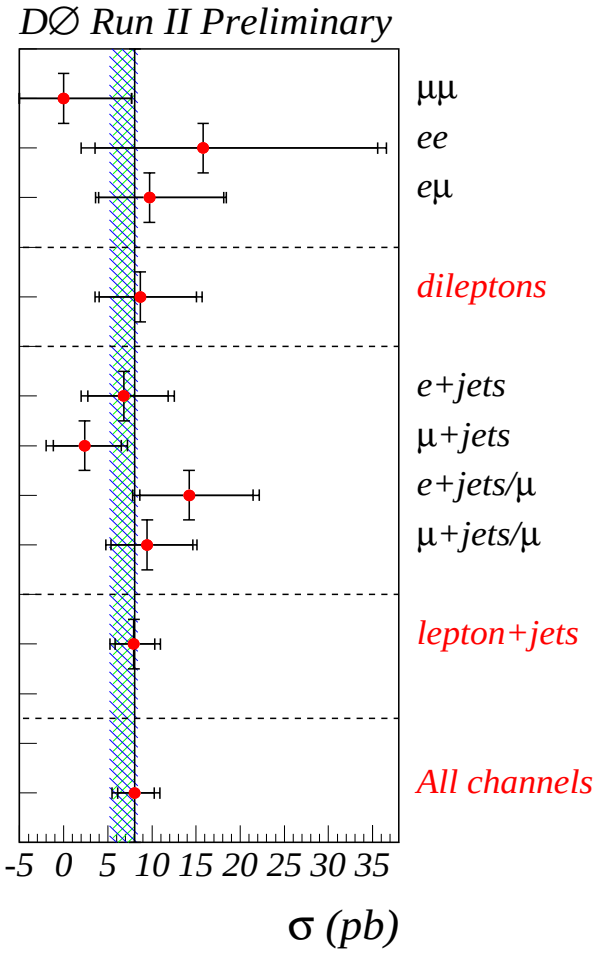

Figure 8.9: Summary of measurements of the top quark production cross section at DØ in Run2.

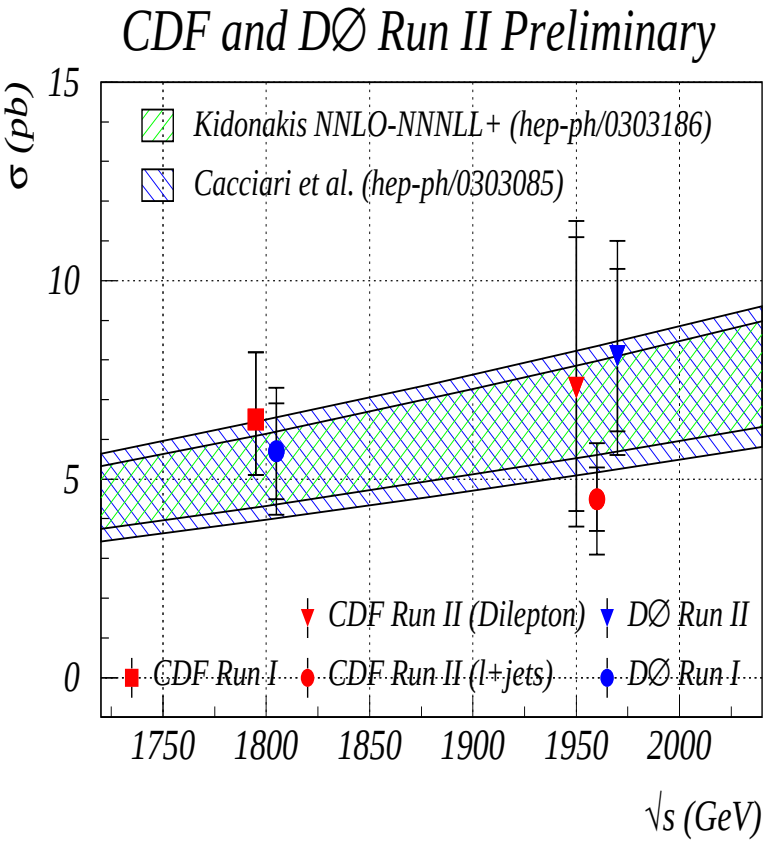

Figure 8.10: Summary of measurements of the top quark production cross section at CDF and DØ in Run1 and Run2.

8.2 Measurement of $\sigma_{WW} \times BR(WW \to e\mu)$

Production of W boson pairs through e^+e^- annihilation has been well measured and characterized by experiments at the LEP ring. The hadronic environment of the Tevatron makes observation of this process much more difficult. Topological isolation of the signal is possible however, with methods similar to those for top quark production.

Decay of WW pairs is characterized by an energetic electron and muon as well as significant missing transverse energy due to two uncaptured energetic neutrinos. Figures 7.1- 7.3 show kinematic distributions for the data and expected contributions. Contributions from $t\bar{t}$ production can be substantially reduced by requiring that no jets are reconstructed in the event. In order to escape the dominant backgrounds of $Z \to \tau\tau$ and misidentified events, one must apply a requirement on the missing transverse energy, see Figure 8.11.

The primary remaining backgrounds will also tend to produce an electron and muon which are directly opposite each other in ϕ; a missing energy threshold which depends on the angle between the leptons can retrieve some sensitivity, see Figure 8.12. We place a requirement on the product of these terms:

$$\xi = \not\!\!E_T \times [\pi - \Delta\phi(e,\mu)] > 10 \text{ GeV}$$

where the point of selection is chosen to minimize the relative error on the measured

cross section by maximizing the quantity $\frac{S}{\sqrt{(S+B)}}$, see Figure 8.13.

This selection produces a sample which is dominated by WW production; the largest background is due to misidentification of electrons. The efficiency of selection for WW events is given in Table 8.5. The number of events after each selection, and the contributions from each source, are listed in Table 8.6.

Four events pass the final selection. The probability for the background to fluctuate from a mean of $b = 0.87$ events to an observed $N = 4$ is 0.0120. Incorporating the uncertainty in the background prediction, and assuming a Gaussian distribution, this probability rises to 0.0123.

The kinematic properties of the candidates are listed in Table 8.7, and their consistency with the decay of two W bosons is analyzed in Figure 8.15.

8.2.1 Production Cross Section

The observed excess over the backgrounds of $N_{bg} = 0.87$ events is

$$N_{sig} = N_{obs} - N_{bg} = 4 - 0.87 = 3.13 \text{ events}$$

The efficiency to trigger, reconstruct and select $WW \to e\mu jj$ events is

$$\varepsilon_{WW} = Acc_{t\bar{t}} \times \kappa_{Data/MC} \times \varepsilon_{trigger} \times \kappa^{\tau} = 0.103 \times 0.664 \times 0.937 \times 1.15 = 0.072$$

Cut	Cumulative ϵ	Marginal ϵ
Vertex	0.945	0.945
μ ID	0.608	0.644
μ Track-match	0.438	0.720
μ $P_T > 15$ GeV	0.402	0.918
e ID	0.218	0.542
e Likelihood	0.197	0.904
e $P_T > 15$ GeV	0.196	0.994
$R(e,\mu) > 0.25, \lvert e_z - mu_z \rvert < 5.0cm$	0.195	0.994
μ isolation	0.180	0.923
μ DCA	0.177	0.985
$N_{jets}^{P_T>15} = 0$	0.143	0.809
Unlike sign	0.143	0.999
$\xi > 10$ GeV	0.103	0.722

Table 8.5: Efficiencies in simulation for $WW \to e\mu$.

Cut	Data	All	WW	MisID	$WZ, W\gamma$	$Z \to \tau\overline{\tau}$	$t\overline{t}$
Inital Sel.	44	$37.93^{\pm 0.33}_{\pm 2.09}$	$4.04^{\pm .01}_{\pm .23}$	$4.85^{\pm 0.15}_{\pm 1.02}$	$0.53^{\pm .00}_{\pm .03}$	$26.13^{\pm 0.00}_{\pm 1.80}$	$2.38^{\pm .10}_{\pm .13}$
$N_{Jets} = 0$	33	$27.34^{\pm 0.79}_{\pm 1.46}$	$3.27^{\pm .07}_{\pm .18}$	$3.12^{\pm 0.66}_{\pm 0.31}$	$0.42^{\pm .01}_{\pm .02}$	$20.51^{\pm .43}_{\pm 1.41}$	$0.02^{\pm .01}_{\pm .01}$
$\xi > 10$	4	$3.29^{\pm 0.13}_{\pm 0.15}$	$2.42^{\pm .05}_{\pm .14}$	$0.59^{\pm .12}_{\pm .06}$	$0.15^{\pm .01}_{\pm .01}$	$0.12^{\pm .01}_{\pm .01}$	$0.02^{\pm .01}_{\pm .01}$

Table 8.6: Data and backgrounds at each level of selection, with statistical errors (*superscript*) and systematic errors (*subscript*).

Run	Event		Electron	Muon	$\not\!\!E_T$
178278	44289575	P_T [GeV]	36.7	28.7	50.5
		ϕ	4.84	0.17	1.61
		η	0.58	-1.41	–
178219	2943709	P_T [GeV]	86.3	29.7	85.1
		ϕ	3.63	1.53	2.10
		η	0.38	1.28	–
176931	25710151	P_T [GeV]	20.4	27.6	19.2
		ϕ	4.83	1.00	2.45
		η	0.87	0.02	–
166485	22552149	P_T [GeV]	30.4	23.8	19.1
		ϕ	2.71	0.33	2.38
		η	0.70	0.25	–

Table 8.7: WW candidate events.

Given a luminosity of 97.7 pb^{-1}, we find

$$\sigma_{WW\to e\mu} = \frac{N_{sig}}{\mathcal{L} \times \varepsilon_{WW}} = 0.12 \text{ pb}$$

and assuming that $BR(WW \to e\mu jj) = 2/81$, we calculate

$$\sigma_{WW} = 18.5^{+13.9}_{-9.9}\ (stat)^{+4.3}_{-4.0}(syst) \text{ pb.}$$

8.2.2 Discussion

In a Run2 data set of similar size, CDF reported [72] observation of 5 candidate $WW \to ll$ events in the $ee, \mu\mu$ and $e\mu$ channels, see Figure 8.16, with an expected background of 2.34 ± 0.38 events for a measurement of the production cross section:

$$\sigma_{WW\to ll} = 5.1^{+5.4}_{-3.6}(stat) \pm 1.3(syst) \pm 0.3(lumi)$$

which is not inconsistent with the measurement in this thesis.

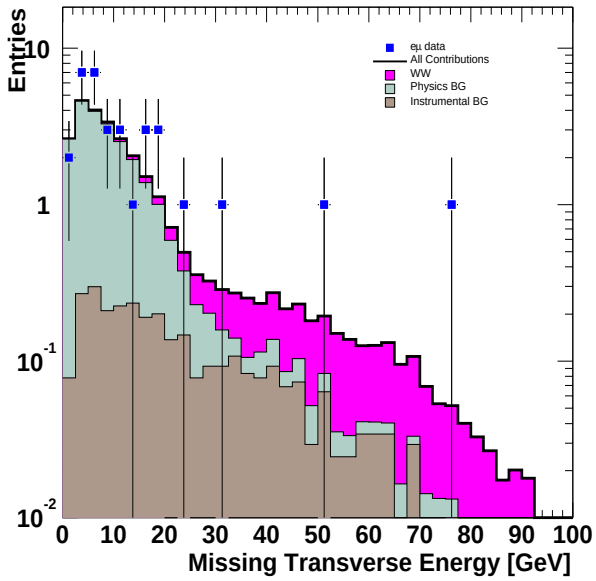

b

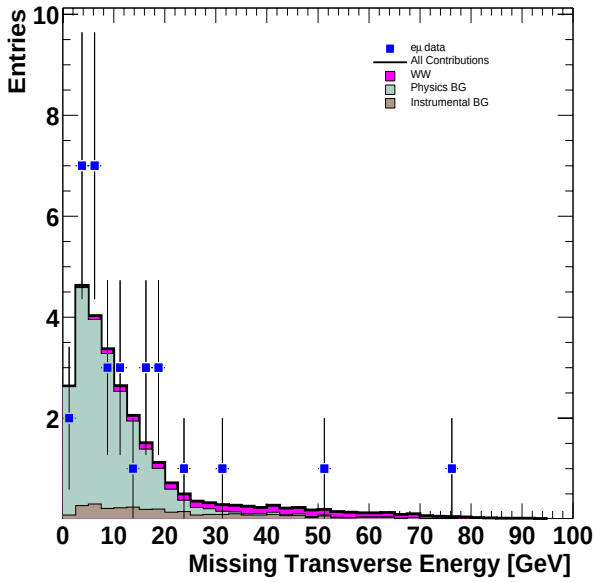

Figure 8.11: Data and backgrounds after requiring no reconstructed jets in order to enhance WW signal.

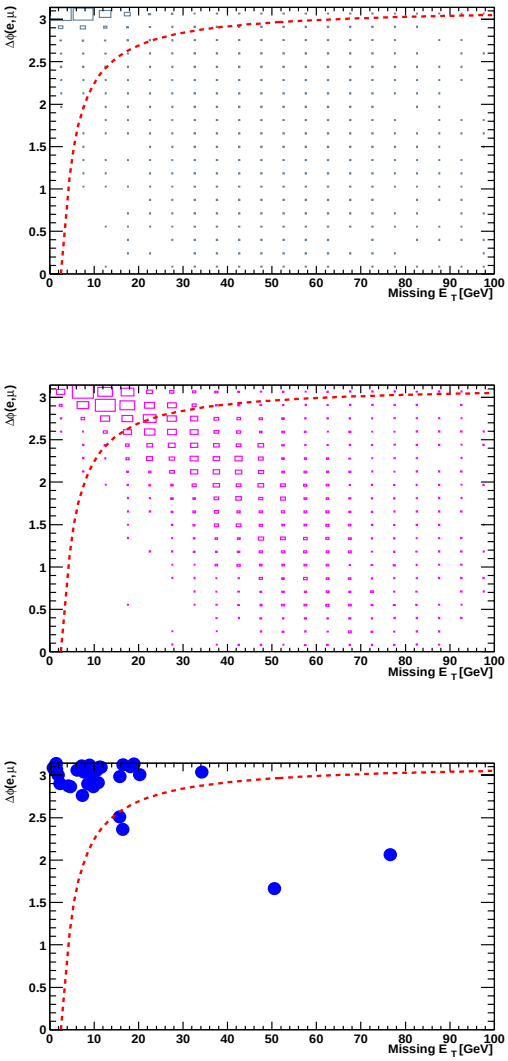

Figure 8.12: Distribution in Missing Transverse Energy and distance in ϕ between leptons; physics backgrounds (*top*), expected signal (*middle*), and data (*bottom*).

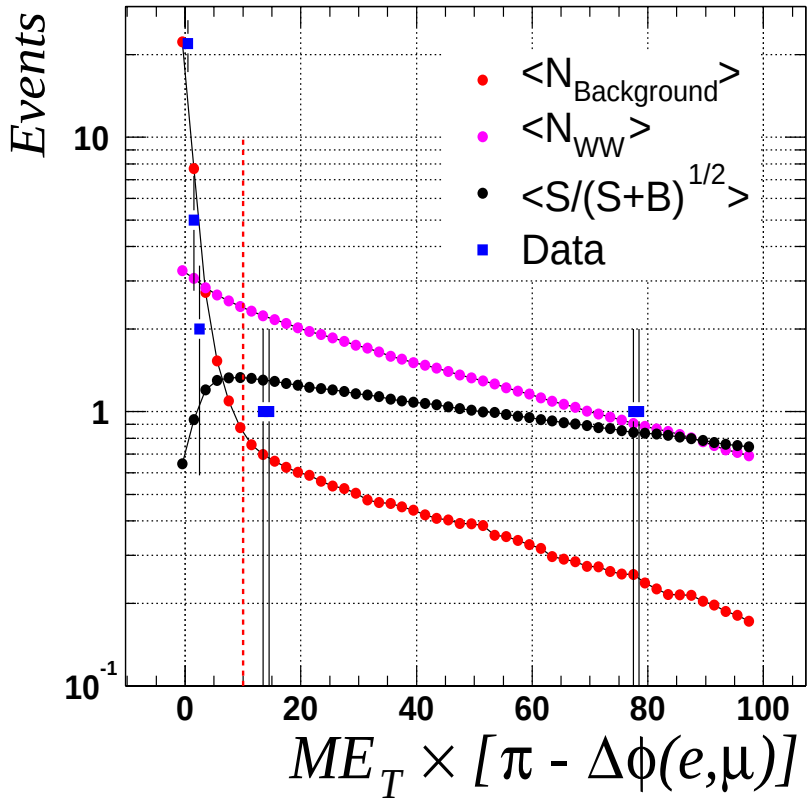

Figure 8.13: Optimization of the point of selection for the quantity $\not\!\!E_T \times [\pi - \Delta\phi(e,\mu)]$ by maximizing $\frac{S}{\sqrt{(S+B)}}$.

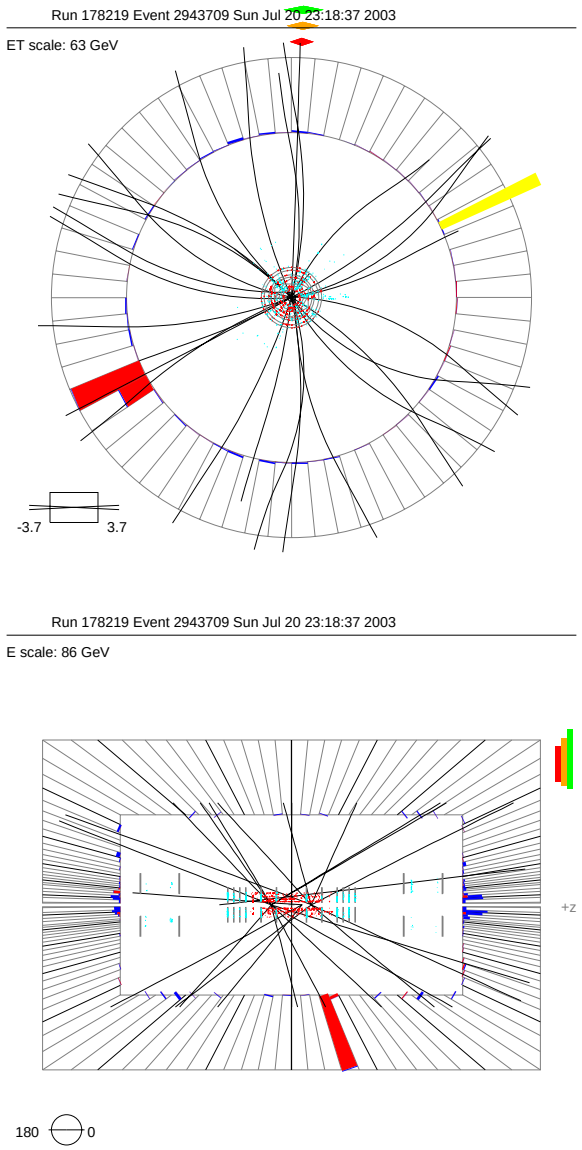

Figure 8.14: XY and RZ views of $WW \to e\mu$ candidate event. The electron appears as electromagnetic (*red*) energy in the calorimeter associated with a central track (*black*); jets appear as electromagnetic and hadronic (*blue*) energy; the muon appears as muon chamber hits (*red, orange, green squares*) and a central track (*black*).

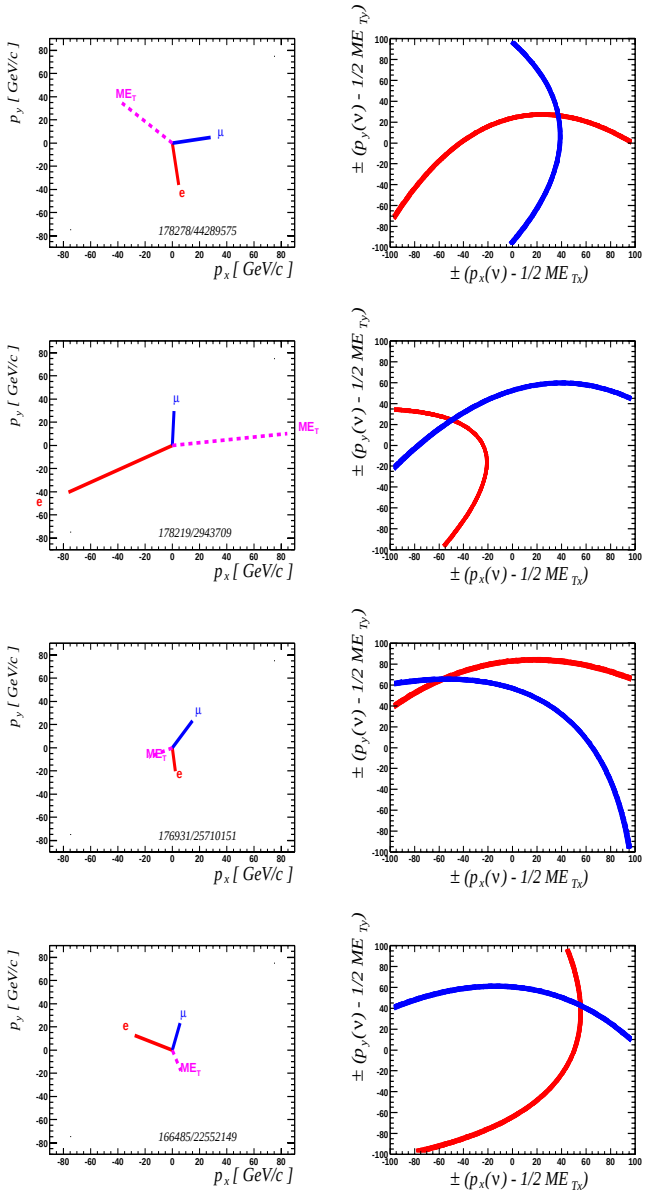

Figure 8.15: Analysis of the consistency of the lepton momenta and missing transverse energy with the hypothesis of the decay of two W bosons. The object energies are shown to the left for each event. In the space of neutrino transverse energy components, countors of constant W mass are parabolae. If $p_{\nu_e} + p_{\nu_\mu} = \not\!\!E_T$, then these parabolae should intersect; here are shown the parabolae corresponding to $m_W = 80.4$ GeV.

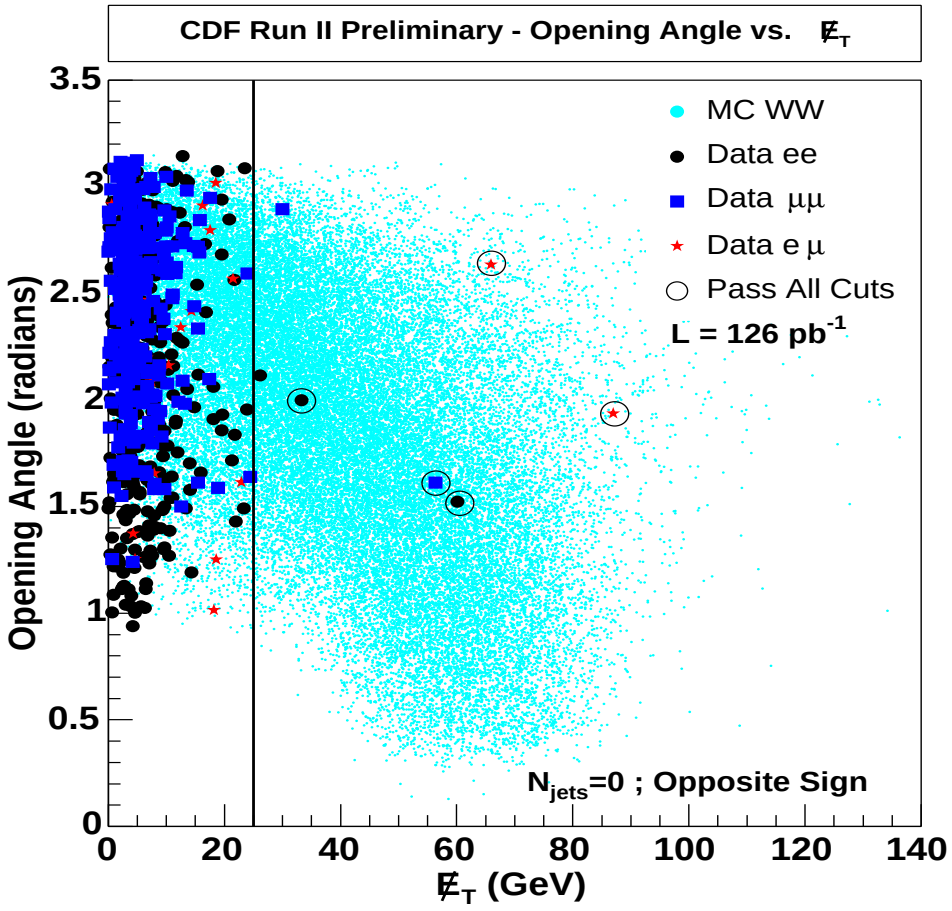

Figure 8.16: Selection of $WW \to ll$ candidates by CDF [72].

Chapter 9

Searches for Exotic Processes

In this chapter, we apply the collected data and the background estimates to searches for the production of particles predicted by specific supersymmetric models, discussed in detail below.

In addition, we examine our sensitivity to unanticipated exotic processes.

9.1 Supersymmetric Models

Investigations into new theoretical structures which solve outstanding problems in the current theory can provide powerful clues in the search for new particles. Discovery of the charm, strange, bottom and top quarks were theoretically anticipated in many respects, and if the Higgs boson is discovered at the Tevatron or the Large Hadron

Collider, it will confirm many years of theoretical effort.

Similarly, the theoretical structures of supersymmetry are very appealing, beyond their potential to connect the Standard Model with gravity or to address the issue of the mass of the Higgs boson.

Supersymmetric (SUSY) models which conserve R-parity are characterized by the lightest supersymmetric particle (LSP), which is the result of a decay chain of heavier SUSY particles produced in pairs. This particle is uncharged, colorless and weakly interacting, giving it the same experimental signature as a neutrino. We choose to examine models in which the LSP is the χ_0^1. Within a SUSY model, there are several processes which are predicted to produce $e\mu$ events. Three of them are detailed below and included in the analysis.

9.1.1 $p\overline{p} \to \chi_1^{\pm}\chi_2^0 \to l\nu\chi_1^0 ll\chi_1^0$

Associated production of χ_2^0 and $\chi_1^{\pm}$ offers an excellent window into SUSY models, as it predicts the production of three stiff leptons, see Figure 9.1; this improves the $e\mu$ selection efficiency significantly. Figure 9.2 shows the electron and muon energy spectrum for selected model points, which are discussed below. Simulated events are generated with PYTHIA, using SUSPECT to calculate the relevant SUSY parameters. The leading order production cross section recieves a significant correction from next-to-leading order contributions [44], see Figure 9.3.

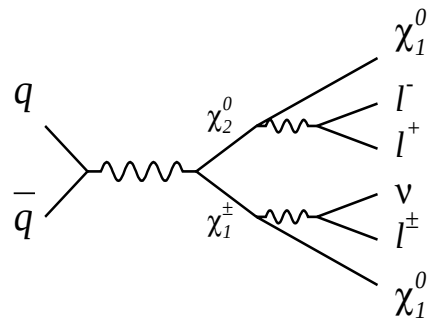

Figure 9.1: Feynman diagram for the leading contribution to the process $p\overline{p} \to \chi_1^\pm \chi_2^0 \to l\nu\chi_1^0 ll\chi_1^0$.

9.1.2 $p\overline{p} \to \chi_1^+\chi_1^- \to l\nu\chi_1^0 l\nu\chi_1^0$

Production of $\chi_1^+\chi_1^-$ is analogous to standard model WW production, and similar in signature, but with additional missing energy, see Figure 9.4. Figure 9.5 shows the electron and muon energy spectrum for selected model points, which are discussed below. The leading order production cross section recieves a significant correction from next-to-leading order contributions [44], see Figure 9.3.

9.1.3 $p\overline{p} \to \tilde{t}_1^+\tilde{t}_1^- \to bb\chi_1^+\chi_1^- \to bbl\nu\chi_1^0 l\nu\chi_1^0$

Production of stop quark pairs is analogous to standard model $t\bar{t}$ pairs, see Figure 9.6, but is produced with significantly more missing energy, and can have dra-

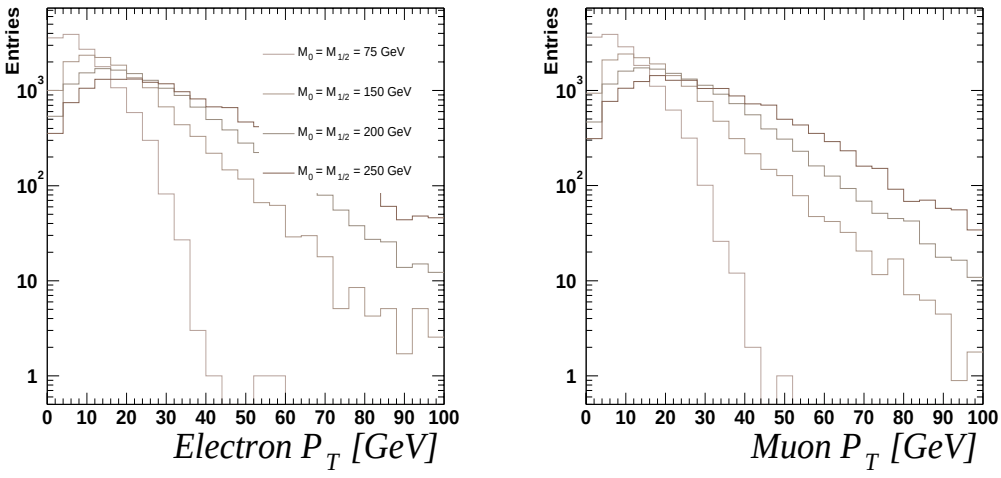

Figure 9.2: Electron and muon energies for $\chi_1^{\pm}\chi_2^0 \rightarrow l\nu\chi_1^0 ll\chi_1^0$ production at selected mSUGRA model points.

matically more transverse energy in the event, depending on the stop mass. Figure 9.7 shows the electron, muon and jet energy spectrum for selected model points, which are discussed below. The leading order production cross section recieves a relatively small correction from next-to-leading order contributions [45].

9.1.4 Choice of Parameters

Supersymmetric theories offer a bewildering number of parameters. In absence of experimental guidence or strong theoretical reasoning, we rely instead on theoretical intuition and prejudice to simplify the number of parameters and their reasonable choices. In this spirit, we choose to work within the subspace of theoretical parameters referred

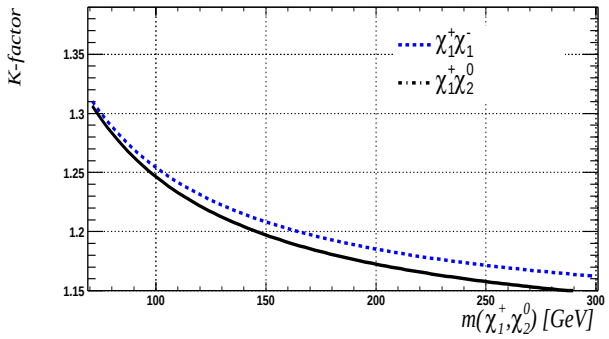

Figure 9.3: Next to leading order corrections to production cross sections for $p\overline{p} \to \chi_1^+\chi_2^0$ and $p\overline{p} \to \chi_1^+\chi_1^-$, adapted from [44].

to as mSUGRA, which has five non-Standard Model parameters, see Section 2.4.1.

Choices of these parameters strongly affect the masses of particles such as $\chi_{1,2}^{\pm}$,$\chi_{1,2}^0$, and $\tilde{t}_{1,2}$, which directly affect the kinematics of the processes we have chosen to probe. We must therefore probe theories in a reasonable range of parameters.

We choose to hold $\tan\beta$ fixed at 2.5, A_0 at zero, and scan the two-dimensional space of m_0 and $m_{\frac{1}{2}}$ for positive and negative values of μ. The detailed results presented below are derived with $\mu > 0$; final results are presented for both choices of sign.

Figure 9.9 shows the range of $\chi_{1,2}^{\pm}$ masses as a function of m_0 and $m_{\frac{1}{2}}$. As one would suspect, this mass is strongly dependent on $m_{\frac{1}{2}}$ and weakly on m_0. Figure 9.8 reveals the same to be true for $\chi_{1,2}^0$ and Figure 9.10 for $\tilde{t}_{1,2}^{\pm}$. Finally, Figure 9.11 shows that the ratios of neutralino and chargino masses are roughly constant, while the ratio of stop to chargino mass varies strongly with $m_{\frac{1}{2}}$ and more weakly with m_0. A factor

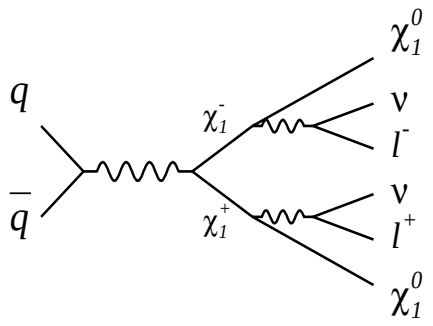

Figure 9.4: Feynman diagram for the leading contribution to the process $p\overline{p} \to \chi_1^+\chi_1^- \to l\nu\chi_1^0 l\nu\chi_1^0$.

which is crucial in determining the transverse momentum of the final state leptons, and therefore our detection efficiency, is the mass difference between LSP (χ_1^0) and the $\chi_1^\pm$ and $\tilde{t}_1^\pm$ which decay to it; the variation in this difference is shown in Figure 9.12.

These observations suggest that we can focus on the variation of a single parameter, $m_{\frac{1}{2}}$; we probe a few variations of m_0 as well to ensure the stability of our results.

9.1.5 Efficiencies and Expected Yields

The fundamental limit produced by such a search is a limit on the production cross section of new physics, σ^{NP}. The ability to set limits on this cross-section is

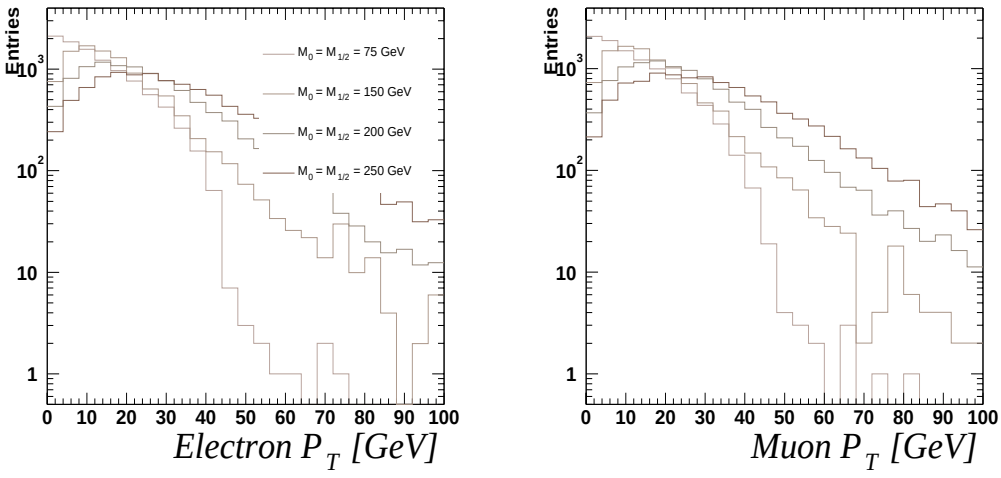

Figure 9.5: Electron and muon energies for $\chi_1^+\chi_1^- \rightarrow l\nu\chi_1^0 l\nu\chi_1^0$ production at selected mSUGRA model points

constrained directly by the efficiency of the detector to trigger, identify and reconstruct an event with energetic isolated electrons and muons, $\epsilon_{e\mu}$.

The most interesting limit produced by such a search, however, is a limit on the cross section above relative to the theoretical predicted cross section for such a process. If our limit is below the theoretical value, then we can claim to have excluded that theory, at our chosen confidence level. In contrast to cross-section limits, our ability to exclude theories is constrained by the *yield*, the product of the efficiency, the luminosity and the theoretical cross section. Tables 9.1, 9.2, and 9.3 give the reconstruction efficiency $\epsilon_{e\mu}$, the theoretical cross section and the expected yield in our dataset, including the correction to the simulated efficiency.

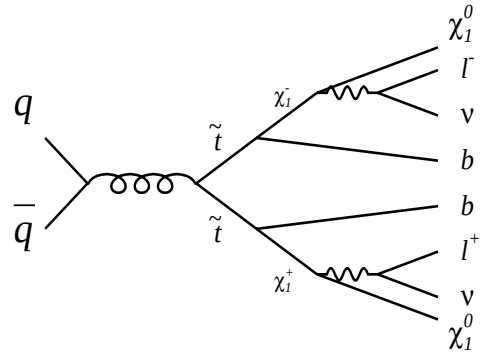

Figure 9.6: Feynman diagram for the leading contribution to the process $p\overline{p} \to \tilde{t}_1^+ \tilde{t}_1^- \to bb\chi_1^+\chi_1^- \to bbl\nu\chi_1^0 l\nu\chi_1^0$.

The feature of the model point which most strongly affects variations in the efficiency is the lepton P_T; Figure 9.13 shows mean electron, muon and $\chi^\pm$ transverse energies for each process at varying model pooints. The lepton P_T dips near $m_0 = m_{\frac{1}{2}} =$ 100 GeV. The energy of the lepton is primarily dependent on the kinematics of the $\chi^\pm$; its mass increases monotonically with $m_0, m_{\frac{1}{2}}$, but its mean transverse energy also dips near 100 GeV. An investigation of points off of the line $m_0 = m_{\frac{1}{2}}$, see Table 9.4, reveals that this efficiency feature is largely a function of $m_{\frac{1}{2}}$ rather than m_0, which is not unexpected.

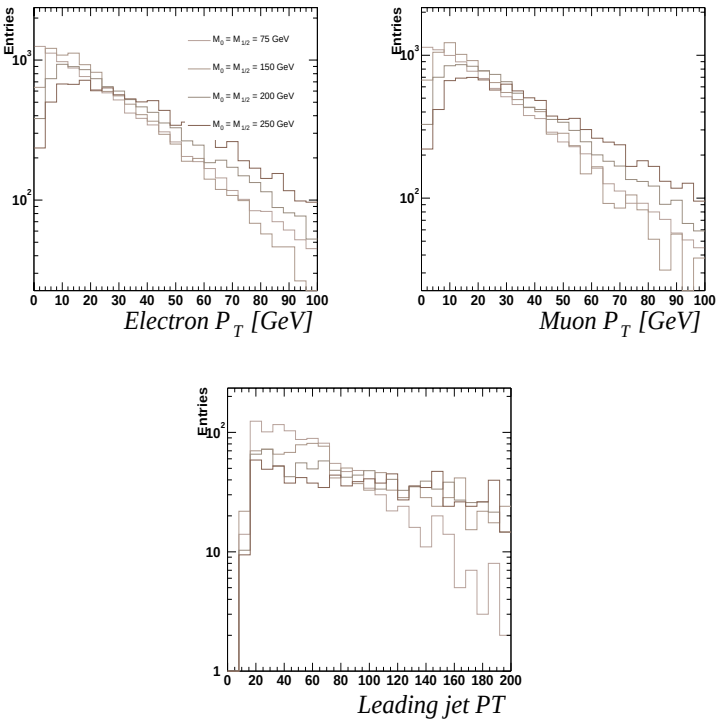

Figure 9.7: Electron, muon and jet energies for $\tilde{t}_1^+\tilde{t}_1^- \rightarrow bl\nu\chi_1^0 bl\nu\chi_1^0$ production atselected mSUGRA model points

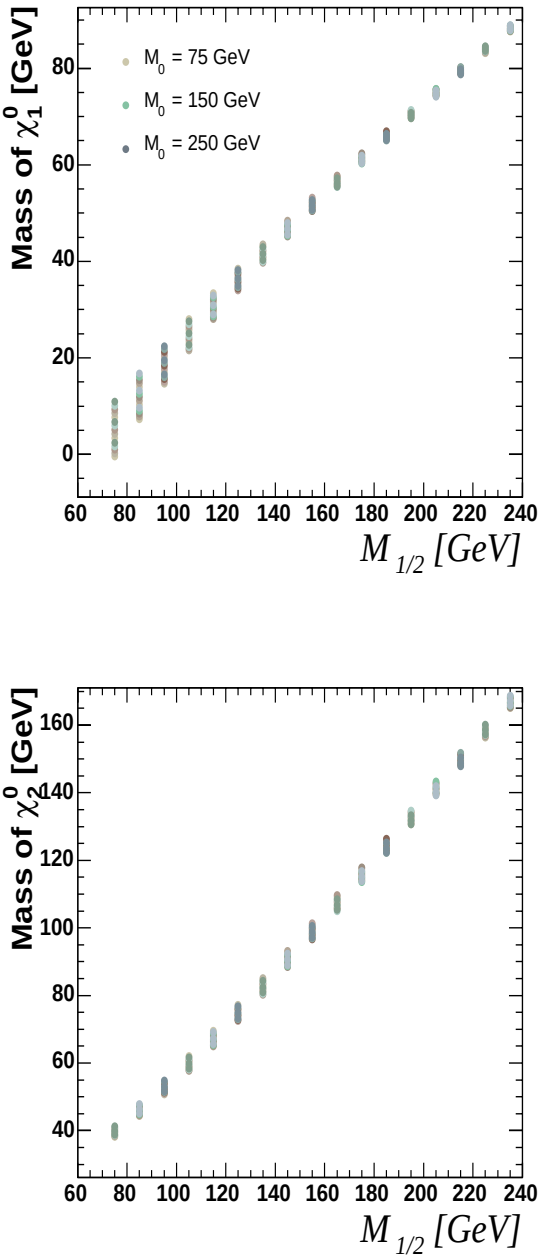

Figure 9.8: Variation in masses of $\chi^0_{1,2}$ with mSUGRA parameter $m_{\frac{1}{2}}$. Various curves demonstrate a scan of m_0 in the region $[75, 250]$ GeV.

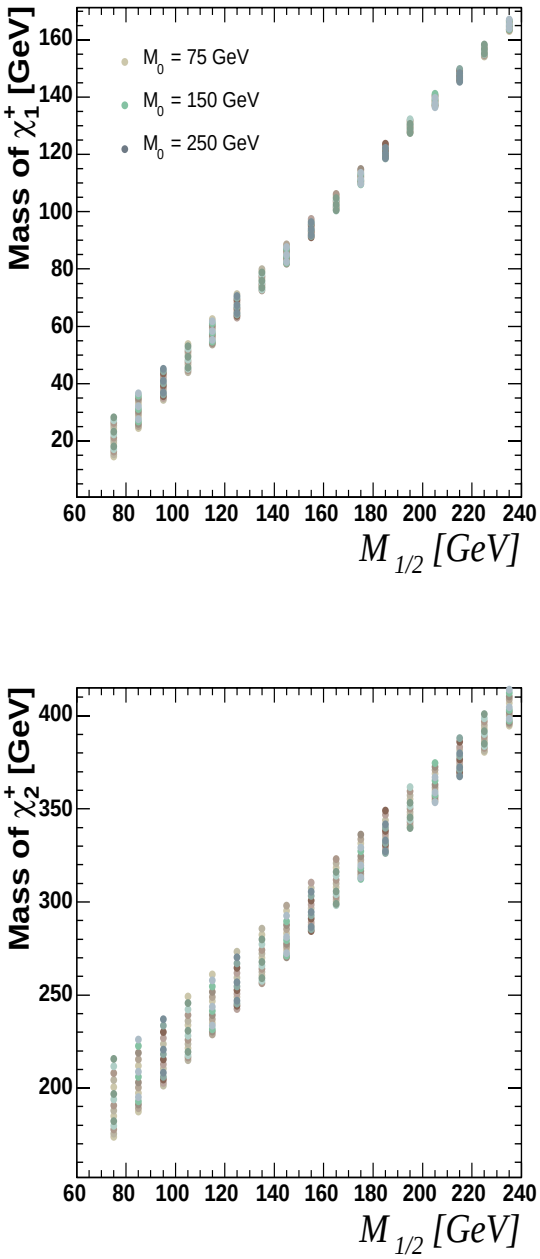

Figure 9.9: Variation in masses of $\chi^{\pm}_{1,2}$ with mSUGRA parameter $m_{\frac{1}{2}}$. Various curves demonstrate a scan of m_0 in the region $[75, 250]$ GeV.

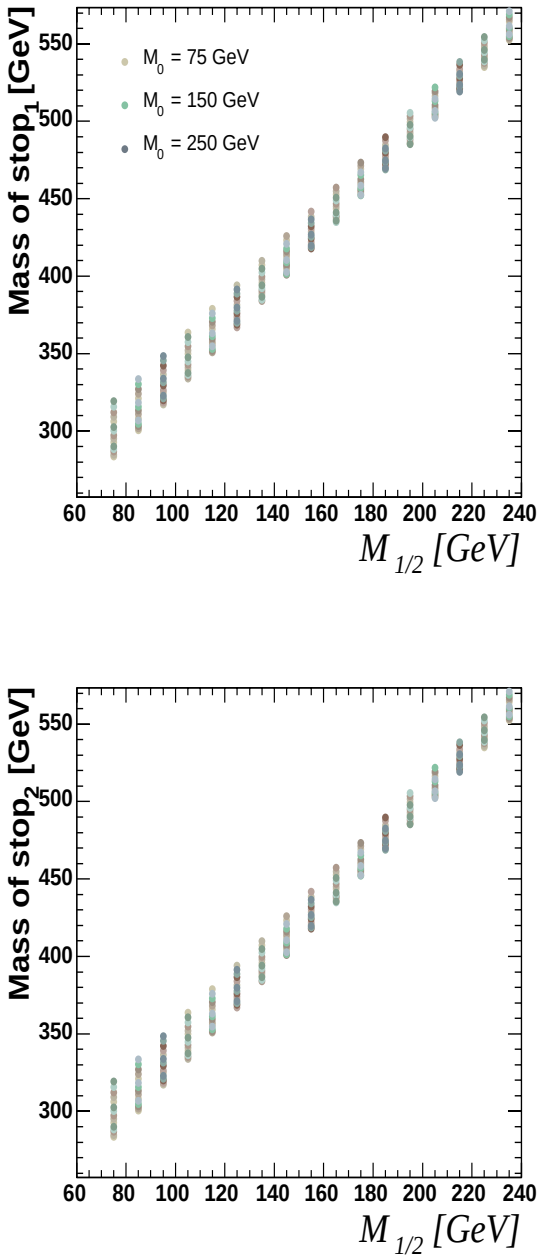

Figure 9.10: Variation in masses of $\tilde{t}_{1,2}$ with mSUGRA parameter $m_{\frac{1}{2}}$. Various curves demonstrate a scan of m_0 in the region $[75, 250]$ GeV.

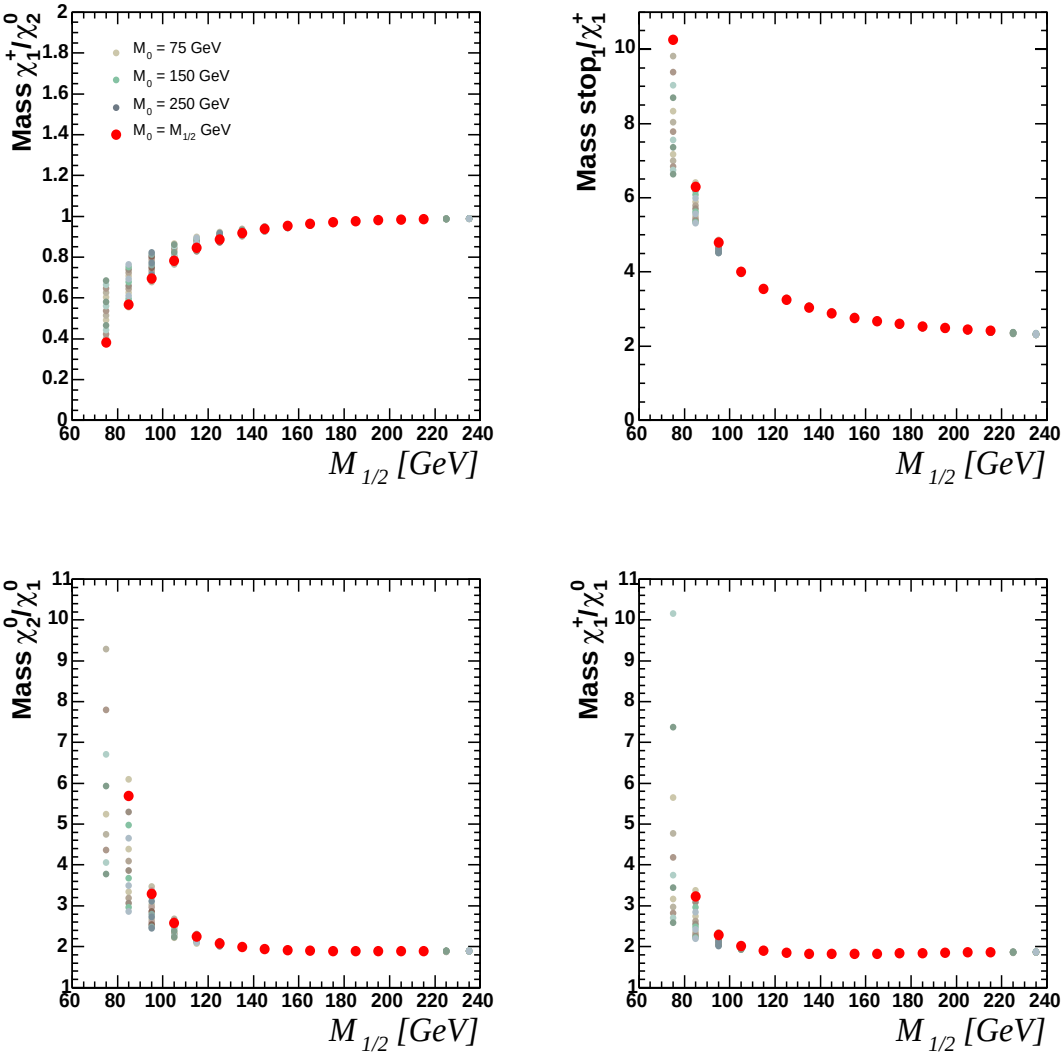

Figure 9.11: Variation in ratios of masses of relevent particles with mSUGRA parameter $m_{\frac{1}{2}}$. Various curves demonstrate a scan of m_0 in the region $[75, 250]$ GeV.

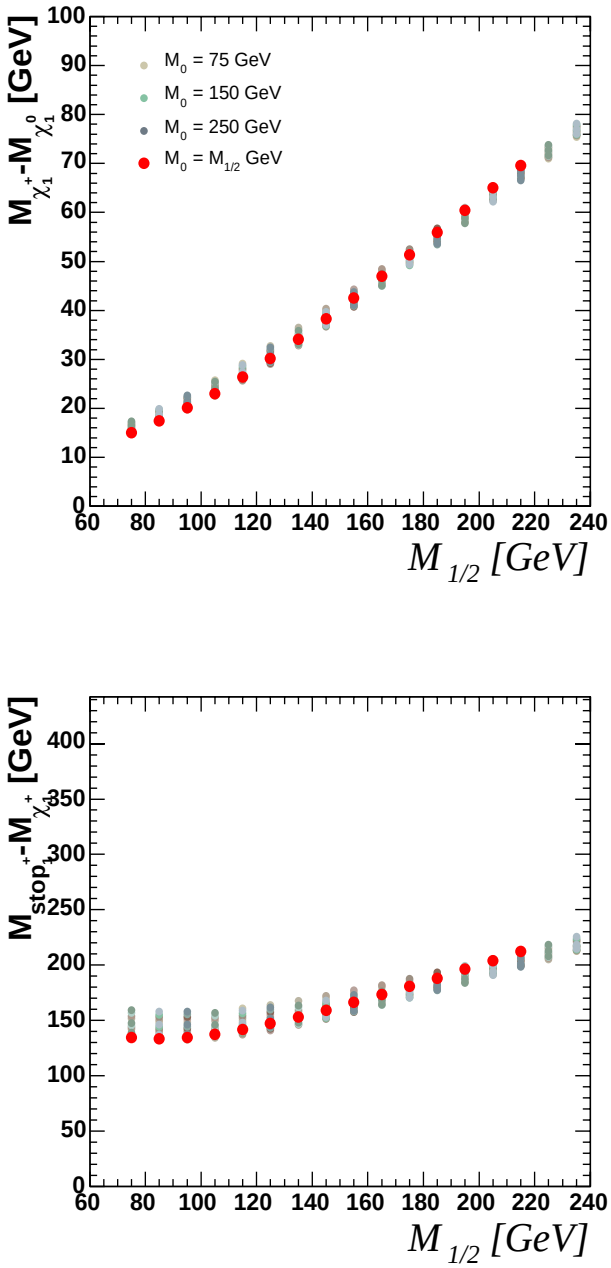

Figure 9.12: Variation in mass differences of relevent particles with mSUGRA parameter $m_{\frac{1}{2}}$. Various curves demonstrate a scan of m_0 in the region $[75, 250]$ GeV.

m_0	$m_{\frac{1}{2}}$	N_{gen}	$\sigma(pb)$	$\epsilon_{e\mu}$	y
75	75	9.5k	90.08	0.7%	41.66
85	85	11.5k	84.13	0.3%	14.03
90	90	22.0k	58.85	0.1%	3.81
100	100	10.0k	1.63	1.1%	1.08
110	110	12.0k	0.65	1.6%	0.65
125	125	9.0k	0.28	3.7%	0.66
150	150	10.9k	0.08	6.0%	0.28
175	175	18.3k	0.02	8.5%	0.12
188	188	16.0k	0.01	9.7%	0.08
200	200	23.8k	0.01	10.6%	0.06
225	225	9.5k	0.00	12.2%	0.03
250	250	4.5k	0.00	13.8%	0.01

Table 9.1: For various mSUGRA model points, the number of generated $\chi_1^{\pm}\chi_2^0$ events, N_{gen}, the theoretical cross section including branching ratios to electrons and muon, σ, the efficiency to pass $e\mu$ selection cuts, $\epsilon_{e\mu}$ and the total expected yield in 97.7 pb^-1 of data, including efficiency correction factors.

m_0	$m_{\frac{1}{2}}$	N_{gen}	$\sigma(pb)$	$\epsilon_{e\mu}$	y
75	75	10.0k	141.06	1.7%	144.04
85	85	10.0k	108.13	0.8%	52.87
90	90	15.0k	96.49	0.5%	28.66
100	100	10.0k	69.00	0.1%	5.12
110	110	12.0k	2.77	0.4%	0.70
125	125	6.5k	0.36	1.7%	0.38
150	150	5.0k	0.08	3.6%	0.18
175	175	7.5k	0.03	5.2%	0.09
188	188	6.0k	0.02	5.6%	0.06
200	200	16.0k	0.01	6.8%	0.05
225	225	7.0k	0.01	8.0%	0.03
250	250	7.3k	0.00	9.1%	0.02

Table 9.2: For various mSUGRA model points, the number of generated $\chi_1^+\chi_-^1$ events, N_{gen}, the theoretical cross section including branching ratios to electrons and muon, σ, the efficiency to pass $e\mu$ selection cuts, $\epsilon_{e\mu}$ and the total expected yield in 97.7 pb^-1 of data, including efficiency correction factors.

m_0	$m_{\frac{1}{2}}$	N_{gen}	$\sigma(pb)$	$\epsilon_{e\mu}$	y
75	75	10.0k	0.259	4.7%	0.757
85	85	5.0k	0.149	4.0%	0.371
90	90	5.0k	0.113	3.9%	0.274
100	100	9.5k	0.067	3.4%	0.142
110	110	3.5k	0.038	3.7%	0.088
125	125	5.0k	0.018	3.6%	0.039
150	150	4.5k	0.005	4.6%	0.015
175	175	5.0k	0.001	5.6%	0.005
188	188	3.0k	0.001	6.8%	0.003
200	200	14.9k	0.000	7.1%	0.002
225	225	4.0k	0.000	8.0%	0.000
250	250	5.0k	0.000	8.3%	0.000

Table 9.3: For various mSUGRA model points, the number of generated $\tilde{t}_1^+\tilde{t}_1^-$ events, N_{gen}, the theoretical cross section including branching ratios to electrons and muon, σ, the efficiency to pass $e\mu$ selection cuts, $\epsilon_{e\mu}$ and the total expected yield in 97.7 pb^-1 of data, including efficiency correction factors.

$\chi_1^{\pm}\chi_2^0$

	$m_{\frac{1}{2}}$ [GeV]				
m_0 [GeV]	75	85	90	100	110
75	0.78%	–	–	1.18%	–
85	–	0.21%	–	1.06%	–
90	–	–	0.11%	0.98%	–
100	0.73%	0.30%	0.11%	1.06%	2.09%
110	–	–	–	1.03%	1.68%

$\chi_1^{+}\chi_1^{-}$

	$m_{\frac{1}{2}}$ [GeV]				
m_0 [GeV]	75	85	90	100	110
75	1.47%	–	–	0.16%	–
85	–	0.83%	–	0.21%	–
90	–	–	0.51%	0.20%	–
100	1.59%	0.64%	0.37%	0.10%	0.32%
110	–	–	–	0.16%	0.34%

$\tilde{t}_1^{+}\tilde{t}_1^{-}$

	$m_{\frac{1}{2}}$ [GeV]				
m_0 [GeV]	75	85	90	100	110
75	4.81%	–	–	3.46%	–
85	–	3.98%	–	3.51%	–
90	–	–	4.10%	3.04%	–
100	4.52%	4.08%	3.67%	3.41%	3.56%
110	–	–	–	3.54%	3.34%

Table 9.4: For various mSUGRA points and each selected process, the efficiency of the $e\mu$ selection.

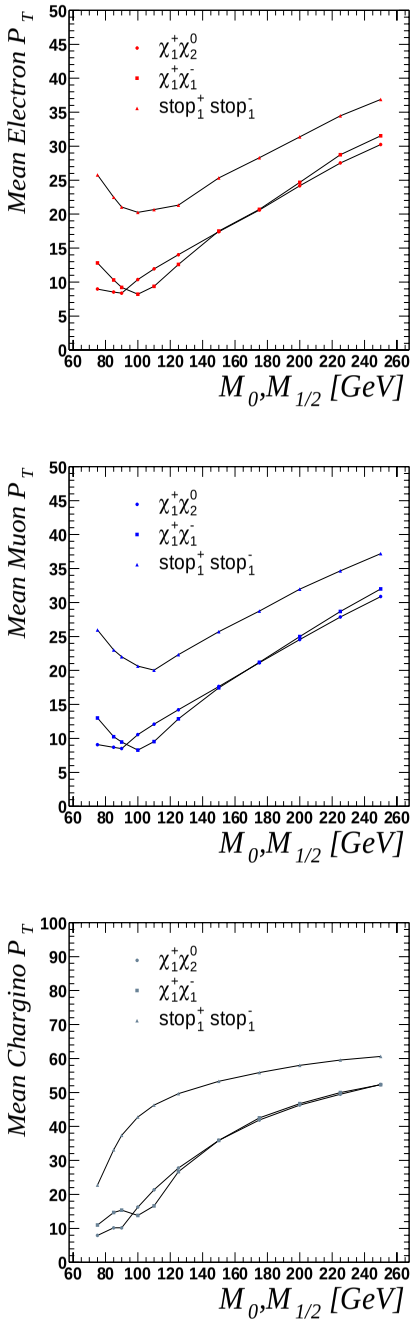

Figure 9.13: Mean electron (*left*) and muon (*center*) and $\chi^{\pm}$ (*right*) transverse momenta with variations in key mSUGRA parameters $m_0 = m_{\frac{1}{2}}$.

9.2 The QUAERO Package

An experimental final state in which the efficiencies, resolutions and backgrounds have been characterized is a powerful scientific tool. With it, one can probe the viability of new hypotheses. To do so, we perform statistical experiments regarding the relative likelihood of a specific hypothesis and the Standard Model. These statistical experiments serve to measure the quantity

$$L = \frac{P(Data|H)}{P(Data|SM)}$$

where H represents a hypothesis and SM represents the baseline for comparison, the Standard Model. Combined with our prior evalution of the relative probabilities, we can convert L into the quantity which is most revealing, the *posterior* probabilities of H and SM,

$$\frac{P(H|Data)}{P(SM|Data)} = L * \frac{P(H)}{P(SM)}.$$

Statistical experiments may examine a wide variety of theoretical hypotheses, but they share at their core the same fundamental machinery. Briefly stated, an experiment in a given final state consists of:

- Selection of regions of sensitivity
- Evaluation of L

For execution of these steps, we use the machinery of the QUAERO[40] package. We discuss each step briefly, and follow the algorithm described in detail in Ref. [40].

9.2.1 Regions of Sensitivity

The selection of sensitive regions is the crucial step of the construction of the statistical experiment. One wishes to choose a region where the hypothesis and the Standard Model differ so that one may make as powerful a statement as possible. On the other hand, a region which is too small will have no statistical power.

The first step is the partitioning of the data into exclusive final states. Each exclusive final state represents a distinct signature, and must be considered separately for maximal sensitivity. A specific final state, however, may not be sensitive in its entirety, but only in a specific region (i.e., high $\not\!\!E_T$, large $\Delta\phi(e,\mu)$, M_{ll} inconsistent with M_Z, ...).

To isolate those subregions, one must first search for variables which have discrimination power. This is done by finding the variables in which the two hypotheses differ most dramatically via calculation of the Kolmogorov-Smirnoff statistic. Ideally, the optimal variable selection algorithm would evaluate potential sets of variables in a multivariate manner, using a measure of sensitivity which accurately reflects the potential of those variables to discriminate between the two hypotheses. Studies along this line have

been done, and have demonstrated that a measure of the one-dimensional discrimination provides a reasonable if slightly less sensitive indicator of variable discrimination power; such a one-dimension evalution is the calculation of the Kolmogorov-Smirnoff statistic.

Once variables have been selected, the machinery examines the possible advantage gained by making selection cuts on those variables, effectively partitioning the space into smaller subregions. If one portion of the parameter space is significantly more powerful, and the statistics of the samples warrant the additional partition, then the space is divided into two or more regions. This is done by placing thresholds on the discriminant

$$D = \frac{P(H)}{P(H) + P(SM)}$$

which function as definitions of contours in the parameter space. The space is partitioned if the sensitivity of the experiment would be increased; an algorithm to determine the optimal partitioning of the discrimant is described in [41].

9.2.2 Evaluation of L

Once the regions of sensitivity have been chosen, the evaluation of L is straightforward. For a given region, the hypothesis H and the Standard Model each predict a certain yield. One may use Poisson statistics to evaluate the relative probability of the observed data, given the two predictions.

9.3 Tests of mSUGRA Processes

9.3.1 Interpretation of L

A value of L which is large indicates strong evidence for the hypothesis in the data, while a small value would indicate evidence against the hypothesis. More illuminating is a variation of a parameter of the hypothesis, the production cross section, σ_H. A signal of new physics in the data would be evidenced by a strong peak with $L \gg 1$ in the quantity

$$L(\sigma_H) = \frac{P(Data|H(\sigma_H))}{P(Data|SM)}.$$

If no significant signal is seen, then $L(\sigma_H)$ provides information for excluding the hypothesis at some confidence level on σ_H.

We construct the posterior probability

$$\frac{P(H(\sigma_H)|Data)}{P(SM|Data)} = L * \frac{P(H(\sigma_H))}{P(SM)}.$$

where $\frac{P(H)}{P(SM)}$ represents the prior probability of hypothesis H. As $P(SM|Data)$ is not dependent on σ_H, it is removed when we require normalization:

$$\int P(H(\sigma_H)|Data)d\sigma_H = 1$$

We assume a flat prior distribution

$$P(H(\sigma_H)) = \frac{1}{\sigma_{max} - \sigma_{min}}$$

where the region $[\sigma_{min,max}]$ is chosen to be large enough such that L, and therefore $P(H(\sigma_H)|Data)$, is negligible outside it.

A confidence limit is calculated by finding σ_{95} such that

$$\int_{\sigma_{min}}^{\sigma_{95}} P(H(\sigma_H)|Data)d\sigma_H = 0.95$$

9.3.2 Test of a Standard Model Process

In the context of the $e\mu$ channel, we can specify the Standard Model hypothesis, against which we compare any model, as

$$\begin{aligned} H_{SM} &= (p\overline{p} \to Z \to \tau\tau) \times \sigma_Z \\ &+(p\overline{p} \to WW) \times \sigma_{WW} \\ &+(p\overline{p} \to t\overline{t}) \times \sigma_{t\overline{t}} \\ &+(misID) \times \sigma_{misID} \end{aligned}$$

the processes whose contribution to $e\mu$ we have considered, at the cross section predicted by the Standard Model.

As a demonstration, we perform a test of a SM process and extract a measurement of its contribution in the data, compared to the theoretical prediction. The largest SM signal in $e\mu$ is $Z/\gamma^* \to \tau\tau$; we measure its rate by comparing the H_{SM} to a hypothesis in which the cross section of Z production has been varied from its SM value of σ_Z to some new value σ_Z':

$$\begin{aligned} H_Z(\sigma_{\mathbf{Z}}') &= (p\overline{p} \to Z \to \tau\tau) \times \sigma_{\mathbf{Z}}' \\ &+ (p\overline{p} \to WW) \times \sigma_{WW} \\ &+ (p\overline{p} \to t\bar{t}) \times \sigma_{t\bar{t}} \\ &+ (misID) \times \sigma_{misID} \end{aligned}$$

The likelihood ratio $L(\sigma_Z')$,

$$L(\sigma_{\mathbf{Z}}') = \frac{P(Data|H_Z(\sigma_{\mathbf{Z}}'))}{P(Data|SM)}$$

will have a peak at the most likely value of σ_Z'. Figure 9.14 shows the posterior probability obtained for varying $H_Z(\sigma_Z')$. The probability peaks at slightly higher than the Standard Model value, consistent with the insignificant excess of events seen in the dataset.

9.3.3 Tests of mSUGRA Models

To probe the viability of a hypothesis which includes a specific process of an mSUGRA model,

$$H_{\chi_1^\pm \chi_2^0} = H_{SM} \wedge (p\overline{p} \rightarrow \chi_1^\pm \chi_2^0)$$

$$H_{\chi_1^+ \chi_1^-} = H_{SM} \wedge (p\overline{p} \rightarrow \chi_1^+ \chi_1^-)$$

$$H_{\tilde{t}_1^+ \tilde{t}_1^-} = H_{SM} \wedge (p\overline{p} \rightarrow \tilde{t}_1^+ \tilde{t}_1^-)$$

we need extract from the data the relative likelihood

$$L = \frac{P(Data|H_{Process})}{P(Data|SM)}.$$

and calculate the posterior probability. In the next sections, we examine the final states in which we are sensitive to each process. To illustrate the methodology, we give details from statistical experiments for a particular process from a particular model. Finally, we scan the parameter space and set limits on the production cross sections and mSUGRA parameters.

$p\overline{p} \rightarrow \chi_1^\pm \chi_2^0$

The process $p\overline{p} \rightarrow \chi_1^\pm \chi_2^0$ produces three stiff leptons. When all three leptons are reconstructed it provides an excellent signature with small backgrounds. The efficiency,

Exclusive State	Population
$e^+\mu^+\not{E}_T$	10%
$e^-\mu^-\not{E}_T$	10%
$e^+\mu^-\not{E}_T$	9%
$e^-\mu^+\not{E}_T$	9%
$e^+\mu^+$	3%
$e^-\mu^-$	3%
$e^+\mu^-$	3%
$e^-\mu^+$	4%
$e^+\mu^+\mu^-\not{E}_T$	2%
$e^-\mu^+\mu^-\not{E}_T$	1%
$e^+e^-\mu^-\not{E}_T$	2%
$e^+e^-\mu^+\not{E}_T$	2%

Table 9.5: Most heavily populated exclusive final state for simulated $p\overline{p} \rightarrow \chi_1^{\pm}\chi_2^0$ ($m_0 = m_{\frac{1}{2}} = 150$ GeV) events.

however, is rather small, given the limits on electron acceptance and lepton tracking efficiency. Another promising signature is that of like-signed leptons; this has a much larger efficiency, though somewhat larger backgrounds.

Table 9.5 shows the population of exclusive final states by simulated $p\overline{p} \rightarrow \chi_1^{\pm}\chi_2^0$ events ($m_0 = m_{\frac{1}{2}} = 150$ GeV) as broken down by QUAERO. As expected, the $e^{\pm}\mu^{\pm}$ final states are roughly equally populated by the signal; those with like-signed leptons, however, will prove to have the lowest backgrounds and provide the most sensitivity.

The backgrounds due to the Standard Model for the like-signed final states, and the events seen in the data are given in Table 9.6 and shown in Figure 9.15.

The trilepton final states ($e^+e^-\mu$ and $\mu^+\mu^-e$) have very small Standard Model

Cut	Data	All	MisID	$WW, WZ, W\gamma$	$Z \to \tau\overline{\tau}$	$t\overline{t}$
$q_e = q_\mu$	1	$2.72^{\pm 0.51}_{\pm 0.24}$	$2.42^{\pm 0.51}_{\pm 0.24}$	$0.29^{\pm 0.01}_{\pm 0.01}$	$0.01^{\pm 0.01}_{\pm 0.01}$	$0.01^{\pm 0.01}_{\pm 0.01}$
$\not\!\!E_T > 15$	1	$1.74^{\pm 0.31}_{\pm 0.15}$	$1.46^{\pm 0.31}_{\pm 0.15}$	$0.27^{\pm 0.01}_{\pm 0.01}$	$0.01^{\pm 0.01}_{\pm 0.01}$	$0.01^{\pm 0.01}_{\pm 0.01}$

Table 9.6: Contributions to the like-signed $e\mu$ final state.

Cut	Data	All	MisID	WZ
$P_T > 0$	0	$0.24^{\pm 0.03(stat)}_{\pm 0.02(syst)}$	$0.152^{\pm 0.03(stat)}_{\pm 0.02(syst)}$	$0.09^{\pm 0.01(stat)}_{\pm 0.01(syst)}$
$P_T > 15$	0	$0.24^{\pm 0.03(stat)}_{\pm 0.02(syst)}$	$0.152^{\pm 0.03(stat)}_{\pm 0.02(syst)}$	$0.09^{\pm 0.01(stat)}_{\pm 0.01(syst)}$
$P_T > 30$	0	$0.12^{\pm 0.01(stat)}_{\pm 0.01(syst)}$	$0.064^{\pm 0.01(stat)}_{\pm 0.01(syst)}$	$0.06^{\pm 0.01(stat)}_{\pm 0.01(syst)}$
$P_T > 45$	0	$0.03^{\pm 0.01(stat)}_{\pm 0.01(syst)}$	$0.015^{\pm 0.01(stat)}_{\pm 0.01(syst)}$	$0.01^{\pm 0.01(stat)}_{\pm 0.01(syst)}$

Table 9.7: Contributions to the trilepton final state.

backgrounds; they also suffer from lower signal efficiencies. Figure 9.16 and Table 9.7 show the Standard Model contributions to these final states.

The final states with the largest sensitivity, measured by the discrepancy between the yields of $H_{\chi_1^\pm \chi_2^0}$ and H_{SM}, are $e^+\mu^+\not\!\!E_T$ and $e^-\mu^-\not\!\!E_T$. The QUAERO package identifies the most discriminating variable as the transverse mass of the leading muon and the missing energy; it builds a discriminant as described in Section 9.2.1 and divides it into four bins of increasing sensitivity. Figure 9.17 shows the resulting binned discriminant for the $e^-\mu^-\not\!\!E_T$ final state; as we expect, the bin with the largest values of the discriminant contains the largest difference between the two hypotheses.

Figure 9.18 shows the combined discriminant, including all contributing final states. The $\chi_1^\pm \chi_2^0$ hypothesis predicts additional events above the background of the

Standard Model; no events are seen, and the result of the statistical experiment slightly favors the Standard Model by a relative probability of

$$L = \frac{P(Data|H)}{P(Data|SM)} = 0.89$$

We explore the shape of the probability as it varies with the cross-section of $p\overline{p} \to \chi_1^{\pm}\chi_2^0$. Figure 9.19 shows results of tests at varying cross-sections. A small peak is evident, representing an insignificant excess of data over the Standard Model backgrounds.

$p\overline{p} \to \chi_1^+\chi_1^-$

Pair production of charginos is the supersymmetric analogy to Standard Model production of WW pairs. It is separated from Z and misidentification backgrounds by its large missing transverse energy, and distinguished from $t\bar{t}$ production by its relatively few jets.

The cleanest final states for searching for $\chi_1^+\chi_1^-$ production are therefore $e^+\mu^-\not\!\!E_T$ and $e^-\mu^+\not\!\!E_T$, where we explicitly exclude events with jets. Table 9.8 and Figure 9.20 show the events in the data which have no reconstructed jets and detail the Standard Model contributions. At large $\not\!\!E_T$, the dominant background is WW production.

QUAERO chooses the most discriminating variable to be the angle between the two leptons; given the significant missing energy expected in $\chi_1^+\chi_1^-$ events, the lep-

Cut	Data	Total BG	MisID	$WW, WZ, W\gamma$	$Z \to \tau\overline{\tau}$	$t\overline{t}$
$N_{Jets} = 0$	33	$27.35^{\pm 0.79(stat)}_{\pm 1.46(syst)}$	$3.12^{\pm 0.66}_{\pm 0.31}$	$3.691^{\pm 0.08}_{\pm 0.21}$	$20.52^{\pm 0.43}_{\pm 1.41}$	$0.03^{\pm 0.01}_{\pm 0.01}$
$\not\!\!E_T > 10$	14	$12.61^{\pm 0.50(stat)}_{\pm 0.56(syst)}$	$2.26^{\pm 0.48}_{\pm 0.23}$	$3.464^{\pm 0.07}_{\pm 0.19}$	$6.86^{\pm 0.15}_{\pm 0.47}$	$0.03^{\pm 0.01}_{\pm 0.01}$
$\not\!\!E_T > 20$	4	$5.34^{\pm 0.30(stat)}_{\pm 0.23(syst)}$	$1.41^{\pm 0.30}_{\pm 0.14}$	$2.962^{\pm 0.06}_{\pm 0.17}$	$0.95^{\pm 0.02}_{\pm 0.07}$	$0.02^{\pm 0.01}_{\pm 0.01}$
$\not\!\!E_T > 30$	3	$3.46^{\pm 0.21(stat)}_{\pm 0.16(syst)}$	$0.95^{\pm 0.20}_{\pm 0.10}$	$2.389^{\pm 0.05}_{\pm 0.13}$	$0.09^{\pm 0.01}_{\pm 0.01}$	$0.02^{\pm 0.01}_{\pm 0.01}$
$\not\!\!E_T > 40$	2	$2.41^{\pm 0.13(stat)}_{\pm 0.12(syst)}$	$0.59^{\pm 0.12}_{\pm 0.06}$	$1.779^{\pm 0.04}_{\pm 0.10}$	$0.03^{\pm 0.01}_{\pm 0.01}$	$0.02^{\pm 0.01}_{\pm 0.01}$

Table 9.8: Data and backgrounds at each cut on $\not\!\!E_T$, for events with no reconstructed jets.

tons are less likely to be directly opposite each other than in events with less missing energy. Figure 9.21 shows the distribution of events for the Standard Model and for the hypothesis $H_{\chi_1^+\chi_1^-}$, and the selection of small relative angle as the most senstive region.

$p\overline{p} \to \tilde{t}_1^+\tilde{t}_1^-$

The production of $\tilde{t}_1^+\tilde{t}_1^-$ mirrors Standard Model $t\overline{t}$ production. Its signal is disentangled from the backgrounds in a similar way, by requiring two reconstructed jets and missing energy. The most sensitive final states to this process are $e^-\mu^+\not\!\!E_T jj$ and $e^+\mu^-\not\!\!E_T jj$. Table 9.9 and Figure 9.22 detail the events in the data with two reconstructed jets and the expected contributions from Standard Model processes.

QUAERO chooses the most discriminating variable to be the angle between the muon and the missing energy in the event. Indeed, the distribution of $H_{\tilde{t}\tilde{t}}$ shows a significant peak near $\Delta(\phi, \not\!\!E_T) \approx 0$ where the Standard Model is flat.

Cut	Data	All	MisID	$WW, WZ, W\gamma$	$Z \to \tau\overline{\tau}$	$t\bar{t}$
Initial Sel.	44	$37.86^{\pm 0.35}_{\pm 2.09}$	$4.85^{\pm 0.15}_{\pm 1.02}$	$4.58^{\pm 0.10}_{\pm 0.26}$	$26.05^{\pm 0.28}_{\pm 1.79}$	$2.39^{\pm 0.10}_{\pm 0.13}$
$N_{jets}^{P_T>15} \geq 2$	4	$3.23^{\pm 0.34}_{\pm 0.17}$	$0.49^{\pm 0.10}_{\pm 0.10}$	$0.11^{\pm 0.01}_{\pm 0.01}$	$0.68^{\pm 0.04}_{\pm 0.05}$	$1.95^{\pm 0.08}_{\pm 0.11}$
$\not\!\!E_T > 10$	4	$2.99^{\pm 0.30}_{\pm 0.15}$	$0.42^{\pm 0.09}_{\pm 0.09}$	$0.10^{\pm 0.01}_{\pm 0.01}$	$0.56^{\pm 0.04}_{\pm 0.04}$	$1.91^{\pm 0.01}_{\pm 0.11}$

Table 9.9: Data and backgrounds at each level of selection, with statistical and systematic errors.

Tests with Multiple Processes

Each supersymmetric process allows us to probe the mSUGRA model space. The prediction of a specific model for each process are not independent; mSUGRA is a coherent theory which predicts the existence of all three processes simultaneously. We can therefore extend our sensitivity by constructiong a combined hypothesis,

$$H_{mSUGRA} = H_{\chi_1^\pm \chi_2^0} \wedge H_{\chi_1^+ \chi_1^-} \wedge H_{\tilde{t}_1^+ \tilde{t}_1^-}$$

with which we can probe the $mSUGRA$ parameter space with our maximal sensitivity.

Limits

Figure 9.24 shows the limits set on various mSUGRA hypotheses, varying $m_{\frac{1}{2}}$ as probed by the $\chi_1^\pm \chi_2^0$ production. As we expect, the limit on the cross section improves as the selection efficiency (Table 9.1) increases with $m_{\frac{1}{2}}$. As a benchmark of the sensitivity of the likelihood ratio limit using the QUAERO package, we present as well limits

set using a Bayesian limit calculator [42, 43] based on straightforward analyses of the like-signed and three-lepton final states.

Where the theoretically predicted cross-section is above our limit, we can exclude the mSUGRA hypothesis at 95% confidence. Figures 9.25 and 9.26 show limits on $\chi_1^+\chi_1^-$ and $\tilde{t}_1^+\tilde{t}_1^-$ production. Figure 9.27 shows the 95% limit that these processes allow us to place on mSUGRA models, as a function of m_0=$m_{\frac{1}{2}}$. Figure 9.28 shows the exclusion in the $m_0, m_{\frac{1}{2}}$ plane, and Figure 9.29 gives the same for negative values of the mSUGRA parameter μ.

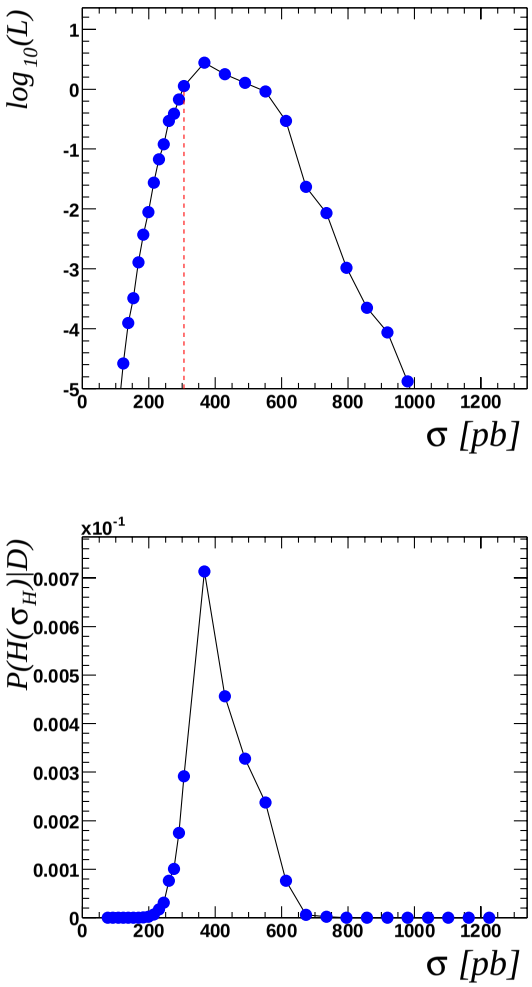

Figure 9.14: Measurement of $Z/\gamma^* \to \tau\tau$ production. The red line indicates the Standard Model value.

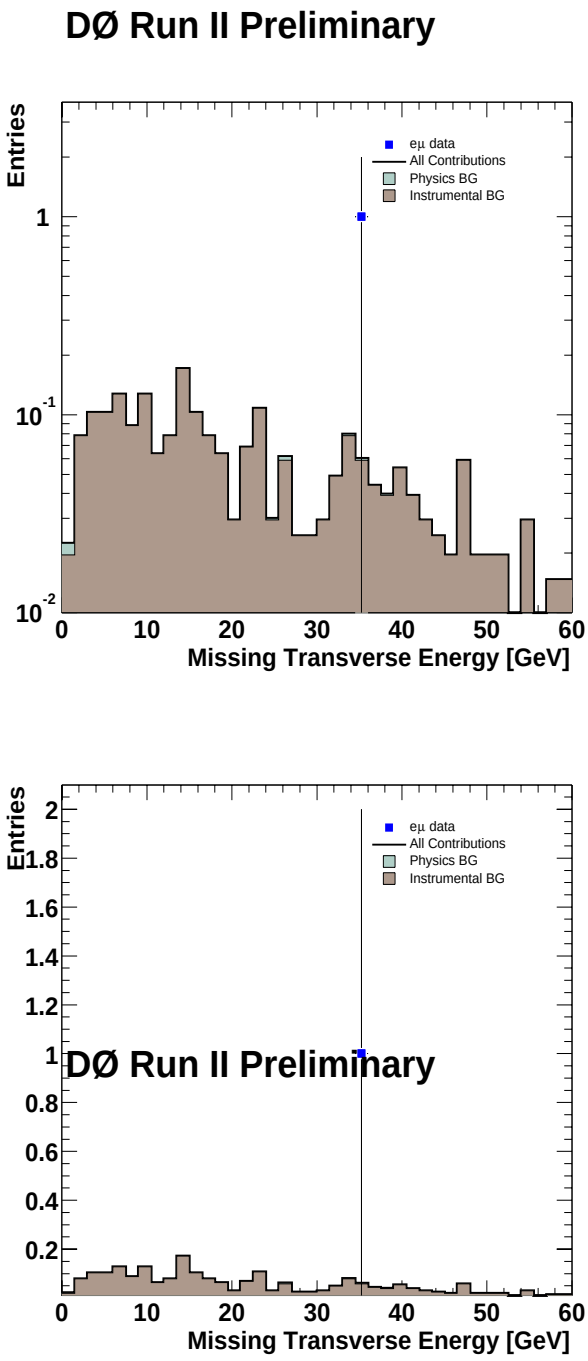

Figure 9.15: Data and expected backgrounds in like-signed $e\mu$ events.

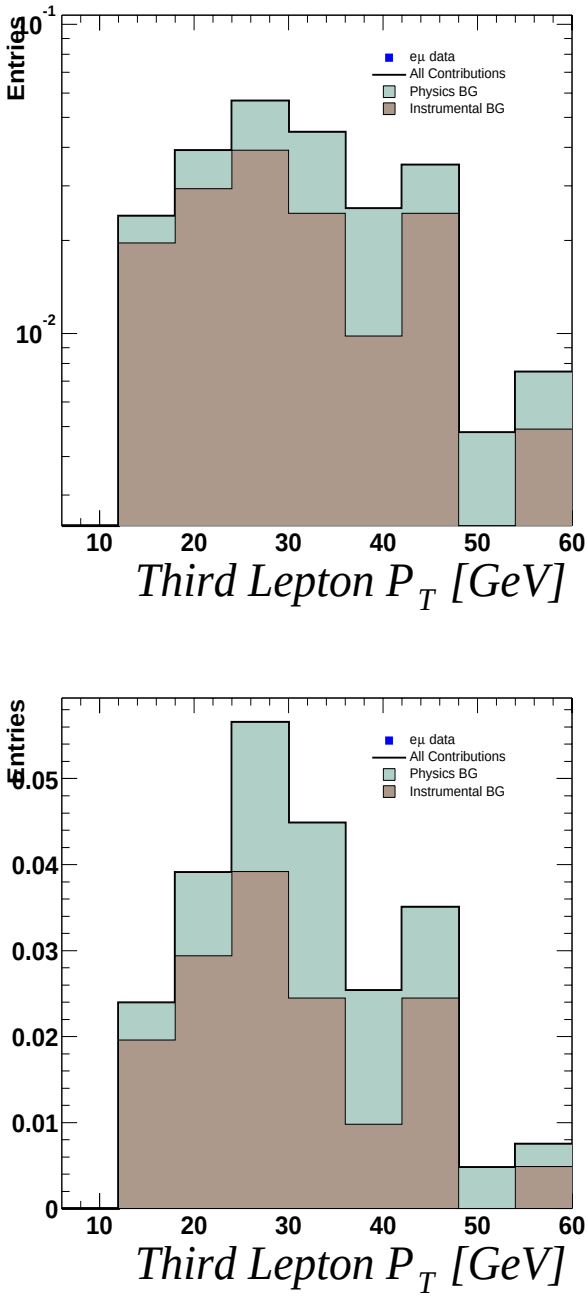

Figure 9.16: Estimation of contributions to trilepton final state. No events are seen in the data

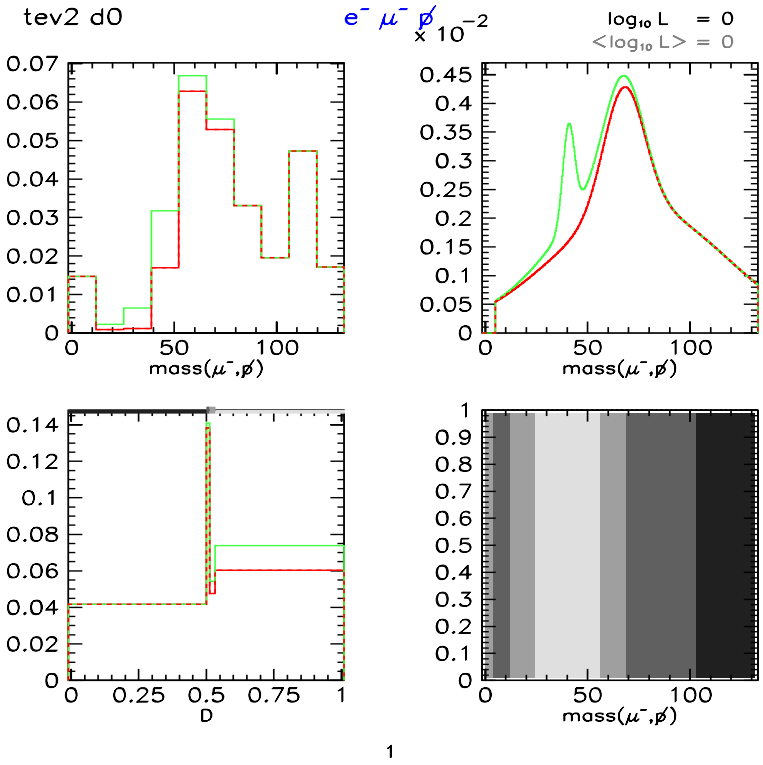

Figure 9.17: Test of the hypothesis $H_{\chi_1^\pm \chi_2^0}$ with $m_0, m_{\frac{1}{2}} = 150$ GeV in the $e^+\mu^+\not{E}_T$ final state. Clockwise from top left: histogrammed events in the selected variable for the Standard Model (*red*) and the new physics hypothesis (*green*); probability densities for each hypothesis; subregions of the variable determined by placing cuts on the discriminant; and binned values of the discriminant for SM and new physics.

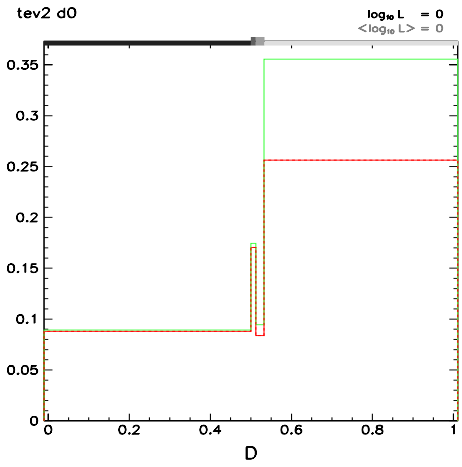

Figure 9.18: Histogram of the discriminant for the Standard Model (*red*) and the new physics $H_{\chi_1^\pm \chi_2^0}$with $m_0, m_{\frac{1}{2}} = 150$ GeV (*red*). All contributing final states have been combined.

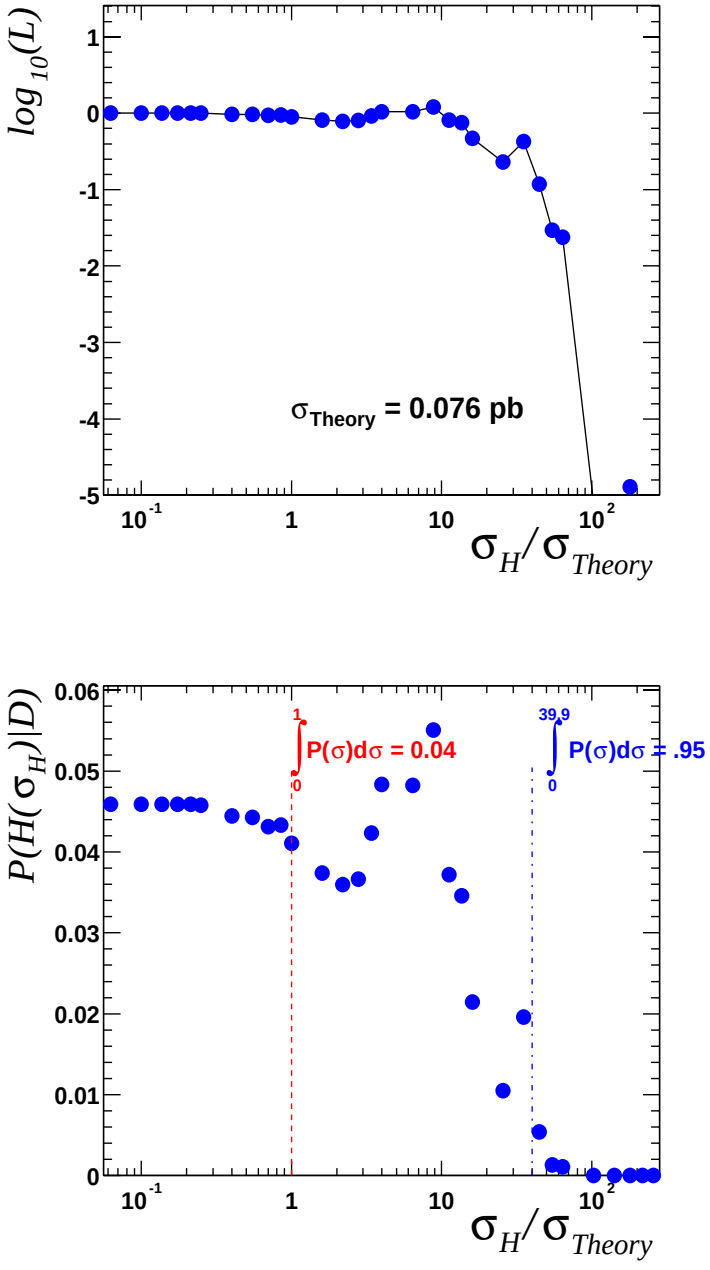

Figure 9.19: Tests of the hypothesis $H_{\chi_1^\pm \chi_2^0}$with $m_0, m_{\frac{1}{2}} = 150$ GeV, at varying cross-sections, relative to the theoretical prediction.

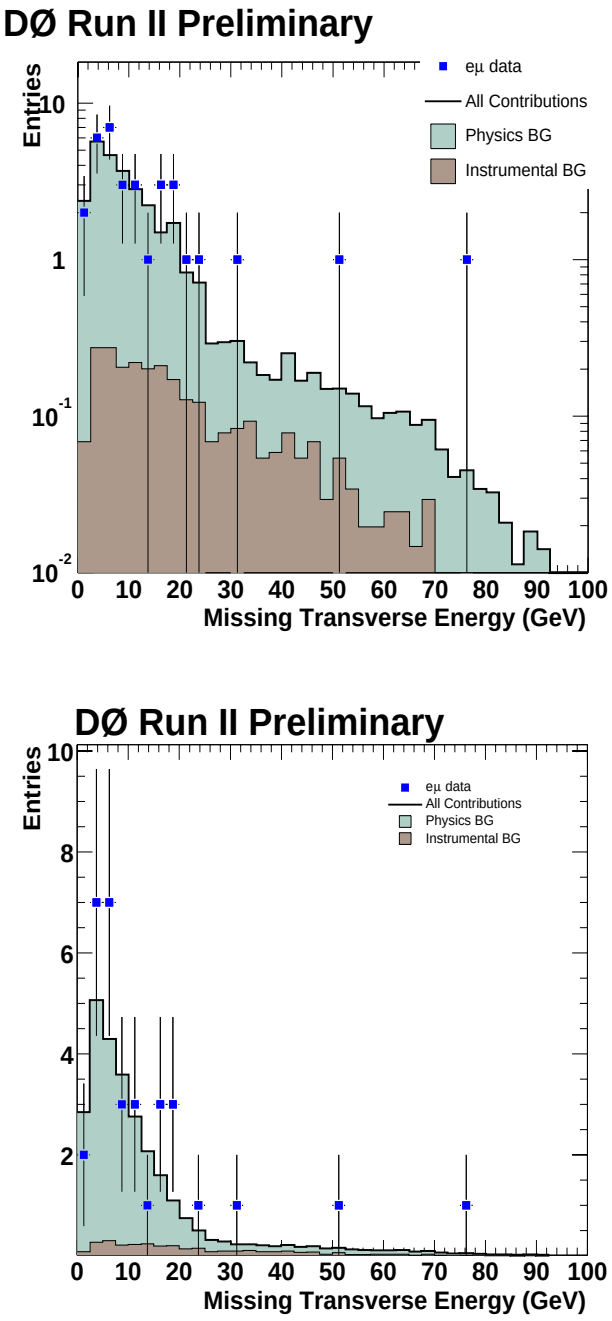

Figure 9.20: Missing transverse energy in $e\mu$ events with no jets, for data and backgrounds in both log and linear scales.

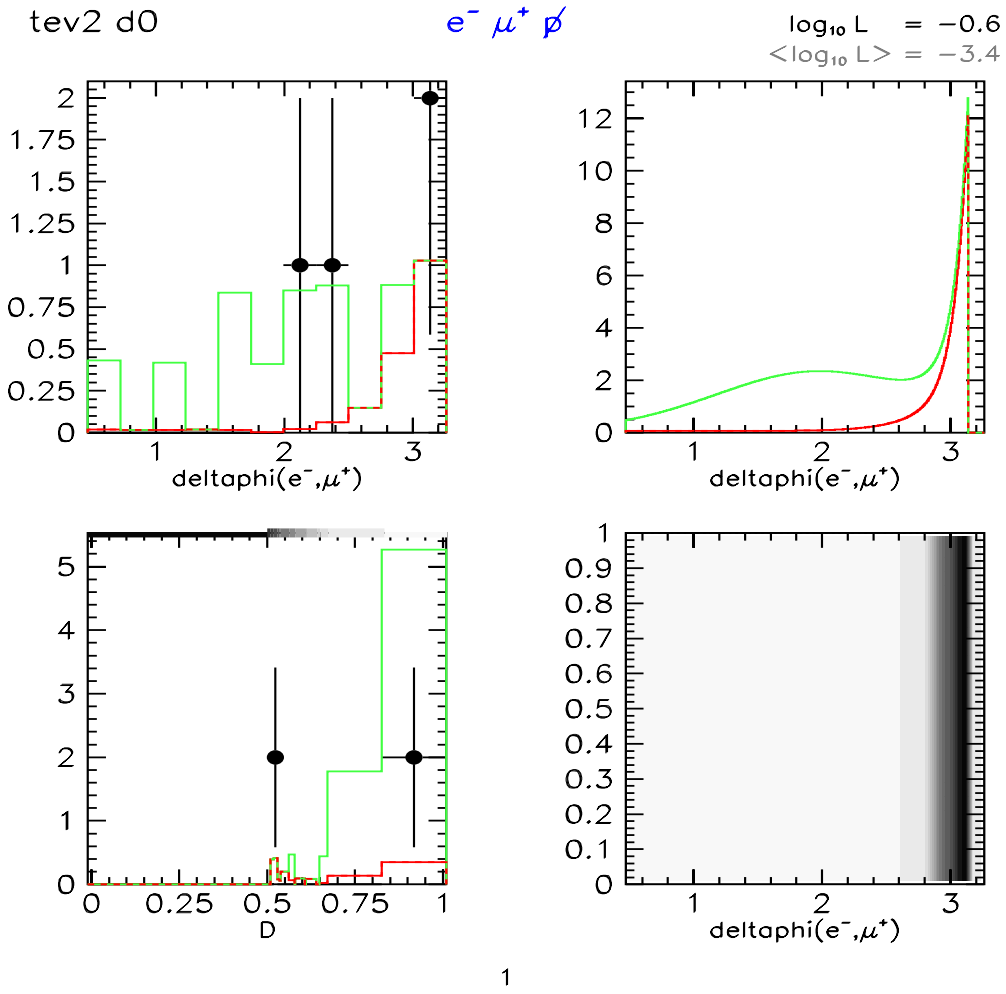

Figure 9.21: Test of the hypothesis $H_{\chi_1^+\chi_1^-}$ with $m_0, m_{\frac{1}{2}} = 150$ GeV in the $e^-\mu^+\not{E}_T$ final state. Clockwise from top left: histogrammed events in the selected variable for the Standard Model (*red*) and the new physics hypothesis (*green*); probability densities for each hypothesis; subregions of the variable determined by placing cuts on the discriminant; and binned values of the discriminant for SM and new physics.

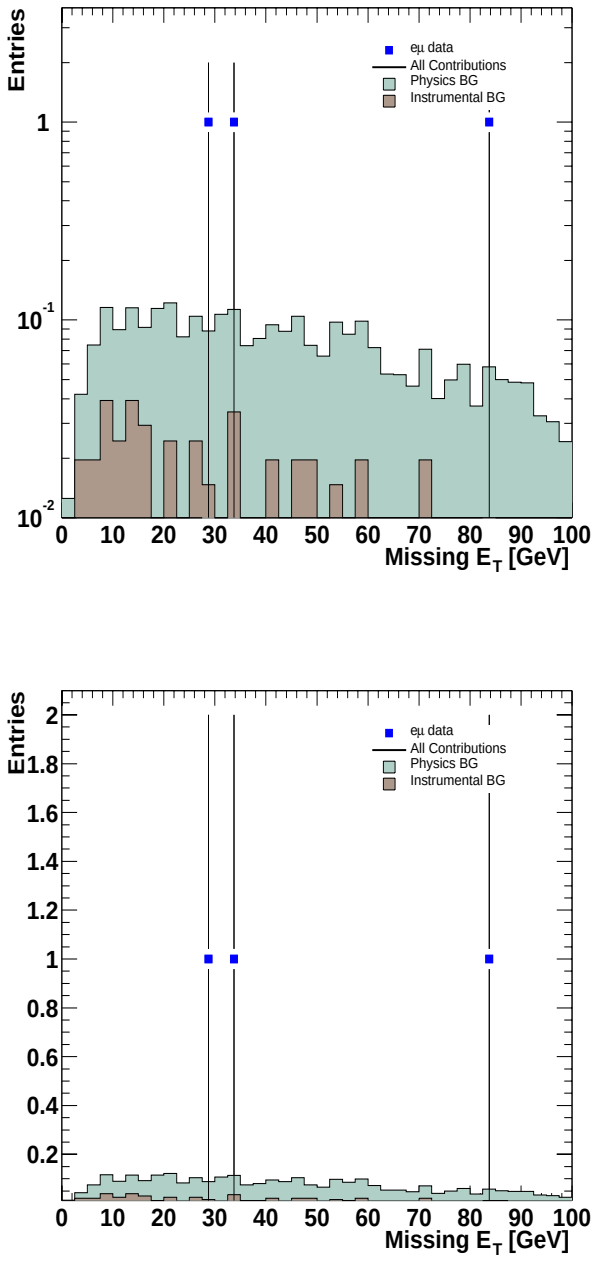

Figure 9.22: Missing transverse energy in $e\mu$ events with 2 reconstructed jets, for data and backgrounds in both log and linear scales.

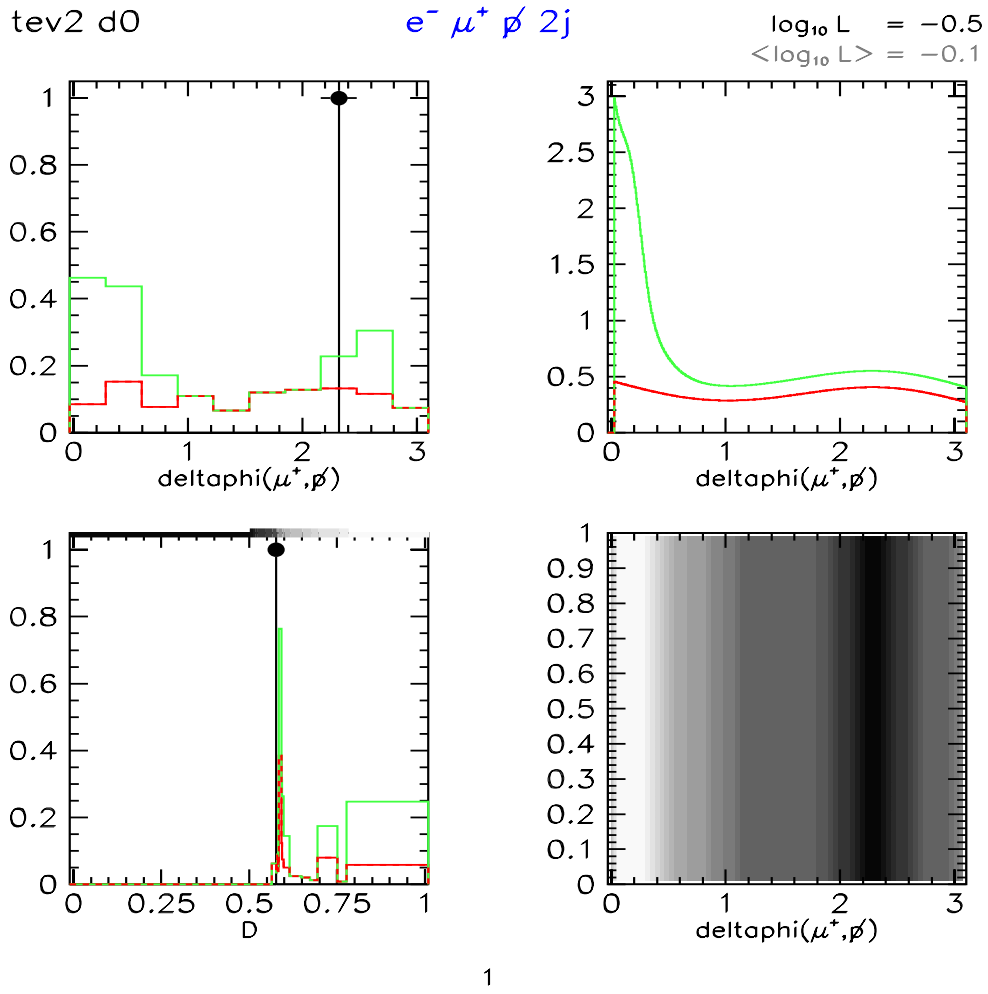

Figure 9.23: Test of the hypothesis $H_{\tilde{t}\tilde{t}}$ with $m_0, m_{\frac{1}{2}} = 150$ GeV in the $e^-\mu^+\not{E}_T jj$ final state. Clockwise from top left: histogrammed events in the selected variable for the Standard Model (*red*) and the new physics hypothesis (*green*); probability densities for each hypothesis; subregions of the variable determined by placing cuts on the discriminant; and binned values of the discriminant for SM and new physics.

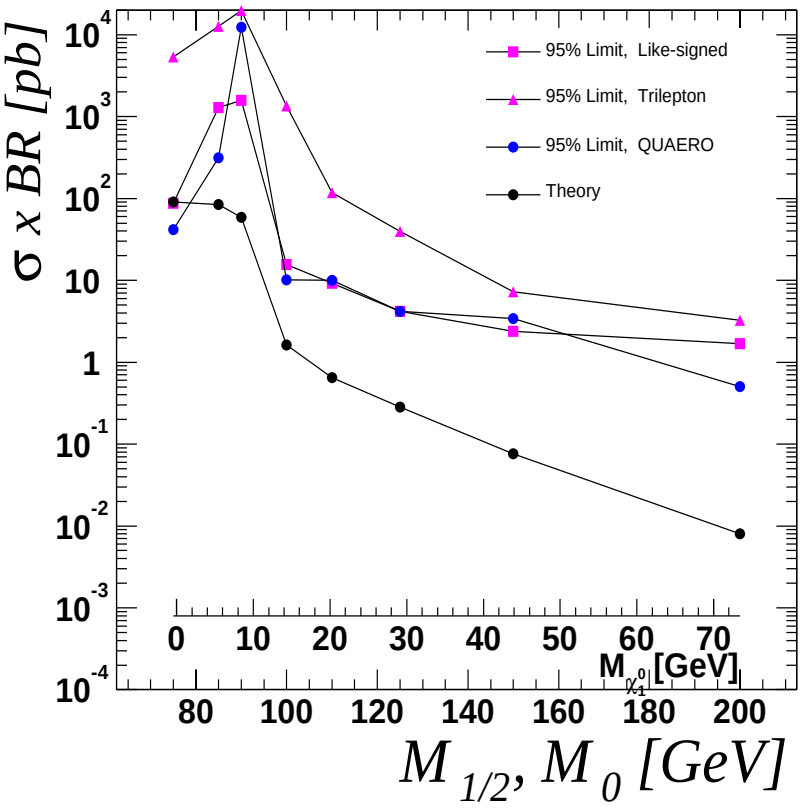

Figure 9.24: Limits on $\sigma_{\chi_1^\pm \chi_2^0}$. $m_0 = m_{\frac{1}{2}}$.

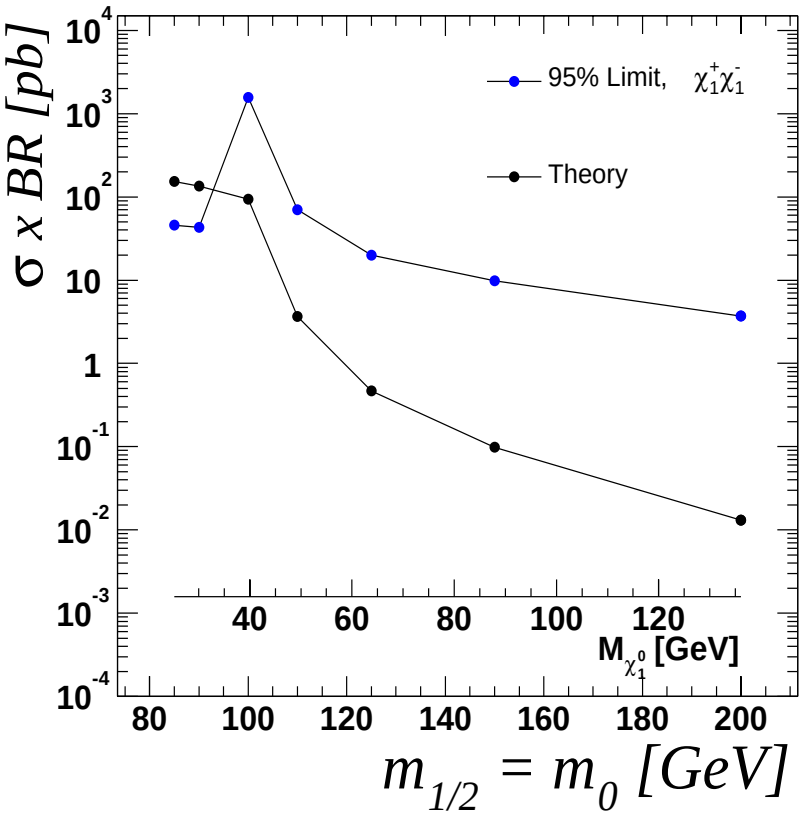

Figure 9.25: Limits on $\sigma_{\chi_1^+\chi_1^-} \times BR(e\mu)$. $m_0 = m_{\frac{1}{2}}$.

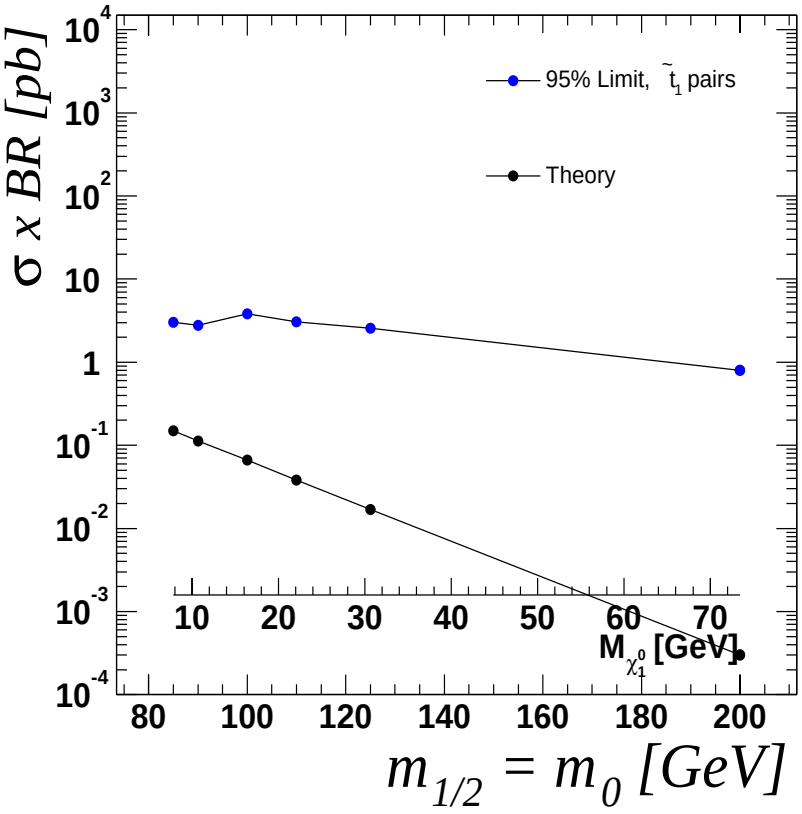

Figure 9.26: Limits on $\sigma_{\tilde{t}_1^+\tilde{t}_1^-} \times BR(e\mu)$. $m_0 = m_{\frac{1}{2}}$.

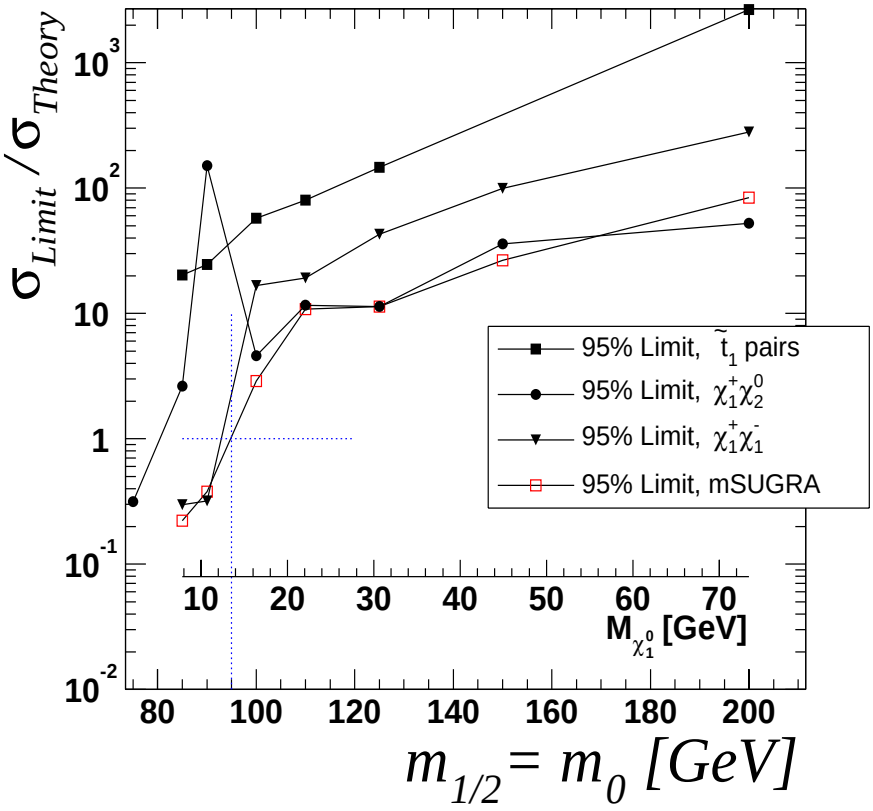

Figure 9.27: Limits on mSUGRA with varying parameters $m_0 = m_{\frac{1}{2}}$.

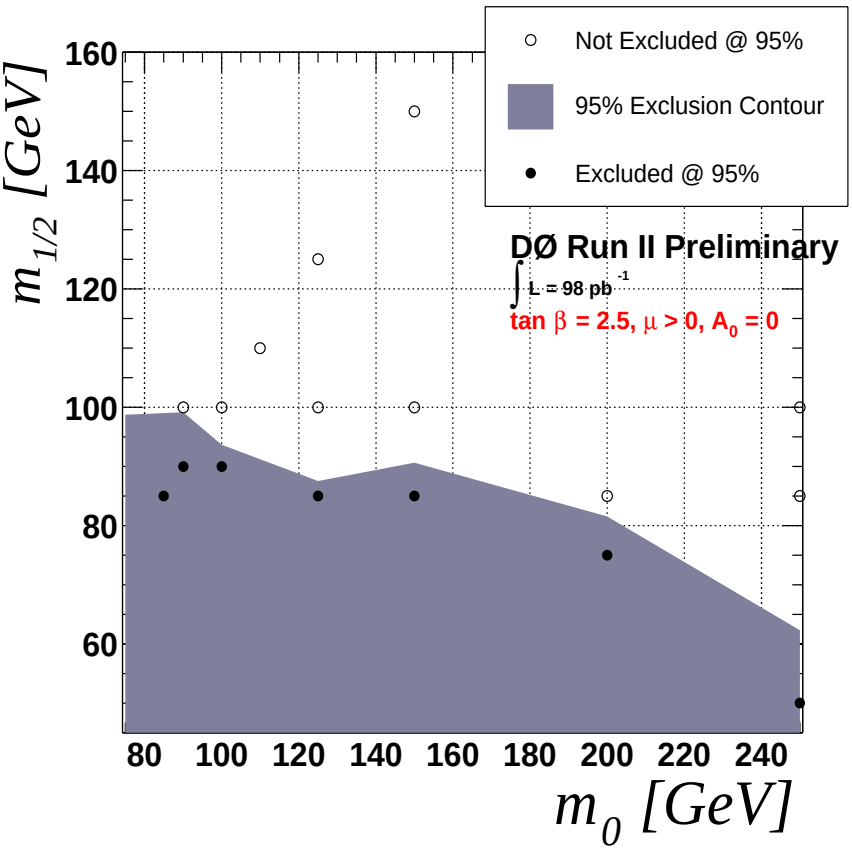

Figure 9.28: Limits on mSUGRA with $\mu > 0$ in the $m_0, m_{\frac{1}{2}}$ plane.

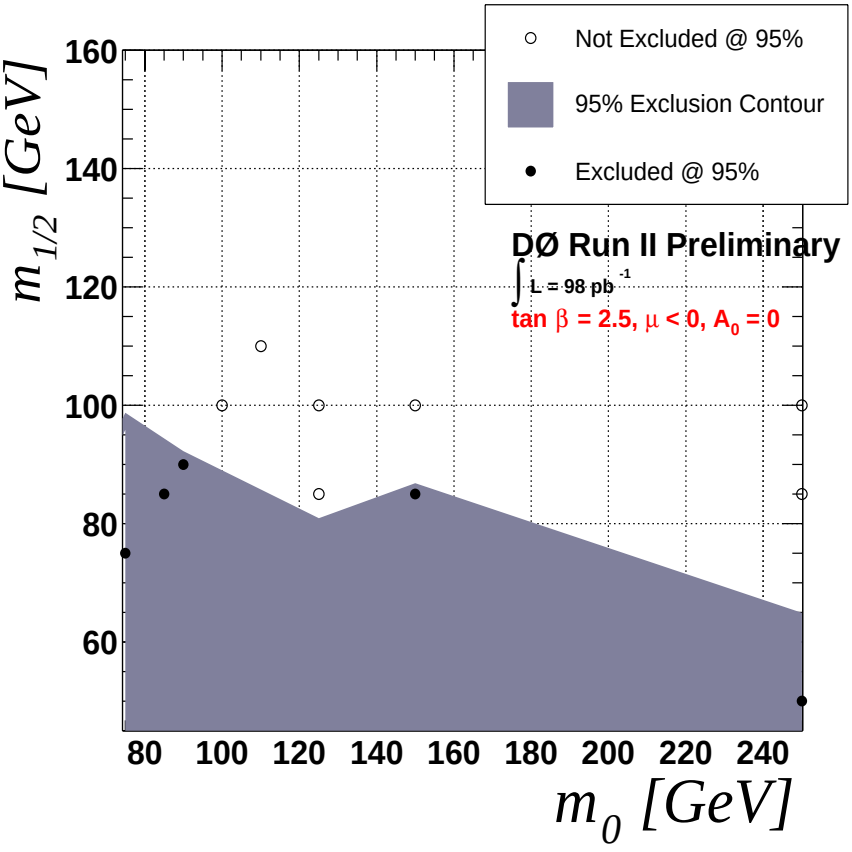

Figure 9.29: Limits on mSUGRA with $\mu < 0$ in the $m_0, m_{\frac{1}{2}}$ plane.

9.3.4 Discussion

These limits extend the exclusion in the $m_0, m_{\frac{1}{2}}$ plane of previous Tevatron searches using leptonic channels, see Figure 9.30. Other signatures have been more powerful.

At the Tevatron, DØ and CDF have searched for squarks and gluinos with the signature of jets and large missing transverse energy, allowing both to exclude regions in the $m_0, m_{\frac{1}{2}}$ plane, see Figure 9.31.

Tevatron limits have been eclipsed by searches at LEP. The lack of observation of direct $\chi_1^+\chi_1^-$ production and searches for hZ production provide stringent limits on in the $m_0, m_{\frac{1}{2}}$ plane, see Figure 9.32. These limits require the mass of the χ_1^0 to exceed 49 GeV [39], see Figure 9.33.

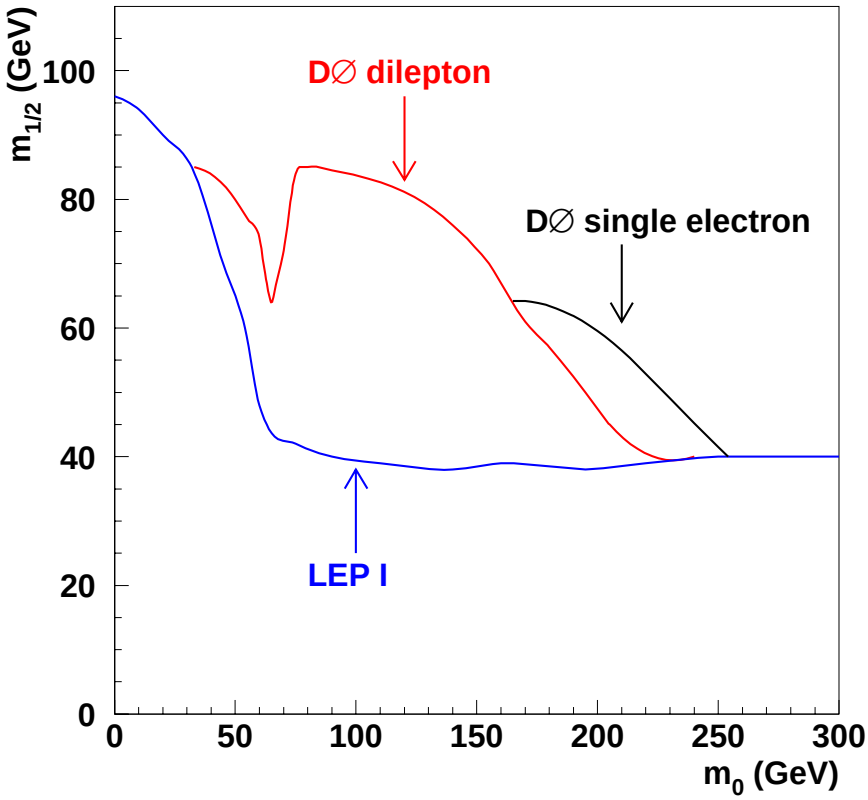

Figure 9.30: Exclusions in the $m_0, m_{\frac{1}{2}}$ using dilepton and electron+jets signatures in Run1, from [75].

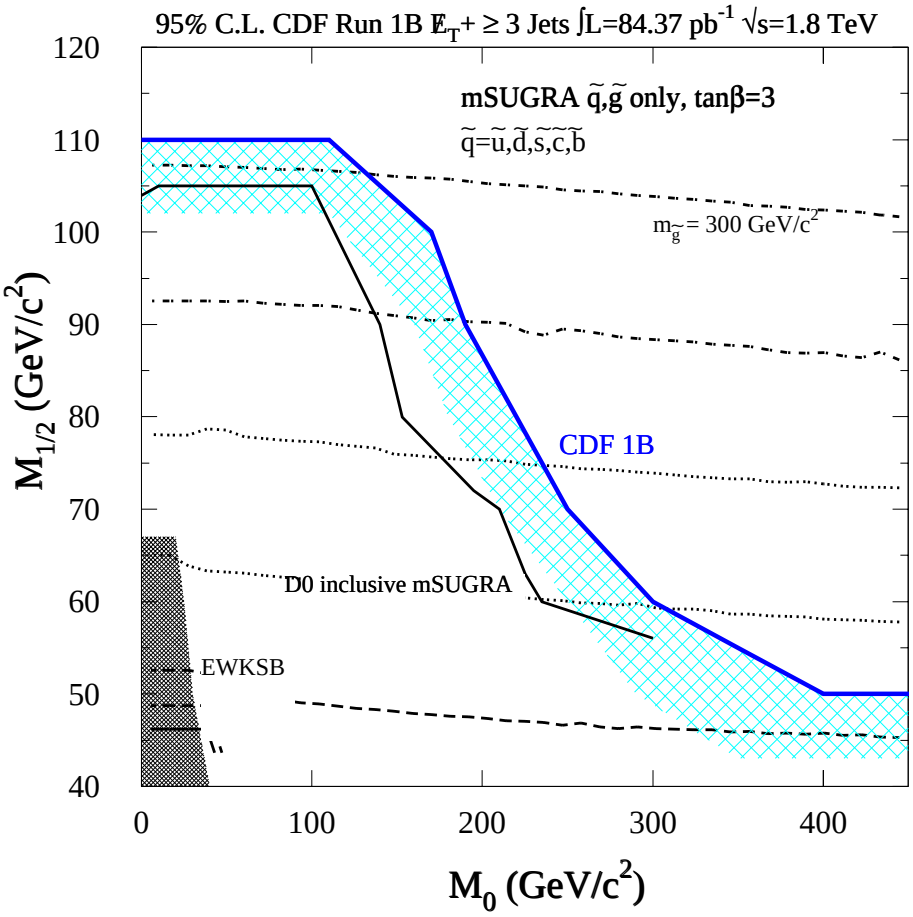

Figure 9.31: Exclusions in the $m_0, m_{\frac{1}{2}}$ plane using jets and $\not\!\!E_T$ signatures in Run1, from [74].

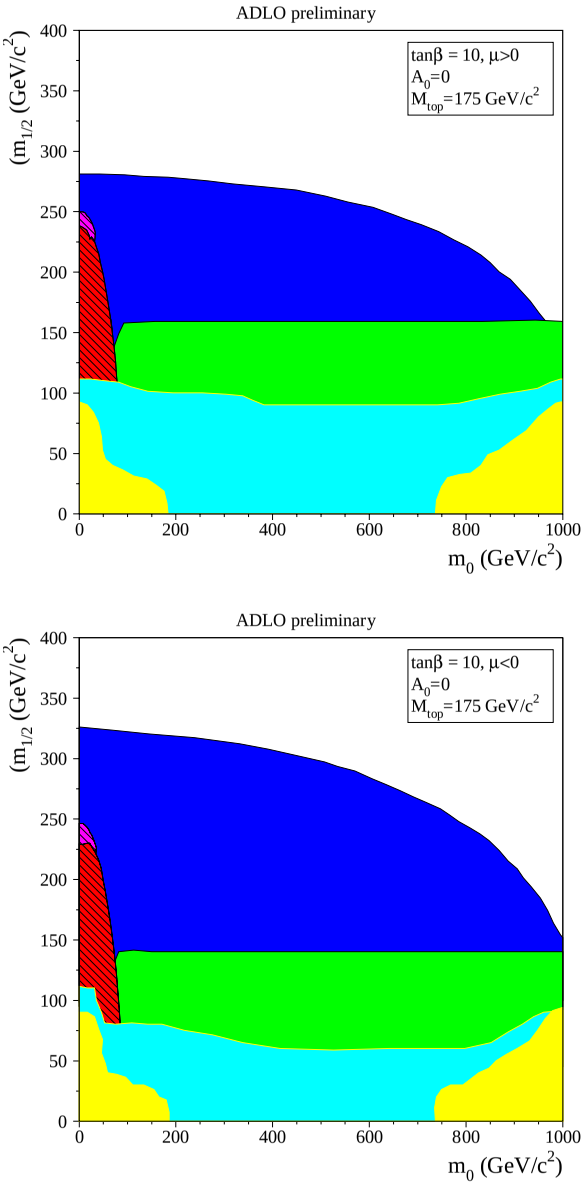

Figure 9.32: Exclusions in the $m_0, m_{\frac{1}{2}}$, based primarily on searches for hZ (*dark blue*), $\chi\chi$ (*green*), and precision electroweak requirements (*light blue*), from [39].

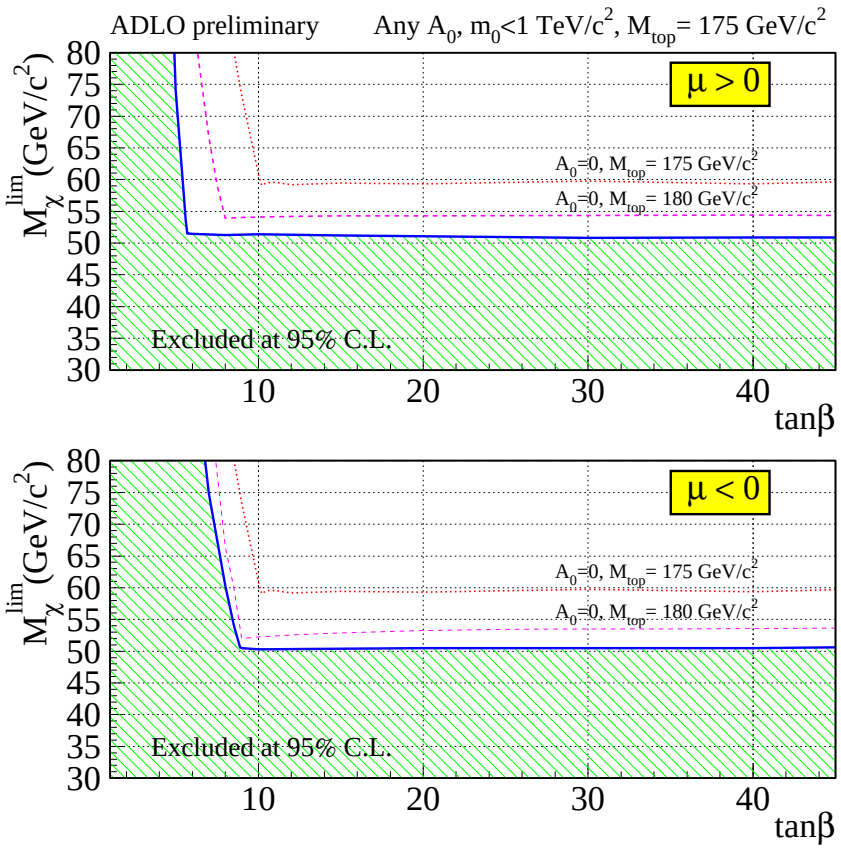

Figure 9.33: Limits on the mass of the lightest supersymmetic particle, derived from limits on $m_{\frac{1}{2}}$, from [39].

9.4 Search for Unanticipated Exotic Processes

The Standard Model is a very successful theory, but it fails in important ways that demonstrate that there must be a theory more fundamental. The theoretical community has constructed alternatives which predict unobserved particles and interactions. While some of these theories make specific and compelling predictions, others predict an uncertain and broad spectrum of particles with little theoretical guidance. Searching for evidence of these predictions is an important part of the dialog between theoretical and experimental physics; just as important, however, is to carefully examine the experimental data for evidence of unanticipated new particles.

Our prediction of the Standard Model contributions to the $e\mu$ final state allows us to search for evidence of new physics in the data which would appear as an excess of events in some region of kinematic space.

We conduct our search in an extremely general manner, by searching for a sheer excess. We focus on the quantity of missing energy in the event, as a kinematic quantity which is likely to be sensitive to new physics. The data set is divided into exclusive states according to jet multiplicity. We consider events only in the populated final states: $e\mu$, $e\mu j$ and $e\mu jj$.

We are not limited to searching for an excess of events in an entire exclusive final state; we employ an increasing missing energy threshold, hoping to isolate any

Cut	Data	Total BG	MisID	$WW, WZ, W\gamma$	$Z \to \tau\overline{\tau}$	$t\bar{t}$
$\not\!\!E_T > 0$	33	$27.35^{\pm 0.79(stat)}_{\pm 1.46(syst)}$	$3.12^{\pm 0.66}_{\pm 0.31}$	$3.69^{\pm 0.08}_{\pm 0.21}$	$20.52^{\pm 0.43}_{\pm 1.41}$	$0.03^{\pm 0.01}_{\pm 0.01}$
$\not\!\!E_T > 5$	24	$20.09^{\pm 0.66(stat)}_{\pm 1.00(syst)}$	$2.77^{\pm 0.59}_{\pm 0.28}$	$3.64^{\pm 0.08}_{\pm 0.20}$	$13.66^{\pm 0.29}_{\pm 0.94}$	$0.03^{\pm 0.01}_{\pm 0.01}$
$\not\!\!E_T > 10$	14	$12.61^{\pm 0.50(stat)}_{\pm 0.56(syst)}$	$2.26^{\pm 0.48}_{\pm 0.23}$	$3.46^{\pm 0.07}_{\pm 0.19}$	$6.86^{\pm 0.15}_{\pm 0.47}$	$0.03^{\pm 0.01}_{\pm 0.01}$
$\not\!\!E_T > 15$	10	$8.03^{\pm 0.39(stat)}_{\pm 0.33(syst)}$	$1.80^{\pm 0.38}_{\pm 0.18}$	$3.23^{\pm 0.07}_{\pm 0.18}$	$2.97^{\pm 0.06}_{\pm 0.20}$	$0.03^{\pm 0.01}_{\pm 0.01}$
$\not\!\!E_T > 20$	4	$5.34^{\pm 0.30(stat)}_{\pm 0.23(syst)}$	$1.41^{\pm 0.30}_{\pm 0.14}$	$2.96^{\pm 0.06}_{\pm 0.17}$	$0.95^{\pm 0.02}_{\pm 0.07}$	$0.02^{\pm 0.01}_{\pm 0.01}$
$\not\!\!E_T > 25$	3	$4.15^{\pm 0.24(stat)}_{\pm 0.19(syst)}$	$1.12^{\pm 0.24}_{\pm 0.11}$	$2.69^{\pm 0.06}_{\pm 0.15}$	$0.31^{\pm 0.01}_{\pm 0.02}$	$0.02^{\pm 0.01}_{\pm 0.01}$
$\not\!\!E_T > 30$	3	$3.46^{\pm 0.21(stat)}_{\pm 0.16(syst)}$	$0.95^{\pm 0.20}_{\pm 0.10}$	$2.39^{\pm 0.05}_{\pm 0.13}$	$0.09^{\pm 0.01}_{\pm 0.01}$	$0.02^{\pm 0.01}_{\pm 0.01}$
$\not\!\!E_T > 35$	2	$2.90^{\pm 0.16(stat)}_{\pm 0.14(syst)}$	$0.75^{\pm 0.16}_{\pm 0.07}$	$2.09^{\pm 0.04}_{\pm 0.12}$	$0.04^{\pm 0.01}_{\pm 0.01}$	$0.02^{\pm 0.01}_{\pm 0.01}$
$\not\!\!E_T > 40$	2	$2.41^{\pm 0.13(stat)}_{\pm 0.12(syst)}$	$0.59^{\pm 0.12}_{\pm 0.06}$	$1.78^{\pm 0.04}_{\pm 0.10}$	$0.03^{\pm 0.01}_{\pm 0.01}$	$0.02^{\pm 0.01}_{\pm 0.01}$

Table 9.10: Data and backgrounds at each cut on $\not\!\!E_T$, for events with no reconstructed jets.

potential excess at high missing energy.

For the events in which no jets were reconstructed, the missing energy is shown in Figure 9.34. The number of events after successive cuts on the $\not\!\!E_T$, and the contributions from each source, are listed in Table 9.10. Missing energy distributions and specific yields in the portion of the data with a single jet are shown in Figure 9.35; those for events with two jets are shown in Figure 9.36.

Statistical errors are dominated by uncertainty in the efficiencies. Systematic errors are dominated by the calculation of the k-factor of the $Z \to \tau\tau$ process, see Section 6.2.3.

Given the rough agreement of the data and the background in the $e\mu$ final state,

Cut	Data	Total BG	MisID	$WW, WZ, W\gamma$	$Z \to \tau\overline{\tau}$	$t\bar{t}$
$\not\!\!E_T > 0$	7	$6.45^{\pm 0.27(stat)}_{\pm 0.27(syst)}$	$1.22^{\pm 0.26}_{\pm 0.12}$	$0.76^{\pm 0.02}_{\pm 0.04}$	$4.14^{\pm 0.09}_{\pm 0.23}$	$0.34^{\pm 0.01}_{\pm 0.02}$
$\not\!\!E_T > 10$	6	$5.29^{\pm 0.22(stat)}_{\pm 0.21(syst)}$	$1.00^{\pm 0.21}_{\pm 0.10}$	$0.73^{\pm 0.02}_{\pm 0.04}$	$3.23^{\pm 0.07}_{\pm 0.18}$	$0.33^{\pm 0.01}_{\pm 0.02}$
$\not\!\!E_T > 20$	5	$3.15^{\pm 0.14(stat)}_{\pm 0.12(syst)}$	$0.65^{\pm 0.14}_{\pm 0.06}$	$0.64^{\pm 0.01}_{\pm 0.04}$	$1.55^{\pm 0.04}_{\pm 0.09}$	$0.32^{\pm 0.01}_{\pm 0.02}$
$\not\!\!E_T > 30$	4	$1.86^{\pm 0.10(stat)}_{\pm 0.07(syst)}$	$0.45^{\pm 0.09}_{\pm 0.04}$	$0.52^{\pm 0.01}_{\pm 0.03}$	$0.60^{\pm 0.02}_{\pm 0.03}$	$0.29^{\pm 0.01}_{\pm 0.02}$
$\not\!\!E_T > 40$	3	$1.18^{\pm 0.06(stat)}_{\pm 0.04(syst)}$	$0.26^{\pm 0.05}_{\pm 0.03}$	$0.40^{\pm 0.01}_{\pm 0.02}$	$0.27^{\pm 0.01}_{\pm 0.02}$	$0.24^{\pm 0.01}_{\pm 0.01}$
$\not\!\!E_T > 50$	2	$0.78^{\pm 0.04(stat)}_{\pm 0.03(syst)}$	$0.16^{\pm 0.03}_{\pm 0.02}$	$0.28^{\pm 0.01}_{\pm 0.02}$	$0.14^{\pm 0.01}_{\pm 0.01}$	$0.20^{\pm 0.01}_{\pm 0.01}$
$\not\!\!E_T > 60$	0	$0.49^{\pm 0.02(stat)}_{\pm 0.02(syst)}$	$0.08^{\pm 0.02}_{\pm 0.01}$	$0.18^{\pm 0.01}_{\pm 0.01}$	$0.09^{\pm 0.01}_{\pm 0.01}$	$0.14^{\pm 0.01}_{\pm 0.01}$
$\not\!\!E_T > 70$	0	$0.28^{\pm 0.01(stat)}_{\pm 0.01(syst)}$	$0.04^{\pm 0.01}_{\pm 0.01}$	$0.10^{\pm 0.01}_{\pm 0.01}$	$0.04^{\pm 0.01}_{\pm 0.01}$	$0.10^{\pm 0.01}_{\pm 0.01}$
$\not\!\!E_T > 80$	0	$0.15^{\pm 0.01(stat)}_{\pm 0.01(syst)}$	$0.01^{\pm 0.01}_{\pm 0.01}$	$0.05^{\pm 0.01}_{\pm 0.01}$	$0.02^{\pm 0.01}_{\pm 0.01}$	$0.06^{\pm 0.01}_{\pm 0.01}$

Table 9.11: Data and backgrounds at each level of selection, for events with a single reconstructed jet.

Cut	Data	Total BG	MisID	$WW, WZ, W\gamma$	$Z \to \tau\overline{\tau}$	$t\bar{t}$
$\not\!\!E_T > 0$	4	$2.40^{\pm 0.10(stat)}_{\pm 0.09(syst)}$	$0.37^{\pm 0.08}_{\pm 0.04}$	$0.093^{\pm 0.00}_{\pm 0.01}$	$0.58^{\pm 0.02}_{\pm 0.03}$	$1.35^{\pm 0.05}_{\pm 0.08}$
$\not\!\!E_T > 11$	4	$2.15^{\pm 0.08(stat)}_{\pm 0.08(syst)}$	$0.29^{\pm 0.06}_{\pm 0.03}$	$0.089^{\pm 0.00}_{\pm 0.00}$	$0.45^{\pm 0.01}_{\pm 0.03}$	$1.31^{\pm 0.05}_{\pm 0.07}$
$\not\!\!E_T > 22$	4	$1.78^{\pm 0.07(stat)}_{\pm 0.07(syst)}$	$0.22^{\pm 0.05}_{\pm 0.02}$	$0.079^{\pm 0.00}_{\pm 0.00}$	$0.27^{\pm 0.01}_{\pm 0.02}$	$1.22^{\pm 0.05}_{\pm 0.07}$
$\not\!\!E_T > 33$	3	$1.45^{\pm 0.06(stat)}_{\pm 0.06(syst)}$	$0.18^{\pm 0.04}_{\pm 0.02}$	$0.066^{\pm 0.00}_{\pm 0.00}$	$0.14^{\pm 0.01}_{\pm 0.01}$	$1.07^{\pm 0.04}_{\pm 0.06}$
$\not\!\!E_T > 44$	2	$1.14^{\pm 0.05(stat)}_{\pm 0.05(syst)}$	$0.12^{\pm 0.02}_{\pm 0.01}$	$0.048^{\pm 0.00}_{\pm 0.00}$	$0.07^{\pm 0.01}_{\pm 0.00}$	$0.91^{\pm 0.04}_{\pm 0.05}$
$\not\!\!E_T > 55$	2	$0.84^{\pm 0.03(stat)}_{\pm 0.04(syst)}$	$0.07^{\pm 0.02}_{\pm 0.01}$	$0.032^{\pm 0.00}_{\pm 0.00}$	$0.03^{\pm 0.01}_{\pm 0.00}$	$0.71^{\pm 0.03}_{\pm 0.04}$
$\not\!\!E_T > 66$	2	$0.59^{\pm 0.02(stat)}_{\pm 0.03(syst)}$	$0.05^{\pm 0.01}_{\pm 0.00}$	$0.017^{\pm 0.00}_{\pm 0.00}$	$0.01^{\pm 0.00}_{\pm 0.00}$	$0.51^{\pm 0.02}_{\pm 0.03}$
$\not\!\!E_T > 77$	2	$0.40^{\pm 0.02(stat)}_{\pm 0.02(syst)}$	$0.02^{\pm 0.01}_{\pm 0.00}$	$0.007^{\pm 0.00}_{\pm 0.00}$	$0.01^{\pm 0.00}_{\pm 0.00}$	$0.36^{\pm 0.02}_{\pm 0.02}$
$\not\!\!E_T > 88$	1	$0.24^{\pm 0.01(stat)}_{\pm 0.01(syst)}$	$0.01^{\pm 0.00}_{\pm 0.00}$	$0.005^{\pm 0.00}_{\pm 0.00}$	$0.01^{\pm 0.00}_{\pm 0.00}$	$0.21^{\pm 0.01}_{\pm 0.01}$

Table 9.12: Data and backgrounds at each level of selection, for events with two reconstructed jets.

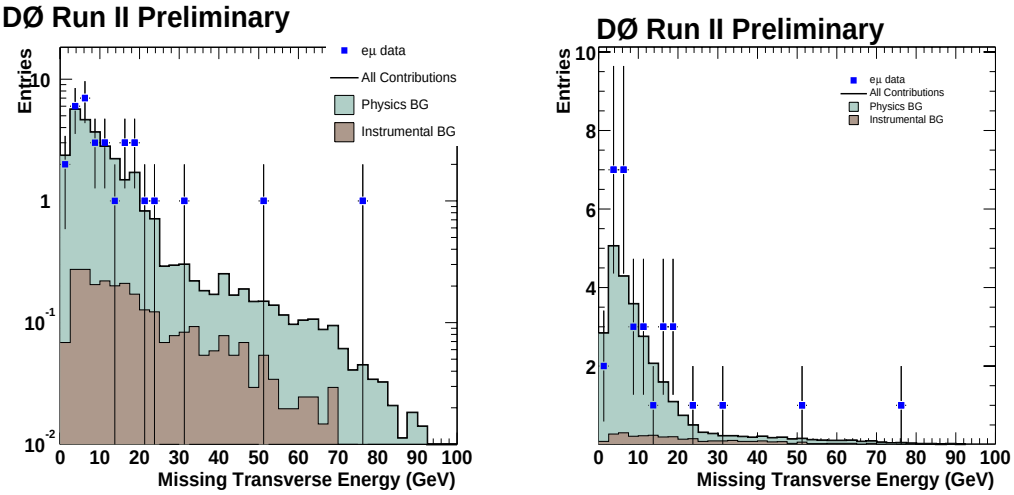

Figure 9.34: Missing transverse energy in $e\mu$ events with no jets, for data and backgrounds in both log and linear scales.

we cannot claim to have observed a significant excess, but instead place a limit on the cross section for the production of new physics. We follow the prescription presented in [42], and use the limit calculator provided in [43]. These limits use a Bayesian approach to calculate the upper limit and requires knowledge of

- Number of data events
- Number of background events, with errors
- Acceptance
- Luminosity

The number of data and background events, as well as the error on the background, can be obtained from Table 9.10. The acceptance can be very intricately dependent on the topology of the signal, especially on the rapidity distributions of the leptons. Rather than deriving a cross-section limit for a specific $e\mu$ process, we quote a limit on the product of the cross-section and the acceptance for the production of clean $e\mu$, see Figures 9.37- 9.39.

For comparison and calibration, we provide the acceptance for a typical clean process, $WW \to e\mu$

$$A^{WW} = 0.131 \pm 0.003_{(stat)} \pm 0.005_{(syst)}$$

and for $WWj \to e\mu j$

$$A^{WWj} = 0.087 \pm 0.004_{(stat)} \pm 0.003_{(syst)}$$

The $e\mu$ event with the largest missing transverse energy is shown in Figure 8.14.

The $e\mu j$ event with the largest missing transverse energy is shown in Figure 9.40.

9.4.1 Discussion

A general search for evidence of new physics in the $e\mu+X$ final state was carried out by DØ in Run1[73] in a similar spirit but with a far more complex strategy, which sought to quantify the consistency of the data with the Standard Model prediction in

terms of a single quantity; here we have chosen the more direct and straightforward but arguably less sensitive approach.

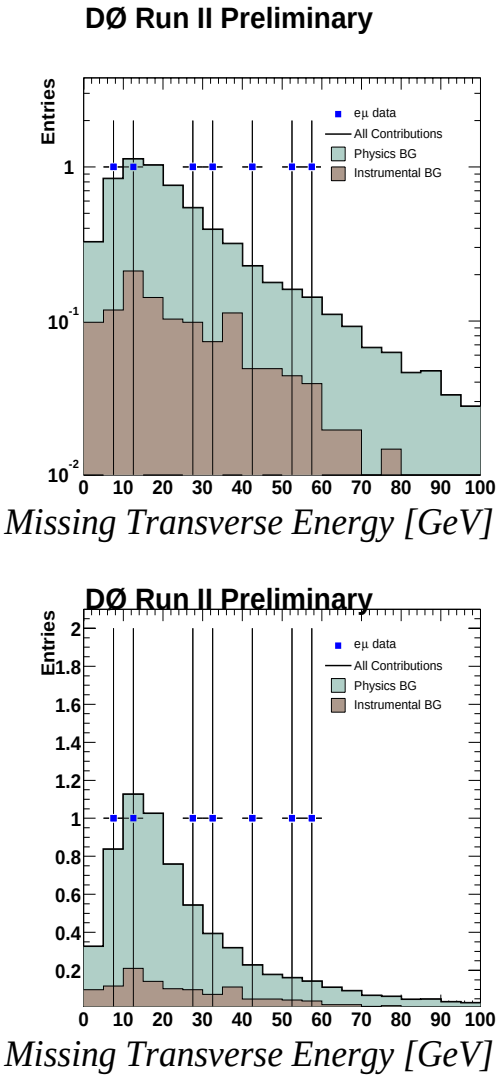

Figure 9.35: Missing transverse energy in $e\mu$ events with a single jet, for data and backgrounds in both log and linear scales.

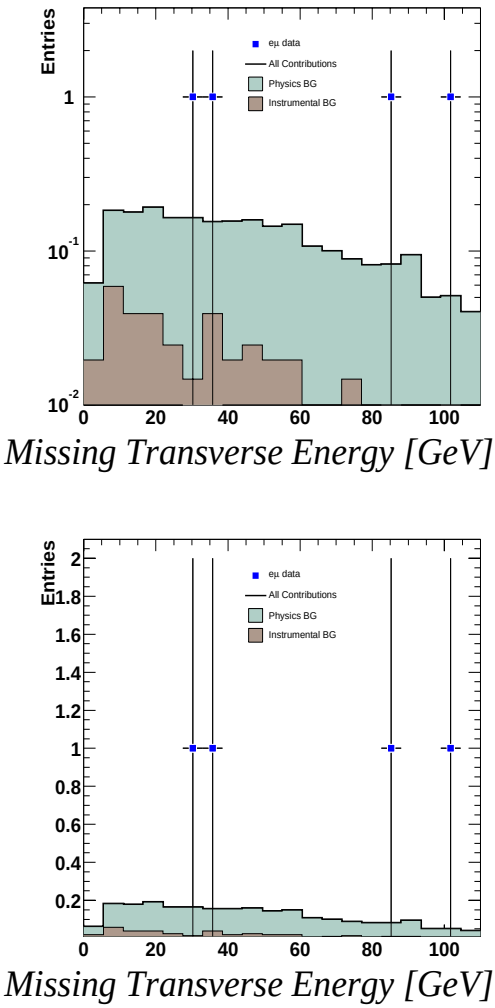

Figure 9.36: Missing transverse energy in $e\mu$ events with two jets, for data and backgrounds in both log and linear scales.

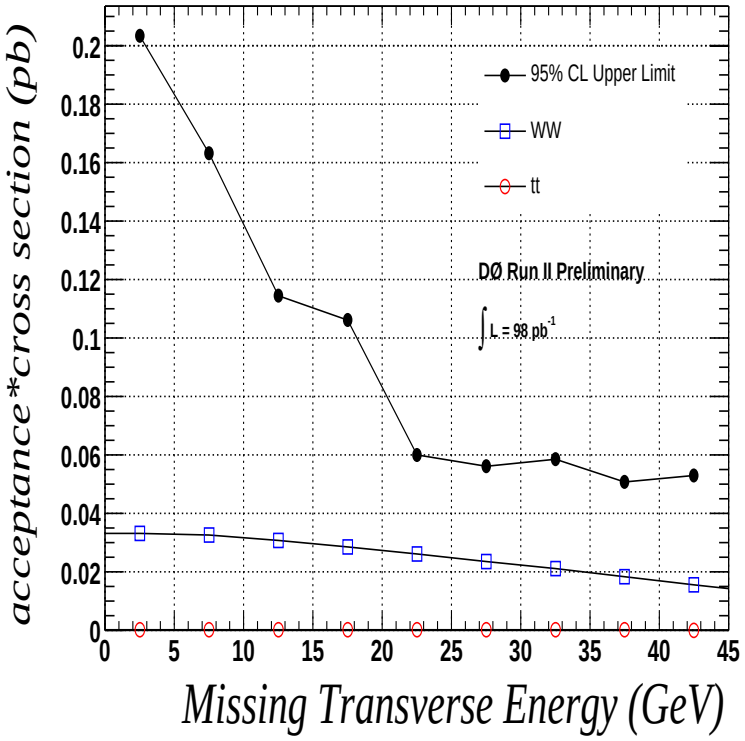

Figure 9.37: Upper limits on the production cross section of new physics in the $e\mu$ channel, as a function of the cut on missing transverse energy in the event.

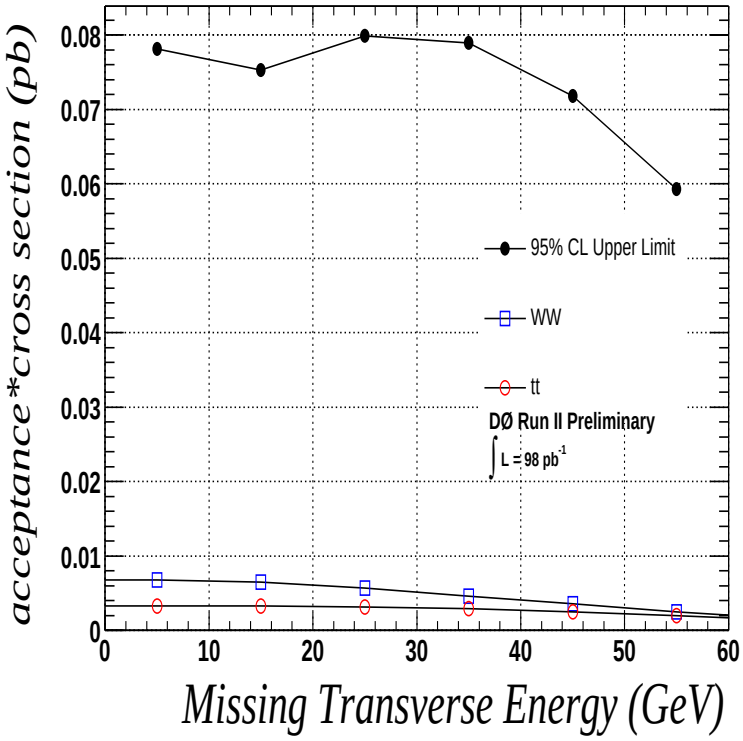

Figure 9.38: Upper limits on the production cross section of new physics in the $e\mu j$ channel, as a function of the lower threshold on missing transverse energy in the event.

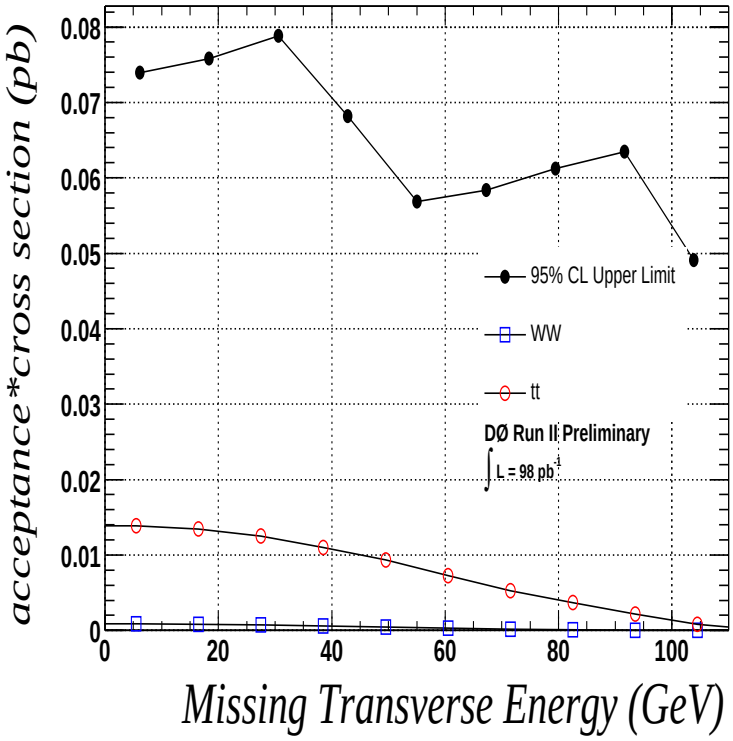

Figure 9.39: Upper limits on the production cross section of new physics in the $e\mu jj$ channel, as a function of the cut on missing transverse energy in the event.

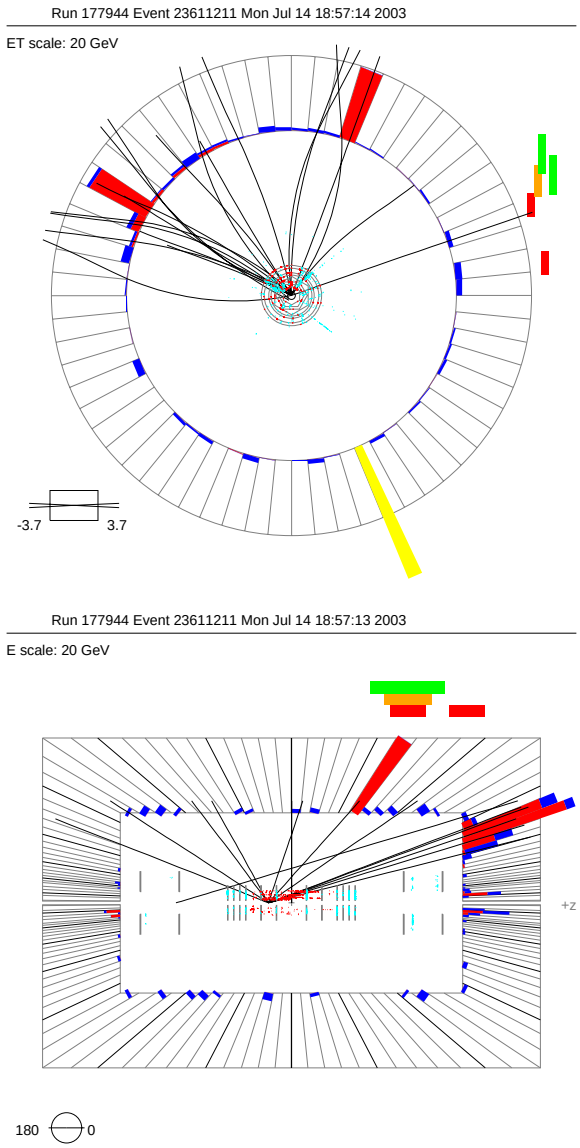

Figure 9.40: XY and RZ views of the highest $\not\!\!E_T$ $e\mu j$ event. The electron appears as electromagnetic (*red*) energy in the calorimeter associated with a central track (*black*); jets appear as electromagnetic and hadronic (*blue*) energy; the muon appears as muon chamber hits (*red, orange, green squares*) and a central track (*black*).

Chapter 10

Discussion

The results presented in this thesis are a portion of the first physics measurements performed with the upgraded DØ detector. A large portion of the effort involved understanding and improving the ability of the detector and the reconstruction software to identify electrons, muons, and jets. Many of the results contained in this document are directly applicable to a wide variety of measurements and searches performed with electrons and muons at DØ.

In the first significant data set collected at Run2, on the basis of analysis and results presented here, we can conclude that events with electrons and muons are consistent with expectations from Standard Model processes, and that no evidence is seen for significant deviation from those predictions. We can exclude the presence of arbitrary processes which would produce electrons, muons and large missing energy, and we can

exclude a portion of the theoretical parameter space for theories of minimal supergravity.

At the time of this writing, the data set accumulated in Run2 has just surpassed the size of that from Run1 of the Tevatron. The next few years of running will see further refinements to the reconstruction methods, dramatic increases to the size of the data set and therefore significant enhancements to the sensitivity of measurements presented here.

Bibliography

[1] M. Perl and B. Richter, Physical Review Letters, 35 1489 (1975)

[2] R. Barnett and L. Hall, Physical Review Letters, 77 3506 (1996)

[3] J. Townsend, *A Modern Approach to Quantum Mechanics*, McGraw-Hill (1992)

[4] P. A. M. Dirac, *Proc. Roy. Soc. London*, A117, 610 (1928)

[5] S. Abachi, *et al.*, [The DØ Collaboration], Nucl. Instrum. Methods Phys. Res. A **338**, 185 (1994)

[6] H1 Collaboration: C. Adloff *et al*, Eur. Phys. J. C 13 (2000) 609

Zeus Collaboration: S. Chekanov *et al*, Eur. Phys. J. C 21 (2001) 443

DØ Collaboration: B. Abbott *et al*, Phys. Rev. Lett. 86 (2001); E866 Collaboration: R. S. Towell *et al*, Phys. Rev. D 64 (2001)

CCFR Collaboration: U. K. Yang *et al*, Phys. Rev. Lett. 86 (2001) 2742

[7] G. Altarelli and G. Parisi, *Nucl. Phys.*, **B126**, 298 (1977)

[8] J. Pumplin *et al*, "New Generation of Parton Distributions with Uncertainties from Global QCD Analysis", hep-ph/0201195

[9] F. Abe *et al*, [The CDF Collaboration], *Observation of Top Quark Production in $p\overline{p}$ Collisions*, Phys. Rev. Lett. 74: 2626-2631 (1995)

[10] S. Abachi *et al*, [The DØ Collaboration], *Observation of The Top Quark*, Phys. Rev. Lett. 74: 2632 (1995)

[11] R.P. Feynman, *QED: The Strange Theory of Light and Matter*, Princeton (1985).

[12] M. Gell-Mann, *A Schematic Model of Baryons and Mesons*, Phys. Lett. 8: 214-215 (1964)

[13] F. Halzen and A. D. Martin, *Quarks and Leptons*, Wiley (1984), Westview Press (1995)

[14] V. Barger and R. Phillips, *Collider Physics*, Pearson Addison Wesley (1987)

[15] M. Peskin and D. Schroeder, *An Introduction to Quantum Field Theory*, Westview Press (1995)

[16] L. Randall, R. Sundrum, *An Alternative to Compactification*, Phys. Rev. Lett. 83:4690-4693 (1999)

[17] J. Goldstone, A. Salam, S. Weinberg, *Broken Symmetries*, Phys. Rev. 127:965-970 (1962)

[18] P. Higgs, *Broken Symmetries and the Masses of Gauge Bosons*, Phys. Rev. Lett 13:508-509 (1964)

[19] T. Affolder *et al* [The CDF Collaboration], *Measurement of the $t\bar{t}$ Production Cross Section in $p\overline{p}$ Collisions at $\sqrt{s} = 1.8$ TeV*, Phys. Rev. D 64, 032003 (2001)

[20] V. Abazov *et al* [The DØ Collaboration, *$t\bar{t}$ Production Cross Section in $p\overline{p}$ Collisions at $\sqrt{s} = 1.8$ TeV*, Phys. Rev. D 67, 012004 (2003)

[21] R. Bonciani *et al*, Nucl. Phys B529 424 (1998)

N. Kidonakis and R. Vogt, Phys. Rev. D 59, 074014 (1999)

N. Kidonakis, Phys. Rev D 64, 014009 (2001)

[22] Kidonakis, *A unified approach to NNLO soft and virtual corrections in electroweak, Higgs, QCD, and SUSY processes*, hep-ph/0303186

[23] J. M. Campbell, R. K. Ellis, *An update on vector boson pair production at hadron colliders*, Phys. Rev. D60 (1999) 113006

[24] H.P. Nilles, Phys. Reports 110, I (1984)

[25] H.E. Haber and G.L. Kane, Phys. Reports 117, 75 (1985)

[26] J. Ellis *et al*, Nucl. Phys B238, 453 (1984)

[27] P. Fayet, Phys. Lett. 69B, 489 (1977)

G. Farrar and P. Fayet, Phys. Lett. 76B, 575 (1978)

[28] L.J. Hall, J. Lykken and S. Weinberg, Phys. Rev D27 2359 (1983)

S.K. Soni and H.A. Welson, Phys. Lett. 126B, 215 (1983)

Y. Kawamura, H. Murayama, and M. Yamaguchi, Phys. Rev. D51, 1337 (1995)

[29] S. Dimopoulos and D. Sutter, Nucl. Phys. B452, 496 (1995)

[30] W. Buchmullter, R. Ruckl and D. Wyler, Phys. Lett. B191 442 (1987)

[31] S. Weinberg, Phys. Rev. D19, 1277 (1979)

L. Susskind, Phys. Rev. D20, 2619 (1979)

[32] The DØ Upgrade, Central Fiber Tracker Technical Design Report.

[33] D. Whiteson, M. Kado, *Muon Isolation Studies*, DØ Note 4070

[34] J. Bantly *et al*, *DØLuminosity Monitor Constant for the 1994-1996 Tevatron Run*, DØ Note 3199

[35] T. Diehl *et al*, *Muon Run Quality*, DØ Note 3938.

[36] S. Grinstein, C. Gerber, R. Piegaia, *Topological Vertex Reconstruction at DØ*, DØ Note 3866

[37] D. Whiteson, L. Phaf, *Electron Likelihood*,, DØ Note 4184

[38] M. Klute,*Top pair production in the μ + jets channel*, DØ Note 4185

[39] LEPSUSYWG, ALEPH, DELPHI, L3 and OPAL experiments, note LEPSUSYWG/02-06.2

[40] B. Knuteson, *The QUAERO Algorithm*,

`http://mit.fnal.gov/~ knuteson/Quaero/quaero/doc/algorithm/algorithm.ps`

[41] B. Knuteson, *Optimal Binning for Likelihood Ratios*,

`http://mit.fnal.gov/~ knuteson/Quaero/quaero/doc/optimalBinning/optimalBinning.ps`

[42] I. Bertram, G. Landsberg, J. Linneman, R. Partridge, M. Paterno, H.B. Prosper *A recipe for the Construction of Confidence Limits*, DØ Note 2775A

[43] J. Hobbs, *Simple Limit Calculator*,

`http://sbheplx.physics.sunysb.edu/~ hobbs/limit_calc.html`

[44] W. Beenakker *et al*, *The Production of Charginos/Neutralinos and Sleptons at Hadron Colliders*, hep-ph/9906298

[45] W. Beenakker *et al*, *SUSY Particle Production at the Tevatron*, hep-ph/9810290

[46] C. Schmitt, *Split CFT Clusters*, DØ Note 4092

[47] Muon ID Certification, v3.0,
`http://www-d0.fnal.gov/phys_id/muon_id/d0_private/muon_id.html`

[48] L. Phaf, I. Iashvili, *Top pair production in the e + jets channel*, DØ Note 4194.

[49] DØ Collaboration, *Measurement of* $\sigma_{p\bar{p}\to Z} * BR(Z \to \mu\mu)$ *at 1960 GeV*, Presented at Moriond 2003

[50] U. Heintz, M. Narain, *A Likelihood Test for Electron ID*, DØ Note 2386.

[51] N.I. Chernov and G.A. Ososkov, *Effective Algorithms for Circle Fitting*, Computer Physics Communications 33 (1984) pp. 329-333

[52] R. Beuselink, `http://www-d0.fnal.gov/~ beuselin/d0_private/trackpar/trackpar.html`

[53] T.C. Hsia, *System Identification*; Lexington Books, Lexington, Mass. ISBN 0-699-99630-0, pp. 22

[54] D. Whiteson, *Global Track Finding at Level 3*, DØ Note 3808

[55] A. Schwartzman, M. Narain, *Track-Jet Studies Using a 3-Dimensional Simple Cone Jet Algorithm*, DØ Note 3919

[56] V.M. Abazov, *et al.* [The DØ Collaboration], *Search for Single Top Quark Production at DØ Using Neural Networks*, Fermilab-Pub-01/103-E

[57] C.J.C. Burges, *A Tutorial on Support Vector Machines for Pattern Recognition*, 1998.

[58] M. Carena, J.S. Conway, H.E. Haber, J.D. Hobbs, *Report of the Tevatron Higgs Working Group*, FERMILAB-CONF-00/ 279-T, `hep-ph/0010338`

[59] P. Cerello, *Grid Computing: Concepts and Applications* in: 3rd International Symposium on Nuclear and Related Techniques, Havana, Cuba, 22 - 26 Oct 2001

[60] C. Chang, C. Lin, *LIBSVM: a Library for Support Vector Machines*, 2002, `http://www.csie.ntu.edu.tw/~ cjlin/libsvm/`

[61] B. Denby, M. Campbell, F. Bedeschi, N. Chriss, C. Bowers and F. Nesti, *Neural Networks for Triggering*, FERMILAB-CONF-90-020

[62] D.E. Groom *et al.*, The European Physics Journal **C15**, 1 (2000)

[63] J.F. Gunion, H.E. Haber, G. Kane and S. Dawson, , (200)

[64] S.L. Glashow, *Nucl. Phys.* **22** (579) 1961;
S. Weinberg, *Phys. Rev. Lett.* **19** (1264) 1967

[65] J.J. Hull, *A Database for Handwritten Text Recognition Research*, in: IEEE Transactions on Pattern Analysis and Machine Intelligence, 16 (05), page 550 (1994)

[66] C. Peterson and T. Rognvaklsson, L. Lönnblad, *Comp. Phys. Commun.* **81** (1994) 185

[67] T. Sjöstrand, P. Edén, C. Friberg, L.Lönnblad, G. Miu, S. Mrenna and E. Norrbin, *Computer Physics Commun.* **135** (2001) 238

[68] M.L. Mangano, M. Moretti, F. Piccinini, R. Pittau, A.D. Polosa, *ALPGEN, a generator for hard multiparton processes in hadronic collisions*, HEP 0307 (2003) 001, hep-ph 0206293

[69] A.J. Smola and B. Schönkopf, *A Tutorial on Support Vector Regression*, 1998, NeuroCOLT2 NC2-TR-1998-030.

[70] DØ Collaboration, FERMI-Conf-03/248-E

[71] CDF Collaboration, FERMI-Conf-03/384-E

[72] Aaron Dominguez, *Recent Results from CDF*, FermiLab Wine and Cheese, August 8 2003.

[73] B. Abbott *et al*, *Search for New Physics in e mu X Data at DØ Using Sleuth: A Quasi-Model-Indepedent Search Strategy for New Physics*, Phys. Rev. D 62 92004 (2000)

[74] T. Affolder *et al*, [The CDF Collaboration], Phys. Rev. Lett. 88, 041801 (2002)

[75] B. Abbott *et al*, *Search for mSUGRA in single-electron events with jets and large missing transverse missing energy in pbarp Collisions at sqrt(s) = 1.8 TeV*, Phys. Rev. D 66, 112011 (2002)

Appendix A

Global Tracking at Level 3

To find particle tracks at Level 3 is to balance requirements for efficiency and speed. A thoroughly efficient but ploddingly slow tracker is useless, as is its converse.

A.1 Requirements

The need for tracking at Level 3 comes primarily from lepton and photon identification tools which use the the presence or absence of central tracks to help confirm or reject candidate objects. In the case of muons, central tracking can significantly improve the momentum resolution, providing additional rejection. Before any tracking begins, these tools have an estimate of the angular location of the track and its momentum, making reconstruction of the entire detector to low P_T unnecessary. Failure to allow

regional track reconstruction with a flexible momentum threshold would be negligent.

The entire time budget for Level 3 is 100 ms. Tracking may acceptably consume a fraction of that time, but not a substantial one.

The global tracking algorithm works with one-dimensional clusters from the Central Fiber Tracker and the Silicon Microstrip Tracker. The invaluable data unpacking and on-the-fly clustering tools for both subdetectors were written by Robert Illingsworth.

In this appendix, I outline the global tracking algorithm implemented in the Level 3 tool `L3TGlobalTracker`.

A.2 Algorithm

The algorithm is neatly broken into two pieces: axial and stereo tracking.

A.2.1 Axial Track Finding

The scope of the axial track finding problem is directly connected to the minimum transverse momentum threshold. Reconstructing tracks to lower momentum thresholds consumes more time, as the number of tracks in the event increases and their greater curvature requires consideration of more possibilities.

In the environment of DØ's magnet, particles with momentum greater than 1.0 GeV show very little curvature. The trajectories of these particles in $R\phi$ can be very

well approximated linearly,

$$\phi(r) = \phi_0 + ar \tag{A.1}$$

where ϕ_0 is the track's ϕ at its point of closest approach to the z-axis, and a is proportional to the inverse transverse momentum. Figure A.1 demonstrates this linearity.

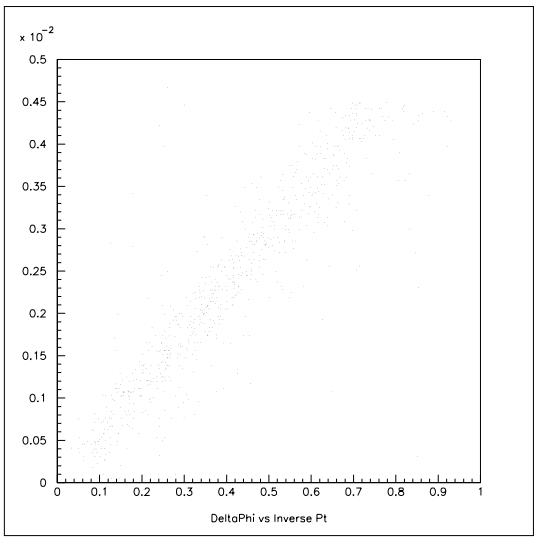

Figure A.1: Distance in ϕ between the outer two axial CFT hits versus inverse P_T for tracks from $Z \to bb$ events. Units of $\Delta\phi$ are radians and of P_T^{-1} are GeV^{-1}.

Selection of a minimum desired transverse momentum P_T^{min} allows the calculation of a maximum value of a. Given the ϕ-position of the track at a given layer of the detector, a small range of potential ϕ positions can therefore be searched at any succeeding layer. We refer to this range as the *cone* of the outer hit. Thus, we have a simple and easily understood parameter which is closely linked to the P_T of the tracks that we can reconstruct and which allows us to eliminate a great many false tracks.

Propagating the Tracks

The axial CFT layers provide an excellent place to begin tracking, because of their high angular precision and lower populations. For any pair of hits in the outer two axial layers for which the inner hit lies within the cone (calculated as described above) of the outer hit, a potential track is formed.

Each potential track is propagated through the remaining axial layers of the CFT and the SMT in a search for additional hits. At each layer, only the range of ϕ positions within the cone of the previous layer are considered. The ϕ prediction at the new layer i is a linear extrapolation from the previous two layers,

$$\phi_i = \phi_{i-1} + (\phi_{i-1} - \phi_{i-2})\frac{r_i - r_{i-1}}{r_{i-1} - r_{i-2}} \tag{A.2}$$

Figure A.2 shows the effectiveness of this prediction. A number, N_{hits}, of the hits closest to the predicted ϕ_i are considered and their contributions to the χ^2 of the track are calculated. If a hit contributes less than χ^2_{max}, it is considered. The track is also allowed to miss the layer. The resulting tracks are discarded if

- They have more than $Miss_{max}$ missed layers
- The $|DCA|$ of the track fit at layer i is greater than DCA^i_{max}

For each surviving track at a given layer, a quality function is evaluated,

$$Q(track) = \chi^2 + Q_{miss} * N_{miss}, \tag{A.3}$$

where N_{miss} is the number of missed layers. The factor of Q_{miss} reflects the penalty for missing a layer. The potential tracks are sorted by Q and the best N_{tracks} are kept and propagated to the next axial layer.

Axial parameter fitting is done using an implementation of the circle fitting algorithm described in [51], implemented as an ALEPH routine called `UFITZS` and adapted for DØ by Ray Beuselinck.

After axial tracking is complete, the set of found axial tracks are examined to remove tracks that share too many axial hits. Of a pair of tracks that share more than $Shared_{max}$, the track with the worse Q-value is pruned.

A.2.2 Stereo Tracking

Once an acceptable axial track is found, the next challenge is to find the matching stereo clusters that allow calculation of z positions for the CFT and SMT axial hits. For a given axial track, the set of stereo clusters which would correspond to a reconstructed z within the physical boundaries of the CFT or the SMT barrel are considered. The problem is then to find a straight line among these points.

Stereo track finding does not enjoy the benefits of simplifying restrictions on parameter ranges, as axial tracking does for P_T and DCA. The axial clusters give us no

clue where the track is in $Z_0 - \tan(\lambda)$ phase space.

A multi-level histogramming method is used to locate the interesting regions of phase space and the clusters that could potentially form a candidate track. Then, a fast linear sequential fitter[53] is used to search through the selected clusters for valid stereo tracks.

The stereo tracking is performed separately for each found axial track. It occurs in four phases

- Identifying the likely regions, using CFT and SMT stereo information
- Finding the best CFT track in each region
- Finding the best matching SMT extension for each CFT track.
- Selecting the best overall stereo track.

The Histogramming Method

The histogramming approach to track finding is based on the Hough transformation. Consider an individual stereo cluster, with a known z position z_c and radius r_c. This cluster lies on an infinite number of potential stereo tracks, each described as a point $(Z_0, tan(\lambda))$ in phase space. These potential stereo tracks are described by the equation:

$$z_c = Z_0 + \tan(\lambda) * r_c \tag{A.4}$$

Put another way, this cluster represents a line drawn in $Z_0 - \tan(\lambda)$ phase space. If one were to draw the lines corresponding to all of the clusters on a track, they would intersect at the point in phase space corresponding to the parameters of that track $(Z_0, \tan(\lambda))$.

The lines from each cluster on a track intersect at a single point only for an ideal set of clusters which lie exactly on the track. In a real tracking environment, they will be some distance from the point representing the actual track parameters.

Finding the intersection analytically is not trivial. Instead, we choose to slice the phase space into bins and build a two dimensional histogram, incrementing the bins crossed by each cluster line. After the histogram is filled with lines from each relevant cluster, the track will appear as a peak.

To account for cluster position errors, the lines that are drawn in the histogram have finite width, proportional to the specific cluster errors.

The selected resolution of the histogram is very important to its performance. A finely binned histogram will resolve the peaks very well, but pay a steep price in time to fill and analyze all of the bins. A compromise is achieved by multi-stage histogramming. The initial histogram is roughly binned, enough to resolve the approximate location of any peaks, but without spending valuable time filling bins in uninteresting regions. The

subsequent histogram has much finer resolution, but it covers only the region indicated by the rough histogram.

The performance can be further improved by considering a rotation of the histogram in $Z_0 - \tan(\lambda)$ phase space. Equation (4) reveals that the slope of the cluster-line relative to the z and $\tan(\lambda)$ axes is r_c, the radial position of the cluster. The range of radial positions varies from approximately 2 cm to approximately 50 cm, meaning that all of the slopes are large and positive, as shown on the lefthand side of Figure A.3. This is a suboptimal use of the histogram, as it results in intersections that are long and stretched out over many bins, and increases the chance of fake peaks.

Note that selection of a rectangular region in which the sides are parallel to the Z_0 and $\tan(\lambda)$ axes is entirely arbitrary. Instead, we can select a rectangular region at an angle to these axes that gives half of the cluster-lines a positive slope and half a negative slope. Since every cluster lies on a one of a small number of fixed radii, we can make an informed choice about their relative slopes. A rotation of the histogram so that the innermost axial layer generates lines that have a slope perpendicular to the outmost layer will yield intersections that cover the smallest possible number of histogram bins. The righthand side of Figure A.3 demonstrates this.

We choose a rotation angle

$$\theta = tan^{-1}(\frac{r_{inner} + r_{outer}}{2})$$

so that half of the layers give lines with positive slopes and half with negative slopes. Further, we choose the ratio of the sides of an individual bin to maximize the angle between the innermost and outermost layers.

Identifying Likely Regions

The first histogram covers the CFT detector acceptance, or $\tan(\lambda) = (-4.0, 4.0)$ and $Z_0 = (-100.0, 100.0)$. For each axial cluster, we examine the stereo clusters that give a z_c position within the volume of the detector (or in the case of the SMT, within the individual barrel).

The CFT clusters alone give a good indication of where the track lies, but the addition of the SMT information helps to confirm true and reject accidental peaks.

A threshold level is calculated, allowing for one missed layer in each of the CFT and SMT. Adjacent cells above the threshold are grouped together. For each set of adjacent cells, a rectangular region in phase space is selected as the region of interest. This region will form the boundaries of the finely binned histogram.

Finding CFT Tracks

For each region of interest, a smaller more finely binned histogram is constructed and filled. For this histogram, we also store a pointer to the cluster which produced each of the lines, for later construction of actual tracks.

Again, adjacent cells of the histogram that are above the threshold are identified and grouped together. For each region, a set of contributing clusters at each layer is collected.

The problem now reduces to finding the best straight-line track among a small set of z positions and errors. For this purpose, a fast sequential linear fitter [53] is used.

Track candidates are constructed from pairs of clusters in the inner and outermost layers. For each candidate, we propagate the track through the remaining layers of the detector. A simple linear extrapolation is used to predict the position at layer i with radius r_i:

$$z_i = Z_0 + tan(\lambda) * r_i$$

At each layer we examine the cluster closest to this predicted position and its contribution to the χ^2_Z of the track. If the χ^2_Z contribution is smaller than $\chi^2_{max_Z}$, then the cluster is incorporated into the stereo candidate, otherwise the layer is missed. Figure A.4 shows the accuracy of this prediction and the distribution of χ^2_Z contributions.

Of the tracks constructed from each pair of clusters, that with the best value of

$$Q_Z = \chi^2_Z + Q_{miss_Z} * N_{miss_Z}$$

is retained.

Extending Stereo Tracks into the SMT

For each region of interest that returns a valid CFT stereo track, a small, very finely binned histogram is constructed in the region surrounding this track's parameters and filled with SMT stereo clusters. As in CFT track finding, peaks are grouped together and their clusters grouped. Valid stereo tracks are found and the best is selected using the same sequential linear fitter.

The SMT track is then combined with the CFT track. If the combined track has a better Q_Z than the CFT track alone, it is selected. Otherwise only the CFT information is used.

A.2.3 Regional Tracking and Caching

Adapting this algorithm to regional tracking is not difficult. The momentum threshold is a natural feature, and the selection of the initial track candidates governs the tracking's angular extent.

Caching the results to avoid repeating previous work is a little more complicated. This requires maintaining a list of previously reconstructed regions, and the tracks found in those regions. When a requested region overlaps a cached region, only the unreconstructed section is searched and the results merged with the cached results

and returned to the user.

When a previously reconstructed region is requested with a value of P_T^{min} lower than was previously used, the region is searched again with the larger cone size and the results merged with the previous results.

A.2.4 Track Parameter Definitions

Tracks at Level 3 are parametrized as helices with five parameters defined following [52] as:

$P_T^{-1} = B_0 qc/R$: inverse transverse momentum. B_0 is the strength of the magnetic field, q is the charge of the particle, and R is the radius of curvature in the $x-y$ plane. Positive q indicates that the track turns counterclockwise.

ϕ_0: the azimuthal angle of the track momentum at the point of closest approach to the z axis.

$\tan(\lambda) = dZ/dS_{xy}$, is the stereo pitch, where S_{xy} is the distance travelled around the arc in $x-y$.

$DCA = S \times d_0$: the Distance of Closest Approach. d_0 is the positive distance to the origin at the point of closest approach to the z axis, and S indicates the sign of angular momentum of the track about the origin.

Z_0: the position of the track on the z axis at the DCA.

A.2.5 Algorithmic Parameters

Typical values of algorithmic parameters, set in RCP files `L3TGlobalTracker.rcp` and `HistogramZTrackFinder.rcp`.

Name	Value
N_{hits}	2
χ^2_{max}	10.0
Q_{miss}	15.0
$Shared_{max}$	2
$\chi^2_{max_Z}$	5.0
Q_{miss_Z}	10.0

Some parameters can have distinct values at each global layer. There are 16 global layers, numbered 1-16 from the innermost SMT layer to the outermost CFT layer, respectively.

Global Layer	$Miss_{max}$	DCA_{max}	N_{tracks}
1	9	1	3
2	8	1	3
3	7	1	3
4	6	1	3
5	5	1	3
6	4	1	3
7	3	1	4
8	2	1	4
9	1	1	3
10	1	1.5	3
11	1	2	3
12	1	3	3
13	1	10	4
14	1	25	4
15	1	10^{10}	4
16	1	10^{10}	4

A.3 Performance

A.3.1 Efficiency for $Z \to e^+e^-$ candidates

An accurate measurement of efficiency requires a careful selection of an extremely pure sample, to avoid apparant dilution of the efficiency with fake objects. We use the sample of $Z \to e^+e^-$ candidates in data; they can be selected with calorimetric information only, and so provide an unbiased sample of candidates.

We select events from runs 144000 through 154000, reconstructed with `p10.15` which contain two tight electrons, according to electron certifiction v1.2, whose combined invariant mass lies within 10 GeV of the mass of the Z, and reconstruct them with `L3TGlobalTracker`. Figure A.6 shows the residual in ϕ and η between the electron

candidates and the closest track.

We define an electron to be axially track-matched if there is a track with $\Delta\phi < 0.025$ and stereo track-matched if it satisfies the additional requirement that $\Delta\eta < 0.03$. Figure A.7 shows the axial and stereo matching rates; if this sample is fully pure, then this is the electron track-matching efficiency.

To confirm that the matched tracks and EM objects are left by the same electron, we can compare the transverse energy measured by the calorimeter and tracker. This information is not used in the matching, and so provides an unbiased assessment of the matching purity. Figure A.8 gives the ratio of the energy measurements.

It is important to note two features regarding the efficiency. First, the efficiency climbs steadily with run number, indicating the status of the detector and readout. Broadly speaking, the more recent runs are more fully instrumented and reliable. Second, the efficiency varies strongly as a function of η. Beyond η of 1.2, for example, the efficiency drops to zero, reflecting the CFT geometric acceptance.

In the central region, the axial track finding efficiency is approximately 65%. Monte Carlo studies suggest that an efficiency of greater than 95% should be achievable. To diagnose the source of these inefficiencies, the most useful resource is data from more recent runs, where the efficiency is the highest and gross hardware problems have been overcome. In these runs, with run number greater than 150,000, the efficiency in the central region is approximately 80%.

The first step to find the cause of the inefficiency is to untangle the algorithmic and clustering contributions. Clustering problems would lead to electrons with missing or misplaced clusters; algorithmic inefficiencies would cause electrons with sufficient CFT clusters to be missed.

For each electron in the sample of late run Z events, we count the number of CFT clusters which lie along its path. Specifically, we propagate the electron backwards from its position in third layer of the EM calorimeter through all eight CFT layers, and search for the closest cluster at each layer. Figure A.9 shows the residual in ϕ between the electron position and the nearest CFT cluster. The width of the distributions is roughly 0.01 radians.

The figure of merit, however, is the number of clusters along an electron's path; here we require the cluster to be within 0.025 radians of the electron position. Figure A.10 shows the number of found clusters for matched and unmatched electrons, and the layer on which clusters are not found.

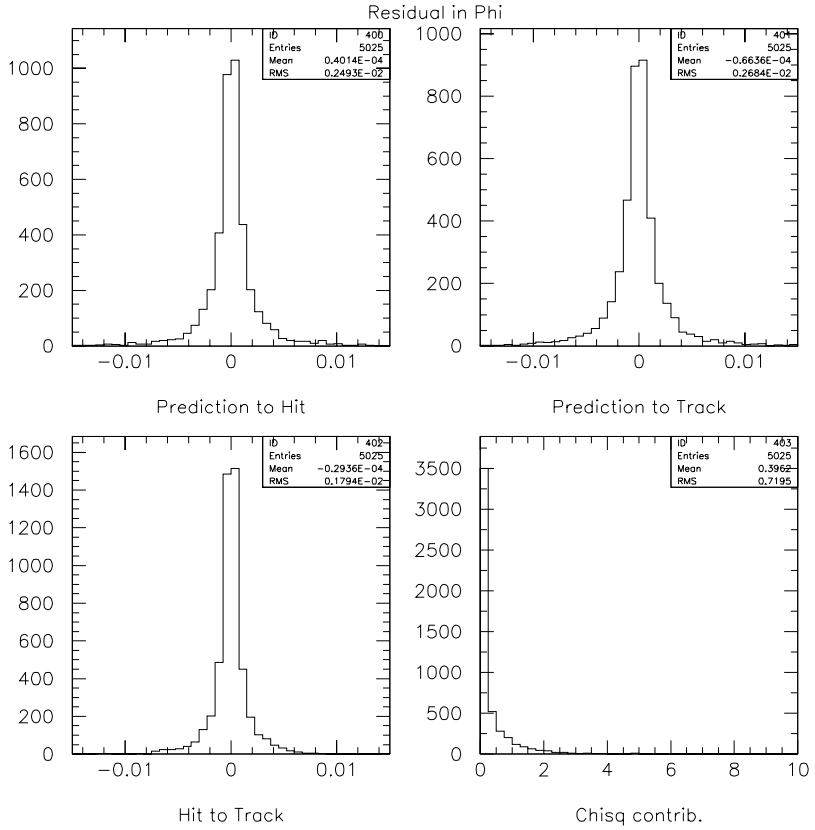

Figure A.2: Residuals in ϕ for axial cluster finding. Clockwise from top left: *(1)* shows the difference between the predicted and actual hit positions. *(2)* shows the difference between the predicted hit position and ϕ_{track}, the ϕ position of the MC track helix at this radius. *(3)* shows the difference between the actual hit position and ϕ_{track}. *(4)* shows the χ^2 contribution. For tracks with $P_t \geq 1.0$ GeV and $|DCA| \leq 1.0$ cm in 10 $t\bar{t}$ events with 1.1 minbias

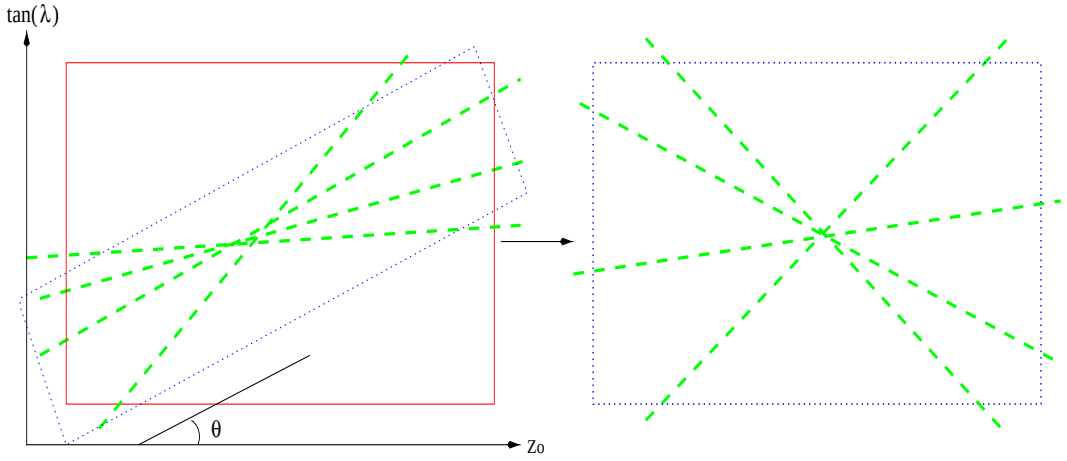

Figure A.3: Effect of rotation of the rectangular histogram. The left image shows an unrotated histogram represented by the solid red box, where lines from clusters (dashed, in green) have similarly large and positive slopes, generating a longer diagonal peak. The rotated histogram is represented by the dotted blue box. As the image on the right demonstrates, this gives a smaller point of intersection and maximizes the angle between the lines from the clusters.

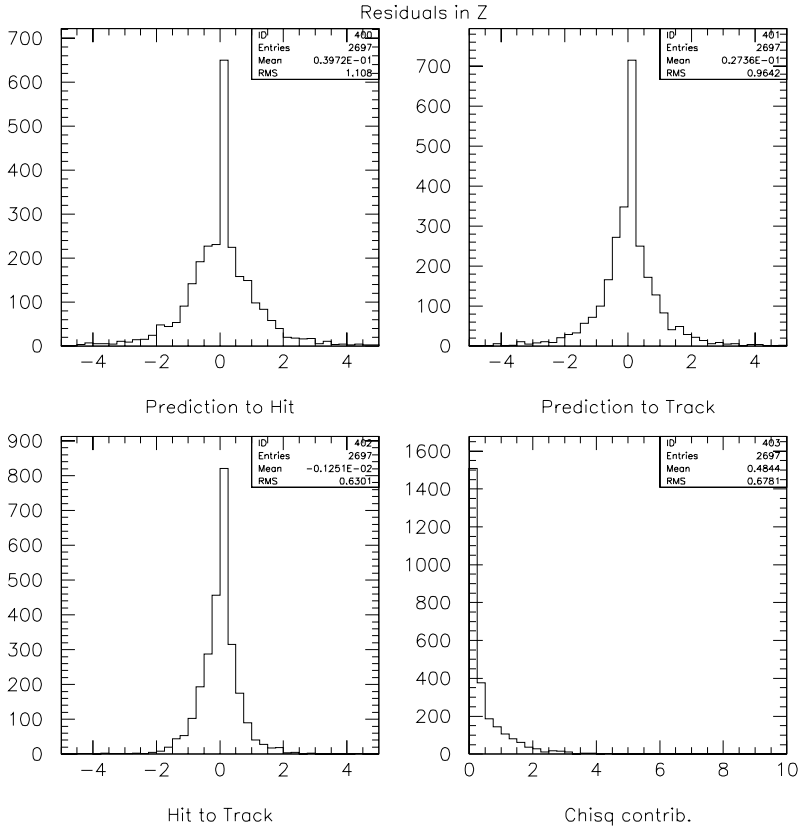

Figure A.4: Residuals in z (cm) for stereo cluster finding. Clockwise from top left: *(1)* shows the difference between the predicted and actual hit positions. *(2)* shows the difference between the predicted hit position and z_{track}, the z position of the MC track at this radius. *(3)* shows the difference between the actual hit position and z_{track}. *(4)* shows the χ^2_Z contribution. For tracks with $P_T \geq 1.0$ GeV and $|DCA| \leq 1.0$ cm in 10 $t\bar{t}$ events with 1.1 minbias.

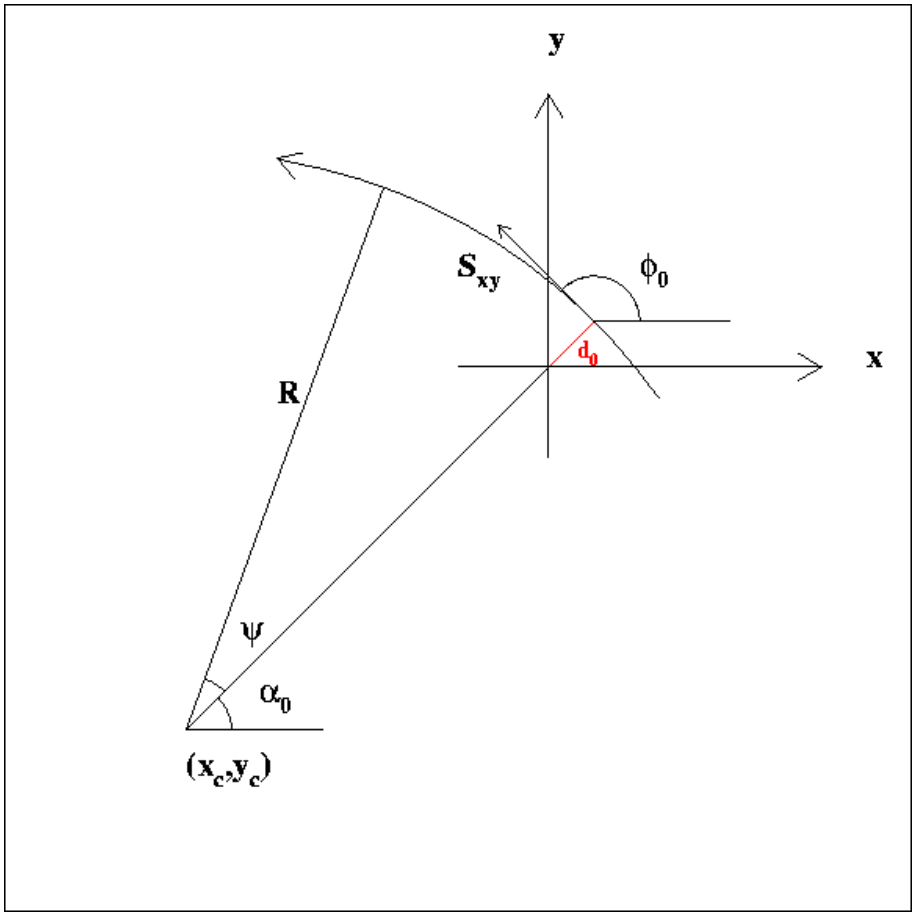

Figure A.5: Track parameter illustration [52]

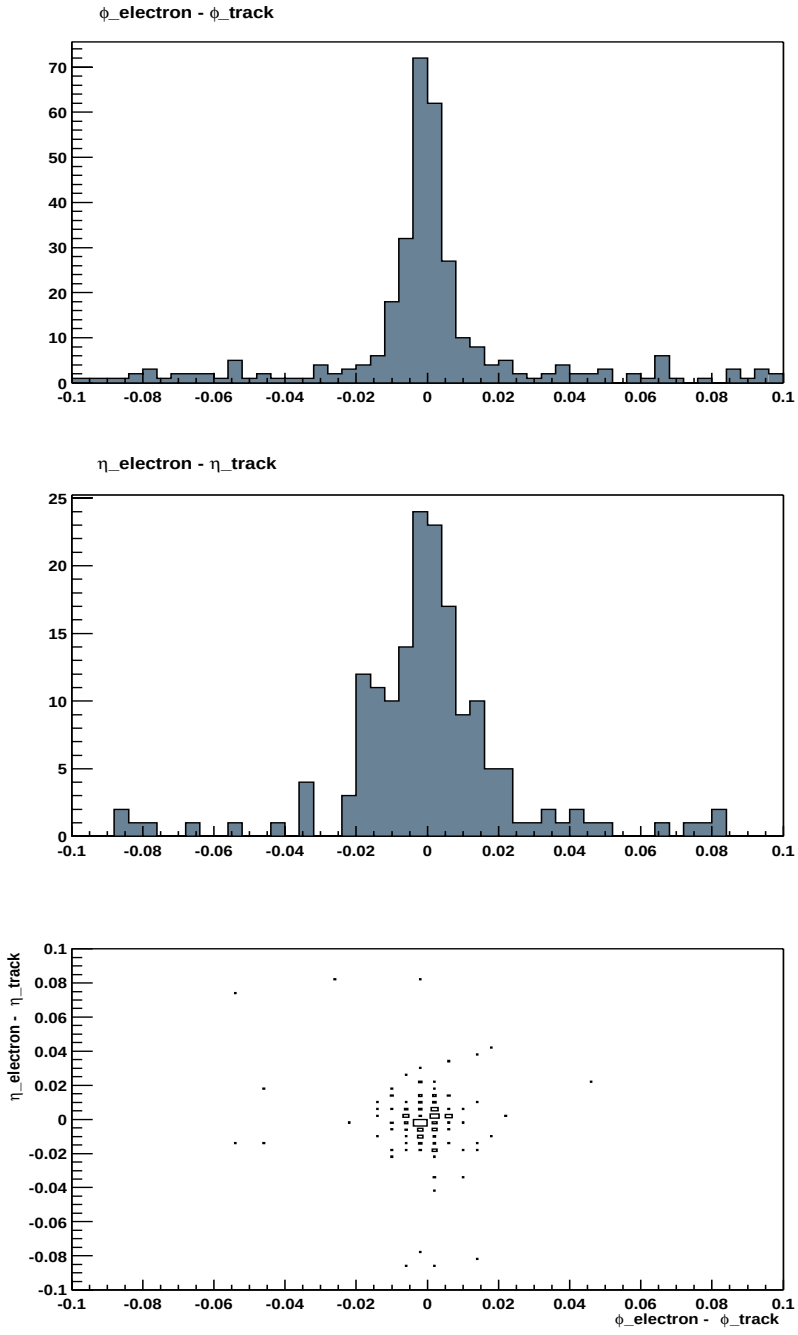

Figure A.6: Residuals between EM object and nearest track in $Z \to e^+e^-$ data. Top is $\Delta\phi$; middle is $\Delta\eta$; bottom shows the correlation.

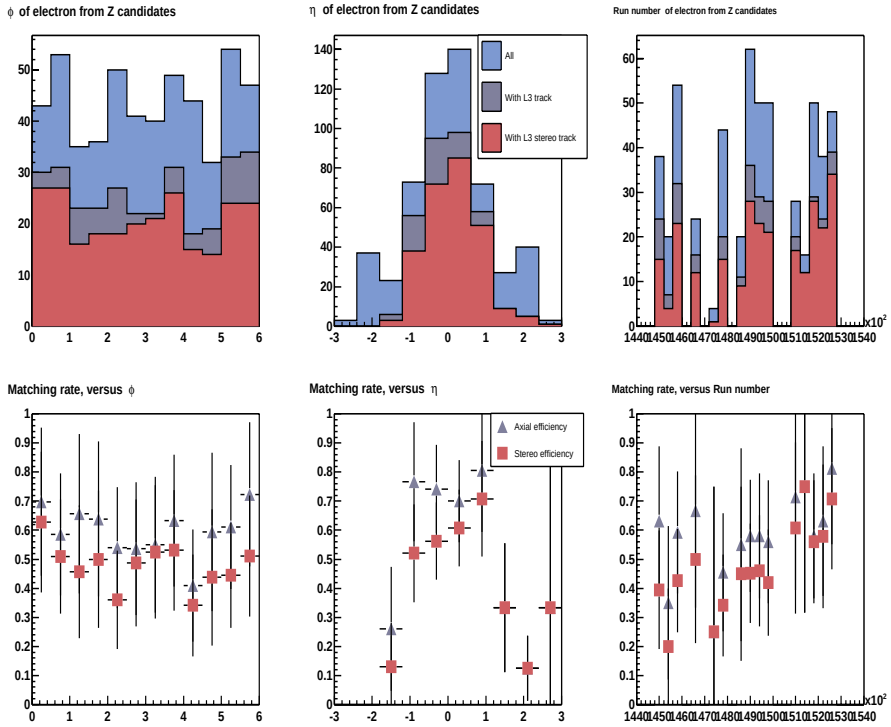

Figure A.7: Efficiency for matching electrons to tracks in $Z \rightarrow e^+e^-$ data. Top row shows the absolute numbers of EM objects, axial matched EM's and stereo matched EM's as a function of ϕ (left),η (middle) and run number (right). Bottom shows the axial and stereo efficiency.

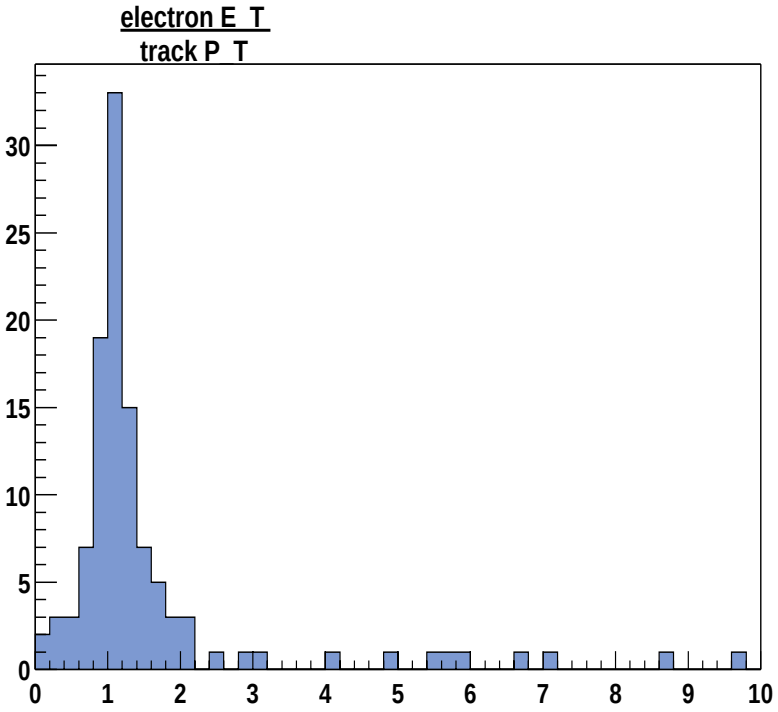

Figure A.8: Ratio of transverse calorimetric energy to transverse track momentum.

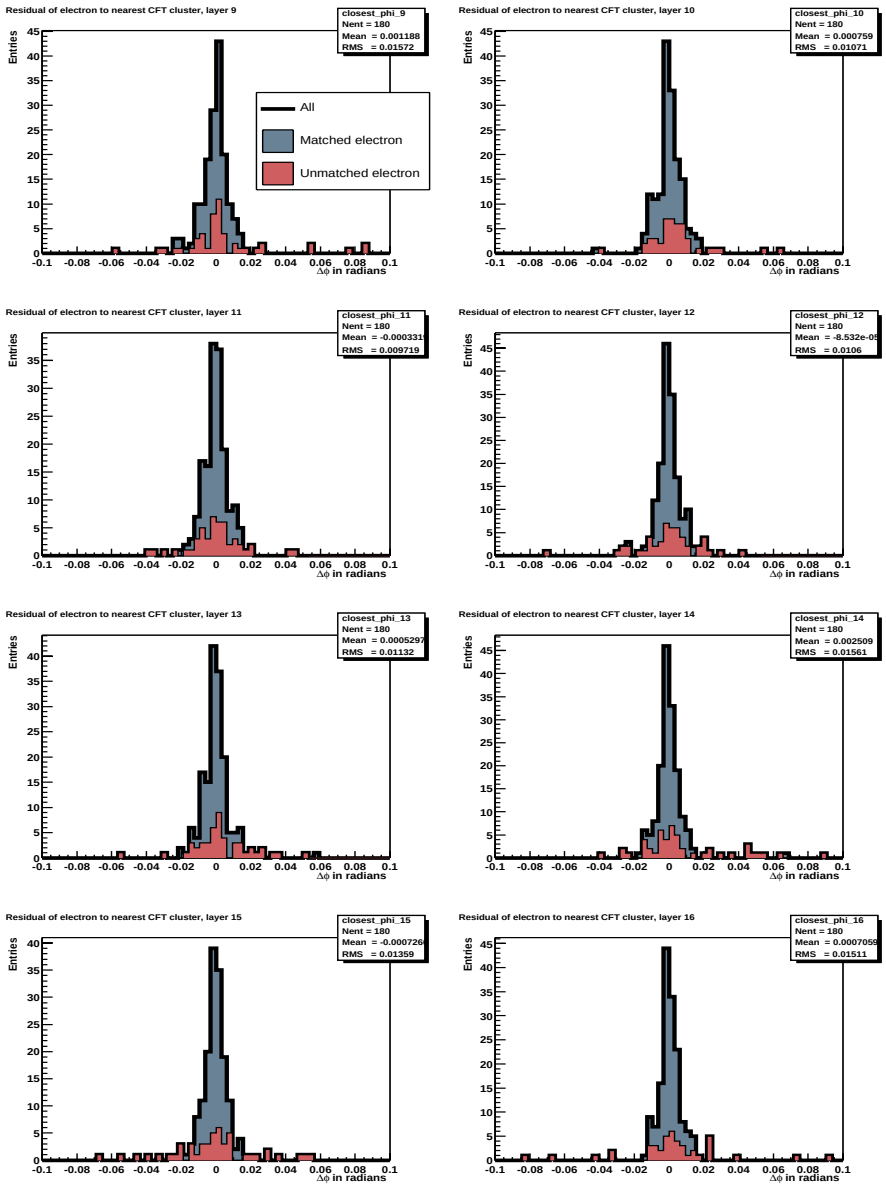

Figure A.9: Residual between electron and the nearest CFT cluster at each of eight axial CFT layers. The solid line shows all the clusters, the blue region shows track matched electrons and the red region shows unmatched electrons.

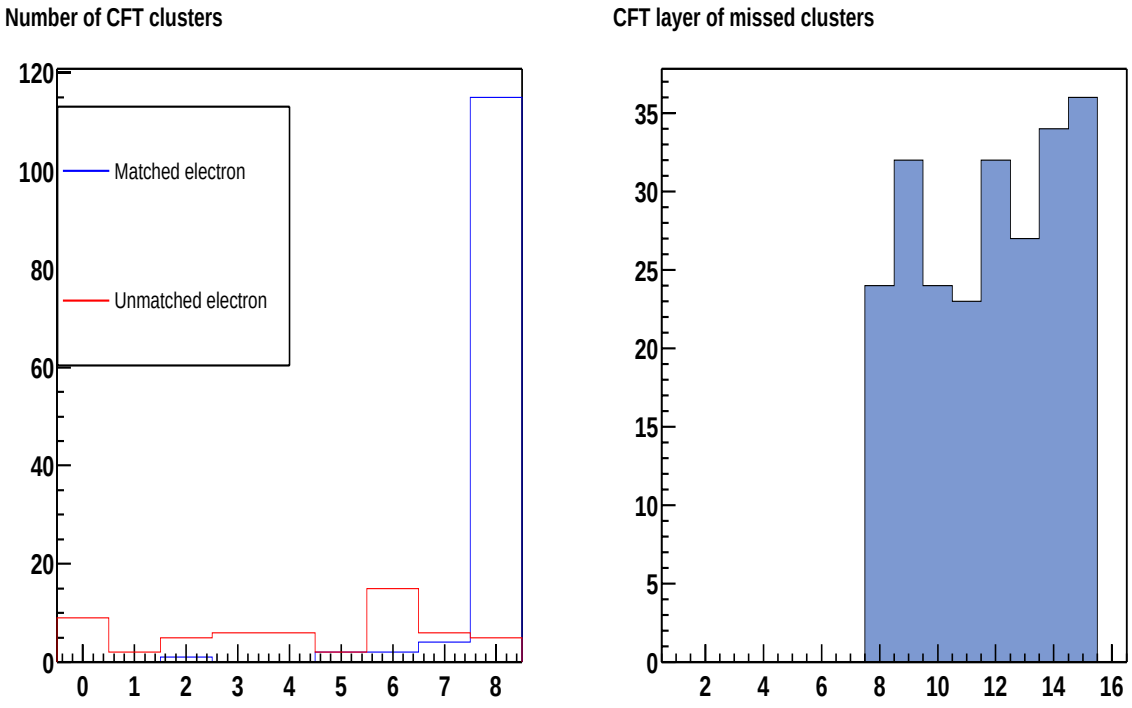

Figure A.10: Left, the number of layers with a CFT cluster within 0.025 radians of the propagated electron position for matched and unmatched electrons. Right, the layers on which clusters were not found.

As one would expect, the matched tracks have either seven or eight CFT clusters along the electron path; the smattering of matched tracks with fewer clusters may be evidence of a small impurity in the sample. The unmatched tracks overwhelmingly have fewer than the requisite seven clusters; these cannot be found by the tracking algorithm and so their loss is due to clustering ineffieciencies. The efficiency for finding a track for an electron within $|\eta| < 1.2$ which leaves at least seven CFT hits is 94%.

A.3.2 Efficiency as a function of P_T^{min}

Each request for track finding is accompanied by a specified minimum P_T threshold, above which maximum efficiency is desired and below which efficiency may be sacrificed for speed. The threshold determines the size of the cone used to search for additional hits on subsequent detector layers and allows the tool to avoid considering many hits and reconstructing many tracks. Ideally, the efficiency would be zero below the threshold such that no time is spent reconstructing tracks of no interest. Further, care must be taken that efficiency for high P_T tracks is not lost as the threshold increases. Figures A.11- A.13 show the details of tracks reconstructed with $0.5 < P_T^{min} < 10.0$ GeV.

As Figure A.13 demonstrates, track finding efficiency at low momentum deteriorates as the P_T^{min} threshold is increased. To estimate the behaviour of the efficiency as a function of momentum and P_T^{min}, we compute the efficiencies relative to the largest

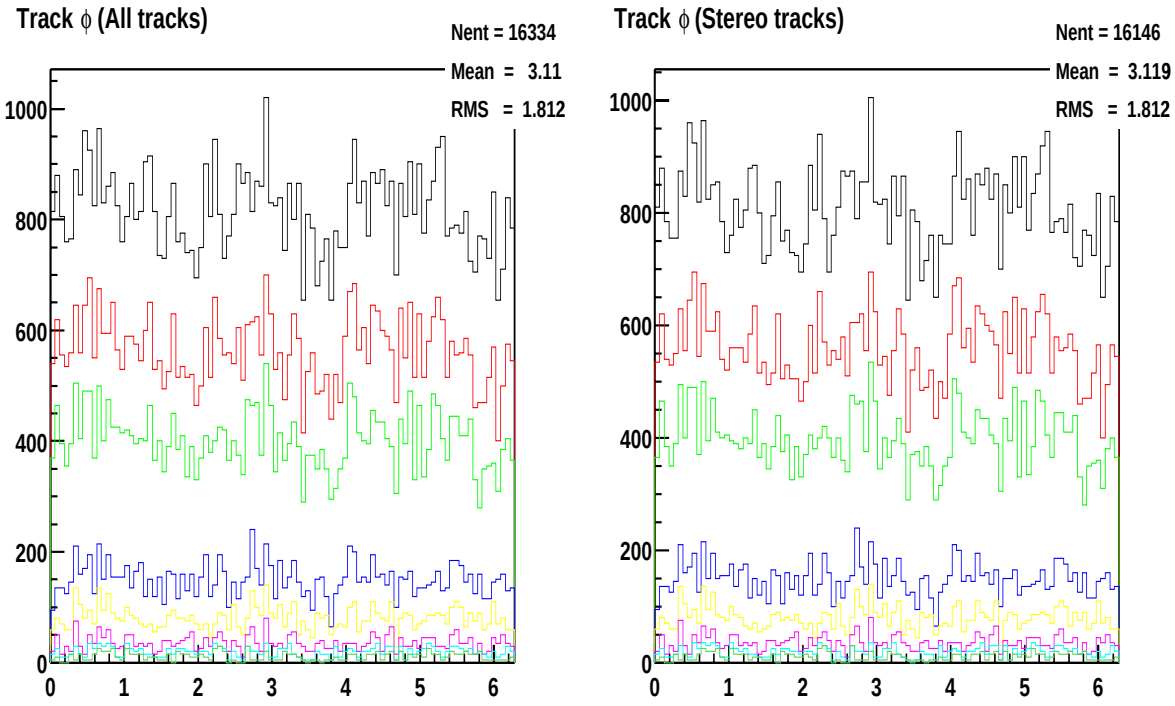

Figure A.11: Track ϕ for varying values of the P_T^{min} threshold.

and least restrictive sample, that with $P_T^{min} = 0.5$ GeV. These efficiencies are shown in Figure A.14; the turn-on curves are modelled as an error function multiplied by a 5-dimensional polynomials. Fitting with a pure error function was attempted, but the resulting modelling was extremely poor due to the asymmetry in the upper and lower edges. These curves model reasonably well the turn-on region and thus give a quantitative estimate of the point of interest, where the efficiency reaches 100%. The P_T at which these curves are fully efficient is shown in Figure A.15. The behaviour is approximately

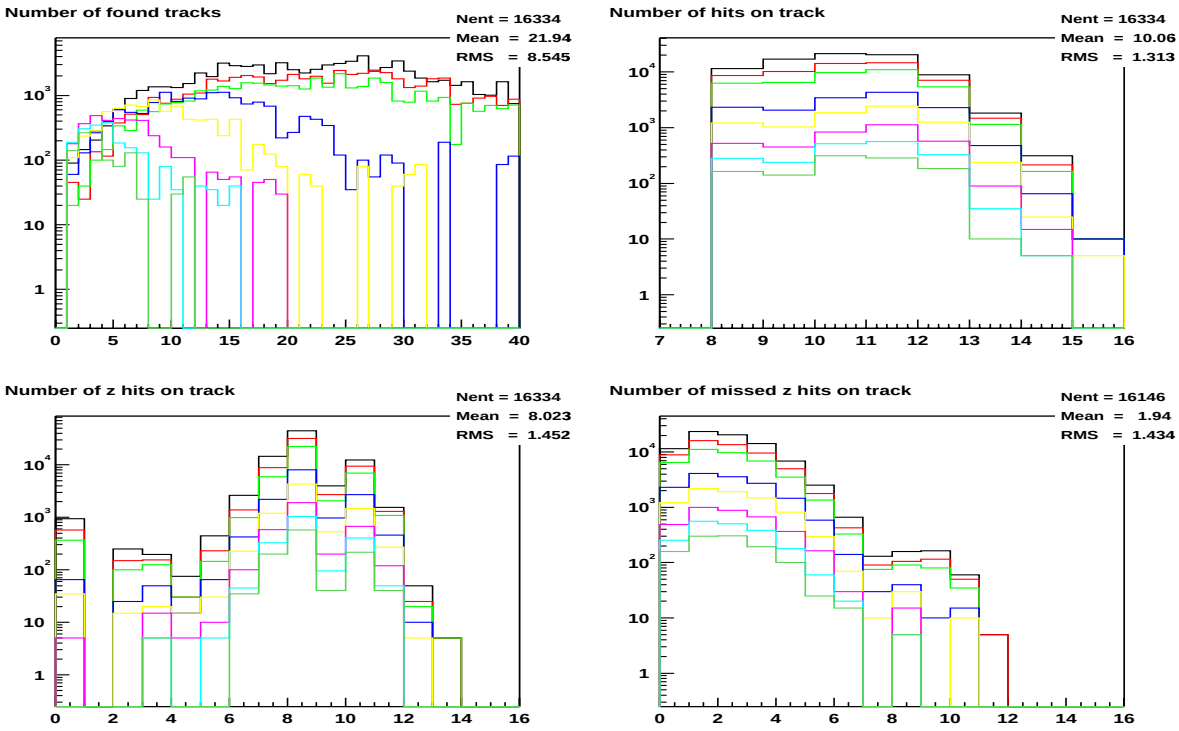

Figure A.12: Track and hit multiplicities for varying values of the P_T^{min} threshold.

linear, and the tuning of the threshold parameter is clearly conservative. That is, the algorithm reaches the desired full efficiency at a P_T below the specified threshold.

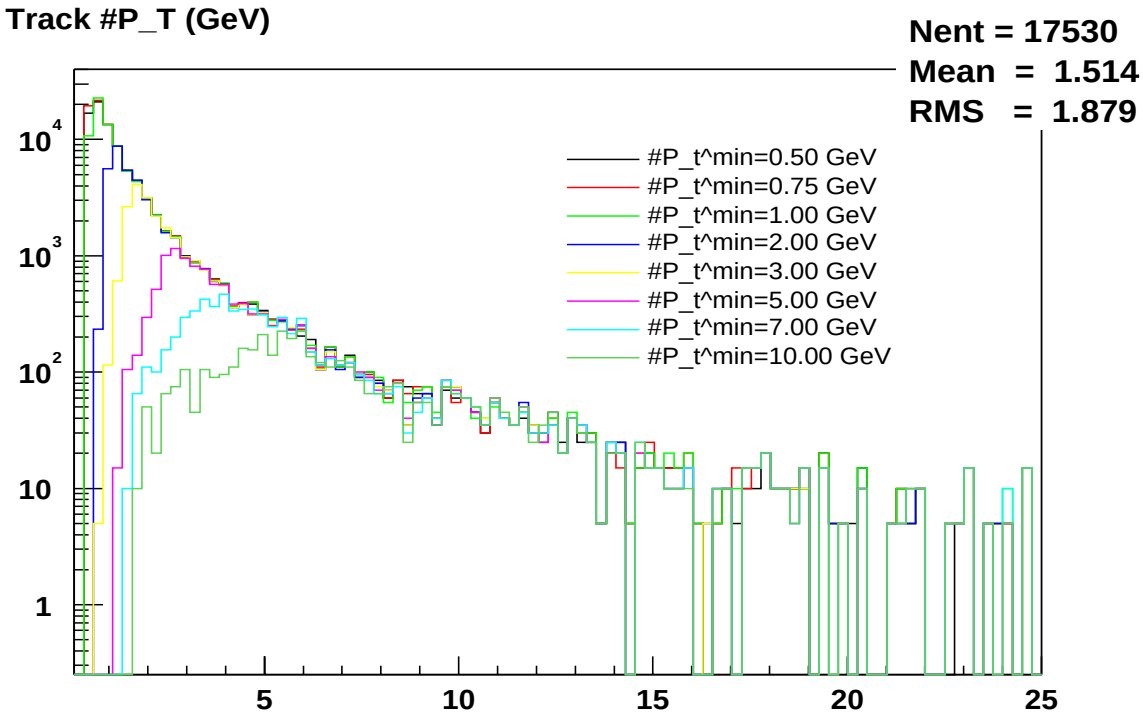

Figure A.13: P_T spectrum for varying values of the P_T^{min} threshold.

A.4 Errors and resolutions

A.4.1 Track Parameter Errors

When the track fitting is done, no track parameter errors are calculated. Instead, the error on each parameter is approximated from studying parameter residuals in Monte Carlo studies.

The residuals are seen to be approximately Gaussian when seperated into cat-

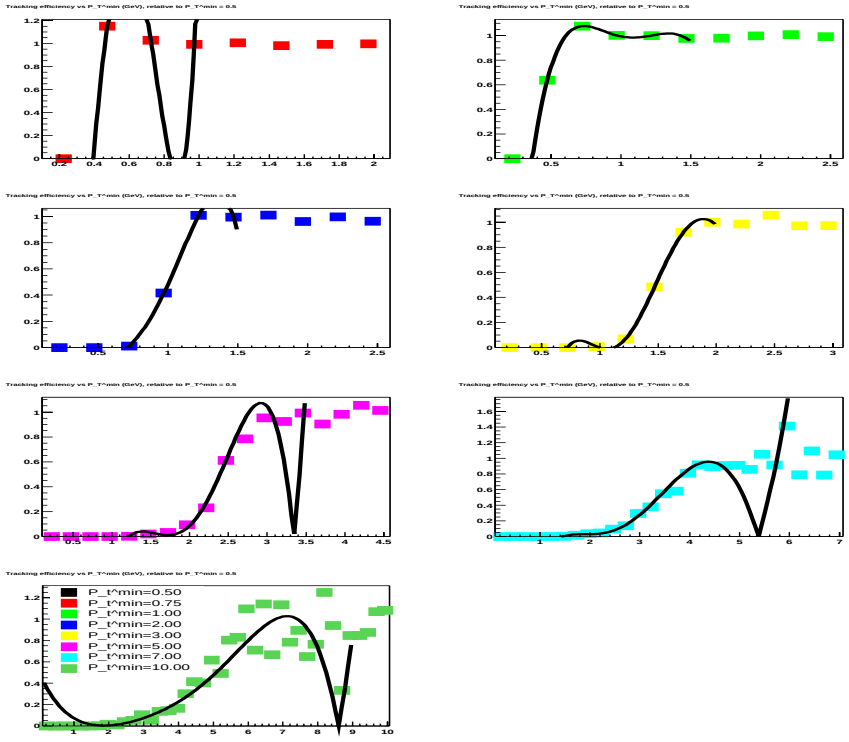

Figure A.14: Estimated tracking efficiency as a function of track P_T.

egories by the number of SMT clusters on the track. Figures A.16-A.20 show the distributions of the errors for each parameter in each category, as well as the fit used to measure the error.

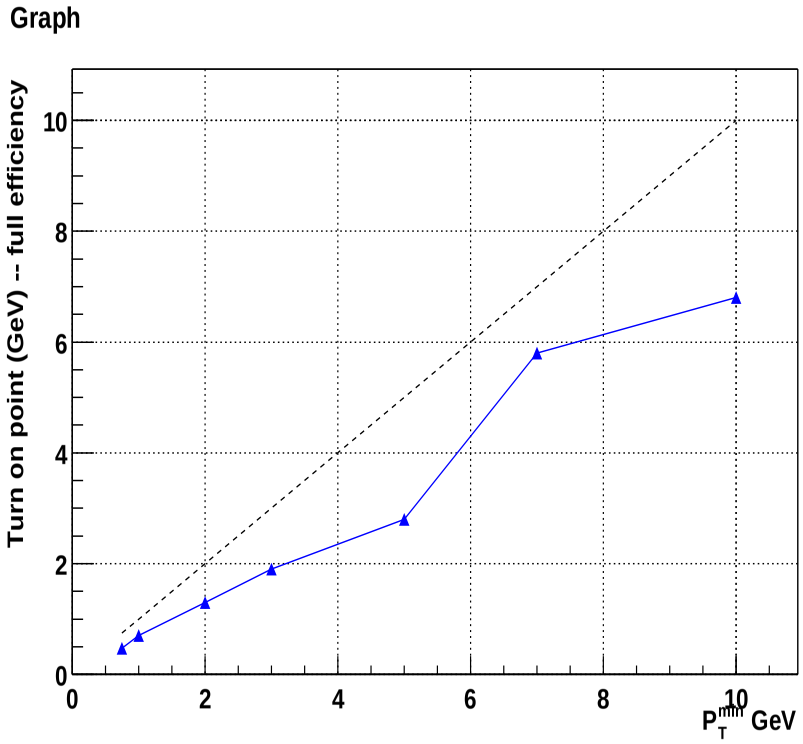

Figure A.15: Variation of full efficiency threshold with P_T^{min}.

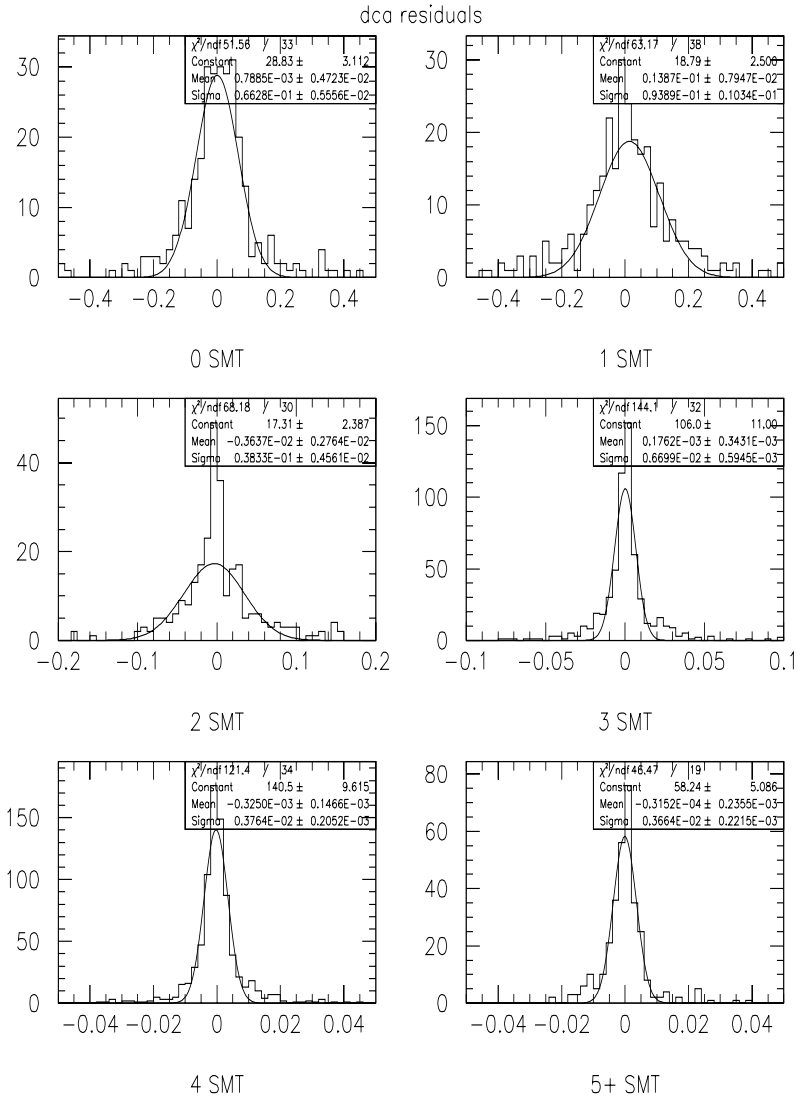

Figure A.16: Residual in the track parameter DCA, for reconstructed and simulated tracks in 100 $t\bar{t} \to lljj$ events, for varying number of SMT clusters on the track.

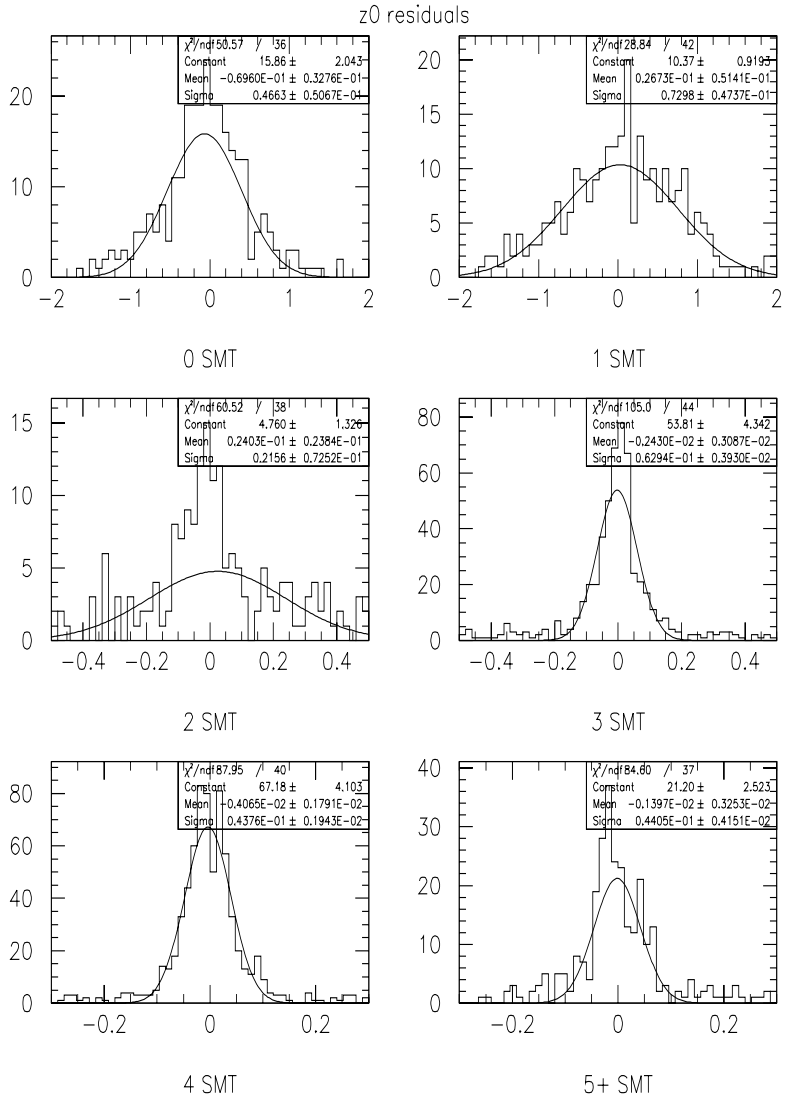

Figure A.17: Residual in the track parameter Z_0, for reconstructed and simulated tracks in 100 $t\bar{t} \to lljj$ events, for varying number of SMT clusters on the track.

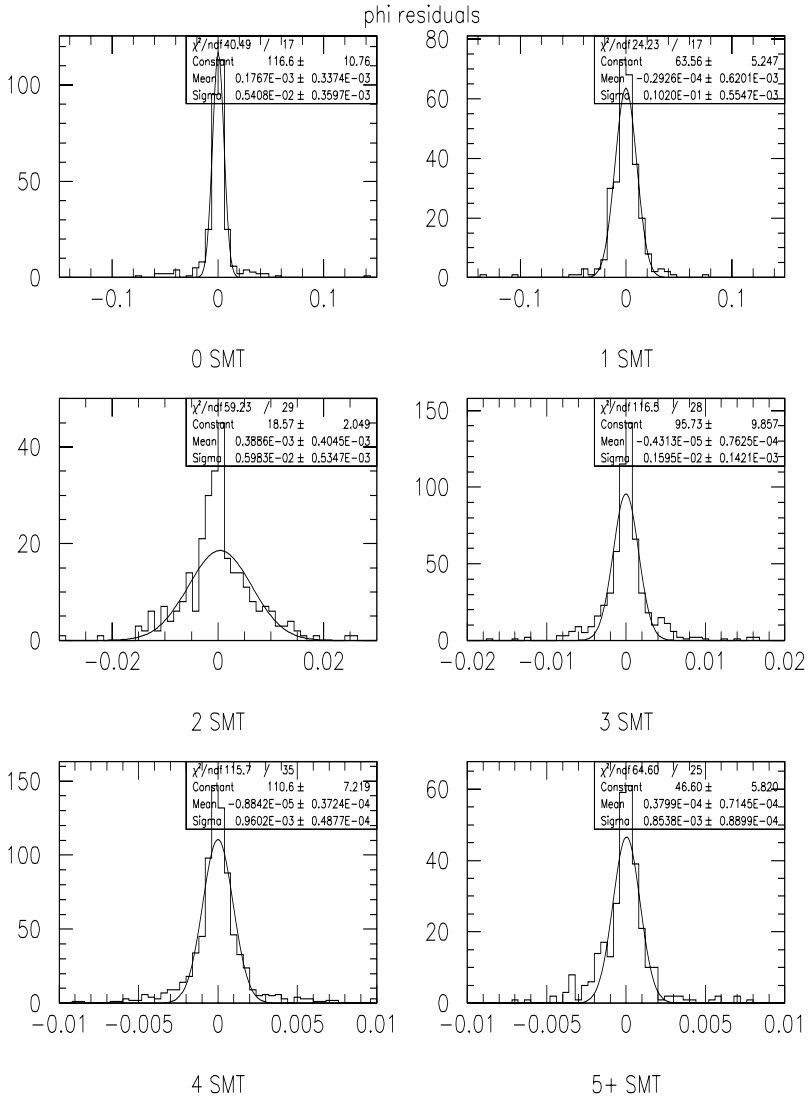

Figure A.18: Residual in the track parameter ϕ_0, for reconstructed and simulated tracks in 100 $t\bar{t} \to lljj$ events, for varying number of SMT clusters on the track.

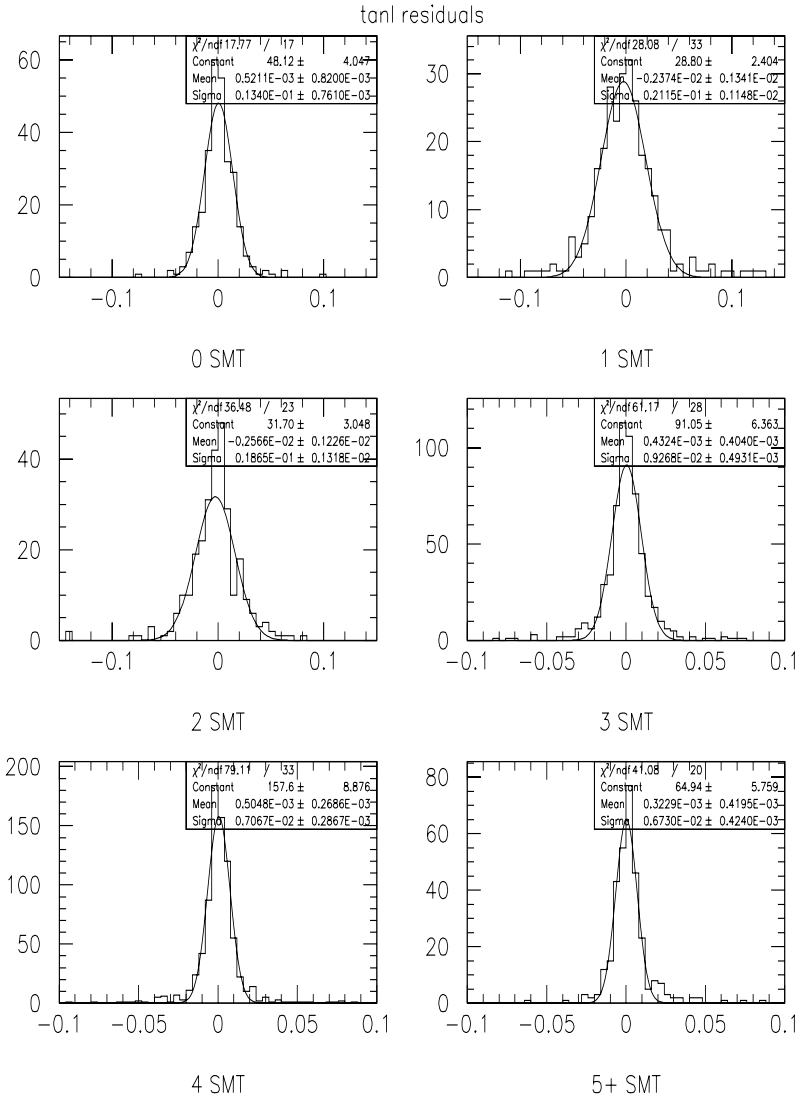

Figure A.19: Residual in the track parameter $\tan\lambda$, for reconstructed and simulated tracks in 100 $t\bar{t} \to lljj$ events, for varying number of SMT clusters on the track.

These errors are assigned to each track based on the number of SMT clusters it has. The track parameter residuals, errors and pulls for the sample of 100 $t\bar{t} \to lljj$ events are shown in Figure A.21. A sample of single electron events were analyzed as a cross-check and the parametrized errors were found reasonable.

A.4.2 Cluster errors

In standard parameter error calculation, the variation of the χ^2 of the track fit is used to measure the errors. This provides a natural connection between the individual cluster errors and the paremter errors. As our parameter errors are not derived from the χ^2, we need to seperately confirm that the cluster errors are reasonable and that the χ^2 value of the tracks are well-behaved.

The individual track cluster errors are constructed in a parametrized fashion as well, based on the width of the cluster, either in fibers or strips for CFT or SMT clusters respectively.

To evaluate the cluster errors, we examine a set of reconstructed tracks. For each hit, the track is refit without that particular hit and the position where the track crosses the detector from which the hit originates is calculated, allowing measurement of the hit to track residual.

Figure A.22 shows the residuals, errors and pulls for tracks reconstructed in simulated single electron events; these events were used to minimize the pollution of fake

hits on the tracks. Figure A.23 shows the results of the same calculations for events from run 160588, and Figure A.24 shows the χ^2 per degree of freedom and the probability.

A.4.3 DCA resolution

The shape of the distribution of the distance of closest approach to the z-axis is a metric by which to measure the tracking performance. The DCA of well-reconstructed tracks from the primary vertex are more likely to be distributed in a narrow Gaussian around the center of the beam than that of poorly reconstructed or fake tracks. The width of the distribution is therefore an indicator of the accuracy of the track parameter fitting and the purity of the sample. The distributions of DCA relative to the center of the beam are given in Figure A.25. Each sample contains only those tracks above the P_T^{min} threshold. Each is fit with a Gaussian and the width extracted; the data was fit to a sum of two Gaussian curves, to represent two classes of tracks. The variation of DCA with P_T^{min} can be seen in Figure A.26.

A.5 Stereo Tracking

As an inspection figure A.11 confirms, the stereo tracking is highly efficient. The ratio of the number of stereo to axial tracks found is given in Figure A.27. The apparant inefficiency is a combination of actual stereo tracking inefficiencies and axial impurities. Figure A.12 shows the stereo hit-finding efficiencies.

A.6 Tests for Online Running

A.6.1 Timing

The P_T^{min} threshold sensitively balances the low-momentum tracking efficiency with tool speed. Figures A.28 and A.30 show the variation of the running time with P_T^{min} for data and Monte Carlo samples. The time consumption drops quickly as a higher threshold decreases the combinatorics.

The timing studies are performed with the non-optimized code on `d0mino`, and the absolute scale should be understood in that context.

A.6.2 Memory Consumption

To gauge the memory consumption, the Level 3 simulator (`Scriptrunner`) was run with a stripped down trigger list over 100,000 events. Figure A.31 shows the total consumption. There are two features, a slow rise at a rate of approximately 100 bytes per event, and several steps which contribute an additional 6 MB of consumption. The first may represent a small memory leak; the second most likely reflects additional memory requested for exceptionally complex events. Both features are being investigated.

A.6.3 Trigger Simulator Verification

A special DAQ run was taken with the tracking turned on at $P_T^{min} = 3.0$ GeV for several filters in full Mark-and-Pass mode, such that it recorded the tracks found in every event and no decisions were made on the results of the tracking. Runs 155603 and 155604 were taken with the special configuration

Offline running confirms that the geometry and calibration files were correctly loaded; this is demonstrated by the total equivalence of CFT and SMT clusters found offline and online. Further, the offline trigger simulator produced results identical to those online.

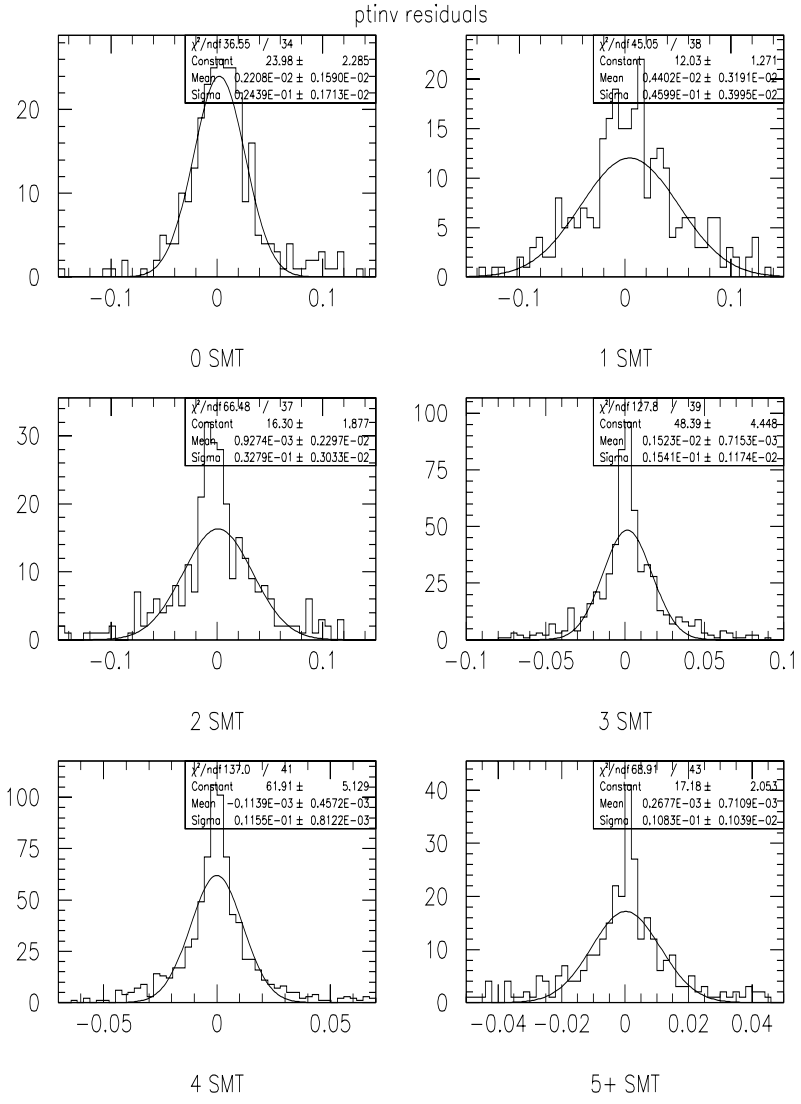

Figure A.20: Residual in the track parameter $\frac{q}{P_T}$, for reconstructed and simulated tracks in 100 $t\bar{t} \to lljj$ events, for varying number of SMT clusters on the track.

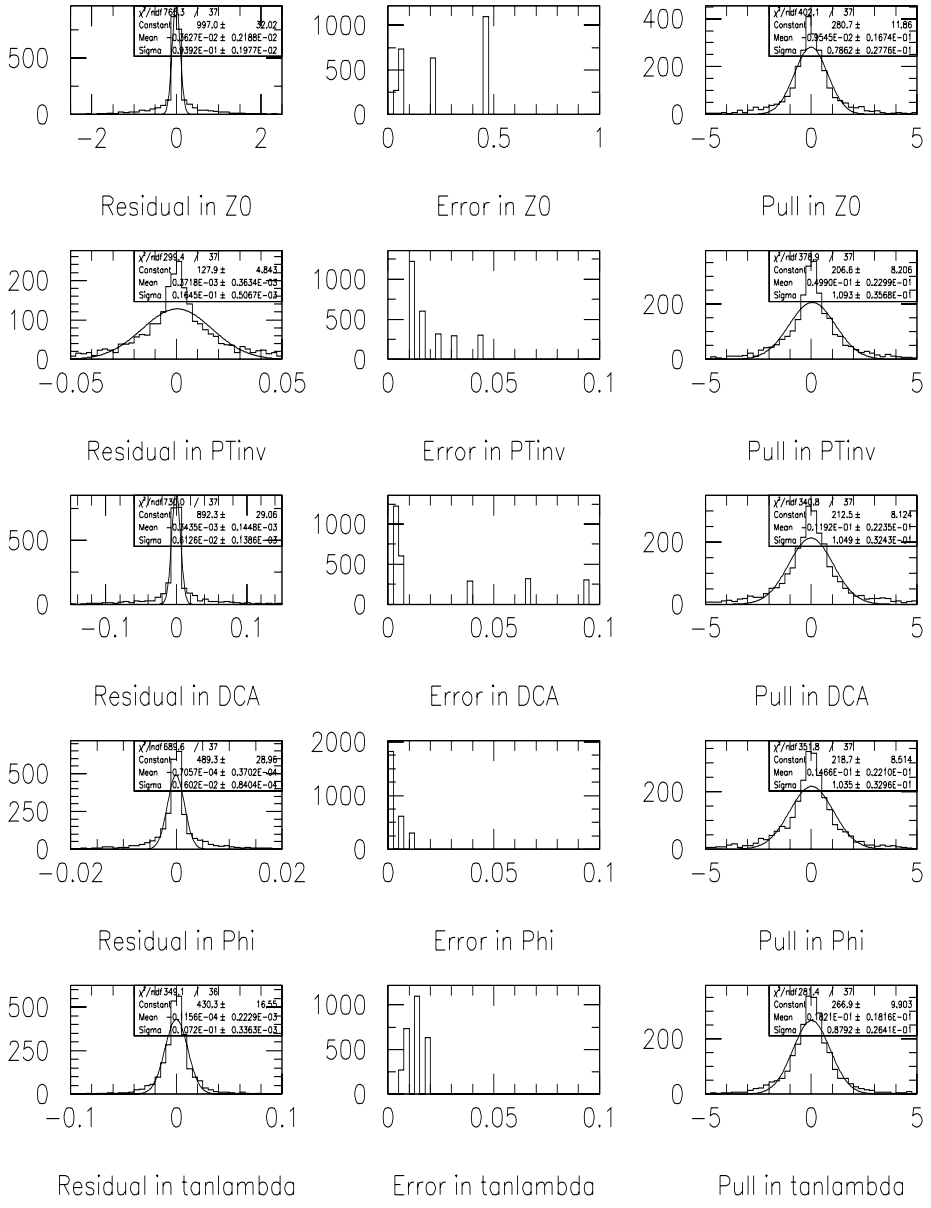

Figure A.21: Residual, error and pull for each of the five track parameters, for reconstructed tracks in 100 $t\bar{t} \to lljj$ events.

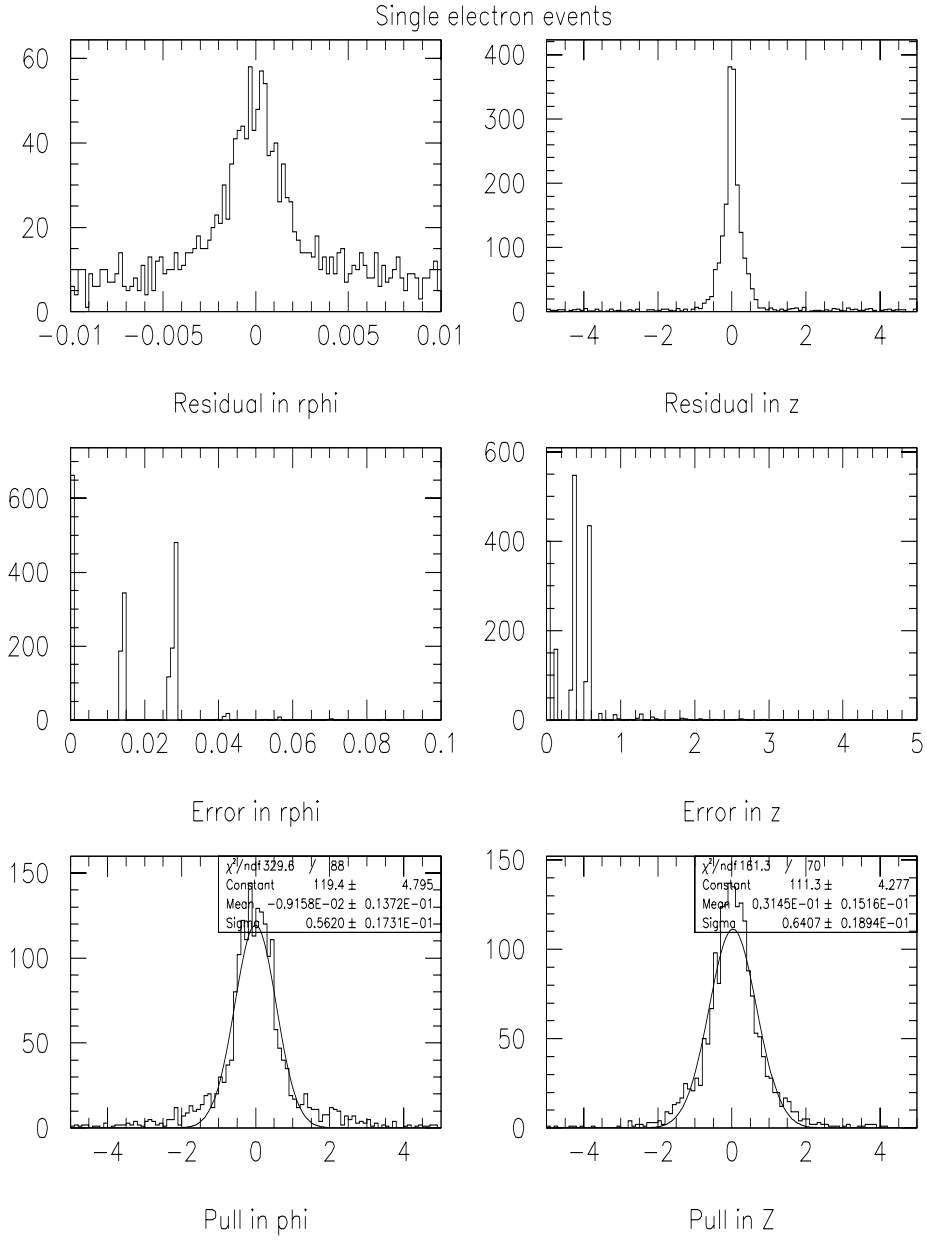

Figure A.22: Top shows hit to track residuals; middle shows cluster errors; bottom shows hit to track pulls. Left column shows quantities in $r\phi$; right column shows quantities in z. From single electron Monte Carlo events.

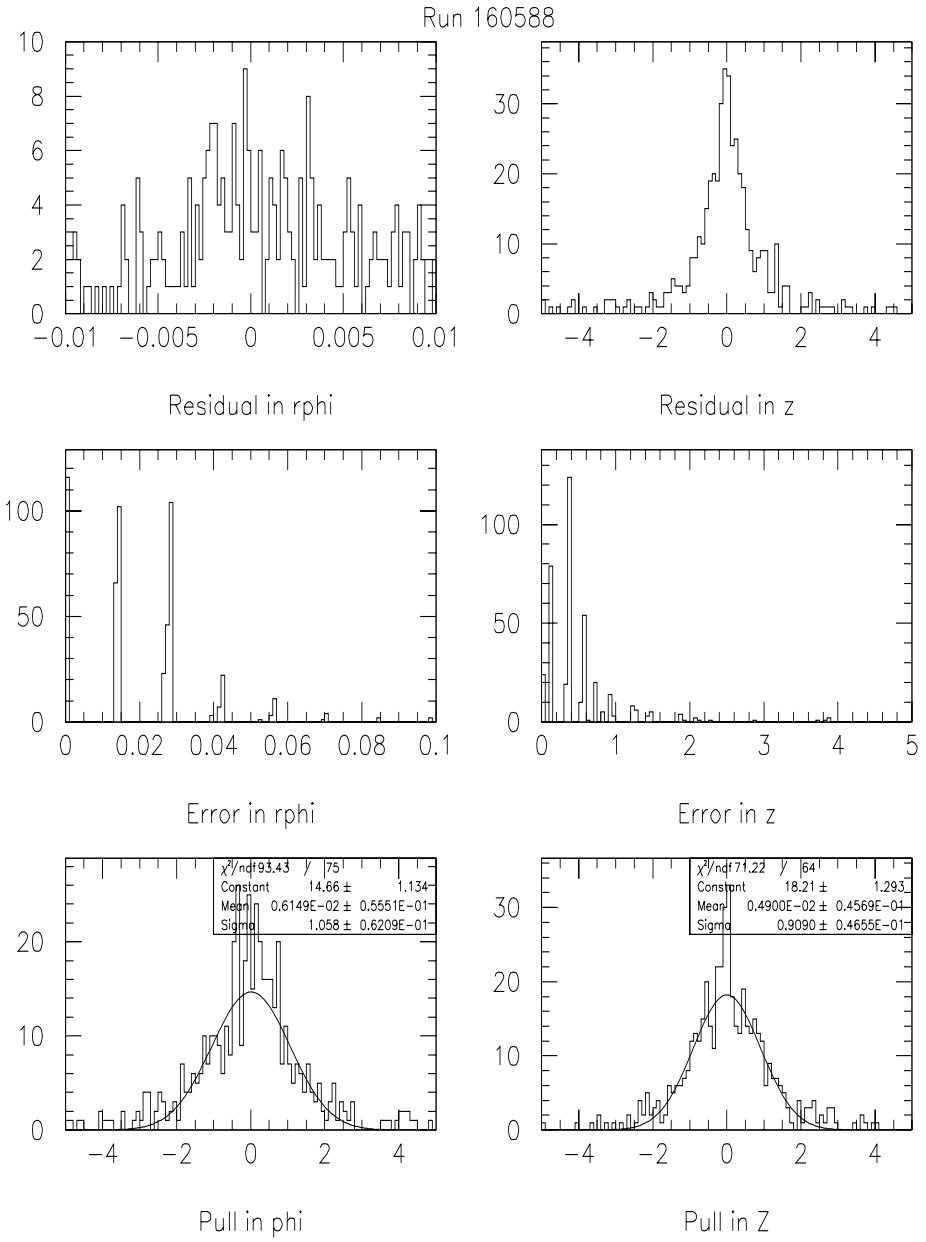

Figure A.23: Top shows hit to track residuals; middle shows cluster errors; bottom shows hit to track pulls. Left column shows quantities in $r\phi$; right column shows quantities in z. From run 160588.

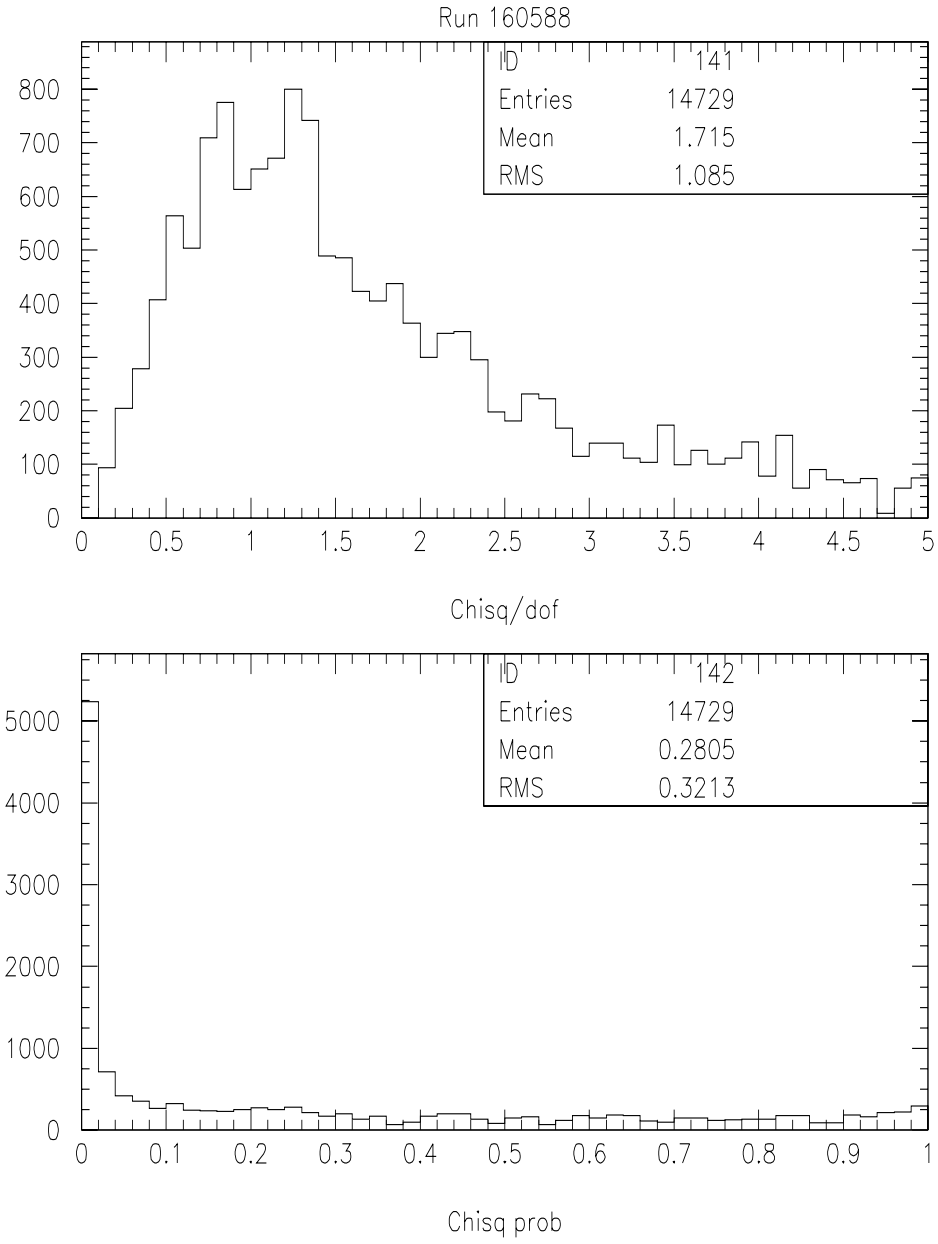

Figure A.24: Top, χ^2/N_{dof} for tracks from run 160588. Bottom, the chi^2 probability for each track.

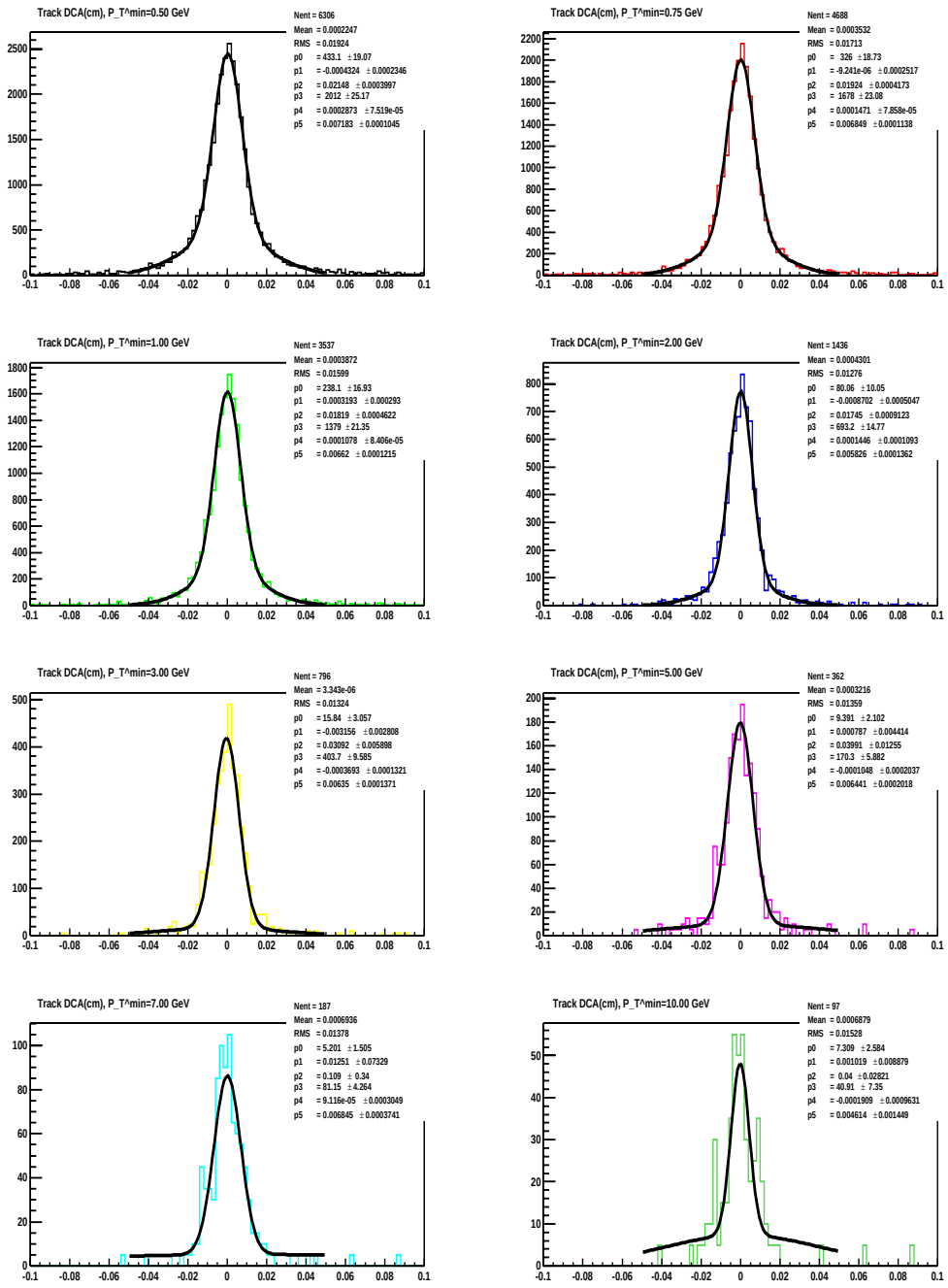

Figure A.25: Distance of closest approach for tracks reconstructed with a given P_T^{min}

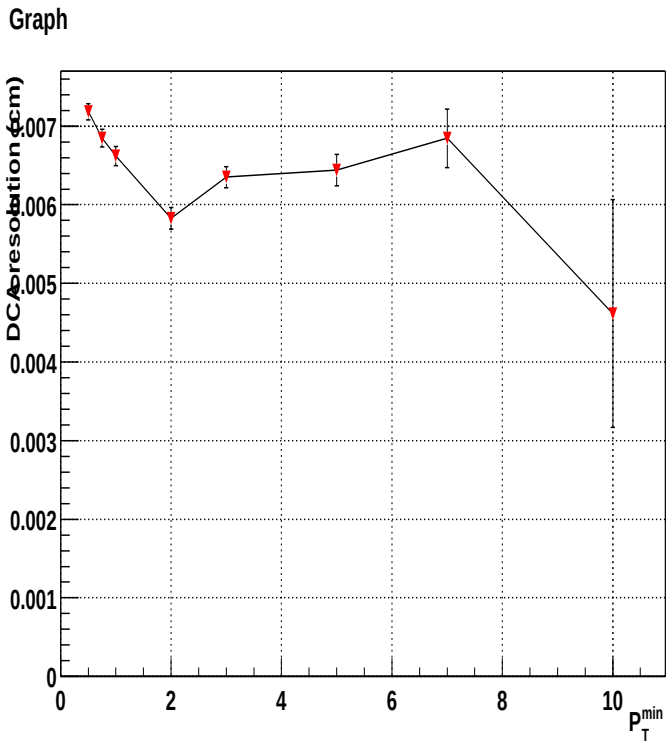

Figure A.26: Variation of fitted DCA width with P_T^{min}

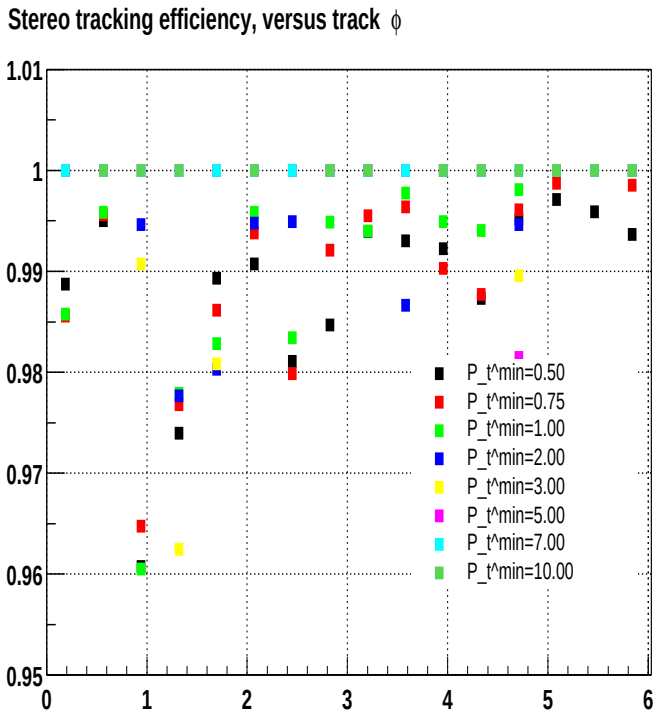

Figure A.27: An estimate of the stereo tracking efficiencies by ϕ, as the ratio of stereo to axial tracks from figure A.11.

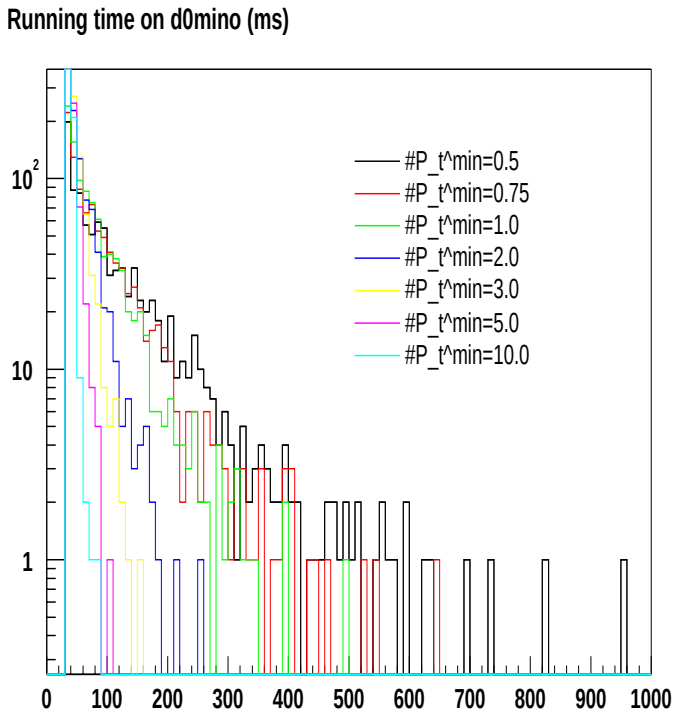

Figure A.28: Distribution of running time on data with varying P_T^{min}.

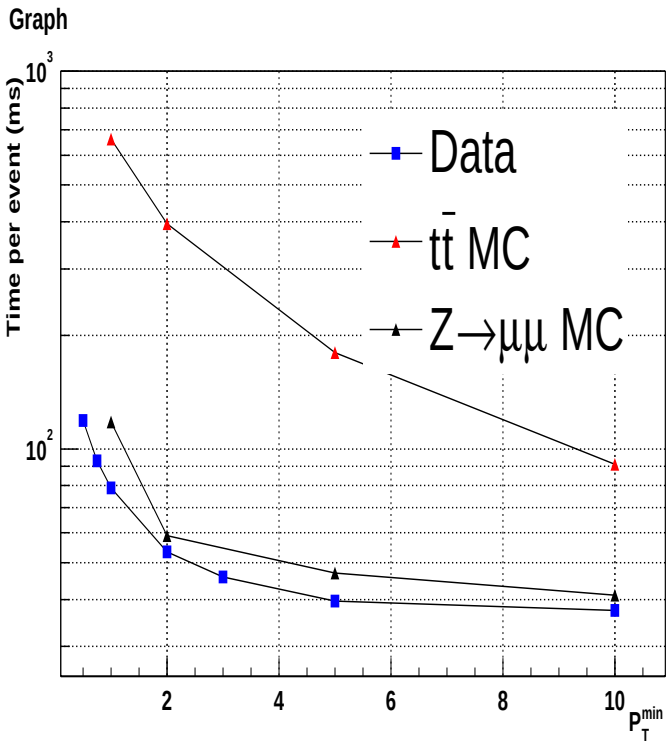

Figure A.29: Variation of timing with P_T^{min}.

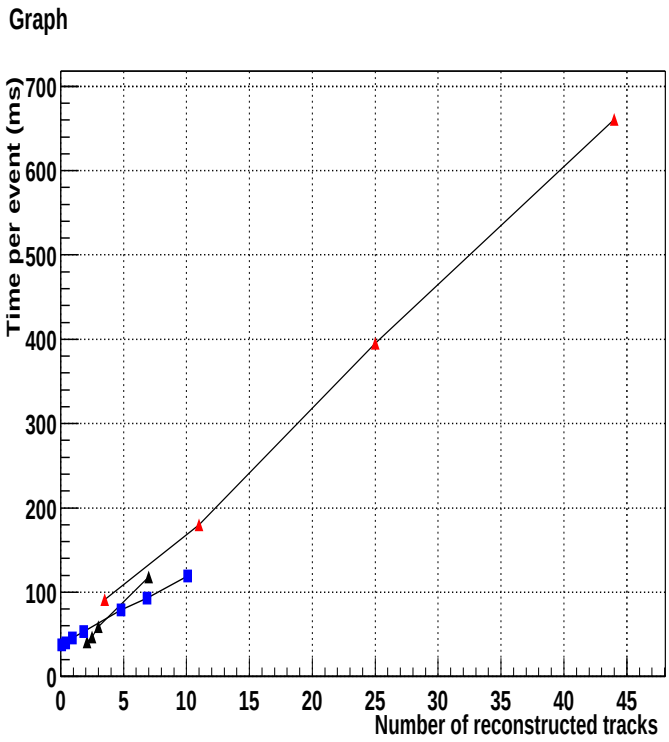

Figure A.30: Variation of timing with number of reconstructed tracks.

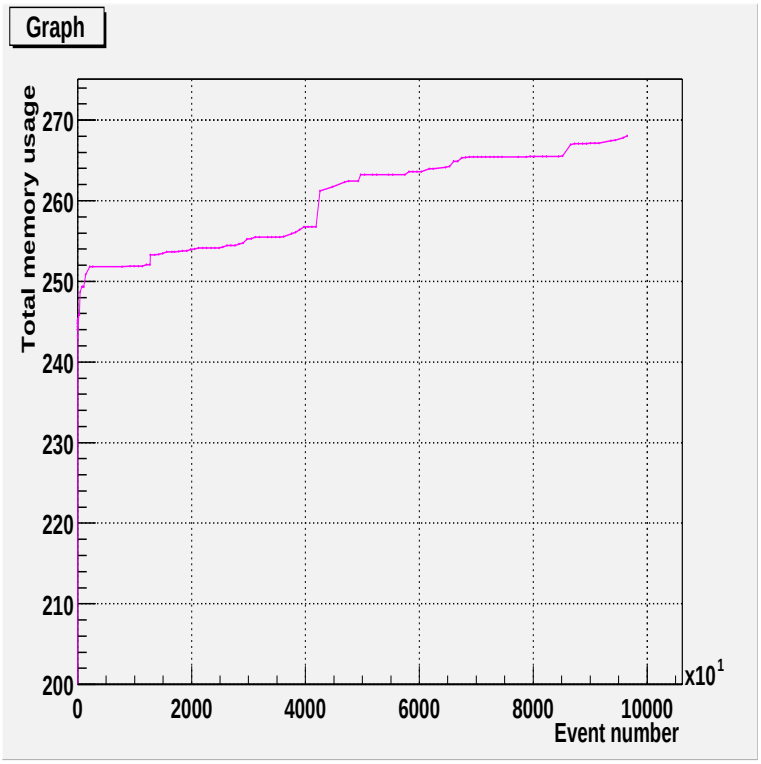

Figure A.31: Total memory consumption by event.

Appendix B

Electron Likelihood

Reconstruction of high momentum electrons is a vital piece of many analyses, including top quark measurements, electroweak processes and searches for new physics. The efficiency of electron reconstruction directly impacts the efficiency to find such events, and the rate at which other objects are misidentified as electrons can limit the sensitivity.

In this note, we present a method for improving the selection of high momentum electrons at the expense of misidentified electrons by replacing the central track confirmation with a likelihood confirmation. A similar approach, with more comprehensive studies of the background components, was done in Run I [50].

B.1 Electron Reconstruction and Variables

Electrons are reconstructed from information in two subdetectors: the calorimeter and the tracking chamber. This typically proceeds in two stages; a cluster is formed in the calorimeter, and subsequently confirmation is sought from the tracking chamber.

Central Track Confirmation

The electron reconstruction in the calorimeter supresses a large portion of the QCD background contamination. However, due to the overwhelming nature of this background, the further rejection of a matching central track has typically been required.

For each EM cluster candidate and each available track, a χ^2, defined as

$$\chi^2_{EM-Track}(\frac{\delta\varphi}{\sigma_\varphi})^2 + (\frac{\delta z}{\sigma_z})^2 + (\frac{E_T/p_T - 1}{\sigma_{E/p}})^2$$

is computed. In these expressions,

- $\delta\varphi$ (resp. δz) denotes the difference between φ (resp. z) of the track impact at the EM3 floor and φ (resp. z) of the cluster position measured therein
- E_T/p_T is the ratio of the measured transverse energy of the cluster to the measured p_T of the track
- σ_φ, σ_z and $\sigma_{E/p}$ are the root-mean-square (RMS) of the experimental distributions of the 3 associated quantities (φ, z and E_T/p_T).

A cluster is matched when the condition $P(\chi^2,\ n_D) > 1\%$ is met by at least one track.

Likelihood Confirmation

The confirmation of an electron by the presence of a central track is a powerful technique. However, in seeking to reduce the background further one may take advantage of further pieces of available information.

We propose to replace the step of track confirmation with a likelihood-based confirmation which has the advantage of taking into account more pieces of information, and which provides characterization of both the background and the signal shapes.

Further, we propose to extract the discrimination in the E_T/p_T variable directly as part of the likelihood, rather than including it in the EM-track match χ^2 quantity. This frees us from assuming the the distribution is Gaussian, and allows us to take advantage of our knowledge of the shape of the background as well. Thus, the likelihood will include six quantities:

- $\chi^2_{spatial} = (\frac{\delta\varphi}{\sigma_\varphi})^2 + (\frac{\delta z}{\sigma_z})^2$
- E_T/p_T, described above.
- H-Matrix, or χ^2_{Cal}, described above.
- EM Fraction, or f_{EM}, described above.

- Distance of Closest Approach (DCA) measures the shortest distance of the selected track to the line parallel to the z axis which passes through the primary vertex position.

- Track Isolation ($\Delta RTrack_2$) measures the distance in R to the track *second* closest to the EM cluster, with the assumption that the closest track is likely to be due to the passage of the electron.

B.2 Sources of Background

As discussed in [50], the predominant sources of background to reconstructed electrons are π^0 showers with an overlapping track from a charged particle and photons converting to e^+e^- pairs. Without a measurement of the energy loss, dE/dx, it is difficult to separate these two components of the background.

In terms of the variables defined above, photon conversions may be marked by the presence of an second track extremeley close to the EM cluster, and a large E_T/p_T; their calorimeter quantities, however, would be nearly identical to that of an electron. Asymmetric conversions would give a nearly irreducible background as the second electron may be very soft.

Neutral pions may also have nearby tracks, as they are produced in association with other charged hadrons; if the track and the EM cluster arise from seperate objects

then their E_T/p_T would not tend to ≈ 1 and their track matching would be poor. Their χ^2_{Cal} and f_{EM} may be worse due to the surrounding hadrons.

Examinations of distributions in these variables do not reveal the existence of subcomponents with distinct shapes. Further examination of correlations between some selected variables, Figure B.2, also fails to reveal clues as to the relative sizes of the components. The broad E_T/p_T and the presence of nearby tracks might suggest a large fraction of photon conversions in the background, for example, but in that case one would expect that the χ^2_{Cal} would more closely resemble that of the signal sample.

B.3 Likelihood formulation

We begin with an empirical description of typical distributions

$$P(\overline{x}|sig), P(\overline{x}|bkg)$$

in a vector of variables $\overline{x}$ for signal and backgroud objects, respectively. Assuming flat prior distributions, we can describe

$$P_{sig}(\overline{x}), P_{bkg}(\overline{x}).$$

We further make the simplying assumption that P is uncorrelated in $\overline{x}$ (see Figure B.2) so that

$$P(\overline{x}) = \prod_i P(x_i)$$

To select between objects that are likely to be signal and those that are likely to be background, we form a simple discriminant,

$$D(\overline{x}) = \frac{P_{sig}(\overline{x})}{P_{sig}(\overline{x}) + P_{bkg}(\overline{x})}$$

B.4 Performance

Dataset definitions

We construct two typical samples, one enriched in electrons and the other in background.

The electron sample is selected from $Z \to ee$ events, requiring

- 2 EM clusters, each with
  - $P_T > 20.0$ GeV
  - $\chi^2_{Cal} < 20, f_{EM} > 0.9, f_{\rm iso} < 0.15$.
- $80 < Mass(e,e) < 100$ GeV

.

The background sample is selected from EM+jet events, which are dominated by QCD di-jet and γ+jet events by requiring

- Exactly 1 EM cluster, with
  - $P_T > 20.0$ GeV
  - $\chi^2_{Cal} < 20, f_{EM} > 0.9, f_{\rm iso} < 0.15$.
- $MET < 15$ GeV
- Exactly 1 jet, with $P_T > 15$ GeV.
- $\Delta R(e, jet) > 2.5$

In both samples, we require that the EM object be associated with a track candidate. This association is make to the track with the largest $Prob(\chi^2_{EM-Track}, N_{dof})$ which satisfies an initial selection

$$|\Delta\phi_{EM,Track}| < 0.05, |\Delta\eta_{EM,Track}| < 0.05.$$

The efficiency to be associated with an track candidate is given in Figure B.5 for both the central region and the endcap calorimeters, and summarized in Table 1.

Sample	Central Cal	Endcap Cal
Signal	77%	63%
Background	6%	15%

Table B.1: Efficiency to have an associated track candidate for signal and background samples, in the central and endcap calorimeters.

Central Calorimeter

In the central calorimeter, we restrict the EM clusters to $|\eta| < 1.1$. Distributions of the six variables are given in Figure B.1 for both signal and background samples. These distributions are used to construct the individual probabilities $P(x_i)$ with which the joint probability $P(\overline{x})$ and the discriminant $D(\overline{x})$ are built. Each of the variables shows some discrimination between the two samples.

We construct the discriminant and measure its separation power by evaluating it on the signal and background samples. Distributions for both samples are shown in Figure B.4 for likelihoods built from increasing subsets of the available variables.

In Figure B.6, we demonstrate the separation power of the likelihood. A simple likelihood which contains the only the information regarding the spatial matching and the E_T/p_T performs just as well as the track matching based on the $\chi^2_{EM-Track}$ quantity, with a small improvement in performance at very high efficiencies. Using the full information available in the six variables, we achieve a marked improvement in background rejection at a given electron efficiency. Note that the signal and background efficiencies assume a candidate track, the efficiency for which is detailed in Table 1.

Threshold	Signal Eff.	Background Eff.
Central Calorimeter		
$D > 0.15$	97%	50%
$D > 0.40$	84%	25%
Endcap Calorimeter		
$D > 0.06$	96%	20%
$D > 0.40$	88%	10%

Table B.2: Sample selection points and their efficiencies

We compare the performance of the likelihood to that of simple square cuts by performing a random grid search over cuts on the 6 likelihood variables. Figure B.8 shows that the likelihood provides superior performance to square cuts.

We investigate the discrimination power of each individual variable by comparing the discrimination achieved by the full likelihood to that achieved by the likelihood constructed without that variable. Figure B.7 shows that each variable, with the surprising exception of $\chi^2_{Spatial}$, contributes unique discrimination.

B.5 Topological Dependence

The construction and efficiency measurements have been conduction on electrons from the decay of the Z. This likelihood discriminant has potential application to other analysis, in which the topology of the event may be very different. We examine the topological dependence of the signal and background efficiencies at a fixed discriminant

threshold. Figure B.9 shows that the efficiencies are fairly stable as a function of jet multiplicity, distance to nearest jet, track multiplicity, vertex z position and electron η.

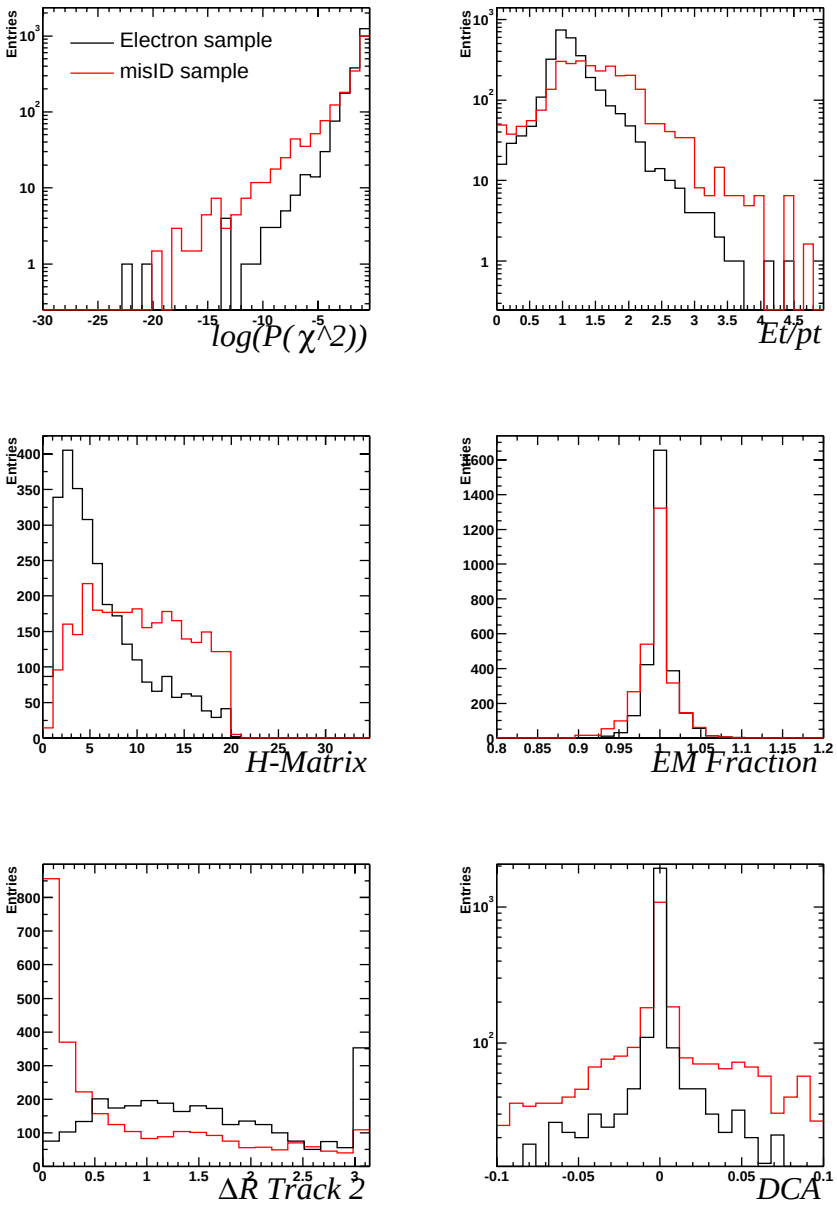

Figure B.1: Distributions of variables used in the likelihood for central calorimeter signal and backgrounds samples, as defined in the text. Distributions are shown only for EM objects which have a track candidate.

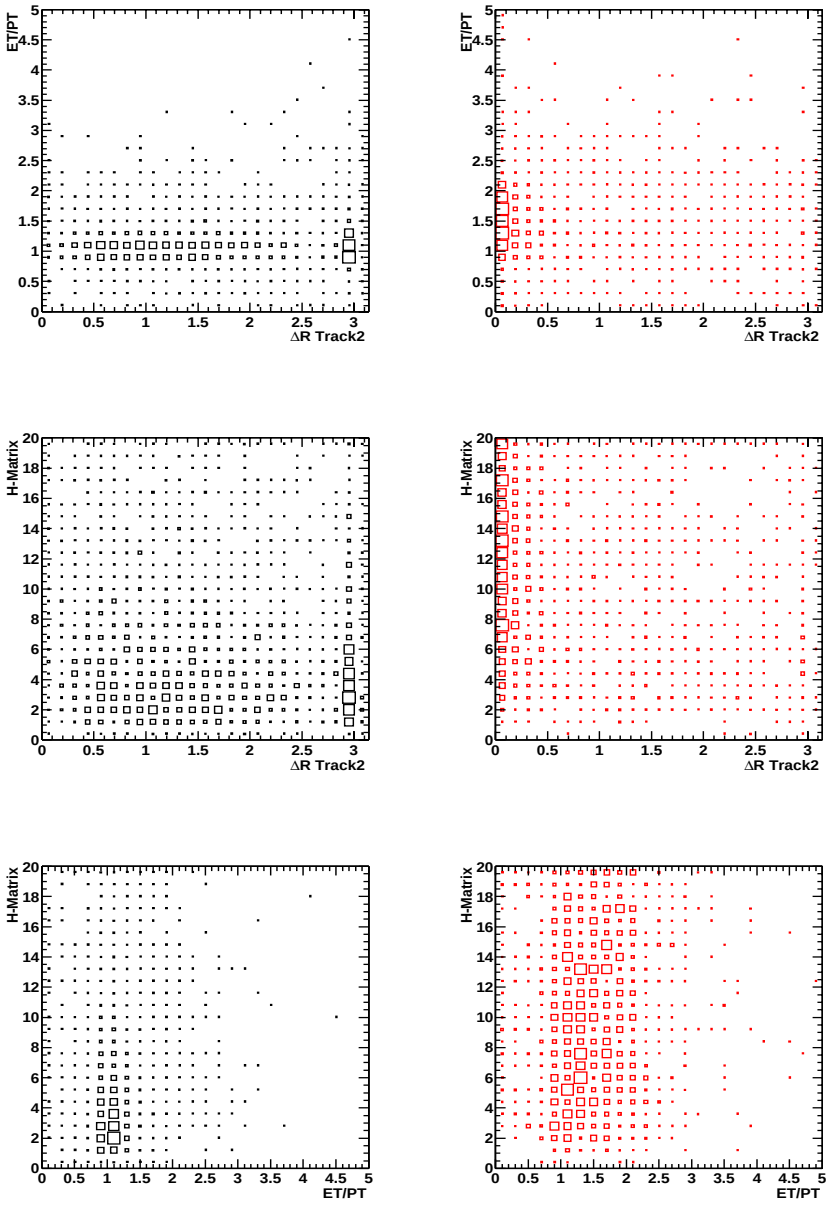

Figure B.2: Correlations between selected variables use in the construction of the likelihood, for the central calorimeter signal sample (*left*) and the background sample (*right*). Distributions are shown only for those electrons which have a track candidate.

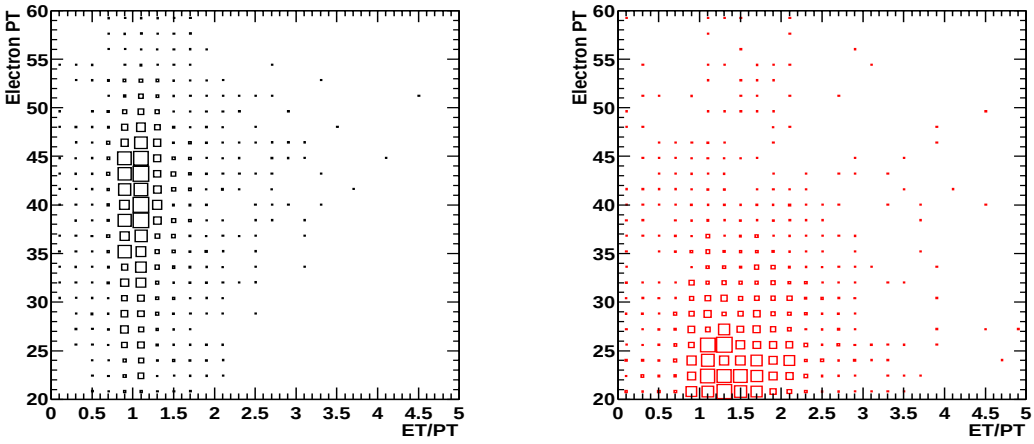

Figure B.3: Correlations between E_T/p_T and electron p_T for the central calorimeter signal sample (*left*) and the background sample (*right*). Distributions are shown only for those electrons which have a track candidate.

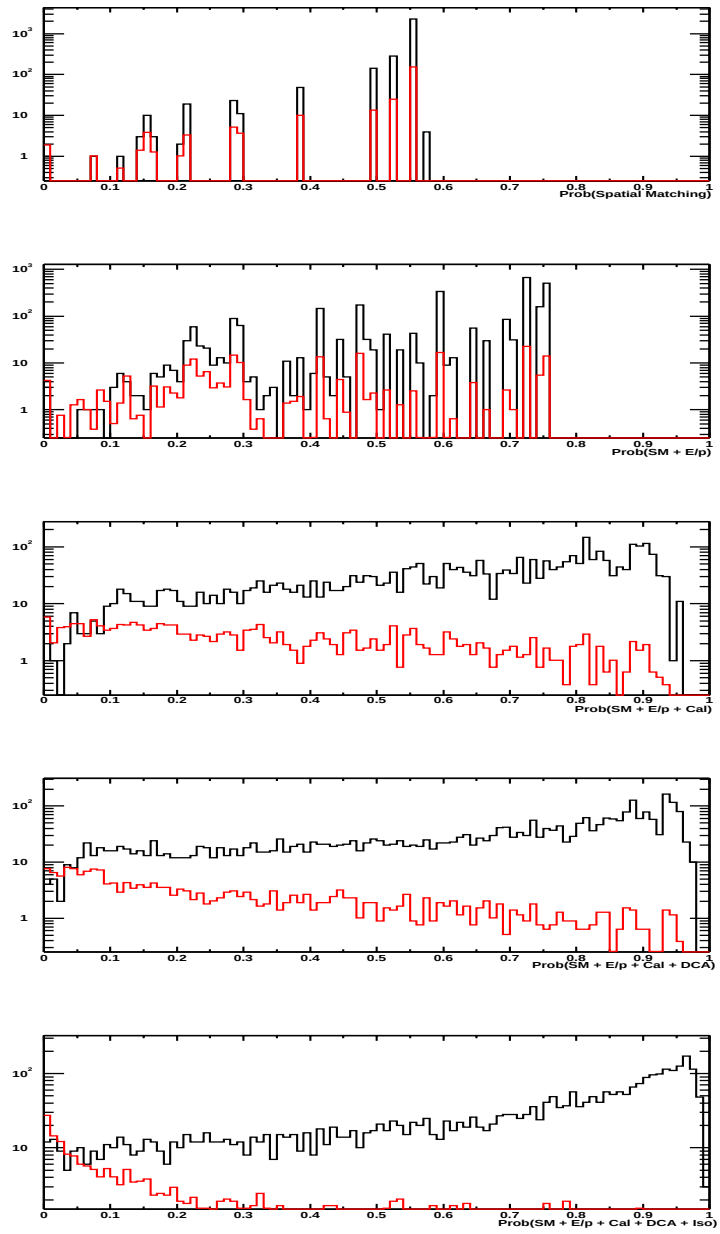

Figure B.4: Distributions of the discriminant $D(\overline{x})$ for central calorimeter signal and background samples, as defined in the text. From top, we begin with the simplist discriminant and add information by including more variables in the joint probability.

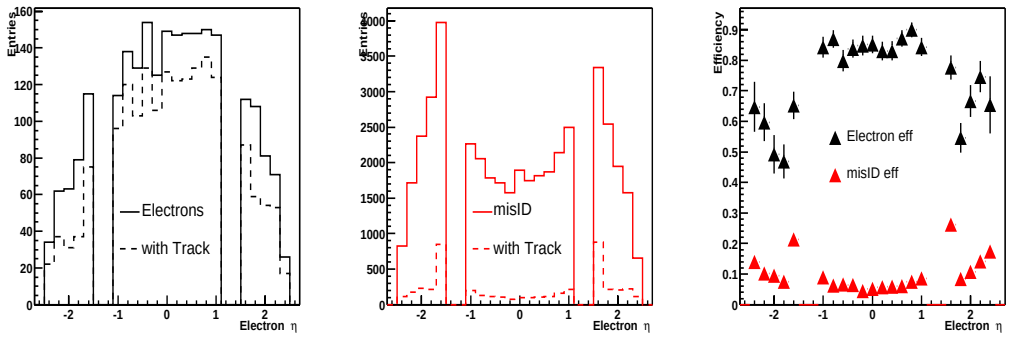

Figure B.5: Efficiencies to have a track candidate for calorimeter EM objects in the signal and background samples.

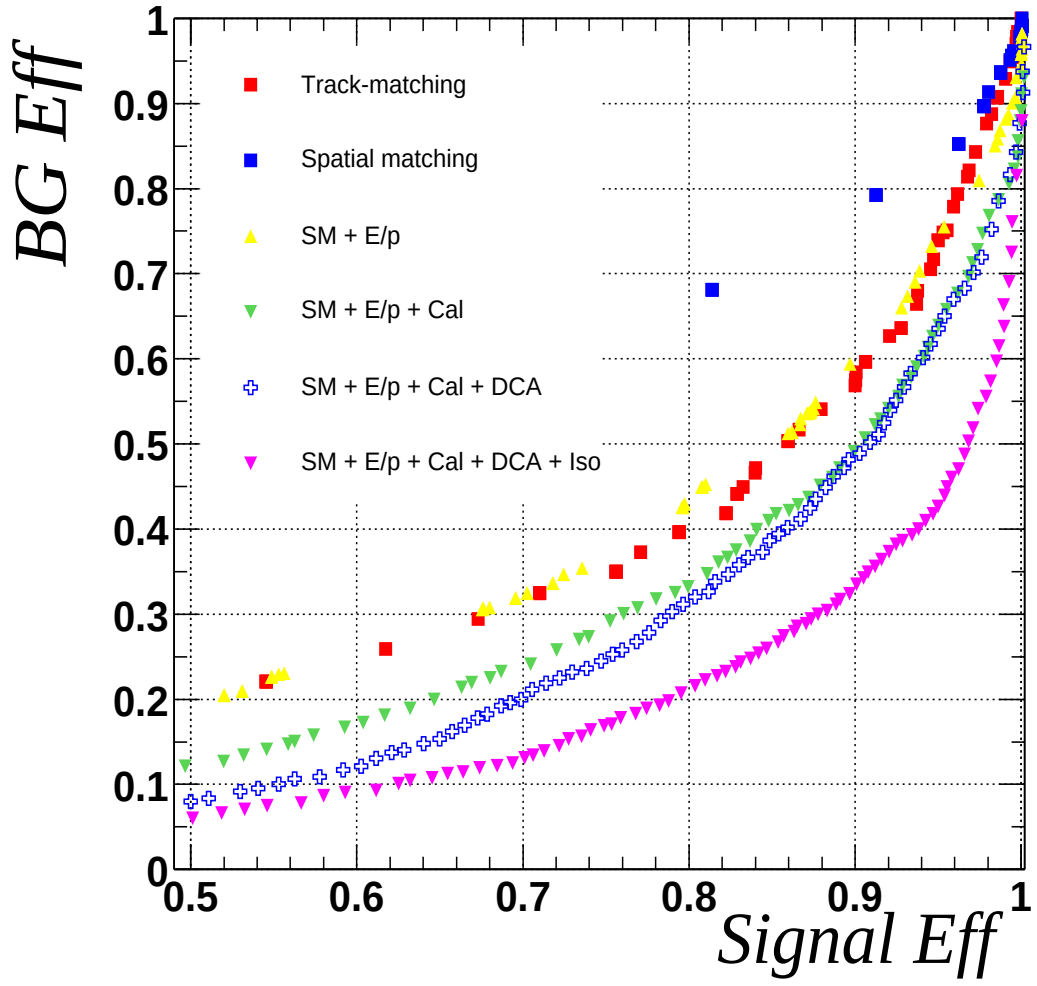

Figure B.6: Signal and background efficiencies in the central calorimeter for varying thresholds of the discriminants shown in Figure B.4. Note that the signal and background efficiencies assume a candidate track, the efficiency for which is detailed in Table 1.

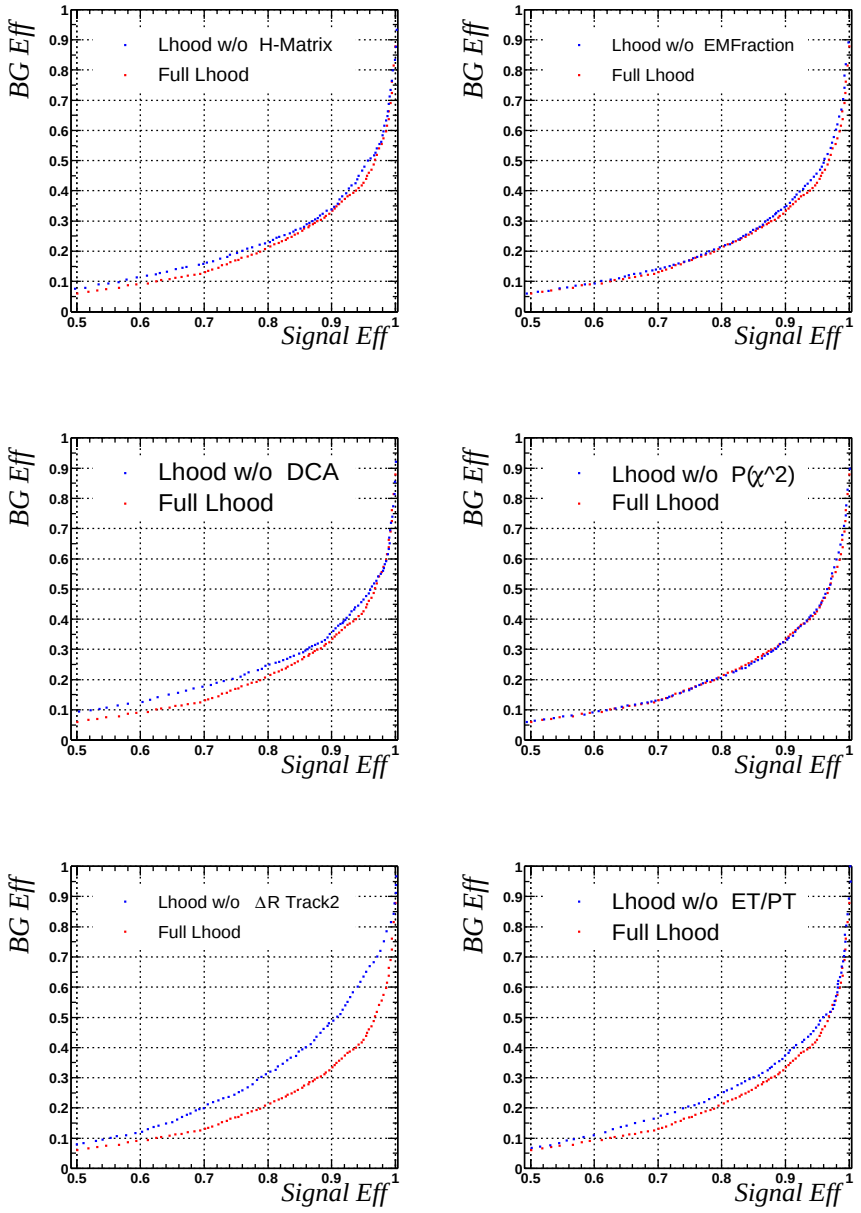

Figure B.7: Signal and background efficiencies in the central calorimeter for varying thresholds of the discriminants, where information from an individual parameter is removed in order to probe its individual discrimination power.Note that the signal and background efficiencies assume a candidate track, the efficiency for which is detailed in Table 1.

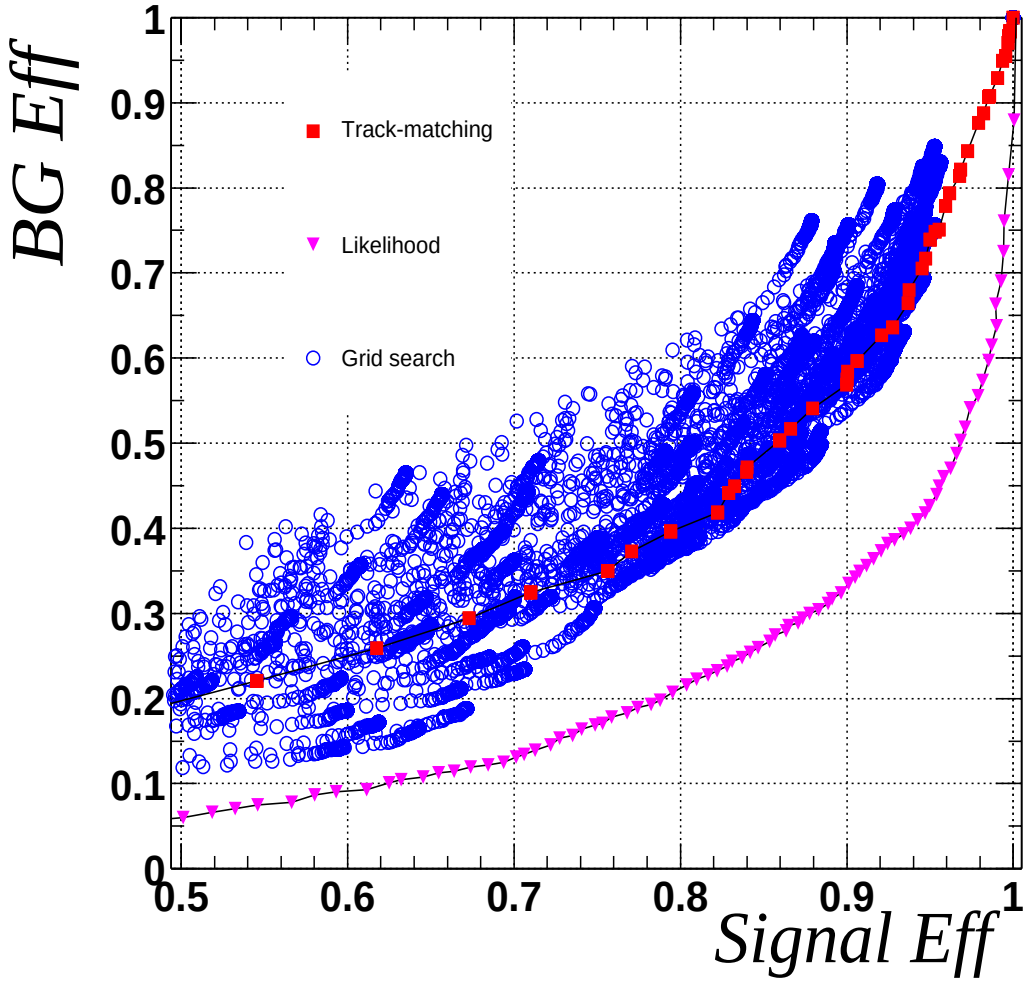

Figure B.8: A comparison of the performance of the track matching, the likelihood and a grid-search in the central calorimeter over the six likelihood variables.

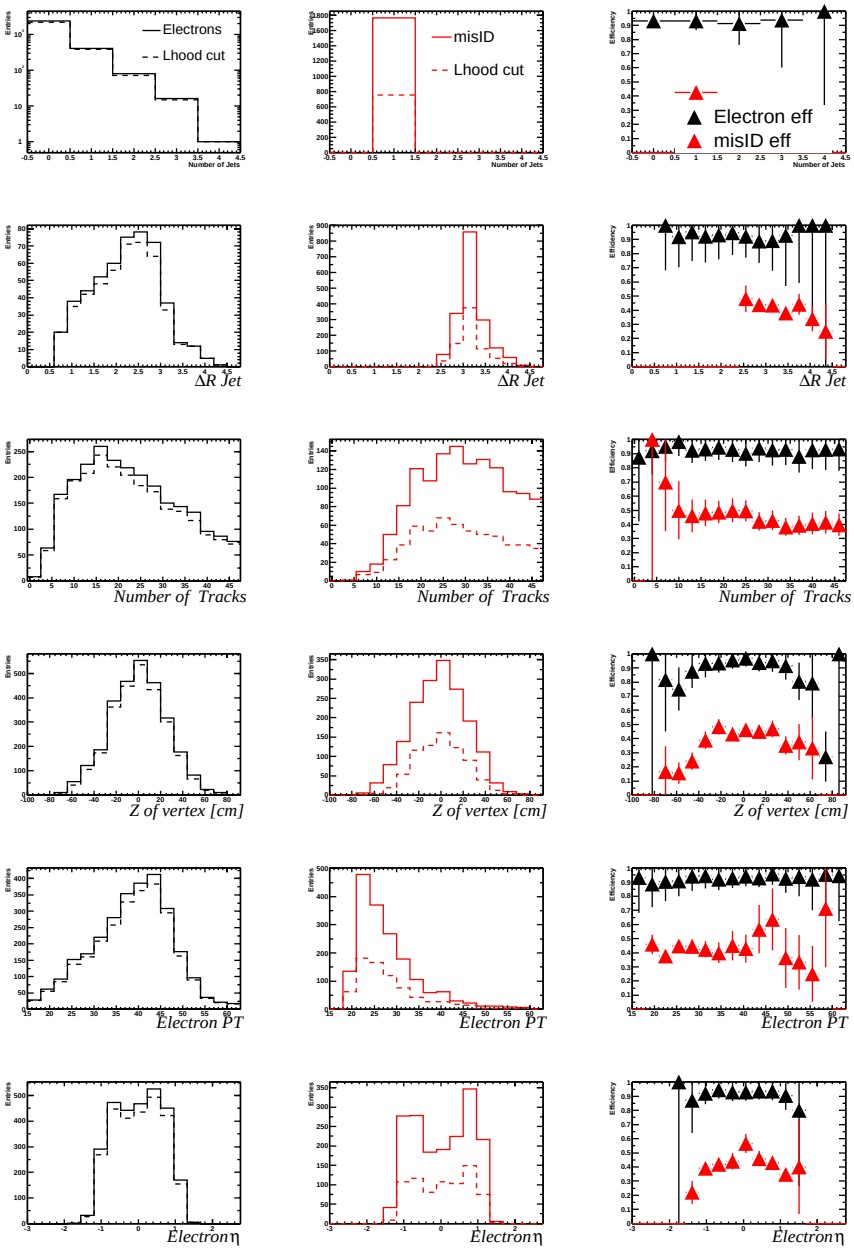

Figure B.9: The topological dependence of the signal and background efficiencies in the central calorimeter given a fixed cut on the discriminant. The distributions in the signal and background samples are the two left columns, respectively. The efficiencies are shown in the rightmost column.

Appendix C

Muon Isolation Strategies

To disentangle high transverse momentum muons due to the decay of W or Z bosons (or any other particle beyond the standard model with similar decay topological features) from the QCD background, it is essential to use the muon's isolation from hadronic activity.. It is thus an inevitable ingredient in analyses such as direct W production, semileptonic top decays, Higgs boson searches and many channels beyond the standard model, for instance searches for charginos and neutralinos. However, as in these topologies the accompanying hadronic activity is variable, defining an universal optimal isolation criteria is impossible. We investigate various isolation strategies and categorize their effectiveness for selecting muons from they decay of Z bosons.

At DØ, the hadronic activity can be measured by three independent components: the calorimeter; the tracker and the preshowers.

Calorimeter energy depositions can be due to noise, to the underlying interactions or to the muon's ionization. The clustering of calorimeter jets yields a measure of the hadronic activity due to a parton from the hard scatering process. The distance between a muon and its nearest jet is one of the simplest criteria for the isolation of a muon. However, as the jet reconstruction is not fully efficient, especially for smaller values of transverse jet momenta, one must construct more elaborate criteria. The tracking activity can also be used to construct isolation criteria; in this case, fake tracks and activity from underlying events must be carefully considered.

Here, isolation criteria which address these difficulties are investigated, optimized and combined. To realistically take into account the experimental running conditions, isolation criteria are studied on data. Direct Z boson production events provides a clean sample of isolated high transverse momentum muons and low missing transverse energy events with a muon are largely dominated by QCD events and can thus serve as background sample. All the isolation criteria discussed herein are thus optimal to select topologies where the hadronic activity is rather low as in direct W boson production. Unfortunately the number of Z events collected to date is too scarse to study isolation criteria with high hard hadronic activity (as in top events) on data. Until more data is available the topology dependence would need to be studied with simulated events. Insiduous biases in the measurement of the efficiencies of isolation criteria should be thouroughly assessed. Effects such as the correlation of the muon P_T with its isolation

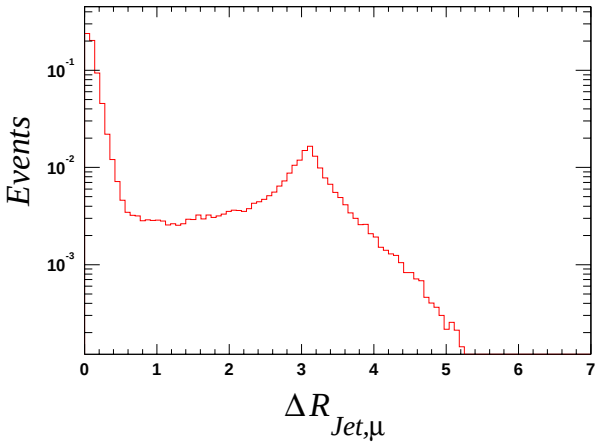

Figure C.1: Distance in R from the muon to closest jet.

in heavy flavor decays, or the influence of isolation on the presence of noise jets can introduce intricate biases.

C.1 Strategies

The strategies of five categories of isolation criteria are discussed. They define isolation with respect to reconstructed jets, reconstructed tracks, reconstructed track-jets, calorimeter energy and track energy.

C.1.1 Jets

To construct a measure of the distance between a muon and a jet consistent with the definition of jets, we define distance as $R = \sqrt{\Delta\phi^2 + \Delta\eta^2}$, also used to define the jet size. It should be noted that this definition is not uniform as a function of pseudo-rapidity. A constant R yields different angles in space at different pseudo-rapidities. A muon will be topologically less isolated at high pseudo-rapidities. Figure C.1 displays the distance R of muons with transverse momentum in excess of 10 GeV/c to their closest jet. This sample is overwhelmingly dominated by QCD background events as no missing energy cut is applied. The distribution shown in Figure C.1 reveals a structure with two peaks. The first, near $R = 0$, contains those events with non-isolated muons where the muon lies within the reconstructed jet. The second smaller peak at $R \approx \pi$ points to a substantial fraction of muons being back-to-back with the closest jet in the event. This effect is even enhanced in heavy flavor semileptonic decays where a large fraction of the energy is taken by the muon and the neutrino thus making it more likely that the jet is not reconstructed. Jet isolation is not a sufficient criterion, especially to distinguish events with low hadron activity.

C.1.2 Calorimeter energy, "Halo Energy"

To skirt the issues of calorimeter jet reconstruction, the calorimeter cell information can be directly used to measure unclustered hadronic activity. The challenge is

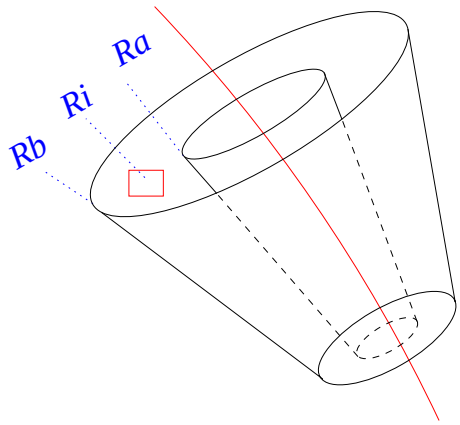

Figure C.2: A hollow cone in R, with inner edge R_a and outer edge R_b surrounding the muon. Calorimeter cell i is included in the cone if $R_b > R_i > R_a$.

therefore to find an algorithm which minimizes the sensitivity to noise, to the underlying event and to the muon's own calorimetric deposits and maximizes the sensitivity to unclustered energy from the hard scattering process. The topological object that was chosen at Run1 to address these requirements was the sum of the transverse energy in the calorimeter cells within a hollow cone in R surrounding the muon, as illustrated in Figure C.2.

$$Halo(R_a, R_b) = \sum_{R_i > R_a}^{R_i < R_b} E_T^i$$

The sizes of the cones defining this variable can be optimized as discussed in Section C.2. Attempts to maximize sensitivity to hadron energy from the hard scattering process considering weighted cell energy sums as a function of their distance to the muon

are investigated ($\propto \frac{1}{R^2}$). Summing the complete cell energies (cell E) and the weighted sum of the cell energies scaled by the distance to the vertex ($\propto 1/r^2$ are also investigated.

C.1.3 Tracks

A measurement of the hadron activity in the event which clearly is not sensitive to noise in the calorimeter is the reconstruction of charged particle tracks. The presence of charged particle tracks is also a measure of jet activity. Furthermore isolation with respect to tracks allows for sensitivity to much smaller transverse jet momenta. Fake tracks due to noise in the tracker and low transverse momentum tracks from the underlying event can also be found. To avoid sensitivty to these tracks a lower cut on the track transverse momentum is required. An optimization of this threshold is discussed in Section C.2.

C.1.4 TrackJets

To generalize this isolation and reduce the sensitivity to individual spurious tracks, one can first cluster the tracks into jets [55]. Track jets are reconstructed using a simple cone algorithm around a seed track and typically require at least two tracks, with a seed above 1 GeV. The advantages of track jets with respect to calorimeter jets are twofold. Track jets are not affected by the large P_T threshold requested for calorimeter jets. Track jets are clustered at the interaction point thus providing an estimation of

the jet width before it is magnified by the deflection of charged particles in the magnetic field. Track jets have the disadvantage to be insensitive to neutral particles.

C.1.5 Track Halo

In analogy to the calorimeter halo variable, we can attempt to avoid the complexity of clustering and the numerous paramater choices it requires by measuring the energy in the tracks surrounding the muon.

$$TrackHalo(R_b) = \sum_{R_i>0}^{R_i<R_b} P_T^i$$

The Track Halo does not require an in inner cone to avoid measuring the contribution from the muon; as muons are required to be matched to a central track, its track energy is perfectly localized. Section C.2 discusses the optimization of the outer edge.

C.2 Performance

C.2.1 Data samples definitions

The data sample used for these studies is comprised of runs 164580 to 166400 reconstructed with reconstruction versions p13.04 and p13.05. No run selection is applied. The definition of a muon requires at least two wire hits in the A and BC segments,

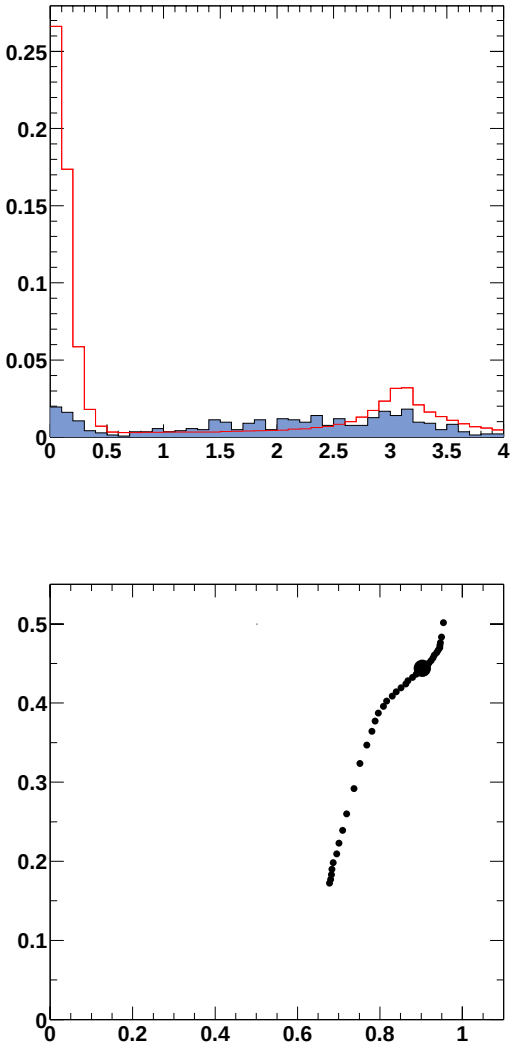

Figure C.3: Distribution of the jet to Muon distance in R (a). Efficiency and purity when R thresholds are varied (b).

at least one scintillator hit in both the A and BC layers, a timing veto (to remove cosmic muons), and a central track match [47]. The muon transverse momentum and charge are given by the global fit to the local muon and central track measurements; if this is not available, the central track information is used.

To measure the performance of isolation criteria, reference samples for both isolated and non-isolated muons are needed. The so-called isolated muon sample, composed of $Z \to \mu^+\mu^-$ events, is selected requiring exactly two oppositely charged muons with P_T greater than 15 GeV within the invariant mass window 75 GeV $< M_{\mu\mu} <$ 105 GeV. No jet requirements or vetoes are made. The sample of non-isolated muons is selected by requiring exactly one muon with transverse momentum in excess of 10 GeV/c and a missing transverse energy (MET) smaller than 15 GeV. The MET is based on the vector sum of the energy of all cells, excepts those part of the coarse hadronic layer, which an energy above 100 MeV. The MET accounts for the transverse momentum of the muon.

The needs of specific analyses differ enough to make a general statement about optimality i it impossible to state with generality which criterion is optimal. To provide a comparison of the isolations which is as general as possible but still informative, we use as a measure of performance the contour in Z-QCD efficiency space. An algorithm whose contour lies outside that of another algorithm (*i.e.* closer to $[Z = 1.0, QCD = 0.0]$) is superior for all choices of Z efficiency (though perhaps not for all topologies). In addition, we quote the QCD efficiency at 90% Z efficiency for purposes of numerical comparison.

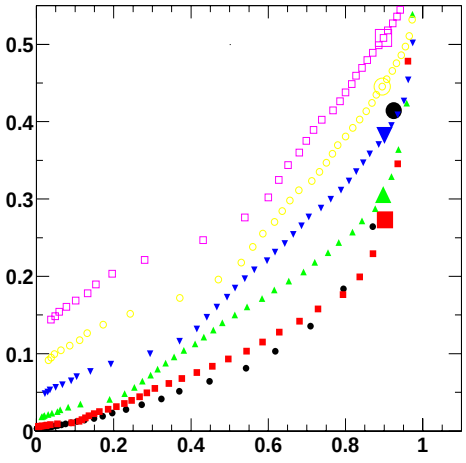

Figure C.4: Efficiency and purity for Track-Muon isolation with different track P_T thresholds.

C.2.2 Jet isolation

Figure C.3a displays the distribution of the distance of muons to the nearest jet distances for both the isolated and non-isolated samples. Despite the low statistic of the isolated muon sample from Z events, when for the background sample the jet in the muon direction is reconstructed the discrimination is striking. The case where the jet is not reconstructed appears also quite clearly in the accumulation of events at $R \sim \pi$. Efficiencies for both samples at various isolation distances are shown in Figure C.3b. Although the lack of data does not allow for fine structures in the signal distribution to be revealed, the shape of the Z versus QCD efficiencies distribution seems to point to an interesting structure (mainly governed by the shape of the background distribution). The first at high efficiency where a clear kink appears at approximately 90% Z efficiency and 45% QCD efficiency. Then down to 70% Z efficiency the gained rejection is not worth the loss in efficiency. Then at lower Z efficiencies the trade off with the rejection becomes slightly more balanced. At 90% Z efficiency, the QCD efficiency is 44.4%.

C.2.3 Track isolation

A track based isolation criterion relies on the minimum requirement imposed on the track transverse momentum. This requirement should be adjusted so that the isolation is not sensitive to unrelated soft particles by considering very low P_T tracks, nor should it lose sensitivity to the jet activity by removing tracks with high P_T. Figure C.4

Isolation	QCD @ 90% Z
Track-Muon, $P_T > 0.5$ GeV	39.2%
Track-Muon, $P_T > 1.0$ GeV	25.7%
Track-Muon, $P_T > 1.5$ GeV	28.9%
Track-Muon, $P_T > 2.0$ GeV	35.9%
Track-Muon, $P_T > 2.5$ GeV	42.7%
Track-Muon, $P_T > 3.0$ GeV	48.6%

Table C.1: QCD efficiencies at 90% Z efficiency for various P_T thresholds for single track isolation.

illustrates the performance of the track-based isolation for various P_T cuts.

Track-based isolation can be done in more than simply two dimensions; one can require that tracks come from the same vertex as the muon. We investigated the possibility to require that the z_0 position of the track is less than 2 cm from the muon, but found no improvement in performance.

C.2.4 Track-Jet isolation

Track jets, as described in [55] are built by clustering tracks around a high-P_T seed. For events with a high-P_T muon, this tends to create a trackjet around the muon in nearly every case. We modified the algorithm to remove the muon track from the list of seeds; the performance is dramatically improved. The performance can be seen in Figure C.10. The QCD efficiency at 90% Z efficiency is 41.3%.

Isolation	QCD @ 90% Z
Track Halo 0.3	28.7%
Track Halo 0.5	26.1%
Track Halo 0.7	30.5%

Table C.2: QCD efficiency at 90%Z efficiency for various track halo cone sizes.

Isolation	QCD @ 90% Z
Halo(0.2, 0.3)	37.7%
Halo(0.2, 0.4)	35.2%
Halo(0.2, 0.5)	34.8%
Halo(0.2, 0.6)	41.0%

Table C.3: QCD efficiency at 90%Z efficiency for various halo outer edges.

C.2.5 Track Halo

Track halo isolation sums the P_T of the tracks surrounding the muon. The inner edge of the cone does not need tuning, only the outer edge. We consider cones of width $0.3, 0.5$ and 0.7, see Figure C.5.

C.2.6 Halo Isolation

Halo isolation calculates the energy deposited in the calorimeter in a hollow cone in R around the muon track. The cone is drawn from the location of the primary vertex in the event, in the direction given by the central track matched to the muon.

At Run1, a cone with edges at (0.2, 0.6) was used. We begin with this cone size and vary the outer edge, as shown in Figure C.7a.

Isolation	QCD @ 90% Z
Halo(0.00, 0.4)	35.4%
Halo(0.05, 0.4)	26.9%
Halo(0.10, 0.4)	23.5%
Halo(0.15, 0.4)	27.9%
Halo(0.20, 0.4)	35.2%
Halo(0.25, 0.4)	40.3%

Table C.4: QCD efficiencies at 90% Z efficiency for various P_T thresholds for various halo inner edges.

An outer edge of 0.4 or 0.5 is preferred; this implies that the extra sensitivity of the larger cone is outweighed by its susceptibility to accumulated noise. We choose 0.4 in order to minimize the effects of noise.

We then vary the inner edge of the cone, see Figure C.7b.

These results suggests that an inner cone width of 0.10 is preferred. To see this more clearly, we measure the variation in background efficiency with the inner cone size, for given signal efficiencies, Figure C.8. The shallow minimum about 0.10 indicates that an inner cone of 0.10 maximizes the sensitivity to nearby jets while cutting out the largest portion of the muon's own energy deposition. The shallowness of the minimum is a measure of the insensitivity of the performance with respect to this parameter; that the performance does not deteriorate rapidly with varying cone sizes is a comforting effect.

Performance of some variations on the simple cone can be seen in Figure C.9.

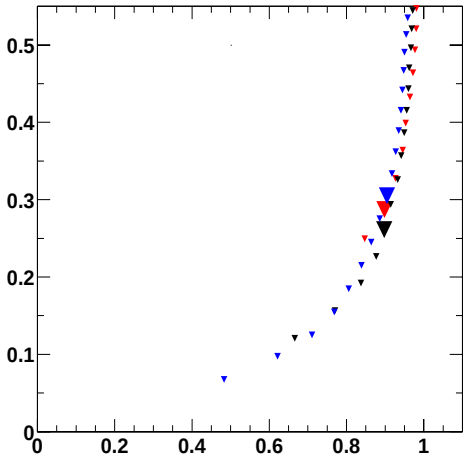

Figure C.5: Efficiency and purity for TrackHalo isolation with different outer cone sizes.

Isolation	QCD @ 90% Z
Halo(0.10, 0.4)	23.5%
Halo(0.10, 0.4) $\propto \frac{1}{R^2}$	28.4%
Halo(0.10, 0.4) $\propto \frac{1}{r^2}$	23.2%
Halo(0.10, 0.4) cell E	25.5%

Table C.5: QCD efficiencies at 90% Z efficiency for various P_T thresholds variations of the simple halo energy.

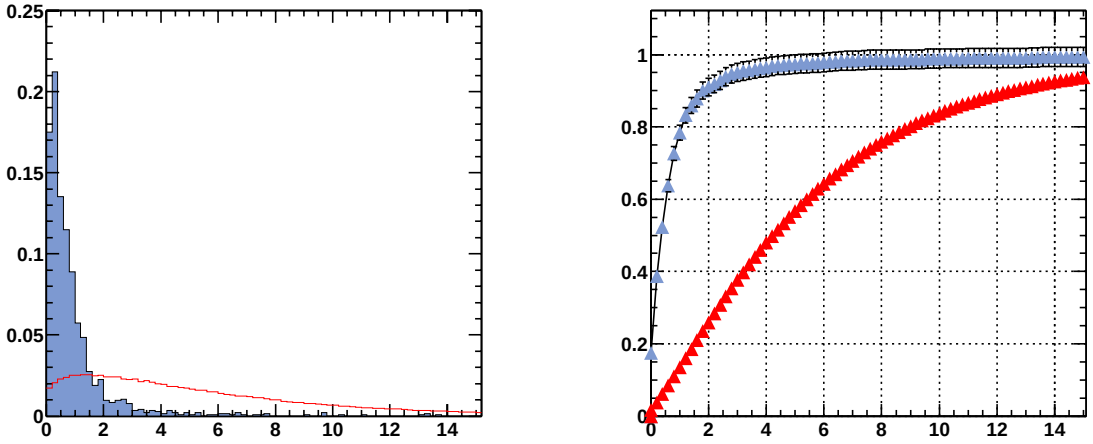

Figure C.6: Halo energies for Z and QCD samples (*left*). Efficiency for both samples as a function of the threshold (*right*).

C.2.7 Individual isolations

For each individual isolation strategy, the optimized performance can be seen in Figure C.8, for both central and forward muons.

C.2.8 Combined Isolations

To obtain an improved performance, one must consider combining two types of isolation strategies to take advantage of the strengths of both. We combine jet, track and track-jet isolation with calorimeter cell (halo) isolation.

We first determine the value of the cut on the calorimeter halo energy by com-

Isolation	QCD @ 90% Z central	forward
Muon-Jet	42.0%	47.1%
Halo(0.1, 0.4)	26.2%	20.6%
Muon-TrackJet	43.1%	39.0%
Muon-Track	28.4%	25.7%
Track Halo	27.1%	24.4%

Table C.6: QCD efficiencies at 90% Z efficiency for various P_T thresholds for individual isolation strategies.

Isolation	QCD @ 90% Z central	forward
Halo(0.1, 0.4) + Muon-Jet	28.8%	28.7%
Halo(0.1, 0.4) + Muon-Track	21.0%	23.2%
Halo(0.1, 0.4) + Muon-TrackJet	24.5%	22.7%
Halo(0.1, 0.4) + Track Halo	20.8%	18.5%

Table C.7: QCD efficiencies at 90% Z efficiency for various P_T thresholds for combined isolation strategies.

paring the performance of track isolation for various cuts in the calorimeter halo energy. Figure C.11 shows the performance of track halo isolation for cuts of $\{2.0, 2.5, 3.5, 5.0\}$ GeV corresponding to efficiencies on the Z sample of $\{90.0\%, 93.0\%, 95.0\%, 98.0\%\}$. Each combined isolation curve has an endpoint which lies on the single halo isolation curve, from where it departs. The contour corresponding to a cut at 2.5 GeV has the best performance.

To evaluate the combined isolations, we fix the cut on the calorimeter halo energy at 2.5 GeV and vary the secondary isolation requirement.

We compare the performance of the combined strategies in Figure C.12.

C.3 Discussion

A set of tools to optimally define the isolation of a muon with respect to hadronic activity from the hard scattering process has been defined. Their performance in discrimination between muons from QCD processes and those from W or Z production has been measured. The results stated in this note are valid for topologies with low hadronic activity; the detailed performance should be carefully studied for any specific analysis.

The simple definition of isolation with respect to reconstructed jets has been demonstrated to be ineffective in comparison with a measure of unclustered calorimeter energy surrounding the muon. In addition, a significant improvement can be made in performance by using information from the tracking detector to further isolate the muon.

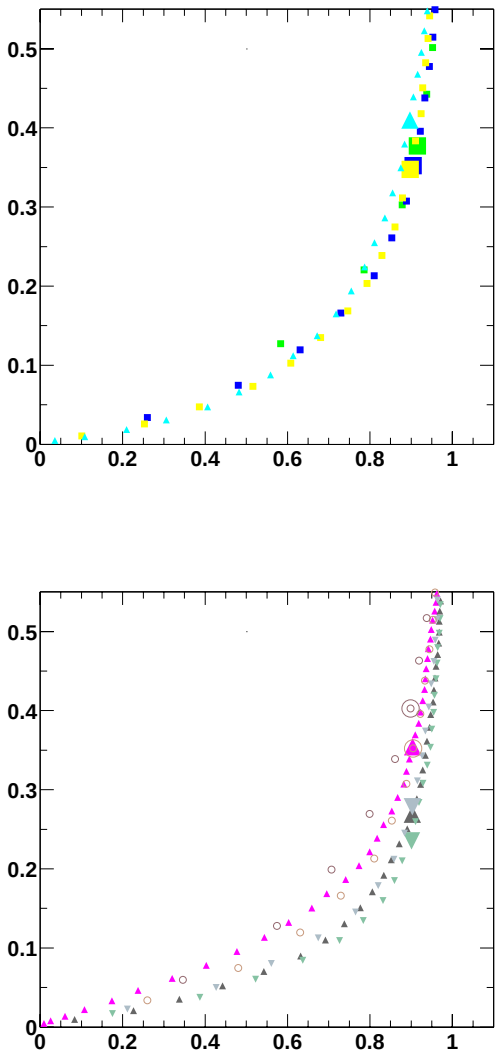

Figure C.7: Efficiency versus purity for varying cone sizes for halo isolation. Optimizing the outer cone (a), and the inner cone (b).

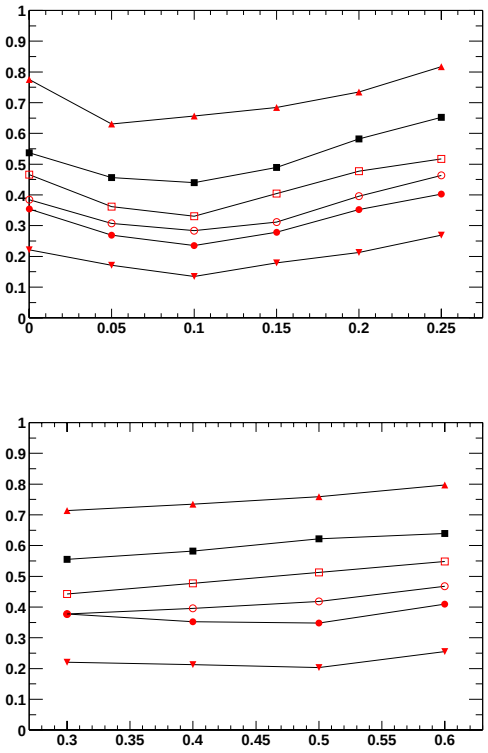

Figure C.8: QCD efficiency for different inner cone sizes, at given signal (Z) efficiencies.

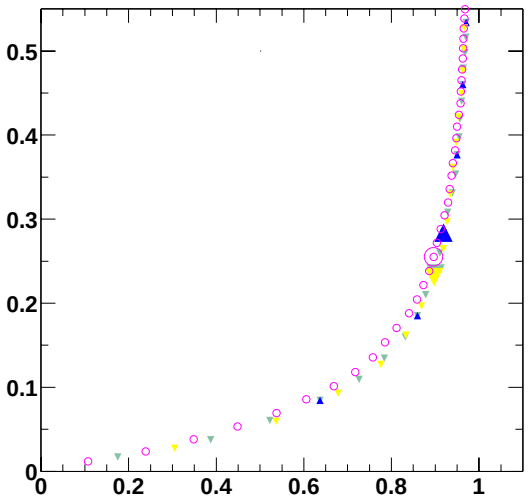

Figure C.9: Signal and background efficiency for variations on the simple cone summation.

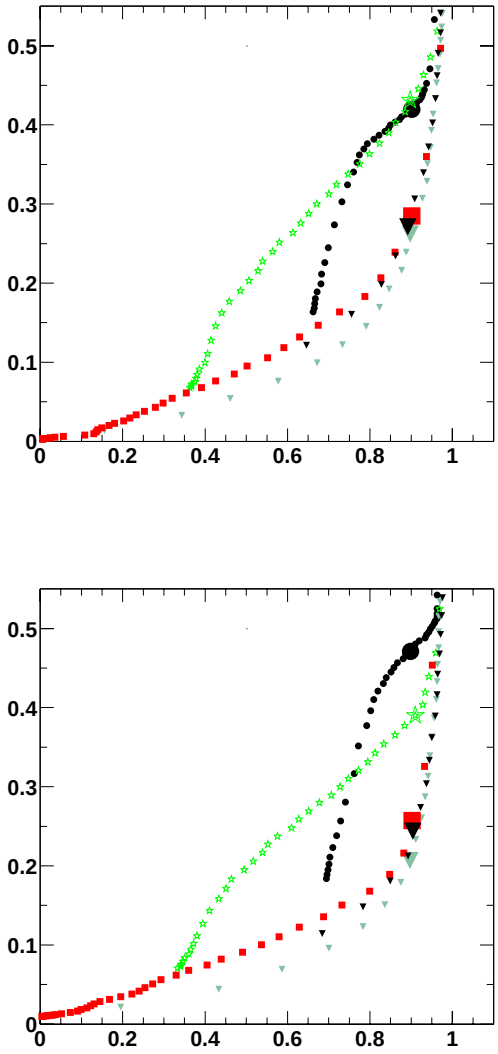

Figure C.10: Signal and background efficiency for isolation strategies for central muons ($|\eta| < 1.0$, *left*) and forward muons ($|\eta| > 1.0$, *right*).

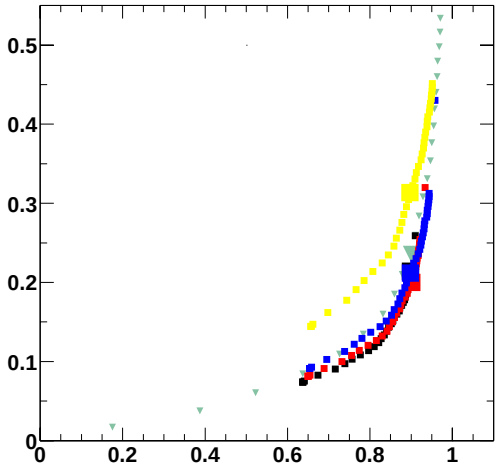

Figure C.11: Efficiency and purity curves for signal and background samples for track halo cuts, with different calorimeter halo cuts. Each curve begins at the calorimeter halo curve and describes the performance of the combined isolations.

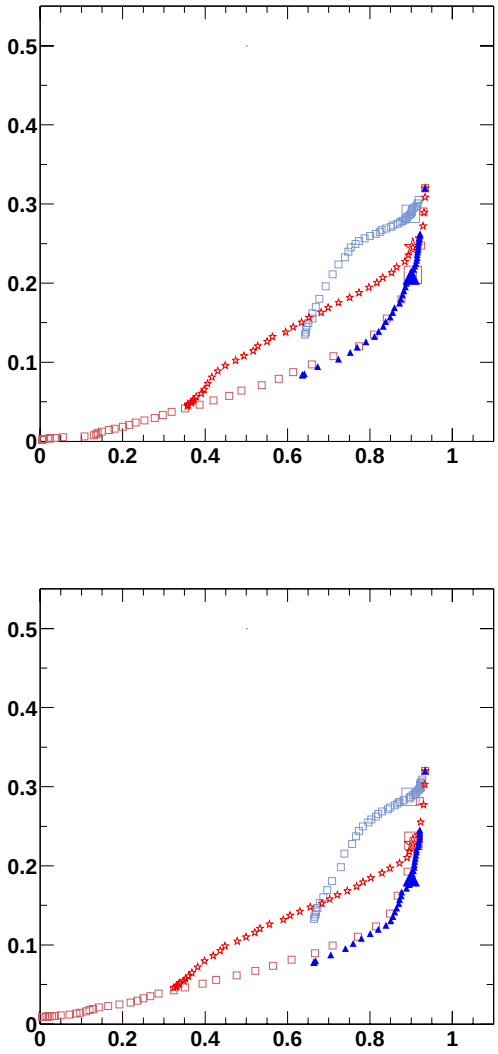

Figure C.12: Signal and background efficiency for isolation strategies for central muons ($|\eta| < 1.0$, *left*) and forward muons ($|\eta| > 1.0$, *right*).

Appendix D

Support Vector Machines

Reconstruction of the products of a collision provides the topology of the final state. This topology can help reveal the kinematics of the collision, but it is rarely sufficient to uniquely identify it. Sophisticated techniques such as neural networks[56, 61] have been successfuly used to take maximal advantage of the topological information in disentangling events produced by a specific process from those processes which may mimic it.

We describe a more modern algorithm, the support vector machine (SVM), [57, 69] which performs the same function in a novel way. SVMs learn the distinctions between different classes of input, such as signal and background, by identifying the essential features of the classes which are crucial for differentiation. As is described below, they transform the problem into a convex optimization problem, guaranteeing

that local performance maxima are global and avoiding the heuristics of nueral network architecture design.

In Section 2, we briefly describe the support vector regression approach to this problem, following [69] and [57]. Section 3 provides a detailed example of its application to the search for a theoretically predicted and experimentally persued particle, the Higgs boson and compares its performance to that of artificial neural networks.

D.1 Support Vector Regression

D.1.1 Linear Regression

The challenge facing any regression algorithm is: given l pieces of training data $\{(\bar{x}_1, y_1), (\bar{x}_2, y_2), \ldots, (\bar{x}_l, y_l)\} \subset \mathbb{R}^n \times \mathbb{R}$, where $\bar{x}_i$ represents a position in an n-dimensional parameter space, find a function $\vec{x} \to f(\vec{x}) : \mathbb{R}^n \to \mathbb{R}$ such that

$$| f(\bar{x}_i) - y_i | < \epsilon. \tag{D.1}$$

In this case, ϵ represents the maximum allowed deviation from the training data. The regressor cannot be measured solely on the basis of its performance on the training sample; we seek to balance the algorithm's training performance with its simplicity. See [57] for discussions of machine capacity. We begin with the simple linear problem, and then show in Section 2.2 how it can be extended to non-linear cases. In the case of a

linear regressor of the form

$$f(\bar{x}) = \bar{x} \cdot \bar{w} + b, \tag{D.2}$$

the function's simplicity is measured by its Euclidean norm, $\|w\|^2$. The problem is formally stated as:

$$\begin{array}{ll} \text{minimize} & \|w\|^2 \\ \text{while} & \mid \bar{x} \cdot \bar{w} + b - y_i \mid < \epsilon. \end{array} \tag{D.3}$$

Formulating the problem in Lagrangian terms, we introduce a positive Lagrange multiplier α_i for each constraint equation in $(D.3)$:

$$L = \frac{1}{2}\|w\|^2 - \sum_{i=1}^{l} \alpha_i(\epsilon + \bar{x} \cdot \bar{w} + b - y_i). \tag{D.4}$$

In noisy systems or nonseparable problems, finding a solution for real applications that exactly satisfies these constraints is rarely possible. One must allow for training errors without sacrificing simplicity. To balance these concerns, we introduce the positive slack variable, ξ_i, which represents a training deviation *beyond* the allowed error ϵ. That is,

$$\xi_i = \begin{cases} 0, & 0 \leq \ |f(\bar{x}_i) - y_i| \leq \epsilon \\ |f(\bar{x}_i) - y_i| - \epsilon, & |f(\bar{x}_i) - y_i| > \epsilon \end{cases} \tag{D.5}$$

The Lagrangian then becomes:

$$L = \frac{1}{2}\|w\|^2 + C\sum_{i=1}^{l} \xi_i - \sum_{i=1}^{l} \alpha_i(\epsilon - \xi_i + \bar{x} \cdot \bar{w} + b - y_i). \tag{D.6}$$

Dual Formulation

The Lagrangian formulation requires us to minimize L with respect to $\bar{w}$ and b, while ensuring that $\frac{\partial L}{\partial \alpha_i = 0}$. However, because this is a convex quadratic programming problem, it is understood that the solution is equivalent to that of the dual problem. In the dual problem, we must instead *maximize* L and ensure that $\frac{\partial L}{\partial w}, \frac{\partial L}{\partial b}, \frac{\partial L}{\partial \xi_i} = 0$. This transformation produces a quadratic optimization problem. The differential conditions give:

$$\frac{\partial L}{\partial \bar{w}} = \bar{w} - \sum_{i=1}^{l} \alpha_i \bar{x}_i = 0 \tag{D.7}$$

$$\frac{\partial L}{\partial b} = \sum_{i=1}^{l} \alpha_i = 0 \tag{D.8}$$

$$\frac{\partial L}{\partial \xi_i} = C - \alpha_i = 0 \tag{D.9}$$

Substituting those into our Lagrangian results in the final form:

$$L = -\frac{1}{2} \sum_{i,j=1}^{l} \alpha_i \alpha_j \bar{x}_i \cdot \bar{x}_j - \epsilon \sum_{i=1}^{l} \alpha_i + \sum_{i=1}^{l} \alpha_i y_i \tag{D.10}$$

$$\text{given} \begin{cases} \sum_{i,j=1}^{l} \alpha_i & = & 0 \\ \alpha_i & \in & [0, C] \end{cases} \tag{D.11}$$

Note that the training data appear only in the form of an inner product, $\bar{x}_i \cdot \bar{x}_j$.

The constraint equation ($D.7$) gives us an explicit form for the $\bar{w}$ in the solution,

$$w = \sum_{i=1}^{l} \alpha_i \bar{x}_i \tag{D.12}$$

as a linear expansion over the training data. Those data with non-zero α_i are called the *support vectors*. The other training data are irrelevant to the solution; omitting them from the training sample would result in an identical regression function.

D.1.2 Non-linear regression: kernel functions

A linear regression function is understandably limited and has little value to real applications. In order to allow applications of the formalism to non-linear problems, one can map the training data

$$\Phi(\bar{x}) : \mathbb{R}^n \longmapsto \mathcal{H} \tag{D.13}$$

to a higher-dimensional space $\mathcal{H}$, in which the problem is again linear. Mapping the terms in our Lagrangian, we note that L depends on the mapping only in the form of $\Phi(\bar{x}_i) \cdot \Phi(\bar{x}_j)$. In principle, it may be very complex to construct and evaluate $\Phi(\bar{x})$. However, if we had a relatively simple *kernel function* $K(\bar{x}_i, \bar{x}_j) = \Phi(\bar{x}_i) \cdot \Phi(\bar{x}_j)$, which we could evaluate in the space of the training data, then we could use this in place of our higher dimensional dot-product and solve the problem in the lower dimensional space, as if it were linear. In this way, we could avoid explicitly constructing the higher-dimensional space or mapping our training data.

In practice it is not possible to obtain a customized kernel function for every set of training data. Instead, we make use of a small stable of kernels which represent typical problems of varying complexity. Such kernel functions, and the spaces they map to are:

$$\begin{aligned} K(\bar{x}_i, \bar{x}_j) &= \mathrm{e}^{(\bar{x}_i - \bar{x}_j)^2/2\sigma^2} \qquad \infty-\text{dimensional} \\ K(\bar{x}_i, \bar{x}_j) &= (\bar{x}_i \cdot \bar{x}_j + 1)^p \qquad p-\text{dimensional} \\ K(\bar{x}_i, \bar{x}_j) &= \tanh(\kappa \bar{x}_i \cdot \bar{x}_j - \delta) \qquad . \end{aligned} \tag{D.14}$$

The choice of kernel function depends entirely on knowledge of the complexity of the problem. In the following sections, we describe applications of SVR with a Gaussian kernel.

D.2 Search for the Higgs Boson

One area of very active research in high energy physics is the search for the theorized Higgs boson; the Higgs plays a key role in the spontaneous breaking of electroweak symmetry and the assignment of masses to fundamental particles[64, 63]. The Higgs boson (h) may appear alongside a W boson at a proton-antiproton collider in a process such as $p\bar{p} \to Wh \to l\nu_l b\bar{b}$; the final state contains a lepton l (electron, muon or tau), its corresponding neutrino ν_l, a bottom quark (b), and an anti-bottom quark ($\bar{b}$), the last two of which appear in the detector as jets of particles. Of course, there are

many other processes that mimic this final state and which occur at much higher rate, R. The three most worrisome are included below.

Process Description	*Process*			R/R_{Wh}
W and Higgs bosons	$p\bar{p}$	$\rightarrow Wh$	$\rightarrow l\nu_l b\bar{b}$	1.0
W boson and bottom quark pair prod.	$p\bar{p}$	$\rightarrow Wb\bar{b}$	$\rightarrow l\nu_l b\bar{b}$	48.2
W & Z^0 bosons	$p\bar{p}$	$\rightarrow WZ^0$	$\rightarrow l\nu_l b\bar{b}$	34.1
top quark pair production.	$p\bar{p}$	$\rightarrow t\bar{t}$	$\rightarrow l\nu_l b\bar{b}$	14.5

Though all of these processes generate events with the same set of final state objects, it is possible to distinguish them from each other. The widely varying topologies produce objects with distinct, though overlapping, tendancies in energies and angular relationships. For example, due to the heaviness of the top quark (t), its final state tends to have more total transverse energy. Further, since the Higgs boson has a specific mass, set to 115 GeV/c^2, the bottom quarks (b) into which it decays have a total energy equal to that mass; this helps to distinguish it from other events, specifically WZ^0, where the bottom quarks have a total energy equal to the Z^0 mass, 92 GeV/c^2. Figure D.1 shows the distributions of four variables from simulated events for Higgs production and all three background processes. Samples were generated using the PYTHIA [67] physics process simulator and the detector response was simulated with SHW [58]. Two thousand events were generated for each sample, not reflecting the expected relative occurances. The samples were split evenly into training and testing samples.

The task of SVR is to construct a function $f(\bar{x}) : \mathbb{R}^4 \rightarrow [-1, 1]$, with $\bar{x}$ a vector of physics parameters for a given event, where a value of f near 1.0 indicates a signal-like vector and f near -1.0 indicates a background-like vector. Accepting only events above a specific value, P_c, would allow us to assemble a sample enriched in signal events at the expense of background. Note that we choose support vector regression rather than support vector discrimination, which allows us to perform a detailed study of the performance at various values of P_c; data analyses are therefore free to make their own choice regarding the relative importance of including signal events or rejecting background.

We construct our support vector regression function using the package LIBSVM [60] with a Gaussian kernel function. The parameter ϵ was set to 0.05, and C to 0.5; the performance did not strongly depend on small variations in these parameters. The choice of kernel widths strongly influenced the performance; details are discussed in Section 3.1.

In order to compare SVR's performance to other standard approaches to this problem, we used the identical data set to train a feed-forward multi-layer artificial neural network. Using the package JETNET [66], we built a three-layer network with eight nodes in the hidden layer, trained with back-propagation. JETNET is one of the most commonly used artificial neural net packages in experimental high energy physics; we use it here to provide a well-understood reference.

The resulting output distributions $F(r)$ for each process, scaled to lie over the range of regression outputs $r = [-1, 1]$, for SVR and ANN are given in Figure D.2. One can see that the signal peaks towards higher values of r while the background prevails at lower values. The crucial evaluator of performance is the balance between the two quantities *efficiency*, ε, which measures the fraction of the signal which survives the selection, defined as

$$\varepsilon(P_c) = \int_{P_c}^{1} dr F_{Wh}(r), \tag{D.15}$$

and *purity*, p, which measures the fraction of the selected data which originates from the signal process,

$$p(P_c) = \frac{R_{Wh} \int_{P_c}^{1} dr F_{Wh}(r)}{\sum_i R_i \int_{P_c}^{1} dr F_i(r)}, \tag{D.16}$$

where $i \in \{Wh, Wb\bar{b}, WZ^0, t\bar{t}\}$ runs over all processes, and R_i is the rate for a process given in Table D.2.

The efficiency of any algorithm decreases as the threshold P_c is increased and a smaller fraction of the signal events are selected. As the signal typically has a larger r than the background, increasing the threshold improves the fraction of the selected events which are signal events, and hence the purity.

The choice of P_c is typically made to be that which balances ε and p by maximizing the *significance*

$$s(P_c) = \frac{R_{Wh} \int_{P_c}^{1} dr F_{Wh}(r)}{\sqrt{(\sum_{bg} R_{bg} \int_{P_c}^{1} dr F_{bg}(r))}} \tag{D.17}$$

where $bg \in \{Wb\bar{b}, WZ^0, t\bar{t}\}$ runs over background processes only.

The values of ε, p and s depend crucially on P_c. The left side of Figure D.3 shows the ε versus p curves for both SVR and ANN; this curve is produced by varying P_c over its range from -1.0 ($\varepsilon = 0$) to 1.0 ($\varepsilon = 1$). The right side of the same figure shows how s varies with P_c. The purity and significance are low due to the low rate of the signal process Wh with respect to the background processes.

It is clear that SVR is a powerful and effective tool in signal discrimination.

D.2.1 Kernel Function Widths

A cursory examination of Figure 1 makes it clear that the distributions have widely varying widths. For support vector regression to effectively discriminate between the input classes, the widths of the Guassian kernel must be narrow enough to resolve key features but broad enough to construct a general rule. We cannot achieve optimal resolution in all parameters if every dimension uses Gaussians of the same width.

We modified the Gaussian kernel in LIBSVM:

$$k(\bar{x}_i, \bar{x}_j) = e^{-\|\bar{x}_i - \bar{x}_j\|^2/2\sigma^2},$$

to allow for Gaussian kernels with widths that vary from dimension to dimension:

$$k(\bar{x}_i, \bar{x}_j) = e^{-\|(\bar{x}_i - \bar{x}_j)/\sqrt{2}\sigma\|^2},$$

where σ is now a vector whose elements the width of the kernel in a given

dimension.

We chose the width in each dimension to maximize significance. Figure D.4 shows the variation of the performance as a function of the widths.

The width in each dimension was varied independently, while the others were held fixed. When the optimal width in a parameter was found, it was fixed and the width varied in the next parameter; hence, the performance increases steadily from the first parameter to the last. The parameter "Di-jet mass" showed the strongest correlation between performance and kernel width; the distribution in this parameter has a sharp discriminating feature and it is clearly important that the width be on the order of the size of this feature.

D.2.2 Training Sample Size

The size of the training sample was varied between ten and one thousand data points; the testing sample was fixed at one thousand points. Figure D.5 shows the performance for each sample size.

SVR performance varied more smoothly with training sample size than did the ANN. As the ANN constructed with nine hundred training points outperformed all other ANNs, this was used to calculate performance measures in the previous sections.

D.3 Discussion

An important issue is the difficulty of the selection of a width of the Gaussian kernel for each parameter. The distributions may vary widely from parameter to parameter; it is important that for each parameter the kernel be narrow enough to resolve important features but wide enough to provide a smoothly varying result. An automatic optimization of each dimension's kernel width would faciliate the use of SVR in high energy physics.

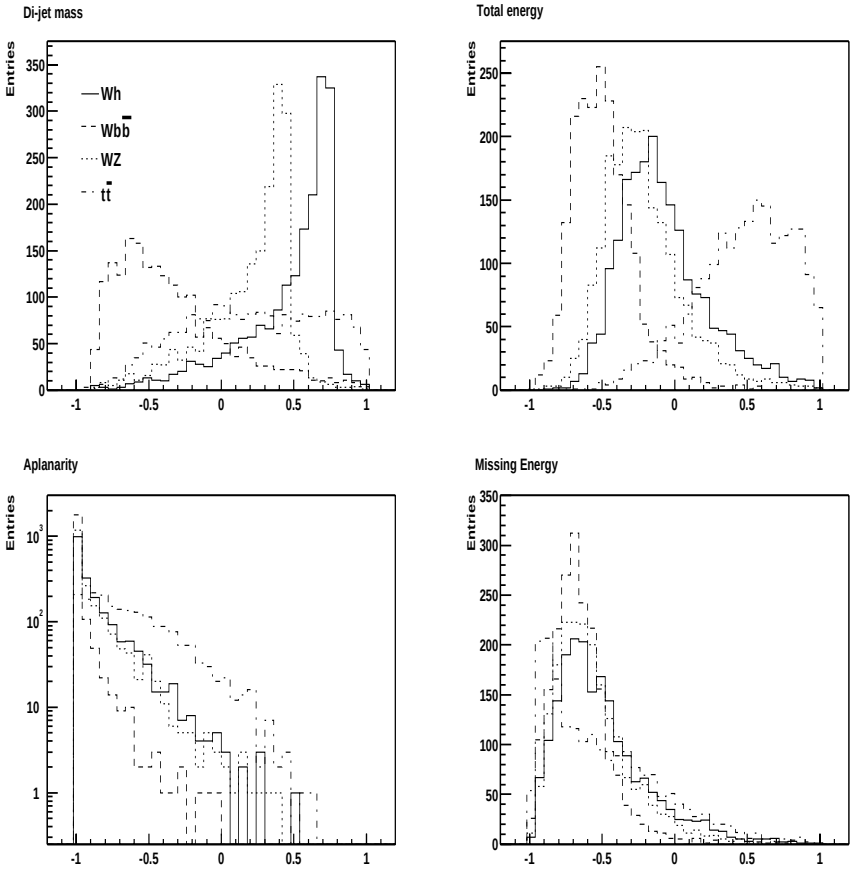

Figure D.1: Distributions in four parameters for the four processes. Clockwise from top left: reconstructed Higgs mass from two jets, total transverse energy, unbalanced or missing transverse energy and aplanarity. All variables are rescaled to $[-1, 1]$.

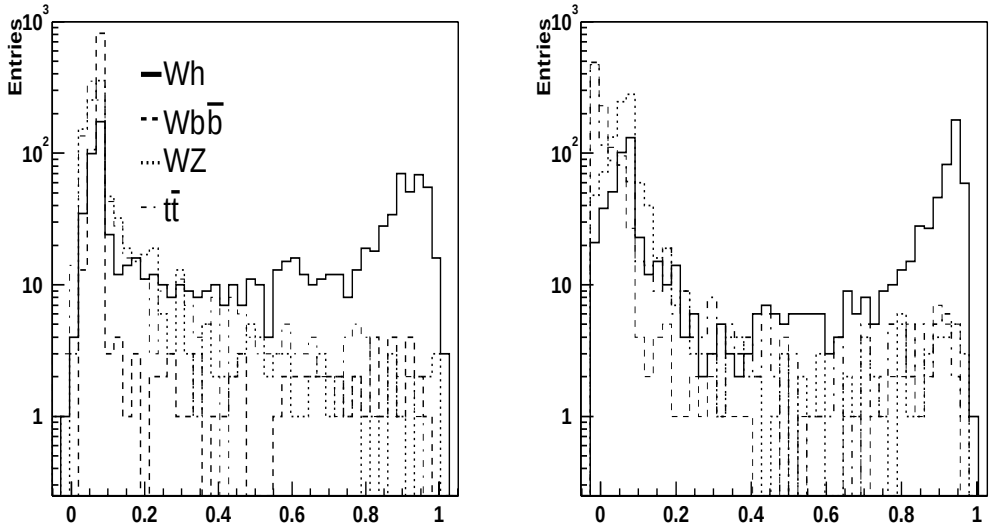

Figure D.2: Support vector regression (*left*), and artificial neural network (*right*) outputs for signal (Wh) and the three background processes ($Wb\bar{b}$, WZ^0, and $t\bar{t}$). Histograms are normalized to 1.

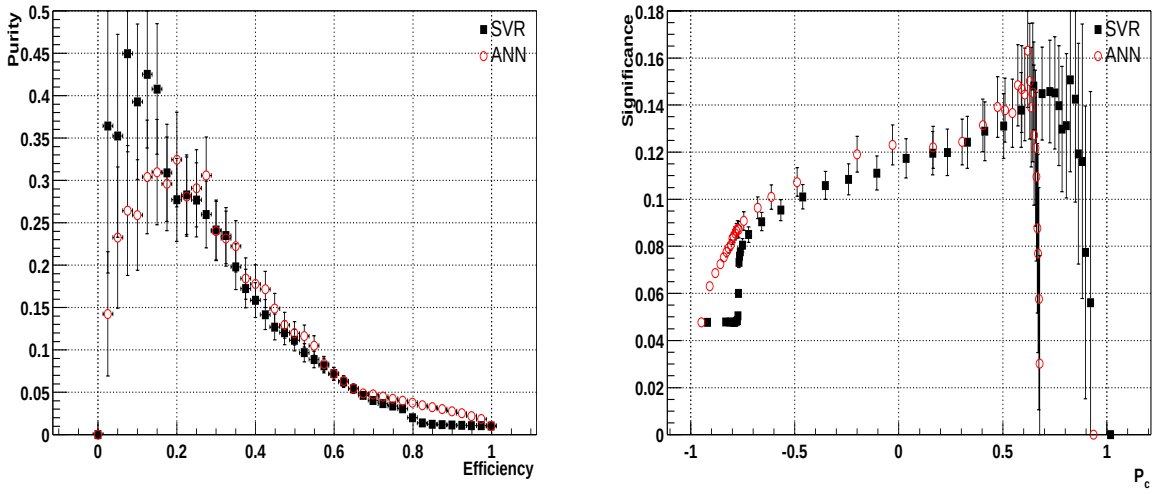

Figure D.3: Left, purity, p and efficiency, ε, as defined in the text, for support vector regression and an artificial neural network algorithm. Right, significance s for both algorithms. See text for detailed discussion.

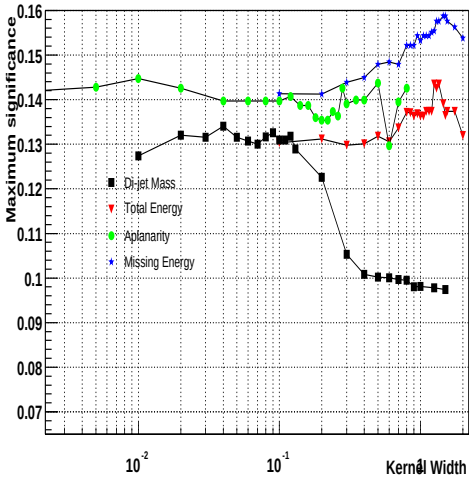

Figure D.4: Variation of support vector regression performance (measured by maximum signficance s, defined in the text), as a function of the width of the Guassian kernel for each physics parameter.

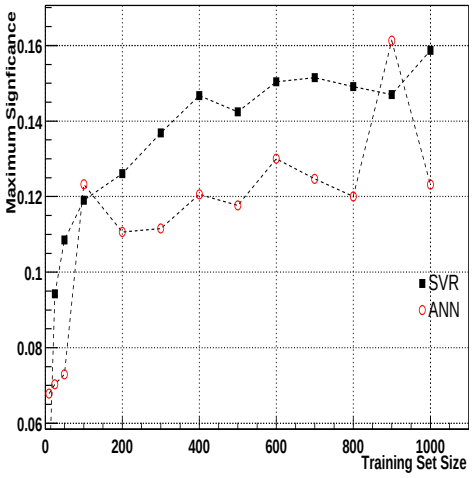

Figure D.5: Variation of support vector regression and artificial neural network performance (measured by maximum significance s, defined in the text), as a function of the size of the training sample.